

Nanomaterials for Medical Applications: Benefits and Risks

Guest Editors: Ecaterina Andronescu, Jared M. Brown, Faik Nuzhet Oktar,
Simeon Agathopoulos, Joshua Chou, and Akiko Obata





Nanomaterials for Medical Applications: Benefits and Risks

Nanomaterials for Medical Applications: Benefits and Risks

Guest Editors: Ecaterina Andronescu, Jared M. Brown,
Faik Nuzhet Oktar, Simeon Agathopoulos, Joshua Chou,
and Akiko Obata



Copyright © 2016 Hindawi Publishing Corporation. All rights reserved.

This is a special issue published in "Journal of Nanomaterials." All articles are open access articles distributed under the Creative Commons Attribution License, which permits unrestricted use, distribution, and reproduction in any medium, provided the original work is properly cited.

Editorial Board

- Domenico Acierno, Italy
Katerina Aifantis, USA
Nageh K. Allam, USA
Margarida Amaral, Portugal
Martin Andersson, Sweden
Raul Arenal, Spain
Ilaria Armentano, Italy
Vincenzo Baglio, Italy
Lavinia Balan, France
Thierry Baron, France
Andrew R. Barron, USA
Reza Bayati, USA
Hongbin Bei, USA
Daniel Bellet, France
Stefano Bellucci, Italy
Enrico Bergamaschi, Italy
Samuel Bernard, France
D. Bhattacharyya, New Zealand
Sergio Bietti, Italy
Giovanni Bongiovanni, Italy
Theodorian Borca-Tasciuc, USA
Mohamed Bououdina, Bahrain
Torsten Brezesinski, Germany
C. Jeffrey Brinker, USA
Christian Brosseau, France
Philippe Caroff, Australia
Victor M. Castaño, Mexico
Albano Cavaleiro, Portugal
Bhanu P. S. Chauhan, USA
Shafiul Chowdhury, USA
Jin-Ho Choy, Republic of Korea
Kwang-Leong Choy, UK
Yu-Lun Chueh, Taiwan
Elisabetta Comini, Italy
Giuseppe Compagnini, Italy
David Cornu, France
Miguel A. Correa-Duarte, Spain
P. Davide Cozzoli, Italy
Shadi A. Dayeh, USA
Luca Deseri, USA
Yong Ding, USA
Philippe Dubois, Belgium
Zehra Durmus, Turkey
Joydeep Dutta, Oman
Ali Eftekhari, USA
- Jeffrey Elam, USA
Samy El-Shall, USA
Ovidiu Ersen, France
Claude Estournès, France
Andrea Falqui, KSA
Matteo Ferroni, Italy
Elena J. Foster, USA
Ilaria Fratoddi, Italy
Alan Fuchs, USA
Miguel A. Garcia, Spain
Siddhartha Ghosh, Singapore
P. K. Giri, India
Russell E. Gorga, USA
Jihua Gou, USA
Jean M. Greneche, France
Smrati Gupta, Germany
Kimberly Hamad-Schifferli, USA
Simo-Pekka Hannula, Finland
Michael Harris, USA
Yasuhiko Hayashi, Japan
F. Hernandez-Ramirez, Spain
Michael Z. Hu, USA
Nay Ming Huang, Malaysia
Shaoming Huang, China
David Hui, USA
Zafar Iqbal, USA
Balachandran Jeyadevan, Japan
Xin Jiang, Germany
Rakesh Joshi, Australia
J.-won Kang, Republic of Korea
Hassan Karimi-Maleh, Iran
Antonios Kelarakis, UK
Alireza Khataee, Iran
Ali Khorsand Zak, Iran
Philippe Knauth, France
Ralph Krupke, Germany
Christian Kübel, Germany
Prashant Kumar, UK
Michele Laus, Italy
Eric Le Bourhis, France
Jun Li, Singapore
Meiyong Liao, Japan
Shijun Liao, China
Silvia Licocchia, Italy
Wei Lin, USA
- Nathan C. Lindquist, USA
Zainovia Lockman, Malaysia
Nico Lovergine, Italy
Jim Low, Australia
Jue Lu, USA
Ed Ma, USA
Laura M. Maestro, Spain
Gaurav Mago, USA
Muhamamd A. Malik, UK
Devanesan Mangalaraj, India
Sanjay R. Mathur, Germany
Tony McNally, UK
Yogendra Mishra, Germany
Paulo Cesar Morais, Brazil
Paul Munroe, Australia
Jae-Min Myoung, Republic of Korea
Rajesh R. Naik, USA
Albert Nasibulin, Russia
Toshiaki Natsuki, Japan
Koichi Niihara, Japan
Natalia Noginova, USA
Sherine Obare, USA
Won-Chun Oh, Republic of Korea
Atsuto Okamoto, Japan
Abdelwahab Omri, Canada
Ungyu Paik, Republic of Korea
Piersandro Pallavicini, Italy
Edward A. Payzant, USA
Alessandro Pegoretti, Italy
Ton Peijs, UK
Oscar Perales-Pérez, Puerto Rico
Jorge Pérez-Juste, Spain
Alexey P. Popov, Finland
Philip D. Rack, USA
Peter Reiss, France
Orlando Rojas, USA
Marco Rossi, Italy
Ilker S. Bayer, Italy
Cengiz S. Ozkan, USA
Sudipta Seal, USA
Shu Seki, Japan
Vladimir Šepelák, Germany
Huaiyu Shao, Japan
Prashant Sharma, USA
Donglu Shi, USA



Bhanu P. Singh, India
Surinder Singh, USA
Vladimir Sivakov, Germany
Ashok Sood, USA
Adolfo Speghini, Italy
Marinella Striccoli, Italy
Xuping Sun, KSA
Ashok K. Sundramoorthy, USA
Angelo Taglietti, Italy
Bo Tan, Canada
Leander Tapfer, Italy
Valeri P. Tolstoy, Russia

Muhammet S. Toprak, Sweden
R. Torrecillas, Spain
Achim Trampert, Germany
Takuya Tsuzuki, Australia
Tamer Uyar, Turkey
Bala Vaidhyanathan, UK
Luca Valentini, Italy
Rajender S. Varma, USA
Ester Vazquez, Spain
Antonio Villaverde, Spain
Ajayan Vinu, Australia
Ruibing Wang, Macau

Shiren Wang, USA
Yong Wang, USA
Magnus Willander, Sweden
Ping Xiao, UK
Zhi Li Xiao, USA
Yangchuan Xing, USA
Doron Yadlovker, Israel
Yoke K. Yap, USA
Kui Yu, Canada
William Yu, USA
Michele Zappalorto, Italy
Renyun Zhang, Sweden

Contents

Nanomaterials for Medical Applications: Benefits and Risks

Ecaterina Andronescu, Jared M. Brown, Faik Nuzhet Oktar, Simeon Agathopoulos, Joshua Chou, and Akiko Obata

Volume 2016, Article ID 8284319, 2 pages

Size Effects of Pt Nanoparticle/Graphene Composite Materials on the Electrochemical Sensing of Hydrogen Peroxide

Chia-Liang Sun, Jheng-Sin Su, Shun-Yi Lai, and Yu-Jen Lu

Volume 2015, Article ID 861061, 7 pages

Case Study on Risk Evaluation of Silver Nanoparticle Exposure from Antibacterial Sprays Containing Silver Nanoparticles

Ellen Kim, Ji Hyun Lee, Jin Kwon Kim, Gun Ho Lee, Kangho Ahn, Jung Duck Park, and Il Je Yu

Volume 2015, Article ID 346586, 8 pages

Interim Clinical Outcomes in Nanocomposite Bone Material Repairing Large Proximal Femoral Defect of Fibrous Dysplasia

Yun Lang, Ze-ping Yu, Yan Xiong, Chong-qi Tu, Cheng Ren, Bin Zhang, Hong-sheng Yang, Fang Yuan, Hong Li, Yong-gang Yan, and Hong Duan

Volume 2015, Article ID 385612, 9 pages

Effects of Nitrogen-Doped Multiwall Carbon Nanotubes on Murine Fibroblasts

J. G. Munguía-Lopez, E. Muñoz-Sandoval, J. Ortiz-Medina, F. J. Rodriguez-Macias, and A. De Leon-Rodriguez

Volume 2015, Article ID 801606, 7 pages

Effect of Lipophilic Bismuth Nanoparticles on Erythrocytes

Rene Hernandez-Delgado, Appala Raju Badireddy, Valentin Zaragoza-Magaña, Rosa Isela Sánchez-Nájera, Shankaraman Chellam, and Claudio Cabral-Romero

Volume 2015, Article ID 264024, 9 pages

Evaluation of Biological Toxicity of CdTe Quantum Dots with Different Coating Reagents according to Protein Expression of Engineering *Escherichia coli*

Wei Xu, Ting Du, Chaoyong Xu, Heyou Han, Jiangong Liang, and Shaobo Xiao

Volume 2015, Article ID 583963, 7 pages

Impact of Silver and Iron Nanoparticle Exposure on Cholesterol Uptake by Macrophages

Jonathan H. Shannahan, Hari Sowrirajan, Indushekhar Persaud, Ramakrishna Podila, and Jared M. Brown

Volume 2015, Article ID 127235, 12 pages

Tetracycline Loaded Collagen/Hydroxyapatite Composite Materials for Biomedical Applications

Laura Cristina Rusu, Ioan Avram Nedelcu, Mădălina Georgiana Albu, Maria Sonmez, Georgeta Voicu, Marius Radulescu, Denisa Ficai, Anton Ficai, Meda-Lavinia Negrutiu, and Cosmin Sinescu

Volume 2015, Article ID 361969, 5 pages

A Review on the Synthesis Methods of CdSeS-Based Nanostructures

Hong Li, Chengbiao Wang, Zhijian Peng, and Xiuli Fu

Volume 2015, Article ID 519385, 16 pages

Editorial

Nanomaterials for Medical Applications: Benefits and Risks

**Ecaterina Andronescu,¹ Jared M. Brown,² Faik Nuzhet Oktar,³
Simeon Agathopoulos,⁴ Joshua Chou,⁵ and Akiko Obata⁶**

¹Department of Science and Engineering of Oxide Materials and Nanomaterials, Faculty of Applied Chemistry and Materials Science, University Politehnica of Bucharest, Bucharest, Romania

²Department of Pharmaceutical Sciences, Skaggs School of Pharmacy, University of Colorado Anschutz Medical Campus, Aurora, CO, USA

³Bioengineering Department, Faculty of Engineering and Advanced Nanomaterials Research Laboratory, Marmara University, Istanbul, Turkey

⁴Materials Science and Engineering Department, Ioannina University, Ioannina, Greece

⁵Advanced Tissue Regeneration & Drug Delivery Group, School of Medical and Molecular Biosciences, University of Technology, Sydney, Australia

⁶Graduate School of Engineering, Nagoya Institute of Technology, Nagoya, Japan

Correspondence should be addressed to Ecaterina Andronescu; ecaterina.andronescu@upb.ro

Received 16 December 2015; Accepted 16 December 2015

Copyright © 2016 Ecaterina Andronescu et al. This is an open access article distributed under the Creative Commons Attribution License, which permits unrestricted use, distribution, and reproduction in any medium, provided the original work is properly cited.

Since their discovery, nanomaterials have been intensively studied for both industrial and medical applications. For the medical sector, one important aspect, which is being increasingly recognized, is the safety concerns related to the handling and use of nanomaterials. Currently, scientists are trying to determine whether the benefits outweigh the risks.

This special issue is structured in several subtopics covering: carbon based materials alone or in association with other nanostructured components; various nanoparticles, including quantum dots; or composite nanomaterials as regenerative or drug delivery systems.

In the field of carbon based materials, two very hot subjects are discussed, namely, the influence of nitrogen-doped multiwall carbon nanotubes on the proliferation of fibroblasts and the possibility of the use of Pt nanoparticle/graphene composite materials as electrochemical sensor of hydrogen peroxide. The efficiency of the Pt/graphene-modified glassy carbon (GC) electrodes was characterized by cyclic voltammetry, the main difference between the samples being the size of the nanoparticles (1.3; 1.7; 2.9; and 4.3 nm). The authors found that best results (highest reduction current, the best detection limit, and the best sensitivity) are obtained for the electrodes containing

1.7 nm Pt nanoparticles. Nitrogen-doped multiwall carbon nanotubes were found to be well tolerated below 7 $\mu\text{g}/\text{mL}$ and consequently are suggested by the authors as safe for use in biomedical applications below certain concentrations. Also, this work highlighted that cytotoxicity is dependent on concentration and exhibits a higher toxicity on enzymatic stressed cells than on the nonstressed ones.

The risk evaluation of different nanoparticles is currently of interest worldwide. Silver and magnetite nanoparticles are also studied in this special issue highlighting the advances from the point of view of application and toxicity. Silver, for instance, was studied from the point of view of risk evaluation of silver nanoparticles exposure from sprays and it was found that, depending on exposure type, the limit of exposure ranges between 59 and 146 for inhalation, much lower than 1000 which means the no-risk level while the dermal exposure risk was between 20 000 and 500 000 ($\sim 2\text{--}50 \mu\text{g}/\text{kg}/\text{day}$). So, the exposure of people to silver containing aerosols is risky. Silver and magnetite nanoparticles were also studied from the point of view of the impact of exposure of these nanoparticles to cholesterol uptake by macrophages. This paper clearly indicates that long-term impact of nanoparticles on cellular function must be taken into account before using

nanoparticles for biomedical applications. Lipophilic bis-muth dimercaptopropanol nanoparticles have a very important antimicrobial activity, but at this moment there are no sufficient data. Based on these results, these nanoparticles at a level of up to 100 μM do not cause damage to blood cells. CdTe quantum dots are good candidates for bioimaging but the evaluation of the toxicity must be done in order to avoid any risks. Based on a newly developed evaluation protocol based on protein expression, it was found that the quantum dot shell plays an important role due to first direct contact with cells. The CdSeS nanostructures were analyzed from the point of view of the correlation between synthesis route and applications, especially based on the toxicity of these nanoparticles depending on the synthesis route and used precursors and solvents. Based on this study, such safe, economic, environment friendly, and suitable for large-scale production of alloyed CdSeS nanostructures with high photoluminescence, high stability, and low/no cytotoxicity are still much desired.

The role of nanocomposites for biomedical applications is also discussed in this special issue. The safe use of nanocomposite bone material was examined in a study of a thirty-one-patient clinical trial. The nanocomposite bone material was ultimately found to be useful in the field of orthopedics. Engineered materials can be also improved by adding beneficial components and consequently new functionalities. In this special issue, novel tetracycline loaded collagen/hydroxyapatite composite materials are presented for use in nanomedicine.

Overall, nanomaterials are expected to solve challenges in the health sector through biosensors, contrast agents, and targeted drug vehicles that can deliver antimicrobial or anti-tumoral agents. Unfortunately, the long-term implications are mainly unknown. However, there are some nanomaterials which already have demonstrated adverse behavior in biological systems. This special issue provides a comprehensive update in the field of nanomaterials, especially highlighting the benefits and risks related to use of nanomaterials.

Ecaterina Andronescu
Jared M. Brown
Faik Nuzhet Oktar
Simeon Agathopoulos
Joshua Chou
Akiko Obata

Research Article

Size Effects of Pt Nanoparticle/Graphene Composite Materials on the Electrochemical Sensing of Hydrogen Peroxide

Chia-Liang Sun,^{1,2} Jheng-Sin Su,¹ Shun-Yi Lai,¹ and Yu-Jen Lu³

¹Department of Chemical and Materials Engineering, Chang Gung University, Guishan, Taoyuan 333, Taiwan

²Biosensor Group, Biomedical Engineering Research Center, Chang Gung University, Guishan, Taoyuan 333, Taiwan

³Department of Neurosurgery, Chang Gung Memorial Hospital, No. 5, Fu-Shing Road, Guishan, Taoyuan 333, Taiwan

Correspondence should be addressed to Chia-Liang Sun; sunchialiang@gmail.com

Received 23 July 2015; Accepted 16 November 2015

Academic Editor: Ecaterina Andronescu

Copyright © 2015 Chia-Liang Sun et al. This is an open access article distributed under the Creative Commons Attribution License, which permits unrestricted use, distribution, and reproduction in any medium, provided the original work is properly cited.

The electrochemical detection of hydrogen peroxide (H_2O_2) has attracted much attention recently. Meanwhile, the size of nanoparticles which significantly influences electrocatalytic activity is crucial for electrocatalysts. Hence, we prepared five different size-selected Pt/graphene-modified glassy carbon (GC) electrodes to characterize H_2O_2 level via electrochemical measurements. During the preparation of the nanocomposites, size-selected Pt nanoparticles (NPs) with the mean diameter of 1.3, 1.7, 2.9, and 4.3 nm were assembled onto the graphene surfaces. The electrochemical measurement results are size-dependent for Pt NPs when sensing H_2O_2 . When all cyclic voltammogram results from various electrodes are compared, the Pt-1.7 nm/G-modified GC electrode has the highest reduction current, the best detection limit, and the best sensitivity.

1. Introduction

Since reliable and fast determination of biomolecules is important in many areas such as biotechnology, clinical diagnostics, and food industry, the development of biosensor has attracted extensive attention recently. In general, there are enzymatic and nonenzymatic biosensors in the literature because the enzyme is easily being affected by the environmental factors such as temperature, humidity, and pH values. In addition, the immobilization of enzyme is a complicated and expensive process. Therefore, the nonenzymatic biosensors start to catch the scientists' eyes and attention. The large surface area and excellent electrical properties of graphene allow it to be used in many applications [1–6]. For example, it can connect between the redox centers of an enzyme or protein and an electrode surface. Rapid electron transfer facilitates accurate and selective detection of biomolecules. Its unique structure and properties, such as high specific surface area, high mechanical strength and conductivity, and

its relatively low price make graphene suitable for potential applications. In our lab, we used graphene, Pt/graphene, CuO/graphene, graphene oxide nanoribbons, and multi-walled carbon nanotube/graphene oxide nanoribbon core-shell heterostructures to detect biomolecules in the past five years [7–10]. Here we want to utilize the same graphene-based materials to further monitor other biomolecules.

H_2O_2 is a chemical used widely in the food, pharmaceutical, paper, and chemical industries. H_2O_2 is also one of the products of reactions catalyzed by enzymes in many biological and environmental processes. Therefore, the development of a biosensor for detecting H_2O_2 is important [11–23]. The electrode materials for H_2O_2 biosensor in the literature can be categorized as polymers, carbon nanotubes, graphene, nanoparticles, their composite materials, and others. After immobilizing horseradish peroxidase (HRP) onto the composite, the H_2O_2 biosensor could be used as a component for investigating bioelectrochemical activity [11–13]. Fan et al. developed a new kind of enzymatic biosensor using

biomimetic graphene capsules (GRCAPS) in 2015 [14]. Polybenzimidazole (PBI), polyamic acids (PAAs), benzothiazole (BT), benzoxazole (BO), and their composites as polymers were used to modify gold electrode to determine H_2O_2 in 2011 [15, 16]. Li et al. fabricated a nonenzymatic H_2O_2 sensor by utilizing MWCNTs as the matrix for electrodeposition of Pt nanoparticles [17]. Karuppiah et al. have constructed a novel glucose and H_2O_2 biosensor based on graphene/ Co_3O_4 NPs composite modified electrode [18]. H_2O_2 showed a better electrochemical response at the nitrogen and boron codoped graphene modified GC electrode (GCE), much higher than that of graphene solely doped with N atoms (N-G) or with B atoms (B-G) [19]. The Prussian blue nanocubes-nitrobenzene-reduced graphene oxide nanocomposites/GCE showed good electrocatalytic ability for the reduction of H_2O_2 with good stability and selectivity [20]. 3D graphene foam supported PtRu on Ni foam exhibited an excellent electrocatalytic activity toward the H_2O_2 detection [21]. The activity of MoS_2 NPs toward the reduction of H_2O_2 released by cells was demonstrated in 2013 [22]. The as-produced AuCu nanowires have been explored toward the detection of H_2O_2 [23].

There are many important factors that influence the catalytic activity of catalysts. One of the very important parameters is the size of the nanoparticles. Although there are studies using nanoparticles on nanocarbons for sensing H_2O_2 , the effects of particle size remain unclear. Therefore, in this study, we try to investigate the size effects of Pt nanoparticle supported on graphene. The electrochemical detection of H_2O_2 was used to evaluate the properties of these graphene-supported Pt catalysts. The size-dependent electrochemical properties will be displayed and discussed in this study.

2. Material and Methods

2.1. Chemicals. Platinum(IV) chloride (PtCl_4 , 99%) was purchased from Acros Organics. Ethyl glycol was purchased from J.T. Baker. Nafion (DuPont, 5 wt.%) was used to generate the ink. NaOH and H_2O_2 were obtained from Sigma. All solutions were prepared with deionized water with a resistivity of 18 M Ω /cm.

2.2. Preparation of Pt Colloidal Solution. Pt nanoparticles were synthesized using the polyol method reported in detail elsewhere [24–27]. In short, 0.4652 g PtCl_4 was dissolved in 50 mL ethylene glycol. In order to control the size of the particles, the appropriate amount of sodium hydroxide (NaOH) was added to the PtCl_4 solutions. The mixture was then stirred at room temperature for 30 min with rotational speed of 600 rpm, heated to 160°C for 3 hr, and finally allowed to cool down to room temperature, forming a Pt colloidal solution (1.3, 1.7, 2.9, and 4.3 nm). The NaOH concentrations for Pt colloids of 1.3, 1.7, 2.9, and 4.3 nm are 0.6, 0.4, 0.3, and 0.1 M, respectively.

2.3. Deposition of Pt Nanoparticles on Graphene. Graphene oxide powders were prepared following Staudenmaier's

method and reduced to graphene powders by annealing at 1050°C under an argon atmosphere. 20 mg of graphene powders was mixed with the Pt colloidal solutions in a 40 mL solution containing 2 M sulfuric acid and ethylene glycol [25–27]. The volume ration between sulfuric acid and ethylene glycol is 1 to 1. The Pt ratio is controlled to be around 20 wt.% for Pt-G catalyst. The solution was then stirred for 24 h and then sonicated using an ultrasonic processor (Part number Q700) for 15 min. The resulting solution was filtered to recuperate the catalyst. Four Pt-G catalysts with different average particle sizes were obtained in this manner.

2.4. Material Characterization. Transmission electron microscopy (JEOL JEM-1230, 100 kV) was used to characterize sample morphologies.

2.5. Electrode Preparation and Electrochemical Measurements. The catalyst ink for electrochemical measurement was prepared with the Pt-graphene powders. 3 mL deionized water, 2 mL ethanol, 60 μL Nafion, and 6 mg Pt-graphene powders were sonicated to make the ink [25–27]. Potentiostat/galvanostat (CHI 405A) was used for electrochemical measurements. The working electrode was 3 mm-diameter glassy carbon (GC) disc electrode on which 10 μL of the catalyst ink was deposited and dried at room temperature. A silver/silver chloride (Ag/AgCl) electrode and a large surface area platinum electrode were used as the reference and counterelectrode, respectively. All potentials in this study are reported with respect to the Ag/AgCl electrode.

3. Results and Discussion

3.1. Controlled Synthesis of Size-Selected Pt Colloids. Figure 1 displays TEM images of Pt nanoparticles with different average sizes varying between 1.7 and 4.3 nm and their histograms. The particle sizes were controlled by changing the pH of the PtCl_4 solution dissolved in ethylene glycol. The histograms show the size distribution of the particles with an average diameter which was taken over 300 individual particles from the TEM pictures. The NaOH concentrations of ethylene glycol with dissolved PtCl_4 are 0.1, 0.3, 0.4, and 0.6 M for making 4.3, 2.9, 1.7, and 1.3 nm Pt colloids. When NaOH concentrations become large, the mean diameters of Pt colloids get small. It is worthwhile to mention that the sequence for mixing PtCl_4 solution is very important. Before adding any NaOH, PtCl_4 needs to be dissolved in ethylene glycol completely. If PtCl_4 was added to the ethylene glycol already with NaOH, there will be no size control effect though Pt nanoparticles can still be formed.

3.2. Material Characterization of Graphene-Supported Pt Nanoparticles. Figure 2 shows the TEM images of the 4.3, 2.9, 1.7, and 1.3 nm particles supported on single graphene sheets. The small dark spots are the Pt nanoparticles adsorbed

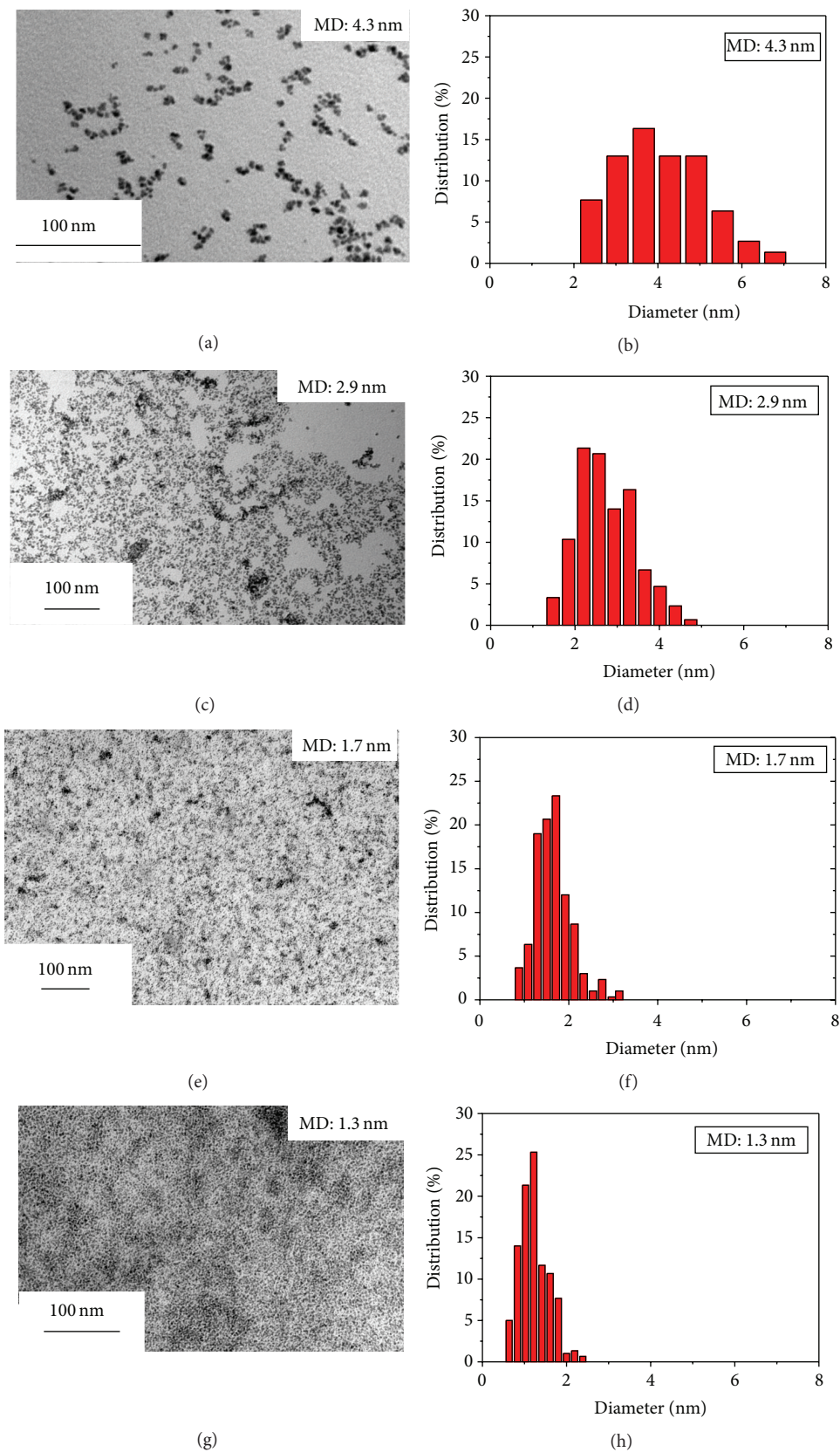


FIGURE 1: Transmission electron microscope images of (a) 4.3 nm-diameter, (c) 2.9 nm-diameter, (e) 1.7 nm-diameter, and (g) 1.3 nm-diameter Pt colloidal nanoparticles. Histograms show the particle size distribution of (b) 4.3 nm-diameter, (d) 2.9 nm-diameter, (f) 1.7 nm-diameter, and (h) 1.3 nm-diameter Pt nanoparticles.

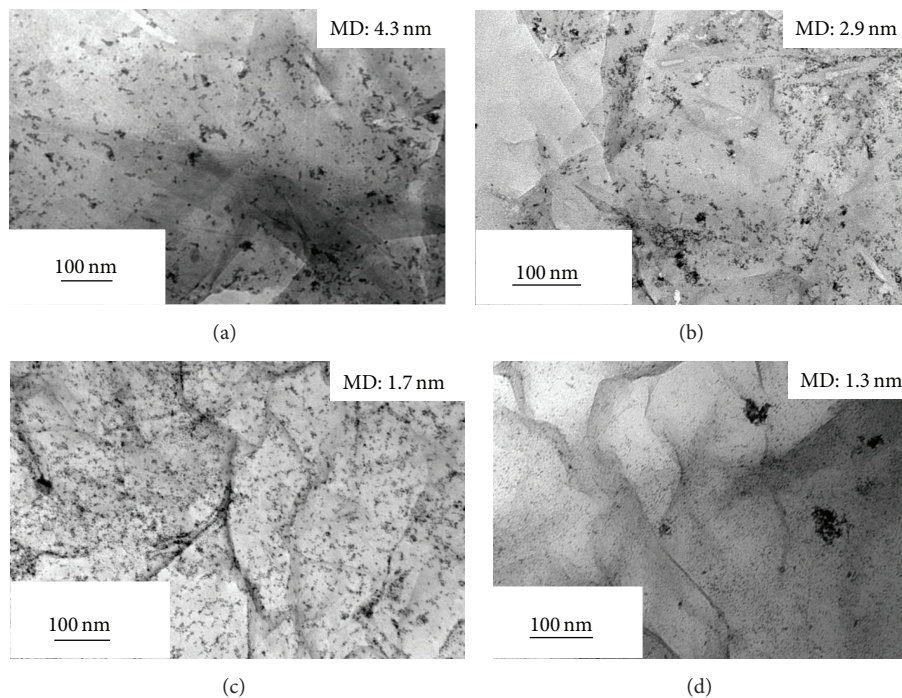


FIGURE 2: Transmission electron microscope images of (a) Pt-4.3 nm/G catalyst, (b) Pt-2.9 nm/G catalyst, (c) Pt-1.7 nm/G catalyst, and (d) Pt-1.3 nm/G catalyst.

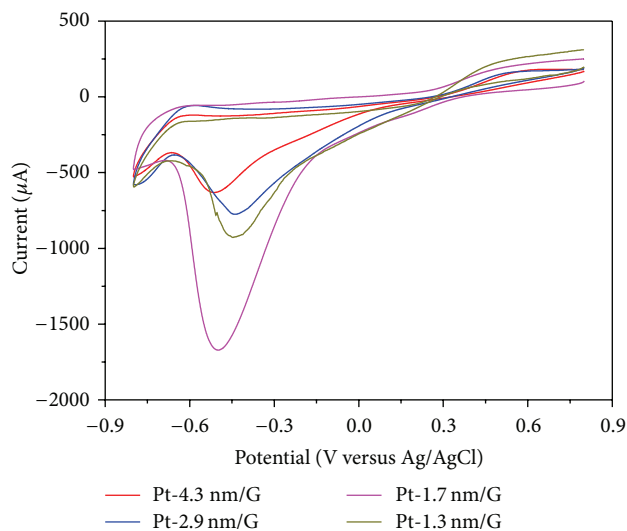


FIGURE 3: Cyclic voltammograms of four Pt/G-modified GC electrodes in 0.1 M PBS (pH 7.0) 10 mM H_2O_2 . Scan rate: 100 mVs^{-1} .

on multilayered graphene as the background that is relatively gray compared to the white hole in other regions of the Cu grid. The wrinkles on single graphene pieces randomly appear in the pictures. Although most of the time the nanoparticles are uniformly distributed on graphene surfaces, sometimes the aggregates could be formed like the two areas in Figure 2(d). This may be owing to the very high surface area of small particles that tend to reduce the total surface energy in the system. It is suggested that the

functional groups on graphene surfaces will help further disperse the small Pt nanoparticles.

3.3. Cyclic Voltammetric Detection of H_2O_2 . Cyclic voltammograms in Figure 3 illustrate the reduction of H_2O_2 for each catalyst. In general, the reduction currents gradually increase when lowering the potential after 0.2 V and there is a main reduction peak for each catalyst. The reduction peaks are

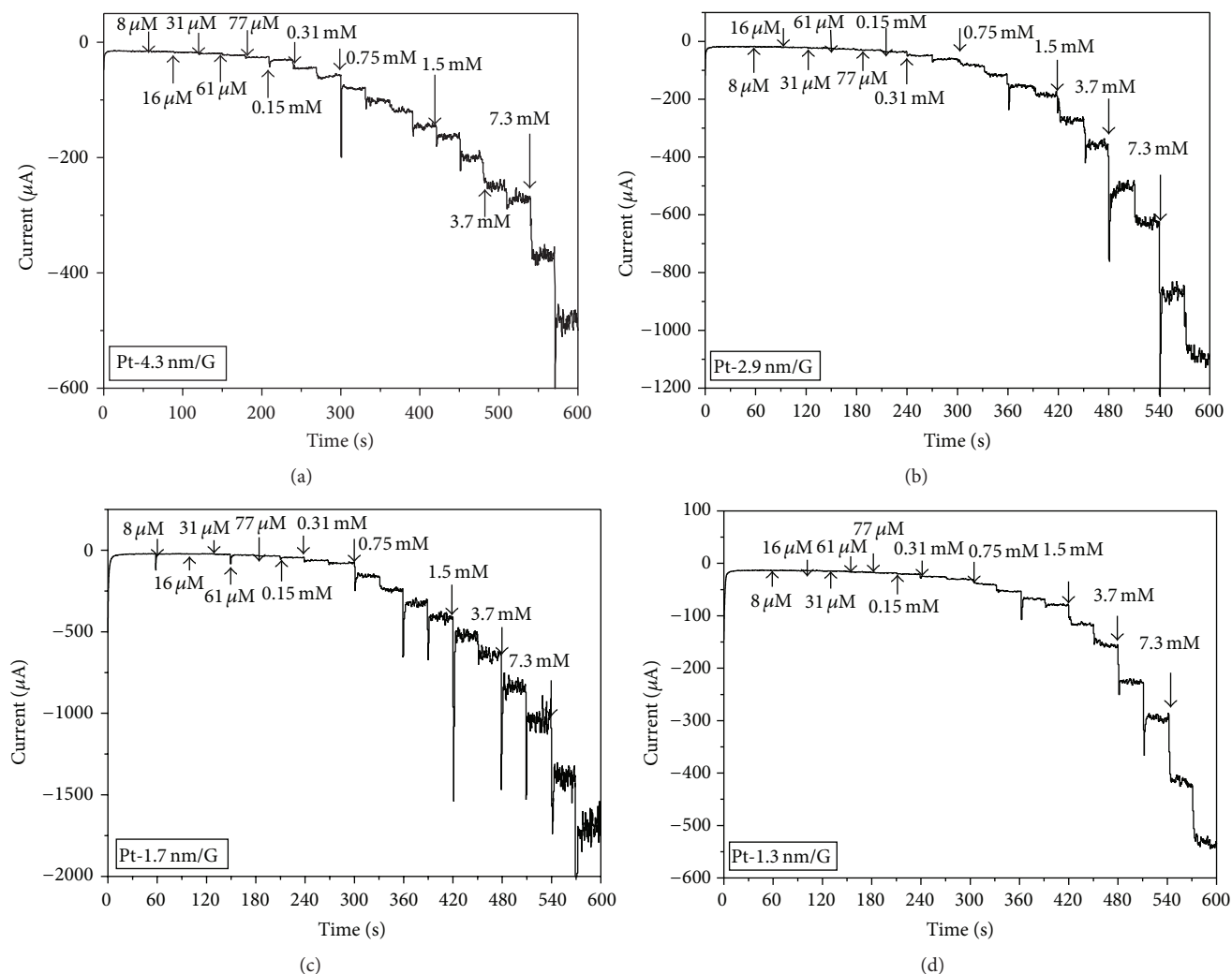


FIGURE 4: Amperometric responses of four Pt/G-modified GC electrodes after the subsequent addition of H_2O_2 in a 0.1 M PBS solution at the potential of -0.5 V.

located around -0.5 V for four catalysts. This is similar to the oxygen reduction reaction (ORR) for the cathode of a fuel cell. The reduction of H_2O_2 is a two-electron process that has low electron transfer number compared to ORR. For the size lower than 10 nm but higher than 1.5 nm, there are three catalysts named Pt-4.3 nm/G, Pt-2.9 nm/G, and Pt-1.7 nm/G. Among these three catalysts, the reduction current will increase along the decrease of particle sizes. Hence the Pt-1.7 nm/G catalyst has the highest reduction current that is 2.5 times higher than that of the Pt-2.5 nm/G one. For the particle sizes more than 10.0 nm and smaller than 1.5 nm, the reduction current becomes smaller than that of Pt-1.7 nm/G catalyst.

3.4. The Amperometric Response of H_2O_2 . The amperometric responses of the modified GC electrode to H_2O_2 are depicted in Figures 4 and 5. After adding analyte solutions with different concentrations, the reduction currents were

monitored at a fixed potential of -0.5 V. In Figure 4, the same trend as in Figure 3 can be observed. With the same concentration of analyte, the Pt-1.7 nm/G catalyst has the highest reduction current. The linear regression equation is given by $I_{\text{H}_2\text{O}_2} = -0.089 C_{\text{H}_2\text{O}_2} + 1.392$, with a correlation coefficient of $r = 0.996$. The sensitivity of Pt-1.7 nm/G catalyst is $1264.6 \mu\text{A mM}^{-1} \text{cm}^{-2}$. This number is higher than 254.8 (Pt-1.3 nm/G), 565.6 (Pt-2.9 nm/G), and 560.8 (Pt-4.3 nm/G) $\mu\text{A mM}^{-1} \text{cm}^{-2}$. The sensitivity numbers among all catalysts are size-dependent.

4. Conclusions

In summary, the particles' size of Pt colloids can influence the electrochemical properties of Pt/G catalysts for electrochemical sensing of H_2O_2 . The Pt-1.7 nm/G catalyst has the highest sensitivity up to $1264.6 \mu\text{A mM}^{-1} \text{cm}^{-2}$, rapid response time of 1.69 s, low detection limit, and good ECSA

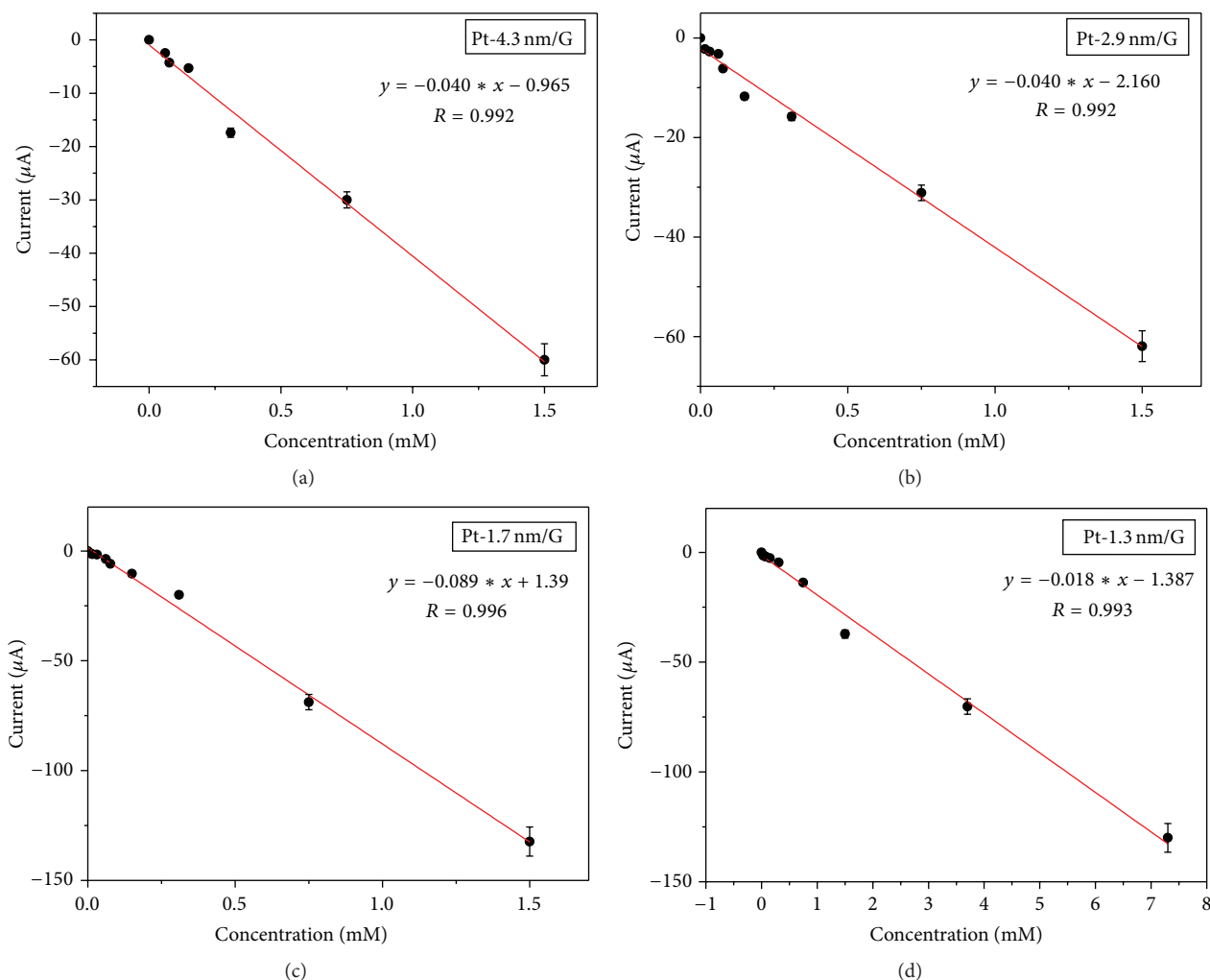


FIGURE 5: The corresponding plots of the reduction current of H_2O_2 ($I_{\text{H}_2\text{O}_2}$) versus the H_2O_2 concentration ($C_{\text{H}_2\text{O}_2}$) using four Pt/G-modified GC electrodes at the potential of -0.5 V.

in the linear range of $8 \mu\text{M}$ to 1.5 mM. Among all catalysts, it was found that the smaller Pt particles on graphene would give the higher sensitivity and wider linear range. Thus, the sensitivity of Pt-1.7 nm/G catalyst is highest among all catalysts. However, after the size is down to 1.3 nm, the linear range of Pt-1.3 nm/G shifts to the high concentration with the much lower sensitivity.

Conflict of Interests

The authors declare that there is no conflict of interests regarding the publication of this paper.

Acknowledgments

The authors thank the Ministry of Science and Technology, Chang Gung University, and Chang Gung Memorial Hospital (CMRPD2C0011) for financially supporting this research.

References

- [1] K. S. Novoselov, A. K. Geim, S. V. Morozov et al., "Electric field effect in atomically thin carbon films," *Science*, vol. 306, no. 5696, pp. 666–669, 2004.
- [2] K. S. Novoselov, A. K. Geim, S. V. Morozov et al., "Two-dimensional gas of massless Dirac fermions in graphene," *Nature*, vol. 438, no. 7065, pp. 197–200, 2005.
- [3] C.-C. Lin and Y.-W. Lin, "Synthesis of carbon nanotube/graphene composites by one-step chemical vapor deposition for electrodes of electrochemical capacitors," *Journal of Nanomaterials*, vol. 2015, Article ID 741928, 8 pages, 2015.
- [4] X. Ma, G. Chen, Q. Liu, G. Zeng, and T. Wu, "Synthesis of LiFePO_4 /graphene nanocomposite and its electrochemical properties as cathode material for Li-ion batteries," *Journal of Nanomaterials*, vol. 2015, Article ID 301731, 6 pages, 2015.
- [5] H.-Y. Tsai, W.-H. Hsu, and Y.-C. Huang, "Characterization of carbon nanotube/graphene on carbon cloth as an electrode for air-cathode microbial fuel cells," *Journal of Nanomaterials*, vol. 2015, Article ID 686891, 7 pages, 2015.

- [6] X. Wang, Y. Liu, J. Xu et al., "Molecular dynamics study of stability and diffusion of graphene-based drug delivery systems," *Journal of Nanomaterials*, vol. 2015, Article ID 872079, 14 pages, 2015.
- [7] Y.-W. Hsu, T.-K. Hsu, C.-L. Sun, Y.-T. Nien, N.-W. Pu, and M.-D. Ger, "Synthesis of CuO/graphene nanocomposites for nonenzymatic electrochemical glucose biosensor applications," *Electrochimica Acta*, vol. 82, pp. 152–157, 2012.
- [8] C.-L. Sun, H.-H. Lee, J.-M. Yang, and C.-C. Wu, "The simultaneous electrochemical detection of ascorbic acid, dopamine, and uric acid using graphene/size-selected Pt nanocomposites," *Biosensors and Bioelectronics*, vol. 26, no. 8, pp. 3450–3455, 2011.
- [9] C.-L. Sun, C.-T. Chang, H.-H. Lee et al., "Microwave-assisted synthesis of a core-shell MWCNT/GONR heterostructure for the electrochemical detection of ascorbic acid, dopamine, and uric acid," *ACS Nano*, vol. 5, no. 10, pp. 7788–7795, 2011.
- [10] C.-L. Sun, C.-H. Su, and J.-J. Wu, "Synthesis of short graphene oxide nanoribbons for improved biomarker detection of Parkinson's disease," *Biosensors and Bioelectronics*, vol. 67, pp. 327–333, 2015.
- [11] J. Shen, X. Yang, Y. Zhu, H. Kang, H. Cao, and C. Li, "Gold-coated silica-fiber hybrid materials for application in a novel hydrogen peroxide biosensor," *Biosensors and Bioelectronics*, vol. 34, no. 1, pp. 132–136, 2012.
- [12] L. Zheng, L. Xiong, D. Zheng et al., "Bilayer lipid membrane biosensor with enhanced stability for amperometric determination of hydrogen peroxide," *Talanta*, vol. 85, no. 1, pp. 43–48, 2011.
- [13] S. Chen, P. Fu, B. Yin, R. Yuan, Y. Chai, and Y. Xiang, "Immobilizing Pt nanoparticles and chitosan hybrid film on polyaniline nanofibers membrane for an amperometric hydrogen peroxide biosensor," *Bioprocess and Biosystems Engineering*, vol. 34, no. 6, pp. 711–719, 2011.
- [14] Z. Fan, Q. Lin, P. Gong, B. Liu, J. Wang, and S. Yang, "A new enzymatic immobilization carrier based on graphene capsule for hydrogen peroxide biosensors," *Electrochimica Acta*, vol. 151, pp. 186–194, 2015.
- [15] M.-Y. Hua, H.-C. Chen, R.-Y. Tsai, and C.-S. Lai, "A novel polybenzimidazole-modified gold electrode for the analytical determination of hydrogen peroxide," *Talanta*, vol. 85, no. 1, pp. 631–637, 2011.
- [16] M.-Y. Hua, H.-C. Chen, C.-K. Chuang et al., "The intrinsic redox reactions of polyamic acid derivatives and their application in hydrogen peroxide sensor," *Biomaterials*, vol. 32, no. 21, pp. 4885–4895, 2011.
- [17] X. Li, X. Liu, W. Wang, L. Li, and X. Lu, "High loading Pt nanoparticles on functionalization of carbon nanotubes for fabricating nonenzyme hydrogen peroxide sensor," *Biosensors and Bioelectronics*, vol. 59, pp. 221–226, 2014.
- [18] C. Karuppiah, S. Palanisamy, S.-M. Chen, V. Veeramani, and P. Periakaruppan, "A novel enzymatic glucose biosensor and sensitive non-enzymatic hydrogen peroxide sensor based on graphene and cobalt oxide nanoparticles composite modified glassy carbon electrode," *Sensors and Actuators B: Chemical*, vol. 196, pp. 450–456, 2014.
- [19] G.-H. Yang, Y.-H. Zhou, J.-J. Wu et al., "Microwave-assisted synthesis of nitrogen and boron co-doped graphene and its application for enhanced electrochemical detection of hydrogen peroxide," *RSC Advances*, vol. 3, no. 44, pp. 22597–22604, 2013.
- [20] L. Wang, Y. Ye, X. Lu et al., "Prussian blue nanocubes on nitrobenzene-functionalized reduced graphene oxide and its application for H₂O₂ biosensing," *Electrochimica Acta*, vol. 114, pp. 223–232, 2013.
- [21] C.-C. Kung, P.-Y. Lin, F. J. Buse et al., "Preparation and characterization of three dimensional graphene foam supported platinum-ruthenium bimetallic nanocatalysts for hydrogen peroxide based electrochemical biosensors," *Biosensors and Bioelectronics*, vol. 52, pp. 1–7, 2014.
- [22] T. Wang, H. Zhu, J. Zhuo et al., "Biosensor based on ultrasmall MoS₂ nanoparticles for electrochemical detection of H₂O₂ released by cells at the nanomolar level," *Analytical Chemistry*, vol. 85, no. 21, pp. 10289–10295, 2013.
- [23] N. Wang, Y. Han, Y. Xu, C. Gao, and X. Cao, "Detection of H₂O₂ at the nanomolar level by electrode modified with ultrathin AuCu nanowires," *Analytical Chemistry*, vol. 87, no. 1, pp. 457–463, 2015.
- [24] C. Bock, C. Paquet, M. Couillard, G. A. Botton, and B. R. MacDougall, "Size-selected synthesis of PtRu nano-catalysts: reaction and size control mechanism," *Journal of the American Chemical Society*, vol. 126, no. 25, pp. 8028–8037, 2004.
- [25] C.-L. Sun, J.-S. Tang, N. Brazeau et al., "Particle size effects of sulfonated graphene supported Pt nanoparticles on ethanol electrooxidation," *Electrochimica Acta*, vol. 162, pp. 282–289, 2015.
- [26] J.-M. Yang, S.-A. Wang, C.-L. Sun, and M.-D. Ger, "Synthesis of size-selected Pt nanoparticles supported on sulfonated graphene with polyvinyl alcohol for methanol oxidation in alkaline solutions," *Journal of Power Sources*, vol. 254, pp. 298–305, 2014.
- [27] C.-L. Sun, J.-S. Su, J.-H. Tang et al., "Investigation of the adsorption of size-selected Pt colloidal nanoparticles on high-surface-area graphene powders for methanol oxidation reaction," *Journal of the Taiwan Institute of Chemical Engineers*, vol. 45, no. 3, pp. 1025–1030, 2014.

Research Article

Case Study on Risk Evaluation of Silver Nanoparticle Exposure from Antibacterial Sprays Containing Silver Nanoparticles

Ellen Kim,¹ Ji Hyun Lee,¹ Jin Kwon Kim,¹ Gun Ho Lee,² Kangho Ahn,²
Jung Duck Park,³ and Il Je Yu¹

¹Institute of Nanoproduct Safety Research, Hoseo University, Asan 31499, Republic of Korea

²Department of Mechanics, Hanyang University, Ansan 15588, Republic of Korea

³College of Medicine, Chung-Ang University, Seoul 06911, Republic of Korea

Correspondence should be addressed to Il Je Yu; u1670916@chollian.net

Received 7 June 2015; Accepted 11 October 2015

Academic Editor: Simeon Agathopoulos

Copyright © 2015 Ellen Kim et al. This is an open access article distributed under the Creative Commons Attribution License, which permits unrestricted use, distribution, and reproduction in any medium, provided the original work is properly cited.

This study evaluated the risk of silver nanoparticle (AgNP) exposure from antibacterial sprays containing AgNPs. Using an exposure simulation chamber as the setting for the experiment, various instruments, including a scanning mobility particle sizer (SMPS), condensation particle counter (CPC), dust monitor, and mixed cellulose esters (MCE) filters, are connected to the chamber to measure the exposure levels of AgNPs when using the sprays. To assess potential risks to consumers, margin of exposure (MOE) approach was used to assess risk in which a calculated MOE was compared with a target MOE. When evaluating the risk of antibacterial sprays to inhalation exposure using the MOE, spraying a whole can and spraying an air conditioner both resulted in a high-risk concern level with a MOE ranging from 59 to 146 that was much lower than the no-risk concern level of 1000, while some spray showed a MOE 2049 with no-risk concern level. The dermal exposure levels with a single layer of clothing were estimated at 2–50 $\mu\text{g}/\text{kg}/\text{day}$ with a MOE ranging from 20,000 to 500,000. Therefore, the current results showed the possibility of high-risk inhalation exposure to AgNPs released when using antibacterial sprays.

1. Introduction

The safety of products containing nanomaterials remains an obstacle to the commercialization of nanotechnologies. An international standard (ISO TS 13830) “Guidance on the voluntary labeling for consumer products containing manufactured nano-objects” has been developed in ISO TC 229 (nanotechnologies) to allow informed choices when purchasing and for the use of consumers [1]. While the initial labeling standard suggested the inclusion of nanoobject release elements if manufactured nanoobjects are released during the product life-cycle, this proposal is currently unfeasible due to the lack of technology for detecting the release of nanoobjects during the product life-cycle. Thus, the present labeling standard only lists the manufactured nanoobjects contained in a product.

Another international collaborative effort to standardize the measurement of nanoparticles released from a product is

the Nanorelease Consumer Products Program organized by ILSI (International Life Science Institute). The program has 3 phases: (1) nanomaterial selection, (2) method evaluation, and (3) interlaboratory studies with an interlaboratory testing group [2]. After reviewing 24 nanomaterials, MWCNTs in polymers were determined as the top-priority nanomaterials. Various measurement methods and exposure/release scenarios were reviewed during different workshops. Therefore, several interlaboratory studies are now underway for method development and refinement [2].

Tracking the expanded application of nanomaterials, the consumer products inventory created by the project on emerging nanotechnologies [3] currently lists 1,628 products, where AgNPs are included in 383 products. In particular, the antimicrobial function of AgNPs has resulted in their widespread use in sprays, bedding, washers, water purification, wound dressings, toothpaste, shampoo and rinse, nipples and nursing bottles, fabrics, deodorants, filters, kitchen

TABLE 1: Inhalation exposure to AgNPs ($\mu\text{g}/\text{m}^3$).

Company	$N^{(a)}$	Pump flow ^(b) (L/min)	Sampling time (min)	Ag conc ($\mu\text{g}/\text{m}^3$)	MOE	Average MOE
Company A ^(d)	8	2.16 ± 0.09	25	0.049 ± 0.004	2714	2049 ± 577
	5	2.07 ± 0.03	25	0.076 ± 0.015	1750	
	6	2.07 ± 0.03	25	0.079 ± 0.005	1684	
Company B ^(d)	8	2.07 ± 0.03	25	0.887 ± 0.371	149	146 ± 12
	6	2.07 ± 0.03	25	1.005 ± 0.414	132	
	6	2.07 ± 0.03	25	0.849 ± 0.373	156	
Company B.1 ^(c)	7	2.17 ± 0.10	25	2.266 ± 0.197	59	59

^(a)Number of sample; ^(b)pump calibration measurements before and after; ^(c)spraying of whole can (10 min); ^(d)spraying on air conditioner (15 sec spraying, 10 min use). MOE = NOAEL/exposure concentration; NOAEL = $133 \mu\text{g}/\text{m}^3$ [5].

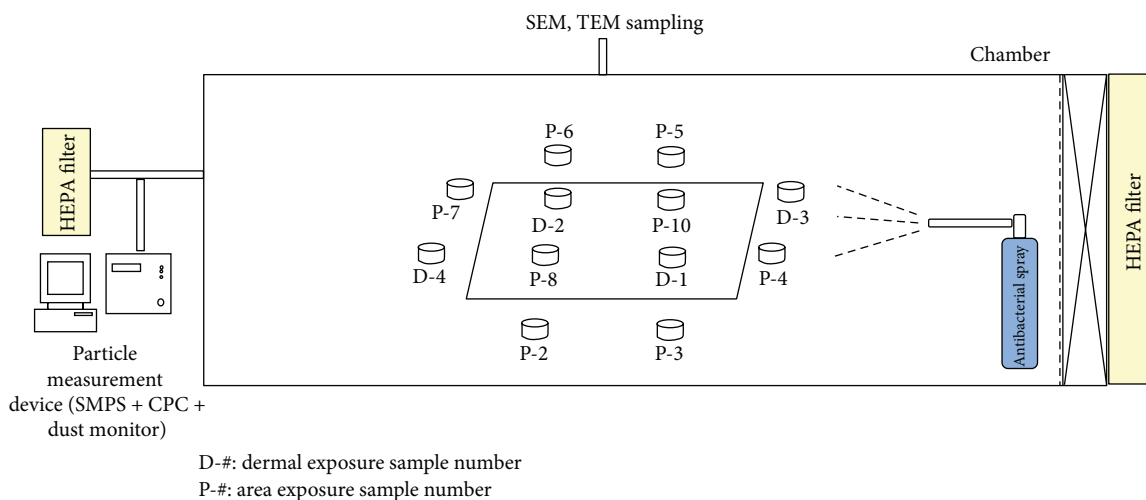


FIGURE 1: Schematic diagram of antibacterial spray exposure assessment system.

utensils, toys, photocatalysts, and humidifiers. Thus, the likelihood of consumers being exposed to AgNPs is increasing.

Antibacterial sprays are used on a wide variety of surfaces, including sinks, toilets, home appliances, air conditioners, tables, and chairs. Thus, the AgNPs in antibacterial sprays can be found in the air or on surfaces, meaning that consumers can be exposed through inhalation or via the skin. In addition, AgNPs sprayed on toilets, sinks, and bathtubs can enter the water system and eventually affect living organisms in the aquatic environment [4]. While antibacterial sprays are regulated by the FIFRA (Federal Insecticide, Fungicide Rodenticide Act) in the USA and Biocide act in the EU, many other parts of the world have no specific regulations.

Accordingly, this report simulates the use of AgNP containing sprays in a chamber system to assess AgNP exposure through inhalation and dermal routes. The human health effects of inhalation and dermal exposure to AgNPs from the use of sprays are also evaluated.

2. Materials and Methods

2.1. Antibacterial Sprays. Two kinds of antibacterial spray containing AgNPs were used, where the ingredients listed on

the cans included fragrance, AgNPs, and incense. The spray cans from Company A and Company B contained $0.08 \mu\text{g}/\text{g}$ and $1.1 \mu\text{g}/\text{g}$ of (Ag), respectively. These average amounts of Ag are listed in Table 1.

2.2. Exposure Simulation Chamber and Real-Time Aerosol Monitoring. The dimensions of the exposure simulation chamber were $1,800 \text{ mm} \times 700 \text{ mm} \times 700 \text{ mm}$ and it was made of acrylic, as shown in Figure 1. To facilitate various measurements, such as the AgNP particle number, size distribution, and mass concentration, a SMPS, CPC, dust monitor, and MCE filters were all connected to the exposure simulation chamber. The SMPS combining a differential mobility analyzer (DMA, HCT Co., Ltd., Icheon, Korea) and CPC (4312, HCT Co., Ltd.) was used to monitor the particle size distribution with an electrical mobility diameter ranging from 7.37 to 289.03 nm, while the dust monitor (Model 1.109, Grimm) was used to observe the particle size distribution with a diameter ranging from 0.25 to $32 \mu\text{m}$. Another CPC (3775, TSI Co., Ltd., $1-10^7$ particles/ cm^3 , detection range) was also used to monitor the number concentration, while the MCE filters were used in adjacent and nearby areas for personal and area sampling. The antibacterial spray was

applied to the air conditioner for 15 seconds, and, for the next 10 minutes including the 15 seconds of spraying, the air conditioner was not used. The air conditioner was then turned on for 50 minutes. The whole experiment took one hour and was repeated three times. Each repeated experiment is done in a clean simulation chamber, where the CPC observed no particles.

2.3. Air Sampling. Air samples were taken by drawing air through MCE filters in sampling cassettes (0.45 μm , 37 mm support pad included) obtained from SKC Inc. The total suspended particulate (TSP) was then measured, followed by a metal component analysis of the TSP and a metal component analysis. Area samples were collected from the chamber floor and 30 cm above using MSA (Escort Elf pump, Zefon International Inc., USA) sampling pumps at a flow rate of 2.07–2.17 L/min. The antibacterial spray was applied to the air conditioner for 15 seconds, and, for the next 10 minutes including the 15 seconds of spraying, the air conditioner was not used. The air conditioner was then turned on for 15 minutes. The whole experiment took 25 minutes and was repeated three times. Each repeated experiment is done in a clean simulation chamber, where the CPC observed no particles.

2.4. Dermal Exposure Estimation. To estimate the dermal exposure, MCE filter cassettes were placed in the chamber for passive sampling with no pump flow. The filters were then analyzed for their Ag concentrations, as described in Section 2.5, which were expressed as $\mu\text{g}/\text{cm}^2/\text{min}$.

2.5. Metal Analysis. After wet digestion, the filter concentrations of residual metals were analyzed using an atomic absorption spectrometer (AAS) equipped with a Zeeman graphite furnace (GF, pinAAcle 900T, Perkin Elmer, Waltham, MA) based on National Institute for Occupational Safety and Health (NIOSH) Manual method 7302 [7]. The filters were digested in a microwave (CEM MARS Xpress, Matthews, NC) for 60 min at 120°C in the presence of nitric acid and perchloric acid at a ratio of 4:1. Thereafter, the samples were allowed to cool and analyzed by AAS/GF. The LOD and LOQ for the AAS Ag analysis were 0.098 and 0.323 ppb, respectively.

2.6. Transmission Electron Microscopy (TEM). TEM, including an energy dispersive X-ray analyzer (EDS), was used to measure the nanoparticles based on NIOSH analytical method 7402 [8]. The nanoparticles on the filter were mounted on a TEM grid (copper grid) and visualized under a field emission transmission electron microscope (FE-TEM, JEM2100F, JEOL, Japan). The particles were measured at a magnification of 100000 and the nanoparticles analyzed using an energy dispersive X-ray spectrometer (EDS, TM200, Oxford, UK) at an accelerating voltage of 75 kV.

2.7. Risk Analysis. A MOE approach was used to assess the risk, where the calculated MOE was compared to a target MOE. Thus, when the calculated MOE is less than the

target MOE, this represents a risk concern level, whereas when the calculated MOE is greater than the target MOE, this represents a no-risk concern level. In this study, the target MOE was set at 1000. The $\text{MOE}_{\text{calc}} = \frac{\text{POD}/\text{dose (NOAEL)}}{\text{exposure concentration}}$, where the POD is the toxicological point of departure according to the estimated dose to which humans will be exposed and the NOAEL is the no-observed-adverse-effect-level. In this study, the POD was 133 $\mu\text{g}/\text{m}^3$ based on the NOAEL from a laboratory AgNP subchronic animal inhalation study [5]. In a previous acute dermal toxicity study based on OECD Test Guide 402, AgNPs did not induce any abnormal signs or death up to 2,000 mg/kg and no abnormal gross findings were reported for any of the treated groups at necropsy [9]. In another 28-day repeated dermal toxicity test based on OECD Test Guideline 410, a NOAEL of 1,000 mg/kg was obtained. Thus, to estimate the AgNP dermal risk, this study used a NOAEL of 1,000 mg/kg. To calculate the total exposure per day, the maximum exposure per day was set at four hours as worst-case scenario based on our simulated use scenario (15 sec spray, 10 min drying, and 10 min use). The dermal absorption factor was set at 0.01 [10], the body surface area for an adult was set at 1.5 m^2 , and the body weight was set at 70 kg [11]. A 50% reduction was assumed in the case of a single layer of clothing based on the US EPA surrogate PHED surrogate exposure guide [12]. Thus, the daily dermal exposure was as follows:

$$\begin{aligned} & \text{Dermal exposure/kg/day} \\ &= (\text{Dermal exposure concentration} \times \text{surface area} \\ & \times \text{work duration}) \times \frac{\text{dermal absorption factor}}{\text{body weight}}. \end{aligned} \quad (1)$$

3. Results

3.1. Inhalation Exposure to AgNPs from Spraying. The Ag concentrations were measured after using the sprays from Company A and Company B (15 seconds of spraying, 25 minutes total sampling time) and Company B.1 (10 minutes of spraying, 25 minutes total sampling time). The Ag concentrations for the sprays from Company A, Company B, and Company B.1 were 0.066 ± 0.016 , 0.911 ± 0.370 , and $2.27 \pm 0.2 \mu\text{g}/\text{m}^3$, respectively. The MOEs for the sprays from Company B and Company B.1 were 146 and 59, respectively, indicating a risk concern level. However, the MOE for the spray from Company A was 2049, indicating a no-risk concern level (Table 1).

3.2. Particle Size Distribution and Number Concentration during Use of Spray. The particle number concentration for the spray from Company A ranged from 5,901.6 to 365,500 particle/ cm^3 when measured using the CPC and from 1,703.3 to 9,521.8 particle/ cm^3 when measured using the dust monitor after the 25 min simulated exposure, and the concentration gradually decreased up to 100 min (Figure 2(a)). The particle size distribution ranged from 10 nm to 200 nm, showing peak at 30 nm, when measured using the SMPS

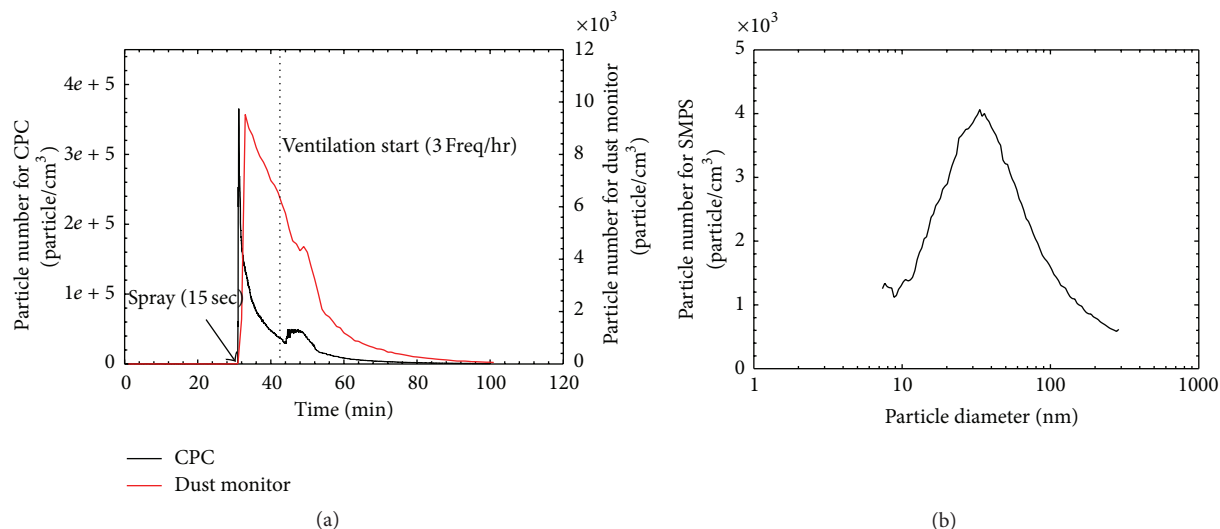


FIGURE 2: Particle number concentrations and particle size distribution. (a) Particle number concentrations for spray from Company A measured using dust monitor and CPC and (b) particle size distribution for spray from Company B measured using SMPS.

(Figure 2(b)). Meanwhile, the particle number concentration for the spray from Company B ranged from 23,952.1 to 582,100 particle/cm³ when measured using the CPC and from 5,152.8 to 9,843.3 particle/cm³ when measured using the dust monitor after the 25 min simulated exposure, and the concentration gradually decreased up to 100 min (Figure 3(a)). The particle size distribution ranged from 10 nm to 200 nm, showing a peak at 40 nm, when measured using the SMPS (Figure 3(b)). Finally, the particle number concentration for the spray from Company B.1 ranged from 16,331.8 to 1,908,000 particle/cm³ when measured using the CPC after the 25 min simulated exposure, and the concentration gradually decreased up to 100 min (Figure 3(c)). The particle size distribution ranged from 10 nm to 200 nm, showing a peak at 40 nm, when measured using the SMPS (Figure 3(d)). Figure 4(a) shows the particle size distribution difference when using the spray from Company B.1: 10–20 nm peak after 15 seconds of spraying, 40 nm after 10 minutes of spraying, and 80 nm after 20–30 minutes of spraying. Figure 4(b) shows the particle size distribution when using the spray from Company B: 30 nm peak after 15 seconds of spraying, 60 nm at 10 minutes after spraying, and 80 nm at 20–30 minutes after spraying. Figure 4(c) shows the particle size distribution when using the spray from Company A: 30 nm peak after 15 seconds of spraying, 50 nm at 10 minutes after spraying, and 50 nm at 20–30 minutes after spraying. The particles captured in the MCE filter analyzed by TEM-EDS showed dispersed AgNP composed of Ag with some Zn and Si component (Figure 5), indicating that the antibacterial Ag spray contained other particles.

3.3. Dermal Exposure to AgNPs from Spraying. The dermal exposure to AgNPs when spraying the whole can and for the 25 min simulation (15 seconds of spraying; 19 minutes

of drying; 15 minutes of ventilation) for the spray from Company B was 0.194 ± 0.072 and 0.006 ± 0.0005 $\mu\text{g}/\text{cm}^2/\text{min}$, respectively. The MOE when using the whole spray can from Company B was 10,000 for no clothing and 20,000 for a single layer of clothing. For the 25 min simulation, the MOE for the spray from Company B was 125,000 for no clothing and 250,000 for a single layer of clothing, while the MOE for the spray from Company A was 333,333 for no clothing and 500,000 for a single layer of clothing (Table 2). Thus, none of the AgNP spray scenarios represented a risk concern level for dermal exposure.

4. Discussion

Knowing about the safety of products containing nanomaterials is an important step for the sustainable growth of nanotechnologies, especially since their usages are gradually increasing. Several products containing nanomaterials have already been withdrawn from the market due to consumer concerns over safety and health risks related to the release of nanomaterials from products containing nanomaterials.

The release of AgNPs from consumer products, such as sock fabrics or home furnishings, has already been evaluated [13, 14]. As a result, the release of nano-Ag ranged up to 45 micrograms per product and the size fractions were both larger and smaller than 100 nm. After reviewing 54 studies of nanomaterial release from solid nanocomposites, the frequent releases were (1) only matrix particles, (2) matrix particles with partially or fully embedded nanomaterials, (3) nanomaterials entirely dissociated from the matrix, and (4) dissolved ionic forms of the added nanomaterials [15].

In 2010, the US EPA published a case study of nanoscale Ag in disinfectant sprays and indicated that the potential for human and biotic nano-Ag toxicity depended on the level

TABLE 2: Dermal exposure to Ag concentrations.

Company (Mean \pm SD)	$N^{(a)}$	Sampling Time (min)	Ag conc. ($\mu\text{g}/\text{cm}^2/\text{min}$)	No clothing ($\mu\text{g}/\text{kg}/\text{day}$)	MOE	Single layer clothing ($\mu\text{g}/\text{kg}/\text{day}$)	MOE
Company A ^(c)	4	25	0.006 ± 0.000				
	4	25	0.006 ± 0.000	3	333,333	2	500,000
	4	25	0.005 ± 0.000				
Company B ^(c)	3	25	0.013 ± 0.001	8	125,000	4	250,000
	4	25	0.015 ± 0.002				
Company B.1 ^(b)	4	25	0.194 ± 0.072	100	10,000	50	20,000

^(a)Number of sample; ^(b)spraying of whole can (10 min); ^(c)spraying of air conditioner (15 sec spraying, 10 min drying, 15 min use). MOE = NOAEL/exposure concentration; NOAEL = 2000 mg/kg [6].

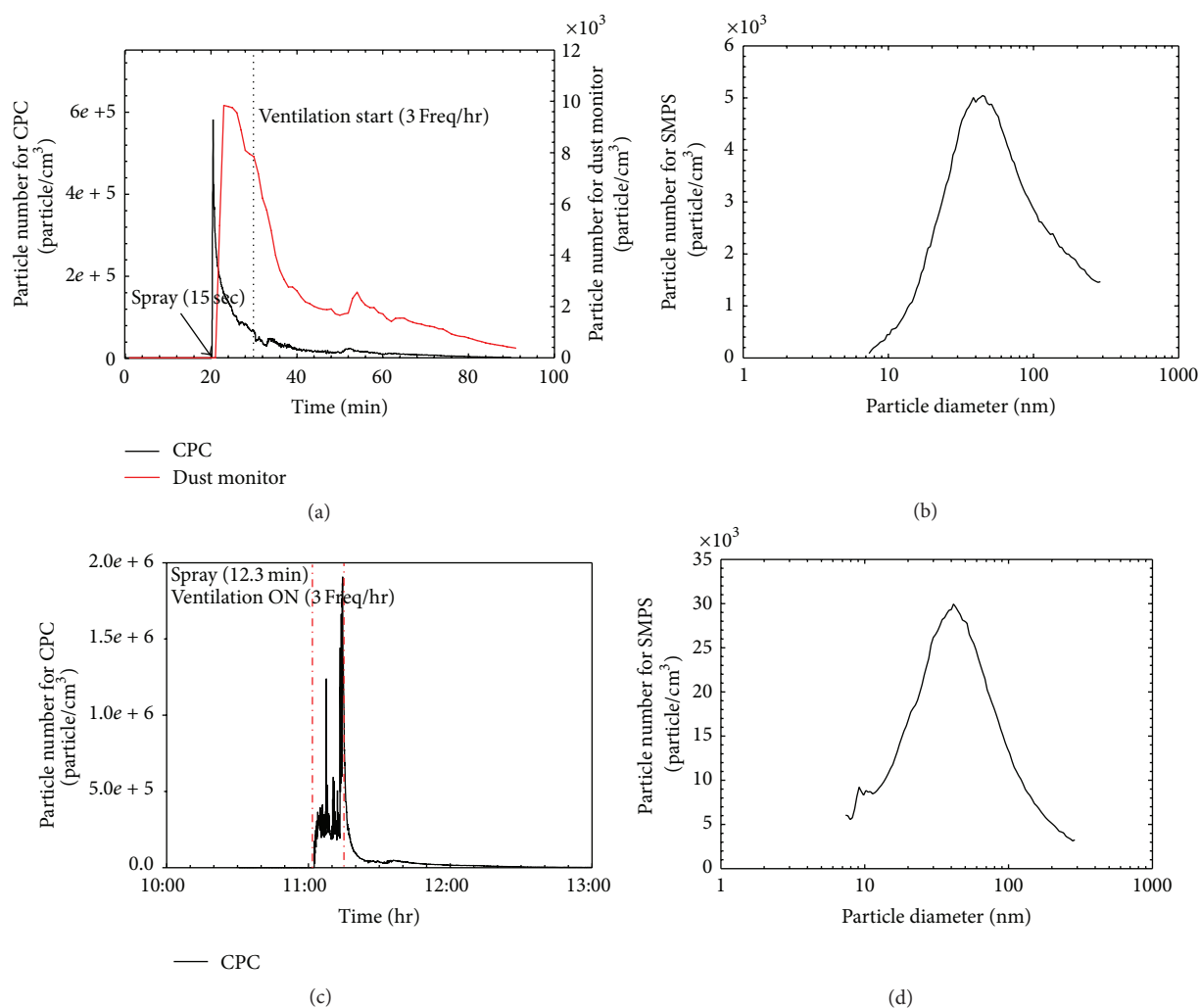


FIGURE 3: Particle number concentrations and particle size distribution. (a) Particle number concentrations for spray from Company A (15 sec spraying) measured using dust monitor and CPC, (b) particle size distribution for spray from Company B (15 sec spraying) measured using SMPS, (c) particle number concentration for spray (whole can, 10 min) from Company B measured using dust monitor and CPC, and (d) particle size distribution for spray from Company B (whole can: 10 min spraying) measured using SMPS.

of exposure to nano-Ag and related Ag compounds from these products, along with aggregate exposure to nano-Ag from other products containing nano-Ag [4]. In addition, following the FIFRA Scientific Advisory Panel meeting in 2009, the US EPA announced a conditional registration for

the pesticide product HeiQ Material Ag (HeiQ) containing nano-Ag as an active ingredient. In this case, the US EPA used a MOE approach and data including the product chemistry, environment fate and effects, human exposure, and toxicology to assess the risks of exposure to HeiQ [16].

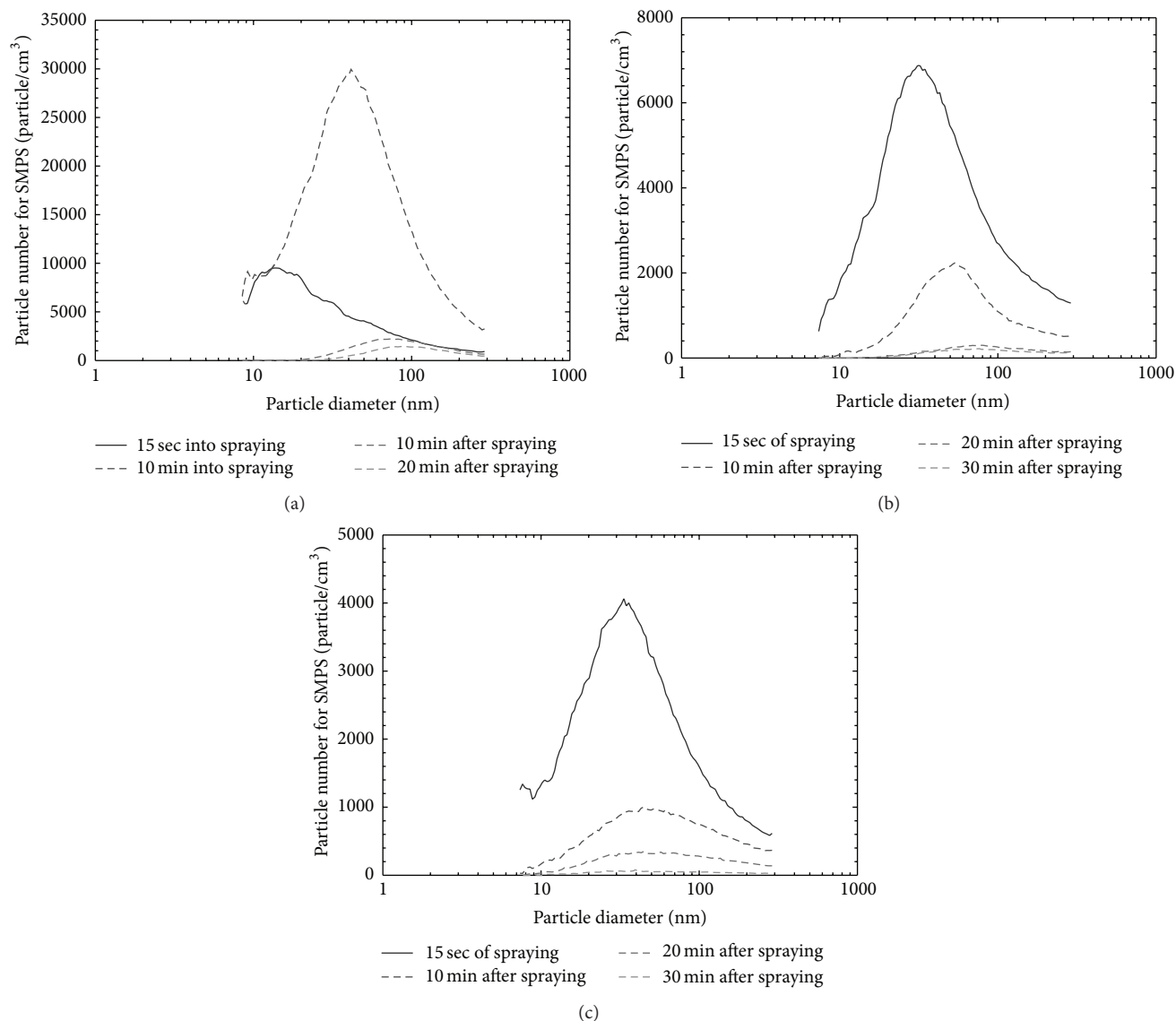


FIGURE 4: Differences in particle size distribution according to spraying time. (a) Particle size distribution for spray from Company B (10 min spraying) measured using SMPS, (b) particle size distribution for spray from Company B (15 sec spraying) measured using SMPS, and (c) particle size distribution for spray from Company A (15 sec spraying) measured using SMPS.

In this paper, a simulated AgNP exposure with a simulated chamber was set up because it is difficult to assess actual exposure condition when using antibacterial spray due to various condition application of use in duration, intensity, and frequency. Furthermore, unlike workers' exposure in workplace, such as attaching personal sampler to the breathing zone, exposure assessment on a consumer is not easy task due to difficulties in obtaining consent on exposure, arranging in exposure assessment, and requesting for actual use condition. Therefore, a simulated chamber was used to control the variables for exposure situation. The chamber study gave several advantages in estimating exposure leading to risk evaluation. It provides a proper condition for spray application, by allowing the assessment of AgNP concentration in terms of number and mass, and gives correct estimation of nanoparticle exposure avoiding

contamination from other particles in ambient air condition. Using a simulated chamber platform, risk of AgNP consumer exposure in use of antibacterial spray can be appropriately evaluated. Additionally, risk evaluation using the MOE approach provided a valuable tool to estimate risk of exposure, improbable in real consumer exposure situation. The limitation of this chamber study could be overestimation of exposure when compared to real-life scenario, since the experiment provides higher frequency and intensity of exposure without circulating ambient air. It is an example that simulates worst-case scenario of exposure situation.

5. Conclusion

This paper used a MOE approach to assess the risk of consumer exposure to nano-Ag released from antibacterial

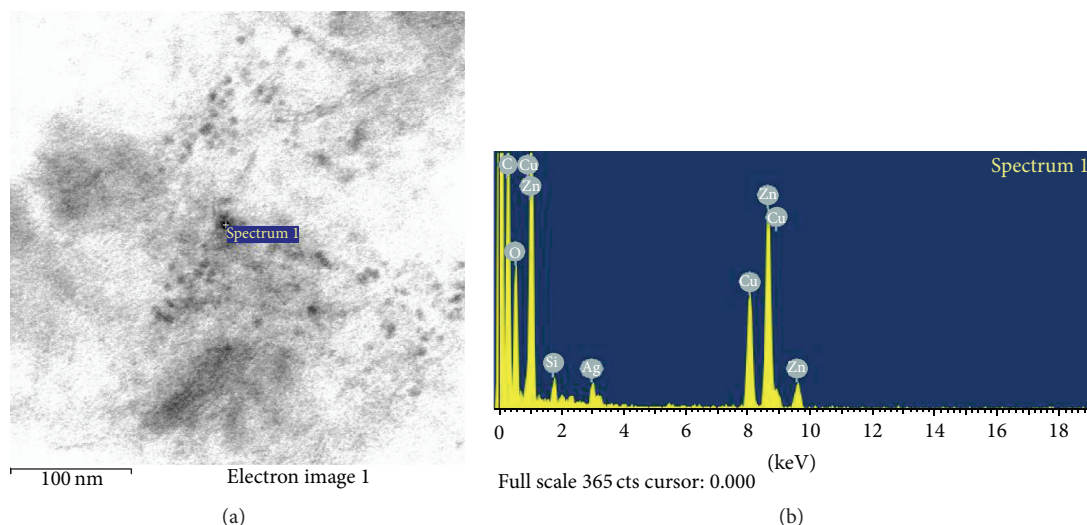


FIGURE 5: TEM-EDS of AgNPs released from spray.

sprays containing AgNPs. To estimate the inhalation and dermal exposure to AgNPs, the antibacterial sprays were used in a simulation chamber and the air concentration of AgNPs was measured in terms of the mass and number concentration, while the dermal exposure was estimated based on passive filter sampling. The results for all the products suggested an excessive risk of inhalation exposure for some of the tested sprays, as the MOE was lower than the no-risk concern level of 1000. In contrast to the inhalation exposure, the dermal exposure results showed no-risk concern levels for the tested sprays. The current simulation setting and methods may be useful for estimating consumer exposure to nanomaterials.

Disclaimer

The authors alone are responsible for the content and writing of this paper.

Conflict of Interests

The authors report no conflict of interests.

Acknowledgment

This research was supported by the “Development of Safety-Evaluation-Based Technology for Nanoproducts to Promote Commercialization (10047829)” and “Development of Highly Usable Nanomaterial Inhalation Toxicity Testing System in Commerce (10052901)” through the Korea Evaluation Institute of Industrial Technology by the Korean Ministry of Trade, Industry & Energy.

References

- [1] ISO/TS 13830, *Nanotechnologies—Guidance on Voluntary Labeling for Consumer Products Containing Manufactured Nano-Objects*, International Organization for Standardization, Geneva, Switzerland, 2013.
- [2] International Life Science Institute (ILSI), “NanoRelease Consumer Products,” 2015, <http://www.ilsilife.org/ResearchFoundation/RSIA/Pages/NanoRelease1.aspx>.
- [3] Woodrow Wilson Center, “Project on emerging nanotechnologies,” 2015, <http://www.nanotechproject.org/cpi/>.
- [4] EPA, *External Review Draft, Nanomaterial Case Study: Nano-scale Silver in Disinfectant Spray, EPA/600/R-10/081*, EPA, Washington, DC, USA, 2010.
- [5] J. H. Sung, J. H. Ji, J. D. Park et al., “Subchronic inhalation toxicity of silver nanoparticles,” *Toxicological Sciences*, vol. 108, no. 2, pp. 452–461, 2009.
- [6] KCL, “Nanoproduct-specific case studies and Safety evaluation,” Tech. Rep., Korea Evaluation Institute of Industrial Technology, Seoul, Republic of Korea, 2014 (Korean).
- [7] National Institute for Occupational Safety and Health (NIOSH), *NIOSH Manual of Analytical Methods 7300. Elements by ICP (Nitric/Perchloric Acid Ashing)*, NIOSH, Cincinnati, Ohio, USA, 2003.
- [8] National Institute for Occupational Safety and Health (NIOSH), *NIOSH Manual of Analytical Methods 7402 Asbestos by TEM*, National Institute for Occupational Safety and Health (NIOSH), Cincinnati, Ohio, USA, 1994.
- [9] J. S. Kim, K. S. Song, J. H. Sung et al., “Genotoxicity, acute oral and dermal toxicity, eye and dermal irritation and corrosion and skin sensitisation evaluation of silver nanoparticles,” *Nanotoxicology*, vol. 7, no. 5, pp. 953–960, 2013.
- [10] F. F. Larese, F. D’Agostin, M. Crosera et al., “Human skin penetration of silver nanoparticles through intact and damaged skin,” *Toxicology*, vol. 255, no. 1-2, pp. 33–37, 2009.
- [11] EPA, *Exposure Factors Handbook. Vol. I–III*, Office of Research and Development, Environmental Protection Agency, Washington, DC, USA, 1997.
- [12] EPA, *PHED Surrogate Exposure Guide*, Office of Pesticide Programs, EPA, Washington, DC, USA, 1998.
- [13] T. M. Benn and P. Westerhoff, “Nanoparticle silver released into water from commercially available sock fabrics,” *Environmental Science and Technology*, vol. 42, no. 11, pp. 4133–4139, 2008.
- [14] T. Benn, B. Cavanagh, K. Hristovski, J. D. Posner, and P. Westerhoff, “The release of nanosilver from consumer products

used in the home,” *Journal of Environmental Quality*, vol. 39, no. 6, pp. 1875–1882, 2010.

- [15] S. J. Froggett, S. F. Clancy, D. R. Boverhof, and R. A. Canady, “A review and perspective of existing research on the release of nanomaterials from solid nanocomposites,” *Particle and Fibre Toxicology*, vol. 11, article 17, 2014.
- [16] EPA, *Proposed Decision Document for the Registration of HeiQ AGS-20 As a Material Preservative in Textiles*, Office of Pesticide Program Antimicrobials Division, EPA, Washington, DC, USA, 2011.

Research Article

Interim Clinical Outcomes in Nanocomposite Bone Material Repairing Large Proximal Femoral Defect of Fibrous Dysplasia

Yun Lang,¹ Ze-ping Yu,¹ Yan Xiong,¹ Chong-qi Tu,¹ Cheng Ren,¹ Bin Zhang,¹
Hong-sheng Yang,¹ Fang Yuan,² Hong Li,³ Yong-gang Yan,³ and Hong Duan¹

¹Department of Orthopedics, West China Hospital, Sichuan University, No. 37 Guo Xue Lane, Chengdu, Sichuan 610064, China

²Department of Radiology, West China Hospital, Sichuan University, Chengdu, China

³School of Physical Science and Technology, Sichuan University, Chengdu, China

Correspondence should be addressed to Chong-qi Tu; tuchongqi@163.com and Hong Duan; duanhong1970@126.com

Received 14 April 2015; Revised 23 June 2015; Accepted 29 June 2015

Academic Editor: Faik Oktar

Copyright © 2015 Yun Lang et al. This is an open access article distributed under the Creative Commons Attribution License, which permits unrestricted use, distribution, and reproduction in any medium, provided the original work is properly cited.

Background and Objectives. To evaluate the clinical effectiveness and safety of using nanocomposite bone material in the repair of large proximal femoral defects that are due to fibrous dysplasia. **Method.** Thirty-one patients were analyzed retrospectively, including 13 males and 18 females, and the mean age was 30.9 years (13–59). The median follow-up period was 50 months (30–78) and the masses of artificial bone transplants were in the range of 15–40 g (average of 23.4 g). Functional and radiographic outcomes were evaluated. **Results.** All wounds healed to grade A. There were no infections, nonspecific inflammatory reactions, rejection reactions, or fractures. One case had fat liquefaction and healed after dressing. All patients had no recurrence until the last follow-up. At the last follow-up, the mean Musculoskeletal Tumor Society's (MSTS) 93 score was 28.42 ± 1.31 , the mean Harris hip score was 84.23 ± 8.97 , and mean radiopaque density ratio was 0.78 ± 0.09 . Radiologic analysis indicated that nanocomposite bone material had been completely incorporated with the host bone within a year. **Conclusions.** This study indicated that the nanocomposite bone material had biological safety and good biocompatibility. In conclusion, the nanocomposite bone material is an ideal artificial bone substitute and worthy of promotion in the field of orthopedics.

1. Introduction

Bones are an important organ in our bodies and provide us the freedom to do the things that we want to do. Bones help us to stand up straight, walk, and jump. Many health problems, such as trauma, infection, and tumors, can cause broken bones [1]. Bone tissue can repair itself for small defects, and sometimes cannot heal large bone defects. The treatment of large bone defects represents a considerable challenge in clinical practice [2, 3]. This situation necessitates the use of bone grafts, including autografts, allografts, and bone substitutes for healing [4]. Autografts have long been acknowledged as the gold standard for bone grafts due to their outstanding osteoinductivity, osteoconductivity, and osteogenicity. However, the following limitations restrict their extensive clinical application: limited supply, donor site injury, and potential risks of infection. Allografts, providing scaffolds for graft sites, are relatively abundant in supply, are osteoconductive,

and have been used successfully in bone grafting procedures. However, allografts have their limitations as well, including a slowly creeping substitution process compared to autografts, high risks of disunion or delayed union, and potential risk of disease transmission and antigenicity that induces host rejections. Bone graft substitutes include organic materials, inorganic materials, and composites. Surgeons encounter a serious challenge in searching for the ideal artificial bone substitute for the repair of large bone defects. Biomaterials, due to their comparability with human bone structure, have been demonstrated to be popular in orthopedic surgery [4].

Fibrous dysplasia (FD) of bone is a rare spontaneous benign skeletal disorder characterized by a focal proliferation of fibrous tissue in the bone marrow that manifests in childhood or early adult life and can affect one bone (monostotic), or multiple bones (polyostotic) [5]. According to Ippolito and colleagues [6], in monostotic FD, the most commonly appearing site is on the femur. Clinical symptoms

TABLE 1: Surgical approach of 31 patients.

Lesion type	Proximal femur	Femoral neck and proximal femur	Total
Bone material grafting	7	4	11
Bone material grafting + internal fixation	8	9	17
Bone material + allograft cortical bone plate grafting + internal fixation	2	1	3
Total	17	14	31

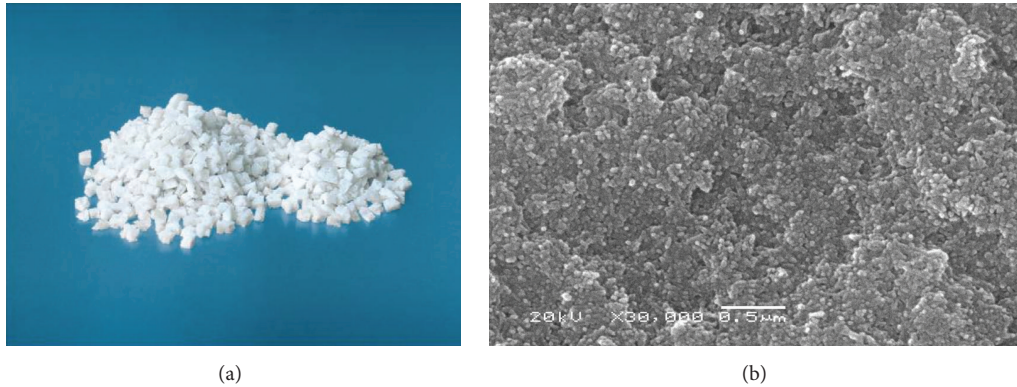


FIGURE 1: The morphology of nanocomposite bone material. Notes: (a) nanocomposite bone material with a size of $4\text{ mm} \times 2\text{ mm} \times 2\text{ mm}$; (b) SEM image ($\times 3,000$ magnification) of nanocomposite bone material with a porosity of 75%–85%. SEM: scanning electron microscope.

of FD include bone pain, bone deformities, and pathological fractures [7]. It is well-known that the surgical management of fibrous dysplasia includes intralesional curettage, correction of the deformity, bone grafting, and rigid internal fixation. Various types of surgical treatment are reported, ranging from lesion curettage after bone grafting to massive cortical bone grafting, particularly in lesions of the femoral neck and for intramedullary fixation in extended lesions with deformations [8–10]. The multiple treatment modalities make FD difficult to manage, especially in the proximal femur.

Nanocomposite bone material resembles human bone in terms of structure and mechanical strength, which is useful as a bone repairing material because it has biocompatibility, bioactivity, and good biomechanical properties as confirmed in various research [11–17].

We reviewed 31 patients and reported on our experience in applying nanocomposite bone material (the porous n-HA/PA66 composite) to repair large proximal femoral defects of FD.

2. Materials and Methods

2.1. Material Introduction. Nanocomposite bone material, which was provided by the Sichuan National Nanotechnology Co., Ltd. (Chengdu, People's Republic of China) and met biological safety standards according to the Chinese GB/T16886 and GB/T16175, was the biomaterial composite and consisted of nanohydroxyapatite (n-HA) and polyamide 66 (PA66) (Figure 1). The diameters of n-HA nanoparticles range from 80 nm to 100 nm and the molecular weight is 1,000, while PA66 has a molecular weight range from 18,000 to 20,000. The mass ratios of n-HA and PA66 in the composite were 35 to 40. The composite pore size, porosity ratio, and

compressive strength were 300 to 700 μm , 75% to 85%, and 2.0 to 10.0 mPa, respectively. For the nanocomposite bone material, it was demonstrated that there was no cytotoxicity or pyrogen. Additionally, the material's hemolysis ratio was 0.59% [17]. Early animal implantation studies showed that a rapid developing process of bone repair was observed in the nanocomposite, the primer mineralization started at the implant near to the neighboring bone tissue, and the new bone started increasing at 4 weeks. After 12 weeks, new bone formed in the pores, progressively linked with each other, and directly connected with materials. After 24 weeks, the new bone gradually reached toward the center of the implant and exhibited good osteoinductivity and osteocompatibility (Figures 2 and 3). The treatments were undertaken with the understanding and written consent of each subject according to the World Medical Association Declaration of Helsinki (version 2008). The study has been independently reviewed and approved by the Ethics committee at West China Hospital of Sichuan University.

2.2. Clinical Data. From December 2007 to October 2011, there were 31 consecutive patients who fulfilled the following inclusion criteria: (1) the diagnosis of FD should be confirmed by clinical feature, imaging data and pathology; (2) lesions should undergo intralesional curettage, biopsy, nanocomposite bone material transplantation, or rigid internal fixation and allograft used according to the type of lesion; (3) there was complete follow-up data. Exclusion criteria were as follows: (1) the patient showed recurrence; (2) patients contraindicated to operation. There were 13 males and 18 females and the mean age was 30.9 years (13–59). The lesion locations are listed in Table 1. The size of the lesions ranged from 6.0 cm \times 2.5 cm \times 2.5 cm to 10.0 cm \times 3.5 cm \times 3.5 cm.

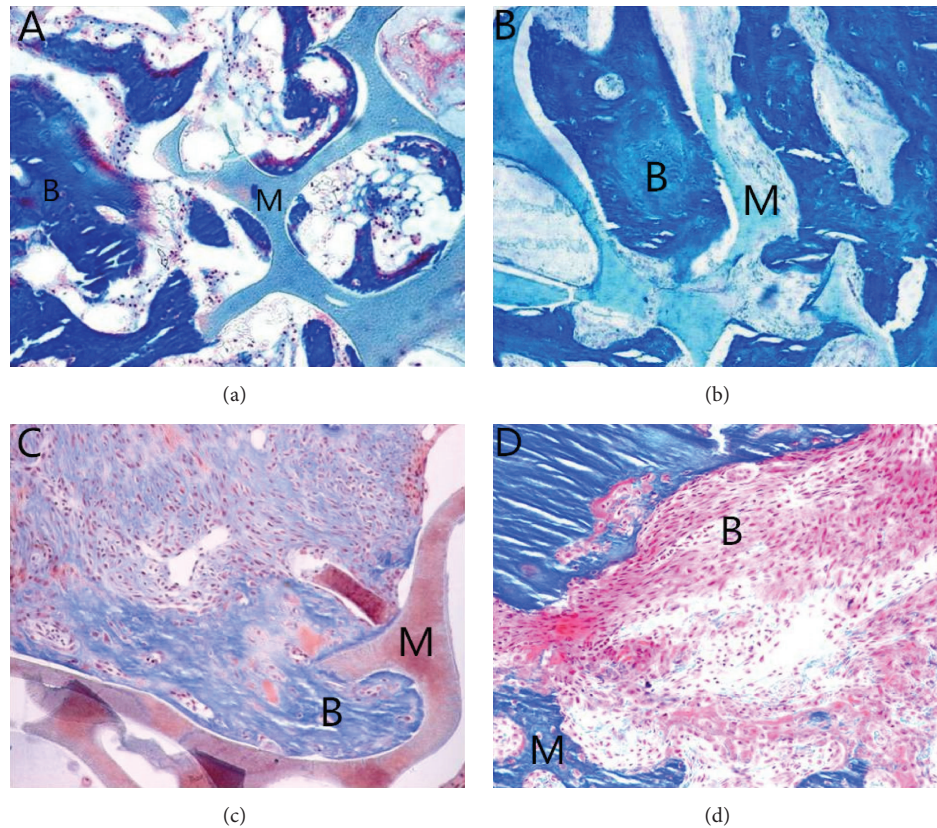


FIGURE 2: Figure showing how the amount of new bone and calcium crystals increased over time. Note: bone and calcium crystals at (a) 2 weeks, (b) 4 weeks, (c) 12 weeks, and (d) 24 weeks. Masson staining was used, $\times 200$ magnification. After 24 weeks, interconnected porosity was filled completely with new bone tissue. M: material; B: bone.

The average of the implant amount of nanocomposite bone material was 23.4 g (15–40). We used a software program (Syngo version V35; Siemens Medical Systems, Erlangen, Germany) for quantitative analysis to measure the X-ray radiopaque density value. The value was measured in the grafting section and nonlesion bone area near the operation section, and the grafting-to-nonlesion count ratio (G/N ratio) was then calculated. The normal value of the G/N ratio was 1.00 [14]. Both preoperatively and postoperatively, all patients underwent blood investigations, biochemical tests, immune function tests, and hemagglutination inspections.

2.3. Surgical Methods. This procedure included four following steps: orderly intralesional curettage, biopsy, inactivated, and filled with nanocomposite bone material. If the cortical bone was seriously affected, the combination application of allogeneic cortex bone plate and nanocomposite bone material grafting was recommended. The femur reconstruction nail or proximal femoral nail antirotation (PFNA) would be planted for those with a deformity, pathologic fracture, or obviously weakened bone strength. Additionally, the deformity cases underwent valgus osteotomy prior to these steps. The surgery procedure option is shown in Table 1, which all patients underwent. 22 patients with hip and/or the femoral varus deformity underwent a single level wedge-shaped valgus osteotomy at subtrochanteric region to ensure

a neck-shaft angle of 120° ; if the deformity combined the femur neck and the subtrochanteric region, double-level valgus osteotomy was performed with the first level at the subtrochanteric region and the second around the dome of the varus femur deformity. Hence, to ensure the healing of the osteotomy site, the second osteotomy site was determined by the host bone quality, with our goal of double-level osteotomy being to restore the neck-shaft angle more than 90° and rebuild the femur alignment. Three cases with lesions involving a bone cross-section over 50% and cortical bone defects over 5 cm underwent double-level osteotomy. Meanwhile, allogeneic cortex bone plate grafting and femur reconstruction nail fixation were performed.

2.4. Postoperative Treatment and Follow-Up. Postoperatively, all patients accepted intravenous infusion cefathiamidine to prevent infection, early isotope exercise of quadriceps, and passive exercise of hips and knees. The clinical evaluation included wound healing, blood investigations, biochemical tests, immune function tests, and hemagglutination inspections one, 2, 3, 6, 9, and 12 months and then every six months after surgery. At the same time, patients were followed up by panoramic X-ray and computed tomography (CT) plain scan, and spiral CT 3D reconstruction was performed to observe the healing of grafted bone and calculate the G/N ratio (image measurement data and statistical data using a double-blind

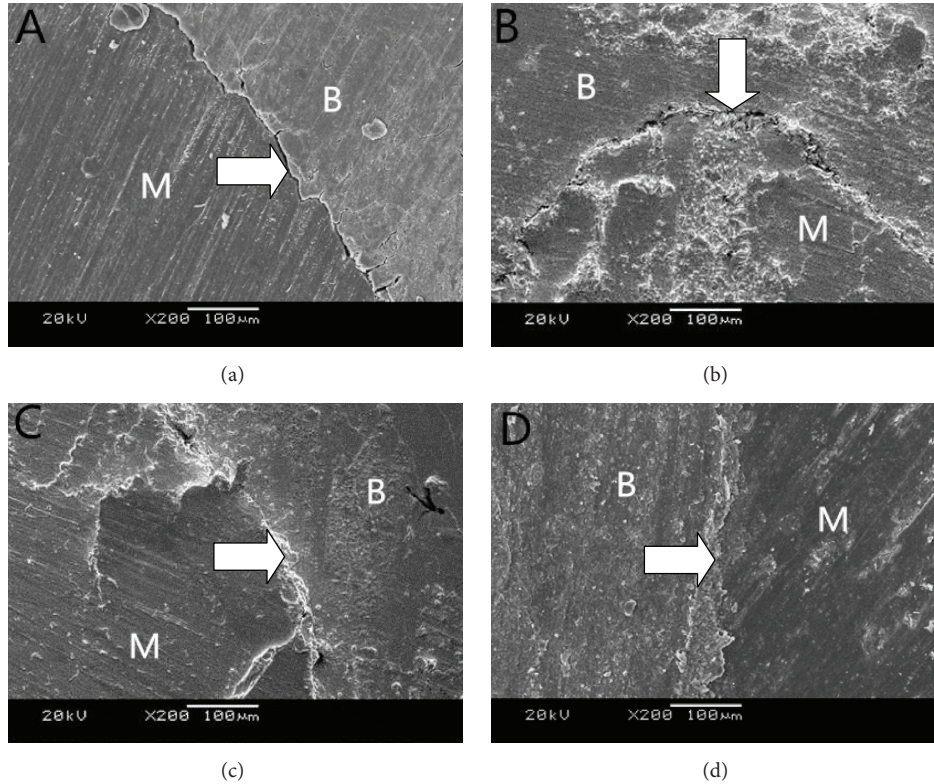


FIGURE 3: The SEM images ($\times 2,000$ magnification) of the nanocomposite bone material with implantation into the rabbit tibia. Note: the interface of material and bone at (a) 2 weeks, (b) 4 weeks, (c) 12 weeks, and (d) 24 weeks. After 24 weeks, the nanocomposite bone material integrated with host bone completely. SEM: scanning electron microscope; M: material; B: bone.

evaluation). The Harris hip score system [18] and MSTS 93 scoring system [19] were used to analyze limb function.

2.5. Statistical Methods. Data were coded and analyzed using SPSS 17.0 (IBM Corporation, Armonk, NY, USA) software. The values are presented as the mean \pm standard deviation (SD). Paired sample *t*-test was used to compare the difference in Harris hip score, MSTS 93 score, and G/N ratio between preoperative and postoperative. One-way analysis of variance (ANOVA) was used to determine differences between the radiopaque density ratios for dependent variables measured at the normal level (age, sex, and bone grafted mass). A value of $P < 0.05$ was considered to be statistically significant.

3. Results

The median follow-up period was 50 months (30–78). After surgery, all patients had a good general condition. One case had fat liquefaction of their postsurgical wound and was healed by meticulous dressing. The other wounds healed to grade A. All of the patients' blood investigations, biochemical tests, immune function tests, and hemagglutination inspections showed no obvious abnormalities from preoperative to postoperative. No nonspecific inflammation, rejection, recurrence, pathologic fractures, internal fixation loosening, local calcification, or heterotopic ossification were encountered. The grafting site did not show signs of osteoporosis. One

case with a severe deformity with increscent femoral neck anteversion angle and proximal femur axis rotation underwent osteotomy. Unfortunately, the dysfunction showed no obvious improvement. This patient accepted another surgery to cut off their adductor, and the function level has gradually improved. Radiographs showed radiolucent zones between the implanted nanocomposite bone material and the neighboring bone tissues. Periodic assessments showed that 25% of grafting zones were replaced by new bones in 2 to 3 months; after 6 to 9 months, new bone formation rose to 50%. The defects were fully occupied by new bone within one year and reached a radiographically observable bony union (Figures 4 and 5). The G/N ratio reflected the differences between grafting and nonlesion areas. New bone grafting area blocked X-ray penetration, and as time went on more new bone grew, the G/N ratio decreased, and after one year this ratio entered into the stationary phase. G/N ratio was 0.78 ± 0.09 one year after surgery (Table 2). There was no significant relationship between age, sex, bone graft mass, and radiopaque density ratio ($P > 0.05$) (Table 3). There was no significant difference in G/N ratio between allograft users and nanocomposite bone material isolate users. The Harris hip score was 84.23 ± 8.97 , and the MSTS score was 28.42 ± 1.31 (Table 2).

4. Discussion

The management of FD in the proximal femur is a tough challenge in the musculoskeletal tumor surgery field. FD

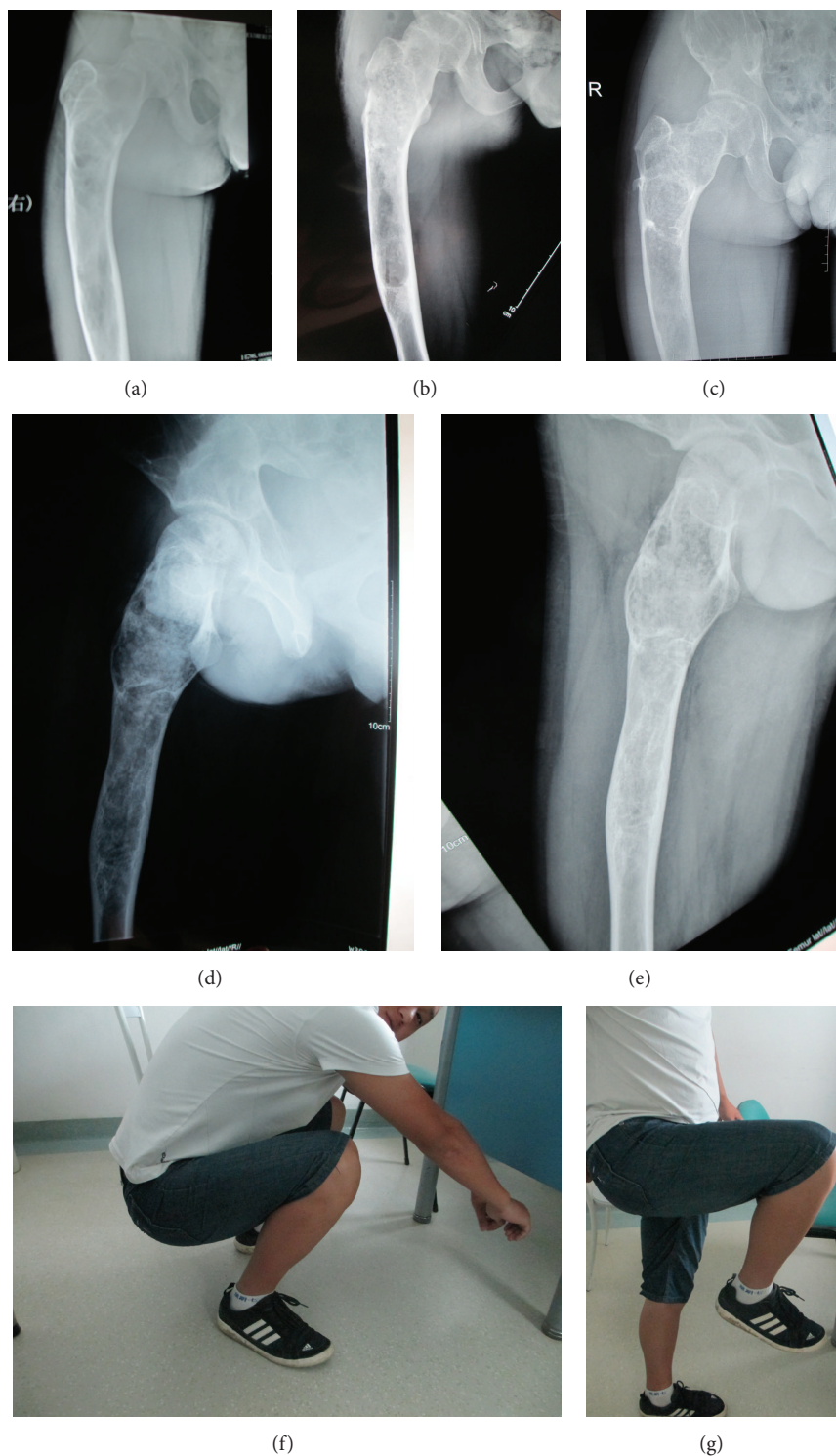


FIGURE 4: A man, 20 years old, suffered from FD of right proximal femur (a). The patient underwent lesion biopsy, curettage, and nanocomposite bone material grafting. Three months after surgery (b); 6 months after surgery (c); one year after surgery (d); and 3 years follow-up (e). (d) and (e) showed that nanocomposite bone material had been completely incorporated with the host bone, and grafting-to-*nonlesion* count ratio was 0.84. The Harris score was 92 and MSTs score was 29 (f, g). The patient was satisfied by the function.

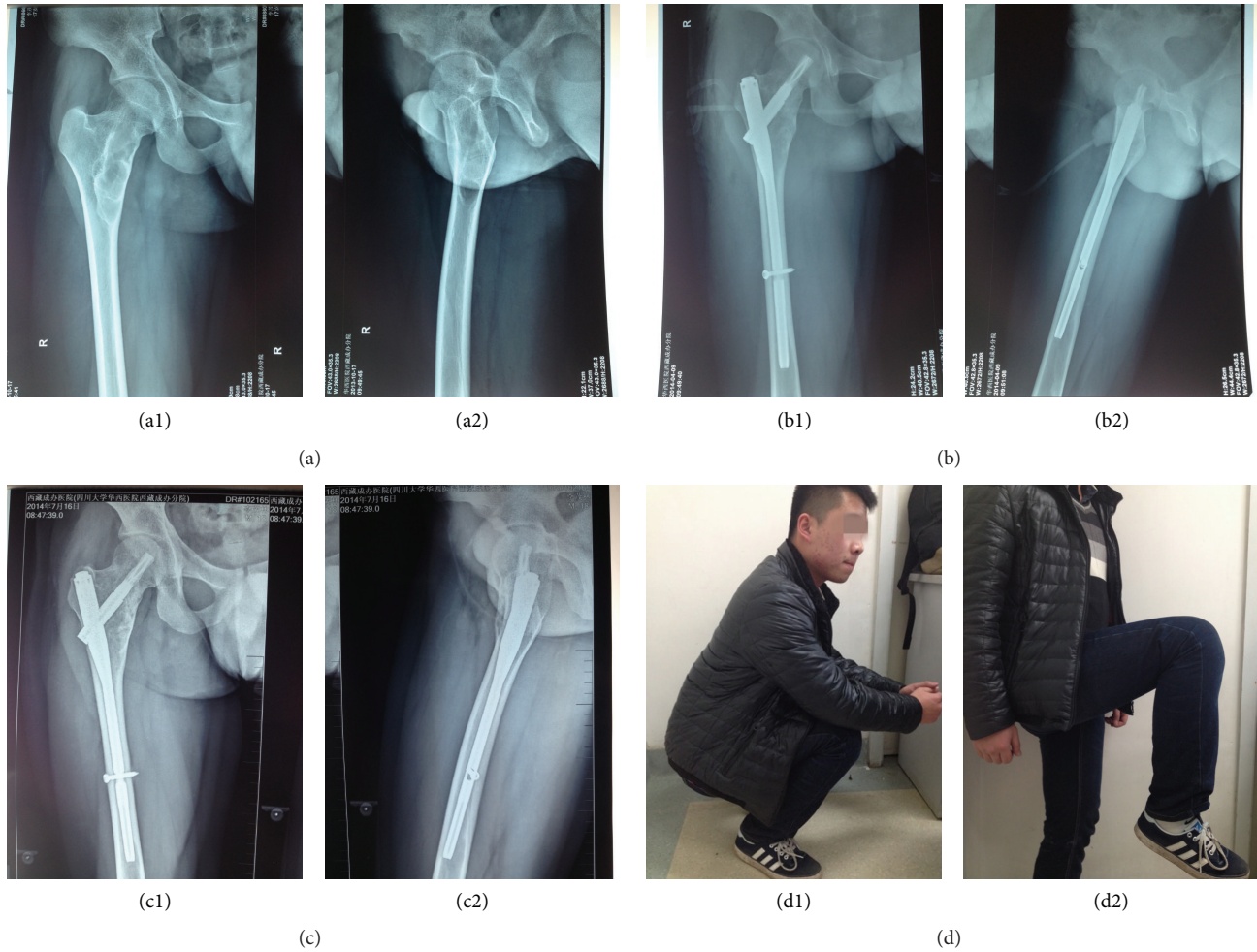


FIGURE 5: A man, 22 years old, suffered from FD of right proximal femur (a1, a2). The patient underwent lesion biopsy, intralesion curettage, nanocomposite bone material grafting, and PFNA intramedullary nail fixation. One year (b1, b2) and 3 years (c1, c2). (c1) and (c2) showed that the nanocomposite bone material had been completely incorporated with the host bone, and the fixation was stable. There was no lesion recurrence. The grafting-to-nonlesion count ratio was 0.80. The Harris score was 93 and MSTS score was 29 (d1, d2). The patient could participate in long distance running.

TABLE 2: Comparison of Harris score, MSTS score, and G/N ratio between preoperative and 1 year follow-up.

Items	Before operation	A year after operation
Harris score	62.06 ± 10.34	84.23 ± 8.97*
MSTS score	23.65 ± 1.47	28.42 ± 1.31*
G/N ratio	0.49 ± 0.06	0.78 ± 0.09*

* Comparison with preoperative evaluation $P < 0.01$.

generally weakens biomechanical strength and destroys the anatomic structure of the femur. With the progression of FD, long-term weight bearing, and the traction of hip muscles can cause hip pain, pathological fractures, and varus deformities, which fundamentally affect limb function and can even lead to a high rate of disability [6, 10, 20, 21]. Therefore, it is highly important to have early detection and treatment of FD. The surgical management procedure for FD should include the following steps [6, 9, 21]: (1) correcting the deformity; (2)

TABLE 3: Statistical data on 31 patients.

Variable	Total (N = 31)	G/N ratio	F	P
Age ¹	31	0.78 ± 0.09	2.403	0.088
Sex ²				
Female	18	0.80 ± 0.06	1.420	0.328
Male	13	0.77 ± 0.12		
Bone grafted mass ²				
<20 g	5	0.71 ± 0.20	1.265	0.309
≥20 g	26	0.80 ± 0.05		

G/N ratio, grafting-to-nonlesion ratio.

¹ Correlation between the two variables was analyzed by linear correlation.

² One-way analysis of variance (ANOVA).

using intralesional curettage, high-speed burring to remove the lesions; (3) bone grafting; (4) rigid internal fixation.

Using intralesional curettage and bone grafting are the principle methods for treating large proximal femoral defects of FD, which can effectively prevent lesion progression,

rebuild anatomic structures, and heighten mechanical properties of the lesion sites. As previously described, considering the limitations of autografts and allografts, scientists continue to explore new artificial bone replacement products, such as nanocomposite bone material in our institution [17, 22].

As a significant component of nanocomposite bone material, n-HA is similar to natural bone in composition and morphology [22]. The early period animal research and *in vitro* experimental studies demonstrated that the n-HA was biologically safe and had good histocompatibility and its hemolysis ratio was given as 0.59% without cytotoxicity, allergenicity, or pyrogen reaction [12, 16, 17, 23–26]. Nanocomposite bone material made up for the deficiencies of autografts and allografts to some extent [27, 28]. Moreover, nanocomposite bone material ensured an adequate supply and was convenient for application without additional damage to patients. Apart from bone autografts and allografts, nanocomposite bone material simplified bone-grafting procedures and shortened operation time. Our investigation determined that the 31 patients responded that their function recovered satisfactorily, and their limb motion scope improved significantly. There were no apparent nonspecific inflammatory or rejection reactions. No obvious lacuna was detected between grafting materials and host bone tissues after one year follow-up. The new bone formed in the residual lumen gradually crawled to the center and connected plate-like bone tissues, which means that the new bone formed close connections between grafting bone materials and host bone (Figures 2 and 3).

Nanocomposite bone material has 300–700 μm macropores and 0.5–50 μm micropores, a maximum porosity ratio of 85%, and a maximum hole rate of 60%. The three-dimensional spatial structure composed by macropores and micropores increases the internal surface area, which is beneficial to adsorb proteins, thus improving the activity of alkaline phosphatase (ALP), facilitating bone biomineralization, promoting the process of cell adhesion, growth, proliferation, differentiation, promoting calcium, and phosphorus sediment deposits on the surface, and accelerating osteogenesis. Higher porosity is also advantageous for the transmission of oxygen and nutrients and for the growth of blood vessels and nerves. Thus, good conditions were provided for new bone formation. At the same time, the compressive strength of n-HA lies in the range of 2.0–10.0 MPa and the content of n-HA in composites was controlled to approximately 65%, which gives it a similar mechanical strength, bending strength, and elastic modulus to cancellous bone. The accumulation of mechanical strength by a porous material structure with the characteristics mentioned above satisfied the requirements to repair bone defects and the demands of early functional exercise after surgery [12, 14, 15, 24]. When a lesion involves the bone cross-sectional area <50%, the sick femur underwent nanocomposite bone material grafting and achieved satisfactorily bone fusion one year after surgery (Figure 4). Yang et al. [23] suggested that the porous materials could improve mechanical strength by providing bone remodeling with mechanical support. Additionally, nanocomposite bone material can effectively avoid the joint collapse of the bone-grafting area or fractures. In our study, 3 patient lesions

involved a bone cross-sectional area > 50% and a diameter of cortical bone defect over 5 cm; therefore, an allogeneic cortex bone plate was tightly embedded in the window of the lesion cortex bone and the femur reconstruction nail was fixed at the same time. Because of the severe lesions, the residual cortical bone is weakened after osteotomy and intralesion curettage, which can cause a large segment of cortical bone defects. Under such conditions, we use allogeneic bone plate grafting to provide longitudinal support and to obtain dispersion axial stress with fixation of femoral reconstruction nails. This can provide a relatively closed frame structure for composite bone grafting and avoid artificial heterotopic ossification in the surrounding soft tissue. In the follow-up period, no nonspecific inflammation, rejection, recurrence, pathologic fractures, or loosened internal fixation was encountered in the 3 patients. The defects were fully occupied by composite bone within a year and a radiographically observable bony union. Meanwhile, there was no significant difference in G/N ratio between allograft users and nanocomposite bone material isolate users. In the last follow-up, the users all had satisfactory limb function.

In early reports, preliminary judgment of postoperative bone healing primarily relied on X-ray. Zhang et al. [15] used X-rays and CT scans to make qualitative evaluations about bone union/disunion and the space between grafted bone and host bone tissues. Xiong et al. [14] estimated the extent of bone union through a postoperative osteoplastic ratio (usually presented as a percentage). They used SIEMENS digital imaging software program to measure the X-ray radiation resistance ratio of normal bone around the grafting zone and nonlesion zone for quantitative analysis and then calculated the G/N ratio (grafting zone/nonlesion zone). In our study, image data, Harris score, and MSTs score were applied to estimate bone union/disunion and function. X-ray and CT scan showed that 25% of grafting zones were replaced by new bones in 2 to 3 months after surgery and 50% in 6 to 9 months after surgery. Bone defects were completely replaced by new bone at one year after surgery, and the mineral density of the bone-grafting areas was closer to normal areas. The mean radiopaque density ratio was 0.78 ± 0.09 one year after operation. Hence, we can quantitatively monitor the condition of bone healed and guide the orthopedists to make proper medical judgments on the basis of the G/N ratio. Meanwhile, the functional scores mentioned above sufficiently showed satisfactory function outcomes. After the lesion heals well, the internal fixation is not considered for removal.

Limitations of the Current Study. It should be noted that this study has included 3 cases that underwent allograft cortex bone plate grafting at the same time. Allografts may impact the bone fusion of nanocomposite bone material. Additionally, this study did not undertake a long term follow-up period, and we need more time to monitor whether there was lesion recurrence, metastasis, or complications caused by the material. In addition, the correcting of deformities, lesion curettage, and solid internal fixation was important to guarantee bone grafting fusion and these factors may affect the results.

5. Conclusions

Nanocomposite bone material has biological safety and good biocompatibility. The material can achieve self-repairing through bone conduction and osteogenic induction and is an efficient bone-grafting material that presents satisfactory effects in the repair of large proximal femoral defects that are due to fibrous dysplasia and should be generalized in the orthopedic field.

Conflict of Interests

The authors declare that they have no conflict of interests.

Authors' Contribution

Yun Lang and Ze-ping Yu participated in the collection of clinical data, performed patient follow-ups, and drafted the paper. Yan Xiong made substantial contributions to conception and design of this research and has reviewed the paper for important intellectual content and given final approval of the version to be published. Hong Li and Yong-gang Yan provided the data of the composites' *in vitro* and animal experiments. Fang Yuan analysed the image data. Hong Duan and Chong-qi Tu were responsible for these operations and participated in project coordination and assisted with the paper. Each author has participated sufficiently in this work to take public responsibility for the appropriate portions of the paper. All authors read and approved the final paper. Yun Lang and Ze-ping Yu contributed equally to this work and should be considered cofirst authors.

Acknowledgment

The result described in this paper was supported by the National Science and Technology Support Program of the People's Republic of China (2007BAE131304).

References

- [1] A. C. Looker, B. Dawson-Hughes, A. N. A. Tosteson, H. Johansson, J. A. Kanis, and L. J. Melton III, "Hip fracture risk in older US adults by treatment eligibility status based on new National Osteoporosis Foundation guidance," *Osteoporosis International*, vol. 22, no. 2, pp. 541–549, 2011.
- [2] W. R. Moore, S. E. Graves, and G. I. Bain, "Synthetic bone graft substitutes," *ANZ Journal of Surgery*, vol. 71, no. 6, pp. 354–361, 2001.
- [3] A. Schorr, W. Campbell, and M. Schenk, *Communication Research and Media Science in Europe: Perspectives for Research and Academic Training in Europe's Changing Media Reality*, Mouton de Gruyter, Berlin, Germany, 2003.
- [4] A. S. Greenwald, S. D. Boden, V. M. Goldberg, Y. Khan, C. T. Laurencin, and R. N. Rosier, "Bone-graft substitutes: facts, fictions, and applications," *Journal of Bone and Joint Surgery A*, vol. 83, supplement 2, pp. 98–103, 2001.
- [5] L. Lichtenstein, "Polyostotic fibrous dysplasia," *Archives of Surgery*, vol. 36, no. 5, pp. 874–898, 1938.
- [6] E. Ippolito, E. W. Bray, A. Corsi et al., "Natural history and treatment of fibrous dysplasia of bone: a multicenter clinicopathologic study promoted by the European Pediatric Orthopaedic Society," *Journal of Pediatric Orthopaedics, Part B*, vol. 12, no. 3, pp. 155–177, 2003.
- [7] M. Riminucci, I. Saggio, P. G. Robey, and P. Bianco, "Fibrous dysplasia as a stem cell disease," *Journal of Bone and Mineral Research*, vol. 21, supplement 2, pp. 125–131, 2006.
- [8] W. F. Enneking and P. F. Gearen, "Fibrous dysplasia of the femoral neck. Treatment by cortical bone-grafting," *The Journal of Bone & Joint Surgery—American Volume*, vol. 68, no. 9, pp. 1415–1422, 1986.
- [9] L. Yang, Y. Jing, D. Hong, and T. Chong-Qi, "Valgus osteotomy combined with intramedullary nail for Shepherd's crook deformity in fibrous dysplasia: 14 femurs with a minimum of 4 years follow-up," *Archives of Orthopaedic and Trauma Surgery*, vol. 130, no. 4, pp. 497–502, 2010.
- [10] J. T. Guille, S. J. Kumar, and G. D. Macewen, "Fibrous dysplasia of the proximal part of the femur: long-term results of curettage and bone-grafting and mechanical realignment," *The Journal of Bone & Joint Surgery—American Volume*, vol. 80, no. 5, pp. 648–658, 1998.
- [11] X. Yang, Q. Chen, L.-M. Liu et al., "Comparison of anterior cervical fusion by titanium mesh cage versus nano-hydroxyapatite/polyamide cage following single-level corpectomy," *International Orthopaedics*, vol. 37, no. 12, pp. 2421–2427, 2013.
- [12] H. Li, Y. B. Li, Y. G. Yan, G. Zhou, M. Wang, and L. Cheng, "Preparation and biological safety evaluation of porous n-HA/PA66 composite," *Journal of Biomedical Engineering*, vol. 25, no. 5, pp. 1126–1129, 2008.
- [13] Y. Zhang, Z.-X. Quan, Z.-H. Zhao et al., "Evaluation of anterior cervical reconstruction with titanium mesh cages versus nano-hydroxyapatite/polyamide66 cages after 1- or 2-level corpectomy for multilevel cervical spondylotic myelopathy: a retrospective study of 117 patients," *PLoS ONE*, vol. 9, no. 5, Article ID e96265, 2014.
- [14] Y. Xiong, C. Ren, B. Zhang et al., "Analyzing the behavior of a porous nano-hydroxyapatite/polyamide 66 (n-HA/PA66) composite for healing of bone defects," *International Journal of Nanomedicine*, vol. 9, no. 1, pp. 485–494, 2014.
- [15] S.-L. Zhang, Y. Zhou, H. Duan et al., "Repairing bone defect with nano-hydroxyapatite and polyamide 66 composite after giant cell tumor operation," *Journal of Sichuan University—Medical Science Edition*, vol. 43, no. 3, pp. 373–377, 2012.
- [16] C.-Y. Meng, H. An, D.-M. Jiang et al., "Repair of bone defect with porous composite of nano-hydroxyapatite and polyamide," *Chinese Journal of Orthopaedic Trauma*, vol. 21, no. 3, pp. 187–191, 2005.
- [17] H. Wang, Y. Li, Y. Zuo, J. Li, S. Ma, and L. Cheng, "Biocompatibility and osteogenesis of biomimetic nano-hydroxyapatite/polyamide composite scaffolds for bone tissue engineering," *Biomaterials*, vol. 28, no. 22, pp. 3338–3348, 2007.
- [18] N. N. Mahomed, D. C. Arndt, B. J. McGrory, and W. H. Harris, "The Harris hip score: comparison of patient self-report with surgeon assessment," *The Journal of Arthroplasty*, vol. 16, no. 5, pp. 575–580, 2001.
- [19] W. F. Enneking, W. Dunham, M. C. Gebhardt, M. Malawar, and D. J. Pritchard, "A system for the functional evaluation of reconstructive procedures after surgical treatment of tumors of the musculoskeletal system," *Clinical Orthopaedics and Related Research*, vol. 1, no. 286, pp. 241–246, 1993.

- [20] T. Lejman and J. Sulko, "Orthopedic management in children with fibrous dysplasia of bone," *Chirurgia Narządów Ruchu i Ortopedia Polska*, vol. 64, no. 3, pp. 303–310, 1999.
- [21] R. P. Stanton, E. Ippolito, D. Springfield, L. Lindaman, S. Wientroub, and A. Leet, "The surgical management of fibrous dysplasia of bone," *Orphanet Journal of Rare Diseases*, vol. 7, supplement 1, article S1, 2012.
- [22] L. Wu, Y.-B. Li, W.-H. Yang, L. Zhang, and J.-M. Han, "Qualitative and quantitative comparison of human cortical bone, nano-HA and nano-HA/PA66," *Chinese Journal of Functional Material*, vol. 36, no. 6, pp. 892–895, 2005.
- [23] K. Yang, J. Wei, C.-Y. Wang, and Y. Li, "A study on in vitro and in vivo bioactivity of nano hydroxyapatite/polymer biocomposite," *Chinese Science Bulletin*, vol. 52, no. 2, pp. 267–271, 2007.
- [24] Q. Xu, H. Lu, J. Zhang, G. Lu, Z. Deng, and A. Mo, "Tissue engineering scaffold material of porous nanohydroxyapatite/polyamide 66," *International Journal of Nanomedicine*, vol. 5, pp. 331–335, 2010.
- [25] B. Qiao, J. Li, Q. Zhu et al., "Bone plate composed of a ternary nano-hydroxyapatite/polyamide 66/glass fiber composite: biomechanical properties and biocompatibility," *International Journal of Nanomedicine*, vol. 9, no. 1, pp. 1423–1432, 2014.
- [26] Y. Qu, P. Wang, Y. Man, Y. Li, Y. Zuo, and J. Li, "Preliminary biocompatible evaluation of nano-hydroxyapatite/polyamide 66 composite porous membrane," *International Journal of Nanomedicine*, vol. 5, no. 1, pp. 429–435, 2010.
- [27] T. J. Cypher and J. P. Grossman, "Biological principles of bone graft healing," *Journal of Foot and Ankle Surgery*, vol. 35, no. 5, pp. 413–417, 1996.
- [28] H. J. Mankin, F. J. Hornicek, and K. A. Raskin, "Infection in massive bone allografts," *Clinical Orthopaedics and Related Research*, vol. 3, no. 432, pp. 210–216, 2005.

Research Article

Effects of Nitrogen-Doped Multiwall Carbon Nanotubes on Murine Fibroblasts

J. G. Munguía-Lopez,¹ E. Muñoz-Sandoval,² J. Ortiz-Medina,^{2,3}
F. J. Rodríguez-Macias,⁴ and A. De Leon-Rodríguez¹

¹Molecular Biology Division, Instituto Potosino de Investigación Científica y Tecnológica (IPICYT), Camino a la Presa San José 2055, Colonia Lomas 4a Sección, 78216 San Luis Potosí, SLP, Mexico

²Advanced Materials Department, Instituto Potosino de Investigación Científica y Tecnológica (IPICYT), Camino a la Presa San José 2055, Colonia Lomas 4a Sección, 78216 San Luis Potosí, SLP, Mexico

³Research Center for Exotic Nanocarbons (JST), Shinshu University, Wakasato 4-17-1, Nagano 380-8553, Japan

⁴Department of Fundamental Chemistry, Universidade Federal de Pernambuco, Avenida Proessor Luiz Freire, 50740-540 Recife, PE, Brazil

Correspondence should be addressed to A. De Leon-Rodríguez; aleonr@ipicyt.edu.mx

Received 13 July 2015; Accepted 11 August 2015

Academic Editor: Faik Oktar

Copyright © 2015 J. G. Munguía-Lopez et al. This is an open access article distributed under the Creative Commons Attribution License, which permits unrestricted use, distribution, and reproduction in any medium, provided the original work is properly cited.

The effect of nitrogen-doped multiwall carbon nanotubes (CN_x) on the proliferation of NIH-3T3 murine fibroblasts is presented. CNTs were dispersed in distilled water and incubated with mammalian cells in order to evaluate their toxicity. Also, the influence of factors such as dosage (7 and 70 µg/mL), exposure time (24 to 96 h), and the exposure route (before and after cell liftoff) on the cell proliferation was evaluated. When the CN_x were simultaneously incubated with the cells, the control culture reached a maximum cell concentration of $1.3 \times 10^5 \pm 3.4 \times 10^4$ cells per well at 96 h, whereas cultures with 7 µg/mL reached a concentration of $2.6 \times 10^4 \pm 5.3 \times 10^3$ cells. In the case of 70 µg/mL of CN_x most of the cells were dead. The CN_x that were added 24 h after cell dissociation showed that live cells decreased, with a cell concentration of $9.6 \times 10^4 \pm 9 \times 10^3$ for 7 µg/mL and $5.5 \times 10^4 \pm 9.5 \times 10^3$ for 70 µg/mL, in contrast to control cultures with $1.1 \times 10^6 \pm 1.5 \times 10^4$. The results showed that the CN_x had cytotoxic effects depending on the concentration and exposure route.

1. Introduction

A wide range of nanomaterials has been developed for several applications over the past few years. Due to their physical, chemical, electrical, and thermal properties, and since their discovery in 1991 [1], carbon nanotubes (CNTs) have shown a potential for use in drug delivery, biosensor, antimicrobial nanocomposite film, and cellular scaffolding. CNTs are tiny hollow cylinders, made from a single, double, or several layers of graphene that are concentrically arranged and capped by fullerene hemispheres. They have diameters ranging from 0.4 to 2 nm for single walled carbon nanotubes (SWCNTs) and from 2 to 200 nm for multiwall carbon nanotubes (MWCNTs), and lengths ranging from hundreds of nanometers to micrometers [1–3]. Since CNTs have an asbestos-like shape,

research into their toxicity and potential risks to human health has been intensified [4–7].

Studies on cellular response in nonfunctionalized or functionalized (addition of functional groups on a graphite surface) MWCNT have been extensive. Chemical doping (carbon atoms substitution) with nitrogen of CNTs (CN_x) was suggested to have positive effects on mice survival [8] and showed an improvement in cell-adhesion strength, viability, and proliferation of mammalian cells [3, 9], in contrast with the MWCNT. However, cytotoxic effects of CN_x have also been reported, where long length CN_x were more toxic than other functionalized CNTs [10]. Researches have demonstrated that cells exhibited variable responses to CNTs depending on different factors such as the method of synthesis, impurities, length and diameter, type (pristine,

functionalized, and doped), degree of dispersion/agglomeration, dispersant, CNT concentration, time exposure, cellular type, and protein adsorption [2, 5, 6, 8, 11, 12]. Due to the inconsistency in CN_x biocompatibility, more studies regarding cell response to these nanomaterials are necessary.

In the body, cell motility and wound healing are carried out by cell detachment, which is generated by proteolytic processes using endogenous proteases [13]. One of the most common enzymatic methods used for cell detachment in adherent-cell-subculture is trypsinization; trypsin cuts adhesion proteins to yield disaggregated cells with a rounded appearance. Although many cells are able to tolerate trypsin digestion during a short period of time, trypsinization causes cell stress affecting cytoskeleton proteins that are involved in regulating cell adhesion, stability, and elasticity [14–16].

CNTs have the capacity to adsorb a wide range of proteins, especially those rich in histidine, tryptophan, and phenylalanine [12], and also adhesion proteins from extracellular matrix (fibronectins, collagen) and transmembrane-proteins (integrins) [17]. Since enzymatic cell detachment can produce residual fragments of adhesion proteins, these fragments could interact with CNTs altering the extracellular matrix metabolism which is regulated by a complex mechanism including cell-cell and cell-matrix interactions [13, 17]. For this reason, the knowledge of cell-CNTs interactions is essential for cell scaffold development that is used in tissue regeneration.

The aim of this study was to evaluate the possible toxic effect of CN_x on NIH-3T3 murine fibroblast stressed by enzymatic detachment and nonstressed cells, in which a natural cell detachment stress was simulated by a trypsin incubation during a short period of time. Exposure route was defined in this work as the way to add nanomaterials to cell cultures (stressed and nonstressed cells). Besides several parameters are required to determine if new materials are safe for biomedical use; the effects of CN_x concentration and exposure time were also evaluated.

2. Materials and Methods

2.1. Synthesis, Purification, and Characterization of CN_x . In this way, CN_x were synthesized by using the chemical vapor deposition (CVD) method. As a chemical precursor 2.5 wt% ferrocene in benzylamine was used; the solution was placed into a reservoir and atomized. The aerosol was carried by an Argon flow at 2.5 L/min into a quartz tube 100 cm in length, placed inside of two tubular furnaces heated at 850°C. After 30 min of synthesis, the quartz tube was then cooled at room temperature and the CN_x were collected by internal scraping. Then, the pristine CN_x were purified and dispersed by using a pulsed probe sonicator in water under reflux, followed by a reflux in 6 M HCl and filtration.

Consequently, the purified CN_x were analyzed by scanning electron microscopy (SEM) as follows: first, the nanomaterials were pounded into a whole powder and separated into equal portions. Then, each portion was loaded into pins and visualized by SEM (Philips-XL 30 SFEG; Dual Beam (FIB/SEM) FEI-Helios Nanolab 600 equipped with an EDX detector) to determine lengths, diameters, and chemical

composition of CN_x . Raman characterization was performed using a laser of 633 nm in Raman Renishaw Micro-Raman equipment.

2.2. Preparation of Dispersion of Purified CN_x . Stocks of purified CN_x were dispersed in distilled water at 1 mg/mL. Then, the samples were sonicated by an ultrasonic bath at 42 kHz and 100 W (Branson 2510 Ultrasonic Cleaner), at 40°C for 8 h, having as a result stable dispersions; these conditions were strong enough to obtain no visible agglomerates of purified CN_x . Finally, all the stocks were stored at 4°C until further use.

2.3. Cytotoxicity Assays. The effects of purified CN_x on the viability of NIH-3T3 murine fibroblast were evaluated by using the Trypan-blue exclusion method. Briefly, the cells were defrosted and cultured in a basal-IMDM (Iscove's Modified Dulbecco's Medium, SIGMA) at pH 7.2 and supplemented with 10% fetal bovine serum (GIBCO), 100 U/mL penicillin, 100 µg/mL streptomycin, and 0.25 µg/mL amphotericin B (SIGMA), using 24-well plates (Corning) over a period of 72 h in a humidity chamber at 37°C and CO₂ 5% (Shell-Lab). After three passes, when 80% of cellular confluence was reached, the cells were washed twice gently with PBS (pH 7.2) and then harvested by incubation with trypsin-EDTA (0.25%-IX, GIBCO) for 10 min. Cell suspensions with a density of 2×10^3 cells per well were added into 96-well plates in absence or presence of purified CN_x at final concentrations of 7 and 70 µg/mL. For exposure route experiments, purified CN_x were added (1) immediately after cell dissociation (stressed cells) or (2) fibroblasts were firstly incubated for 24 h and then purified CN_x were added into each well (non-stressed cells). Samples were washed twice gently with PBS, incubated with trypsin for 6 min, and cells were counted by using the Trypan-blue method. During the 96 h of exposure with the nanomaterial, samples were taken each 24 h. NIH-3T3 cell cultures without nanomaterials were used as control. To avoid variation on purified CN_x concentration in cell cultures when medium was changed, kinetics were carried out using a working volume of 250 µL without medium replacement.

2.4. Statistics. The data is presented as the mean \pm standard deviation, with a statistical comparison of one- and two-way ANOVA. We used Dunnett's posttests to compare treatments with control groups, and p values <0.05 were considered significant. All experiments were done in triplicate.

3. Results and Discussion

3.1. Determination of Length and Diameter of Purified CN_x . Figure 1 shows SEM micrographs and size distribution of purified CN_x . Micrographs by the XL30 and Helios are shown in Figures 1(a) and 1(c), respectively. A few bundles were found in purified CN_x samples to determine the lengths of nanomaterials (Figure 1(a)). The length range was 10 to 130 µm, being the most abundant lengths of 40–50 µm (Figure 1(b)). In micrographs of purified CN_x , the nanomaterials seemed to have similar diameters (Figure 1(c)), but, after

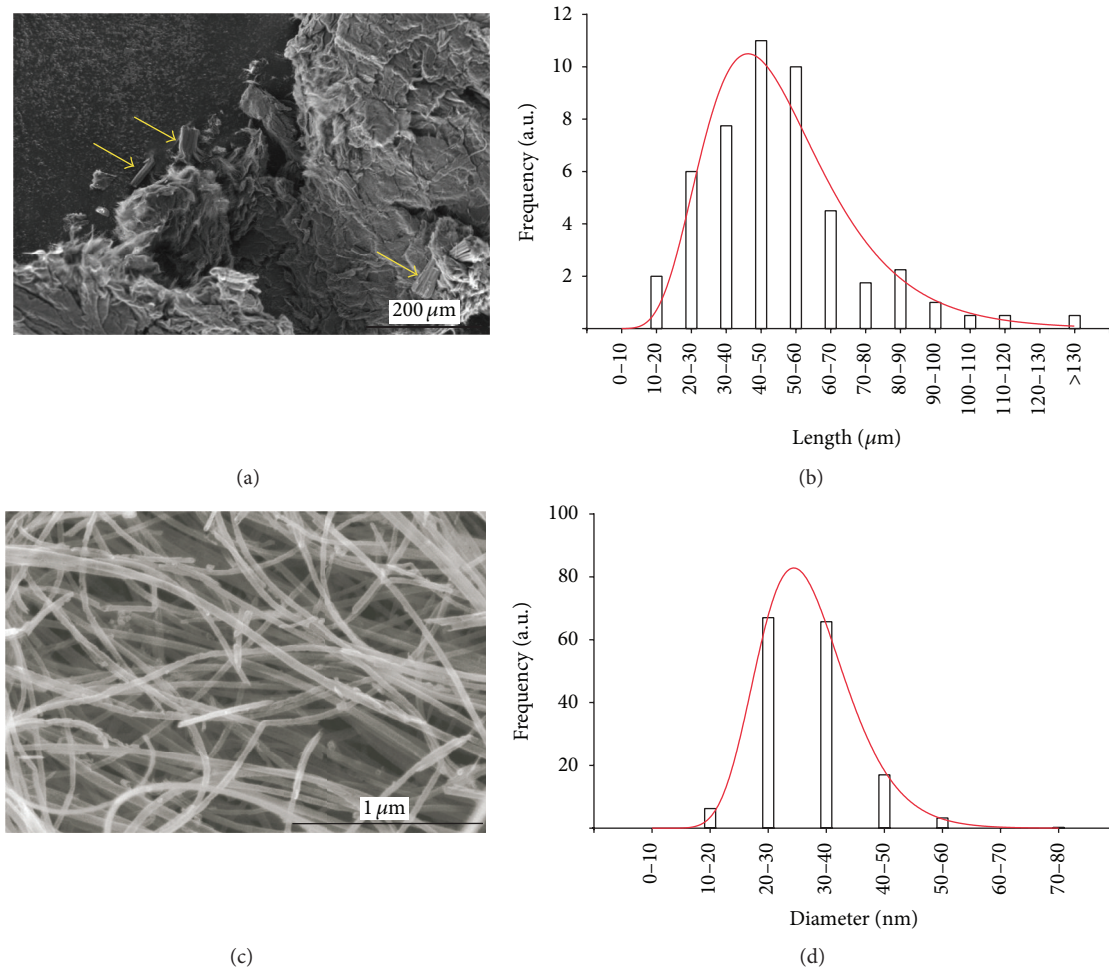


FIGURE 1: SEM micrographs of CN_x morphology and size distribution. Lengths were obtained from bundles of purified CN_x ((a), pointed with yellow arrows) and plotted to generate distribution patterns. Diameters were obtained from individual tubes from Helios SEM images (c) and distribution was plotted (d).

an analysis with the Helios microscopy, the diameter sizes were around 10–80 nm, with a diameter predominance of 20–40 nm (Figure 1(d)).

Nanomaterial sizes were obtained from their own bundles and short “fibrous” structures (Figure 2). The number of bundles among different samples of purified CN_x was small (around 38 bundles) (Figures 2(a)–2(c), yellow arrows), as well as in between the same sample (Figures 2(d)–2(f)). Since purified CN_x samples were mostly agglomerated in big structures by dry process, the determination of their total lengths was difficult; thus only the bundles lengths were reported. The presence of amino groups in the CN_x could be the reason to find less bundles in samples, due to their weaker van der Waals interactions, resulting in lower formation of bundles [8].

3.2. Raman and EDX Characterization of Pristine and Purified CN_x. Figure 3 shows the Raman spectra of pristine and purified CN_x plotted between 100 and 3000 cm⁻¹. The bands D (defect mode), G (graphite mode), and G' (second order mode) situated at 1340, 1592, and 2686 cm⁻¹, respectively, are

the typical peaks corresponding to carbonaceous materials. In the case of purified CN_x, the shifting to higher frequencies of G band suggests that nitrogen doping decreased. The I_D/I_G values were 1.1488 and 1.2815 for pristine and purified CN_x, respectively. This increasing in I_D/I_G ratio has been suggested as an evidence for sidewall functionalization of CNTs [18, 19].

With respect to chemical composition of our CN_x (pristine and purified), EDX analysis was carried out. Figures S1 and S2 (see Supplementary Material available online at <http://dx.doi.org/10.1155/2015/801606>) show the SEM images and their respective EDX graphs. The average quantity of iron in pristine samples was of 2.22 wt% (Figure S1), which decreased after purification process to 0.61 wt% (Figure S2), indicating the elimination of this contaminant (see Supplementary Material for the quantities of carbon, nitrogen, and oxygen elements).

3.3. Effect of Purified CN_x on Murine Fibroblasts Nonstressed and Stressed. 3T3 murine fibroblasts were used as a model for stromal cells, which can be found in matrix and connective tissue throughout the body. Figure 4 shows the kinetics of

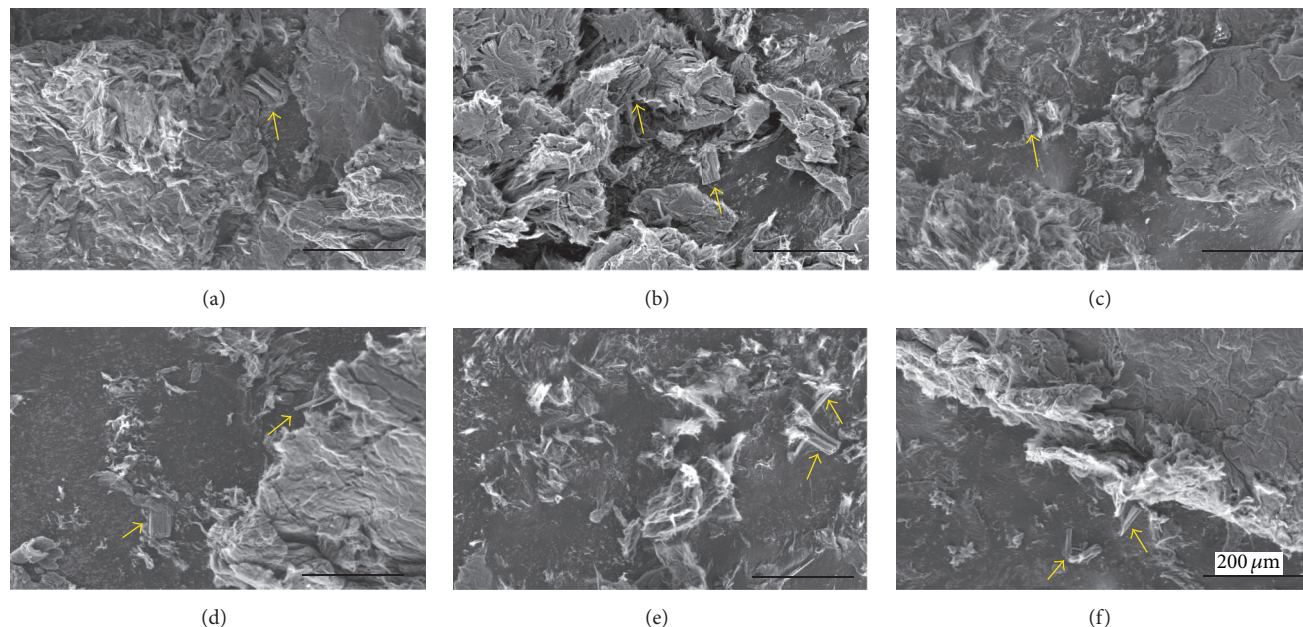


FIGURE 2: Representative SEM images of whole sample dry purified CN_x . (a–c) Different parts of sample from whole sample; (d–f) the same sample different fields. Yellow arrows pointed to bundles of purified CN_x . Big structures are agglomerates of CNTs which were easy to disperse in water.

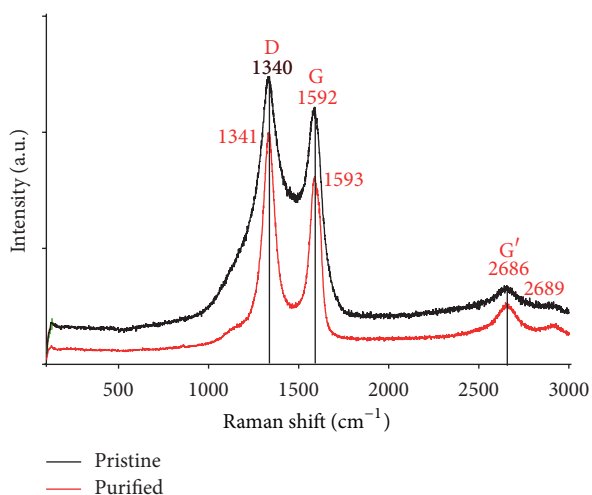


FIGURE 3: Raman spectra of pristine and purified CN_x at 633 nm.

fibroblasts growth with water-dispersed purified CN_x . When the cells were incubated simultaneously with the purified CN_x , the control culture (without purified CN_x) reached a maximum live cell concentration of $1.3 \times 10^5 \pm 3.4 \times 10^4$ cells per well at 96 h; meanwhile cultures with $7 \mu\text{g/mL}$ reached $2.6 \times 10^4 \pm 5.3 \times 10^3$ cells, and a drastic no cell survival was at $70 \mu\text{g/mL}$ of purified CN_x (Figure 4(a)). Purified CN_x added after 24 h of cell dissociation showed a decreased live cell, with a cell concentration of $9.6 \times 10^4 \pm 9 \times 10^3$ for $7 \mu\text{g/mL}$ and $5.5 \times 10^4 \pm 9.5 \times 10^3$ for $70 \mu\text{g/mL}$, compared to control culture with $1.1 \times 10^6 \pm 1.5 \times 10^4$, at 96 h of exposure (Figure 4(b)). Results suggest that nanomaterials exhibited

toxic effects, in concentration and exposure route-dependent manner. No effects concerning time exposure were observed.

Murine fibroblasts were susceptible to purified CN_x in concentration and exposure route-dependent manner. As previously mentioned, toxicity/biocompatibility of CNTs (SWCNT, MWCNT, and functionalized CNTs) on mammalian cells depends on different factors [6, 20, 21]. A lot of data research has shown the toxicity of CNTs [22–25] in human mesenchymal stem cells [26], 3T3 L1 fibroblasts [27], 3T3 fibroblast, telomerase, immortalized human bronchiolar epithelial cells, RAW 264.7 macrophages [6], mouse fibroblast cell L929, and mouse adipose-derived stem cells [3], but, to our knowledge, no experiments about the effects of CNTs have been reported on mammalian cells stressed by enzymatic detachment, which is a natural process in the body. Treatments with water-dispersed purified CN_x immediately added after cell liftoff (stressed cells by trypsin) were more toxic than purified CN_x added after 24 h of cell dissociation, suggesting that exposure route factor had negative effects on cell proliferation. This could have been caused by interaction of CNTs with residual fragments of adhesion proteins generated after cell trypsinization [12], which can still adversely affect cytoskeleton proteins that are involved in regulating cell adhesion, stability, and elasticity [14–16, 28]. However, in this work, only the cell proliferation was evaluated as a first approach to determine the purified CN_x toxicity; therefore, more studies are required and are currently underway.

Specific growth rate (μ) was calculated from exponential growth phase of fibroblasts and used as a parameter to evaluate the effect of purified CN_x on cell growth. In $7 \mu\text{g/mL}$ of dispersed-water purified CN_x incubated simultaneously with cells, μ was lower ($0.031 \pm 0.004 \text{ h}^{-1}$) than control cultivation

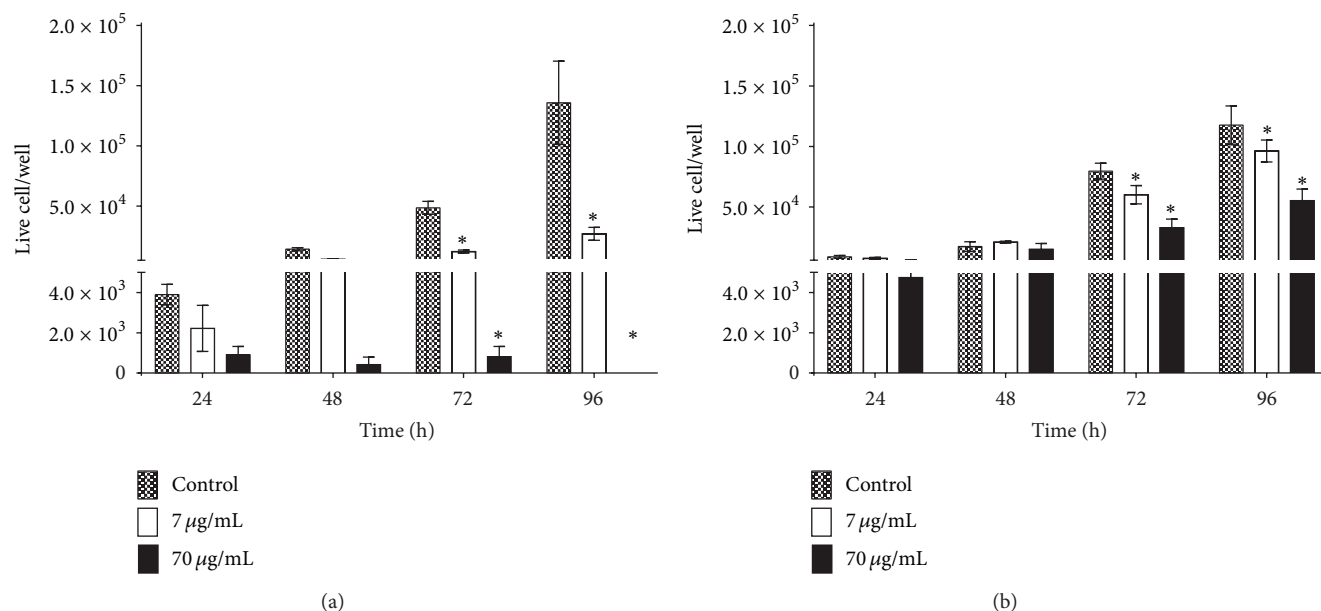


FIGURE 4: Effects of water-dispersed purified CN_x on NIH-3T3 murine fibroblast proliferation. Purified CN_x were incubated with fibroblast immediately after cell dissociation (a) or 24 h after cellular liftoff (b). Data are presented as mean ± SD. * indicates significant difference compared to untreated controls ($p < 0.05$); $n \geq 3$.

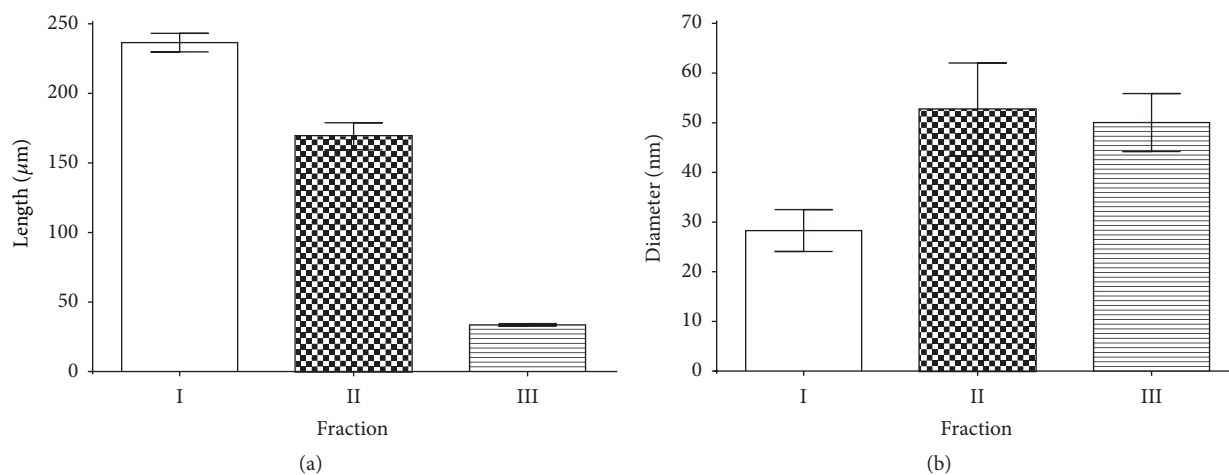


FIGURE 5: Variations in pristine CN_x length (a) and diameters (b) obtained from three different fractions of the same batch.

($0.048 \pm 0.004 \text{ h}^{-1}$); since no cells survived at $70 \mu\text{g/mL}$, μ was not determined. Concerning incubation of cells with nanomaterials for 24 h after cell liftoff, values of μ were $0.044 \pm 0.002 \text{ h}^{-1}$ for control culture and $0.037 \pm 0.002 \text{ h}^{-1}$ and $0.035 \pm 0.001 \text{ h}^{-1}$ for purified CN_x at 7 and $70 \mu\text{g/mL}$, respectively; both concentrations affected negatively μ . Results confirm a cytotoxic effect that is concentration and exposure route dependent.

3.4. Morphology Diversity of Pristine CN_x. In several investigations about cytotoxic effects of CNTs, these nanomaterials are purchased from companies, which are synthesized by CVD. However, researchers have reported different patterns in the bulk growth of CNTs during their synthesis, showing

that the CVD method produces a wide range of CNTs morphologies with varieties of lengths and diameters [29]. In preliminary results, different fractions from the same batch were analyzed by SEM showing a wide collection of pristine CN_x sizes (Figure 5), with lengths of range between 30 and 250 µm (Figure 5(a)) and diameters of 24–60 nm (Figure 5(b)). Figure 6 shows a SEM micrograph gallery of the morphology of the different pristine CN_x fractions, where the variations in lengths (Figures 6(a)–6(c)) and diameters (Figures 6(d)–6(f)) among three fractions are clear. The morphology variation of CNTs could be the reason behind having contradictory results regarding cytotoxicity/biocompatibility of CNTs reported in several researches, and this issue should be studied in order to understand the relationship between CNTs and mammalian cell response.

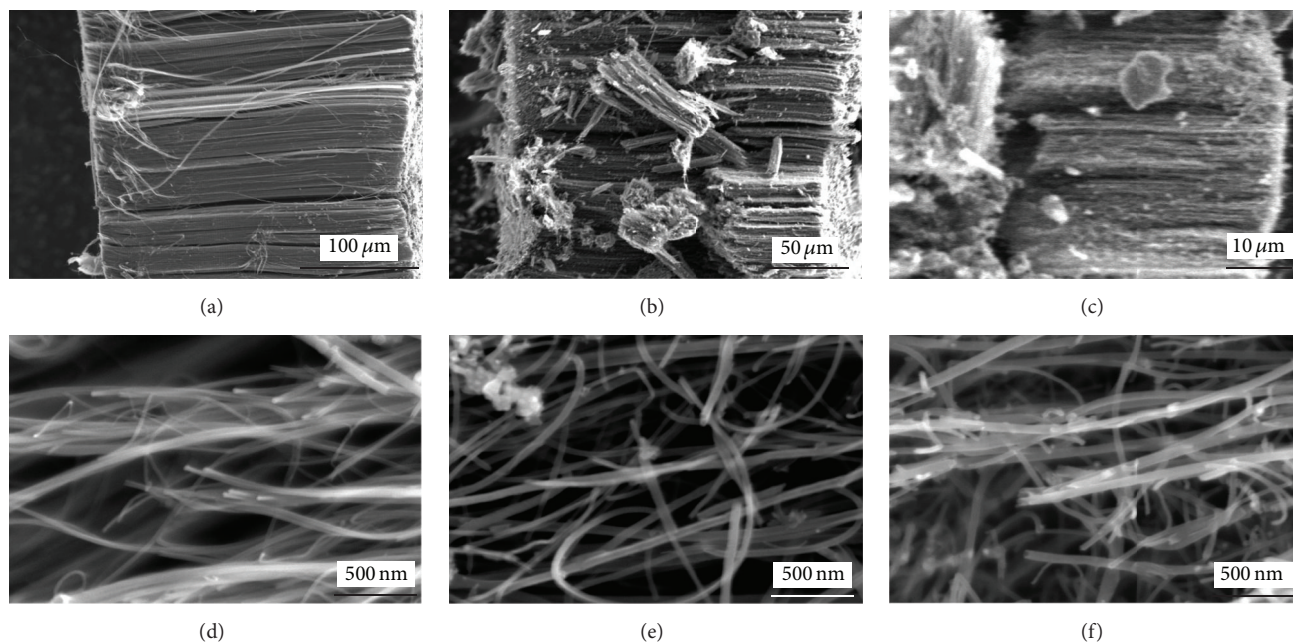


FIGURE 6: Electron micrograph gallery depicting the size diversity of pristine CN_x found in three different locations (fractions) from the quartz tube. Fractions: I (a, d), II (b, e), and III (c, f). Lengths (a–c) and diameters (d–f) of CN_x .

4. Conclusion

Finally, purified CN_x have a cytotoxicity effect that is directly dependent on their concentration; also purified CN_x showed a more toxic effect in enzymatic stressed cells than in the non-stressed ones. Since cells in the body are exposed to enzymatic processes of detachment, the present study of the effects on overstressed cells by enzymatic digestion is important for the development and potential uses of these nanomaterials in the biomedical field. On the other hand, chemical synthesis of pristine CN_x yields heterogenic product with substantial differences on length and diameter size, which have distinctive cytotoxic effects on the proliferation of NIH-3T3 cells. There is still a long path that we must take in order to understand the relationship between nanomaterials and mammalian cells. However, concentrations up to $7 \mu\text{g/mL}$ of nanotubes are well tolerated by the cells, and they could be used in biomedical applications.

Conflict of Interests

The authors declare that there is no conflict of interests regarding the publication of this paper.

Acknowledgments

The authors thank the Marcos Moshinsky Foundation and CONACYT-Mexico Grants 107082 (JFRM), CB-2013-220744 (EMS) for partial funding. J. Gil Munguía-López thanks CONACYT for its Scholarship 250279. They also thank L. Aldana for the English review and L. Ordoñez, B. A. Rivera-Escoto, and G. J. Labrada-Delgado for their technical assistance.

References

- [1] S. Iijima, "Helical microtubules of graphitic carbon," *Nature*, vol. 354, no. 6348, pp. 56–58, 1991.
- [2] H.-F. Cui, S. K. Vashist, K. Al-Rubeaan, J. H. T. Luong, and F.-S. Sheu, "Interfacing carbon nanotubes with living mammalian cells and cytotoxicity issues," *Chemical Research in Toxicology*, vol. 23, no. 7, pp. 1131–1147, 2010.
- [3] M. L. Zhao, D. J. Li, L. Yuan, Y. C. Yue, H. Liu, and X. Sun, "Differences in cytocompatibility and hemocompatibility between carbon nanotubes and nitrogen-doped carbon nanotubes," *Carbon*, vol. 49, no. 9, pp. 3125–3133, 2011.
- [4] X. Wang, T. Xia, M. C. Duch et al., "Pluronic F108 coating decreases the lung fibrosis potential of multiwall carbon nanotubes by reducing lysosomal injury," *Nano Letters*, vol. 12, no. 6, pp. 3050–3061, 2012.
- [5] H. Haniu, N. Saito, Y. Matsuda et al., "Effect of dispersants of multi-walled carbon nanotubes on cellular uptake and biological responses," *International Journal of Nanomedicine*, vol. 6, pp. 3295–3307, 2011.
- [6] S. K. Sohaebuddin, P. T. Thevenot, D. Baker, J. W. Eaton, and L. Tang, "Nanomaterial cytotoxicity is composition, size, and cell type dependent," *Particle and Fibre Toxicology*, vol. 7, article 22, 2010.
- [7] A. Kunzmann, B. Andersson, T. Thurnherr, H. Krug, A. Scheynius, and B. Fadeel, "Toxicology of engineered nanomaterials: focus on biocompatibility, biodistribution and biodegradation," *Biochimica et Biophysica Acta (BBA)—General Subjects*, vol. 1810, no. 3, pp. 361–373, 2011.
- [8] J. C. Carrero-Sánchez, A. L. Elías, R. Mancilla et al., "Biocompatibility and toxicological studies of carbon nanotubes doped with nitrogen," *Nano Letters*, vol. 6, no. 8, pp. 1609–1616, 2006.
- [9] D. J. Li and L. F. Niu, "Influence of N atomic percentages on cell attachment for CN_x coatings," *Bulletin of Materials Science*, vol. 26, no. 4, pp. 371–375, 2003.

- [10] S. Boncel, K. H. Müller, J. N. Skepper, K. Z. Walczak, and K. K. K. Koziol, "Tunable chemistry and morphology of multi-wall carbon nanotubes as a route to non-toxic, theranostic systems," *Biomaterials*, vol. 32, no. 30, pp. 7677–7686, 2011.
- [11] D. Li, L. Yuan, Y. Yang et al., "Adsorption and adhesion of blood proteins and fibroblasts on multi-wall carbon nanotubes," *Science in China, Series C: Life Sciences*, vol. 52, no. 5, pp. 479–482, 2009.
- [12] X. Cai, R. Ramalingam, H. S. Wong et al., "Characterization of carbon nanotube protein corona by using quantitative proteomics," *Nanomedicine: Nanotechnology, Biology, and Medicine*, vol. 9, no. 5, pp. 583–593, 2013.
- [13] R. J. McAnulty, "Fibroblasts and myofibroblasts: their source, function and role in disease," *International Journal of Biochemistry & Cell Biology*, vol. 39, no. 4, pp. 666–671, 2007.
- [14] Q. Zheng, S. M. Iqbal, and Y. Wan, "Cell detachment: post-isolation challenges," *Biotechnology Advances*, vol. 31, no. 8, pp. 1664–1675, 2013.
- [15] H. E. Canavan, X. Cheng, D. J. Graham, B. D. Ratner, and D. G. Castner, "Cell sheet detachment affects the extracellular matrix: a surface science study comparing thermal liftoff, enzymatic, and mechanical methods," *Journal of Biomedical Materials Research—Part A*, vol. 75, no. 1, pp. 1–13, 2005.
- [16] H.-L. Huang, H.-W. Hsing, T.-C. Lai et al., "Trypsin-induced proteome alteration during cell subculture in mammalian cells," *Journal of Biomedical Science*, vol. 17, no. 1, article 36, 2010.
- [17] J.-P. Kaiser, T. Buerki-Thurnherr, and P. Wick, "Influence of single walled carbon nanotubes at subtoxic concentrations on cell adhesion and other cell parameters of human epithelial cells," *Journal of King Saud University—Science*, vol. 25, no. 1, pp. 15–27, 2013.
- [18] S. Lee, J.-W. Peng, and C.-H. Liu, "Raman study of carbon nanotube purification using atmospheric pressure plasma," *Carbon*, vol. 46, no. 15, pp. 2124–2132, 2008.
- [19] S. Banerjee and S. S. Wong, "Rational sidewall functionalization and purification of single-walled carbon nanotubes by solution-phase ozonolysis," *The Journal of Physical Chemistry B*, vol. 106, no. 47, pp. 12144–12151, 2002.
- [20] L. Meng, A. Jiang, R. Chen et al., "Inhibitory effects of multiwall carbon nanotubes with high iron impurity on viability and neuronal differentiation in cultured PC12 cells," *Toxicology*, vol. 313, no. 1, pp. 49–58, 2013.
- [21] P. M. V. Raja, J. Connolley, G. P. Ganesan et al., "Impact of carbon nanotube exposure, dosage and aggregation on smooth muscle cells," *Toxicology Letters*, vol. 169, no. 1, pp. 51–63, 2007.
- [22] C. L. Ursini, D. Cavallo, A. M. Fresegna et al., "Comparative cyto-genotoxicity assessment of functionalized and pristine multiwalled carbon nanotubes on human lung epithelial cells," *Toxicology in Vitro*, vol. 26, no. 6, pp. 831–840, 2012.
- [23] M. Bottini, S. Bruckner, K. Nika et al., "Multi-walled carbon nanotubes induce T lymphocyte apoptosis," *Toxicology Letters*, vol. 160, no. 2, pp. 121–126, 2006.
- [24] D. Liu, C. Yi, D. Zhang, J. Zhang, and M. Yang, "Inhibition of proliferation and differentiation of mesenchymal stem cells by carboxylated carbon nanotubes," *ACS Nano*, vol. 4, no. 4, pp. 2185–2195, 2010.
- [25] F. A. Witzmann and N. A. Monteiro-Riviere, "Multi-walled carbon nanotube exposure alters protein expression in human keratinocytes," *Nanomedicine: Nanotechnology, Biology, and Medicine*, vol. 2, no. 3, pp. 158–168, 2006.
- [26] E. Mooney, P. Dockery, U. Greiser, M. Murphy, and V. Barron, "Carbon nanotubes and mesenchymal stem cells: biocompatibility, proliferation and differentiation," *Nano Letters*, vol. 8, no. 8, pp. 2137–2143, 2008.
- [27] J. Meng, M. Yang, L. Song et al., "Concentration control of carbon nanotubes in aqueous solution and its influence on the growth behavior of fibroblasts," *Colloids and Surfaces B: Biointerfaces*, vol. 71, no. 1, pp. 148–153, 2009.
- [28] R. Umegaki, M. Kino-Oka, and M. Taya, "Assessment of cell detachment and growth potential of human keratinocyte based on observed changes in individual cell area during trypsinization," *Biochemical Engineering Journal*, vol. 17, no. 1, pp. 49–55, 2004.
- [29] S. S. Meysami, F. Dillon, A. A. Koós, Z. Aslam, and N. Grobert, "Aerosol-assisted chemical vapour deposition synthesis of multi-wall carbon nanotubes: I. Mapping the reactor," *Carbon*, vol. 58, pp. 151–158, 2013.

Research Article

Effect of Lipophilic Bismuth Nanoparticles on Erythrocytes

Rene Hernandez-Delgadillo,¹ Appala Raju Badireddy,² Valentin Zaragoza-Magaña,¹ Rosa Isela Sánchez-Nájera,¹ Shankararaman Chellam,³ and Claudio Cabral-Romero¹

¹Facultad de Odontología, Universidad Autónoma de Nuevo Leon (UANL), Monterrey, NL, Mexico

²School of Engineering, The University of Vermont, 33 Colchester Avenue, Burlington, VT 05405, USA

³Zachry Department of Civil Engineering, Texas A&M University, College Station, TX 77843-3136, USA

Correspondence should be addressed to Shankararaman Chellam; chellam@tamu.edu and Claudio Cabral-Romero; claudiohubble@hotmail.com

Received 29 June 2015; Accepted 13 August 2015

Academic Editor: Ecaterina Andronescu

Copyright © 2015 Rene Hernandez-Delgadillo et al. This is an open access article distributed under the Creative Commons Attribution License, which permits unrestricted use, distribution, and reproduction in any medium, provided the original work is properly cited.

Lipophilic bismuth dimercaptopropanol nanoparticles (BisBAL NPs) have a very important antimicrobial activity; however their effect on human cells or tissues has not been completely studied. Undesirable effects of bismuth include anemia which could result from suicidal erythrocyte death or eryptosis. The objective of this research was to determine the effect of bismuth dimercaptopropanol nanoparticles on blood cells. The nanoparticles are composed of 53 nm crystallites on average and have a spherical structure, agglomerating into clusters of small nanoparticles. Based on cell viability assays and optical microscopy, cytotoxicity on erythrocytes was observed after growing with 500 and 1000 μM of BisBAL NPs for 24 h. AM Calcein was retained inside erythrocytes when they were exposed to 100 μM (or lower concentrations) of BisBAL NPs for 24 h, suggesting the absence of damage in plasmatic membrane. Genotoxic assays revealed no damage to genomic DNA of blood cells after 24 h of exposition to BisBAL NPs. Finally, 100–1000 μM of bismuth nanoparticles promotes apoptosis between blood cells after 24 h of incubation. Hence BisBAL NPs at concentrations lower than 100 μM do not cause damage on blood cells; they could potentially be used by humans without affecting erythrocytes and leukocytes.

1. Introduction

Bismuth is used in industry and for treatment of gastrointestinal diseases [1, 2]. Previous reports described the very interesting antimicrobial and antibiofilm properties of bismuth nanoparticles with significant potential to be used in biomedical sciences [3–5]. Since elemental bismuth has very low water solubility, it has been chelated with compounds containing hydroxyl and sulfhydryl groups to produce water soluble and biocompatible complexes that are employed in pharmaceutical and personal care products (e.g., Pepto Bismol, De-Nol, and Tirtac (Pylorid), catalysts, alloys, and pigments) [6].

Early, the antimicrobial activity of nanostructures of several metals like silver, gold, zinc, titanium, and bismuth has been described with very good results [7–11]. However, most of them present high toxicity on human cells, limiting their

use [12–15]. Several approaches were made to reduce the undesired effects of metal nanoparticles; the most followed one is adding a biocompatible cover of cellulose, chitosan, or polymers like poly(lactic-co-glycolic acid) PLGA [16].

The toxicological aspects of bismuth compounds are well established and the reported side effects may include nephropathy, hepatitis, and encephalopathy [17]. Several studies described the absence of cytotoxicity of bismuth and their compounds on human cells [18–20], and our group has reported no cytotoxicity of 2 mM bismuth oxide nanoparticles on monkey kidney cells, after 24 hours of exposition [4]. The untoward effects of bismuth include anemia [21], which could at least in theory result from stimulation of suicidal erythrocyte death or eryptosis.

Eryptosis, the suicidal death of erythrocytes, is caused by several anemia-inducing endogenous substances, diabetes, chronic renal failure, hemolytic uremic syndrome, sepsis,

malaria, iron deficiency, and exogenous substances [22]. Several drugs have been described to trigger eryptosis, like alantolactone, gramicidin, naphthazarin, nelfinavir, hemolysin, listeriolysin, paclitaxel, chlorpromazine, cyclosporine, methylglyoxal, amyloid peptides, anandamide, Bay-5884, curcumin, valinomycin, aluminium, mercury, lead, and copper [22–26]. Eryptosis is characterized by phosphatidylserine exposure at the erythrocyte surface [27]. Phosphatidylserine exposing erythrocytes are rapidly cleared from circulating blood and result from phospholipid scrambling of the cell membrane [28].

The objective of this work was to determine whether BisBAL NPs trigger eryptosis in a cell culture. The effect of BisBAL nanoparticles with an average diameter of 53 nm and spherical shape was evaluated on blood cells. Based on cell viability assays and optical microscopy, cytotoxicity on erythrocytes was observed after growing with high concentrations (500–1000 μM) of BisBAL NPs for 24 h. This data correlates with hemoglobin level of erythrocytes exposed to the same concentrations of bismuth nanoparticles. Calcein AM was retained inside erythrocytes when they were exposed to 100 μM (or lower concentrations) of BisBAL NPs for 24 h, suggesting the absence of damage in plasmatic membrane of host cells. Genotoxic assays revealed no damage to genomic DNA of blood cells after 24 h of exposition to BisBAL NPs and finally 500–1000 μM of bismuth nanoparticles promotes apoptosis between blood cells after 24 h of incubation. All together, these results suggest that $\leq 100 \mu\text{M}$ of BisBAL NPs does not present side effects on blood cells and could be used in humans.

2. Material and Methods

2.1. Synthesis of BisBAL Nanoparticles. For the synthesis of bismuth nanostructures, the following chemical reagents were used: bismuth pentahydrate ($\text{Bi}(\text{NO}_3)_3 \cdot 5\text{H}_2\text{O}$), 2,3-dimercapto-1-propanol (BAL), sodium borohydride (NaBH_4), and propylene glycol, which were all analytical grade reagents purchased from Sigma-Aldrich (St. Louis, MO). Ultrapure water (Barnstead Nanopure Diamond) was used to prepare solutions and dilutions. BisBAL nanoparticles were synthesized using a method that was described in our recent publications. A stock solution of 2:1 molar ratio of Bi (Bis) to 2,3-dimercapto-1-propanol (BAL) (a.k.a. BisBAL) served as a cationic precursor for the BisBAL nanoparticles and the choice of molar ratio was based on the previous work, which showed BisBAL was stable over a wide pH range (4–11) and effective against microbial biofilm formation [29]. During the course of BisBAL reduction with NaBH_4 , the pink color of soluble BisBAL instantly transformed to a black colored suspension composed of BisBAL nanoparticles. The stock suspensions of 25 mM of BisBAL nanoparticles in 10 mL batches were prepared and stored at 4°C until use.

2.2. Characterization of BisBAL Nanoparticles. The nanoparticle size distribution was measured by dynamic light scattering (DLS, ALV-GmbH, Germany, scattering angle set at 90°). Information on the shape and size of nanoparticles was obtained using scanning electron microscopy (SEM; FEI

Tecnai G2 Twin, Hillsboro, OR; 160 kV accelerating voltage). Absorbance spectra of the nanoparticle suspensions were collected using the UV-Visible spectrophotometer (SpectraMax Plus384 Absorbance Microplate Reader, Molecular Devices, LLC, Sunnyvale, CA). The rhombohedral crystallinity and crystallite size were determined using the X-Ray Diffractometer (XRD: Panalytical X'Pert PRO MRD) equipped with $\text{Cu K}\alpha$ as X-ray source ($\lambda = 1.541874 \text{ \AA}$). Diffractograms were interpreted using the Debye-Scherrer formula (Panalytical X'Pert Data Viewer software) to estimate the rhombohedral structure and crystallite size. The lipophilicity of BisBAL nanoparticles was determined based on the affinity of nanoparticles to 1-octanol in 1-octanol-water phase mixture incubated for 30 minutes. The absorbance of nanoparticles in a phase was measured at 330 nm.

2.3. Blood Cells Culture and Their Quantification by MTT Assay. From a blood sample without anticoagulant erythrocytes, neutrophils and leucocytes were collected and separated by centrifugation at 14000 r.p.m. for 10 minutes [30]. After that, serum was retired from pellet of each fraction and cells were washed three times with cold PBS 1x. Erythrocytes, neutrophils, and leucocytes were cultured in minimum essential medium (MEM) supplemented with 10% of fetal bovine serum, respectively (FBS, Biowest, Nuaillé, France), onto 96-well plates (10^5 /well for 24 h) in triplicate at 37°C in a humidified incubator containing 5% CO_2 . The cell viability was evaluated by the amount of viable cells stained by 3-(4,5-dimethylthiazol-2-yl)-2,5-diphenyltetrazolium bromide (Biotium, Hayward, CA) which was released with dimethyl sulfoxide (DMSO, Sigma-Aldrich Inc., St. Louis, MO, USA). The optical density was detected at 595 nm using a microplate absorbance reader (Biotek, Winooski, VT). The killing effect of bismuth nanoparticles on blood cells was calculated as cell viability, which was indicated as follows: (the percentage of viable cells) = (absorbance of treated wells – absorbance of blank wells)/(absorbance of the control wells – absorbance of blank wells) $\times 100\%$.

2.4. Influence of BisBAL NPs on Morphology of Erythrocytes Culture by Optic Microscopy. From a blood sample without anticoagulant, a monolayer of erythrocytes was obtained by seeding 1×10^5 cells in a 96-well microtiter plate (Thermo Fisher Scientific, MA, USA) in 100 μL of minimum essential medium (MEM) supplemented with 10% of fetal bovine serum (FBS, Biowest, Nuaillé, France) and incubated at 37°C with 5% of CO_2 . 50, 100, 500, and 1000 μM of BisBAL NPs were added to cell culture and incubated for 1 hour at 37°C with 5% of CO_2 and their effect on cell morphology was observed by optical microscopy using an inverted microscope (Motic, Hong Kong). The presence of cytopathic effect was identified by amorphous shape, light refractive cells, and loss of confluent monolayer.

2.5. Effect of BisBAL NPs on Blood Cells. The possible cytotoxicity of BisBAL NPs against erythrocytes, leukocytes, and neutrophils was studied using the cell viability MTT [3-(4,5-dimethylthiazol-2-yl)-2,5-diphenyltetrazolium bromide] assay (Biotium, Hayward, CA) [31]. Following the protocol

described above, 1×10^5 cells were incubated at 37°C and 5% of CO_2 overnight with 0, 5, 10, and $20 \mu\text{M}$ of BisBAL NPs and free drug cells with culture medium alone as untreated cells. After incubation, $10 \mu\text{L}$ of MTT was added to each well and incubated at 37°C and 5% of CO_2 for 2 hours in dark conditions, following which the medium was removed and $100 \mu\text{L}$ of dimethyl sulfoxide (DMSO) was added to dissolve the reduced MTT formazan product. The reduced MTT was then assayed at 595 nm using a microplate absorbance reader (Biotek, Winooski, VT) and DMSO was employed as blank. The assay was done in triplicate and the measured optical density was further analyzed by descriptive statistics.

2.6. Effect of BisBAL NPs on Hemoglobin Level. To analyze the hypothesis if the addition of BisBAL NPs to a cell culture could trigger erythrosis, the hemoglobin (Hb) level was determined by Coulter STKS [32] (Coulter Corporation, Hialeah, FL, USA), following the instructions of provider. After 24 h incubation, the nanoparticles solution was removed from cell culture and washed three times with PBS 1x and the level of Hb was measured. The assay was done in triplicate and the measured concentration was further analyzed by descriptive statistics.

2.7. Influence of Bismuth Nanoparticles on Plasmatic Membrane of Erythrocytes by AM Calcein Assay and Fluorescence Microscopy. Based on the protocol described above, the influence of BisBAL NPs on erythrocytes was evaluated by AM Calcein assay and fluorescence microscopy. After treatment with 50–1000 μM of BisBAL NPs over 24 hours, cells were washed three times with PBS and stained with AM Calcein (Biotium, Hayward, CA) [33, 34]. The cytotoxicity and integrity of cell membrane were interpreted as not Calcein AM retained in the interior of cells with FITC filter at 485 nm (Thornwood, NY).

2.8. BisBAL NPs on Genomic DNA of Erythrocytes by Comet Assay. To determine the possible damage in genomic DNA of erythrocytes after exposition to BisBAL NPs, Oxiselect Comet Assay was employed (Cell Biolabs, Inc., CA, USA), following the instructions of provider [35]. Briefly, erythrocytes were incubated at 37°C and 5% of CO_2 overnight with $20 \mu\text{M}$ of BisBAL NPs or 10% H_2O_2 (Sigma, SL., USA) as positive control and free drug cells with culture medium alone as untreated cells. After incubation, cells were collected by centrifugation at $700 \times g$ for 2 minutes and discarding the supernatant. Cells were washed with PBS and combined with comet agarose at ratio 1:10 and pipetted $75 \mu\text{L}$ /well onto the Oxiselect Comet Slide. The slide was maintained horizontally and it was transferred to 4°C in the dark for 15 minutes. Carefully, the slide was transferred to a container with lysis buffer (25 mL/slide) and was incubated for 30 minutes at 4°C in the dark. The lysis buffer was replaced with alkaline solution (25 mL/slide) and was again incubated for 30 minutes at 4°C in the dark. The slide was transferred to a horizontal electrophoresis chamber applying a current setting of 300 mA for 30 minutes. After that, the slide was washed with sterile milliQ water and water was replaced with cold 70% ethanol for 5 minutes. Ethanol was removed and slide was allowed

to air dry. Once the agarose and slide were completely dry, it was added to $100 \mu\text{L}$ /well of diluted vista green DNA dye and incubated at room temperature for 15 minutes. Slides were viewed by epifluorescence microscopy using a FITC filter (Thornwood, NY).

2.9. Apoptotic Effect of BisBAL Nanoparticles on Erythrocytes. To analyze if BisBAL NPs could lead to apoptosis after incubation with erythrocytes, the CF 488A/7-AAD Apoptosis Assay kit was employed [36]. Following the instructions of provider (Biotium, Hayward, CA), a confluent monolayer of erythrocytes grown with $20 \mu\text{M}$ of BisBAL NPs for 24 hrs was harvested and washed with 1x of PBS. After that, cells were resuspended with 1x binding buffer and aliquots of $100 \mu\text{L}$ /tube were made. $5 \mu\text{L}$ of CF488A-Annexin V and $2 \mu\text{L}$ of 7-AAD working solution were added to the cells and incubated at room temperature for 30 minutes in the dark. Finally, $400 \mu\text{L}$ of binding buffer was added to each tube and cells were analyzed by flow cytometry at 488 nm in a flow cytometer BD Accuri C6 (BD Biosciences, San Jose, CA, USA).

3. Results

3.1. Characterization of BisBAL NPs. Bismuth nanoparticles obtained were spherical in shape with the number-weighted average hydrodynamic diameter of 53 nm (Figure 1). The nanoparticles are composed of rhombohedral crystallites (≈ 18 nm) with dithiols as lipophilic surface chemical groups and the lattice spacing of individual crystallite was 0.325, which is consistent with nanoscale bismuth nanoparticles [37]. UV-Vis absorbance measurements revealed that the nanoparticles had greater ($\approx 70\%$) affinity towards 1-octanol rather than water, which further suggests that lipophilic property of the nanoparticles arises from the dithiols bounds to nanoparticle surface.

3.2. Morphology of Erythrocytes after Exposition to BisBAL NPs. In order to determine a possible alteration in the morphology of erythrocytes growing with lipophilic bismuth nanoparticles, a monolayer of erythrocytes was exposed to several concentrations of BisBAL NPs (5, 20, 50, 100, and $1000 \mu\text{M}$) for 1 hour. After this time, cells were observed finding changes in cell morphology among cells growing with 500 and $1000 \mu\text{M}$ of BisBAL NPs (Figure 2). These cells were light refractive and become rounded out of monolayer. In contrast, cells growing with 5–100 μM of BisBAL NPs did not show significant changes in their appearance when they were compared with cells growing in culture media without any drug.

3.3. Impact of BisBAL Nanoparticles on Erythrocytes, Leukocytes, and Neutrophils Count and Hemoglobin Level. With the objective of characterizing in deep the effect of BisBAL NPs on blood cells, cell viability MTT assays and hemoglobin level were carried out. The results obtained described a little decrease in the count of blood cells and hemoglobin level when 50–1000 μM of BisBAL NPs was added to culture cells for 18 h (Figure 3). The addition of 1% SDS or bulk ($1000 \mu\text{M}$ of bismuth nitrate) reduced cell growing in approximately

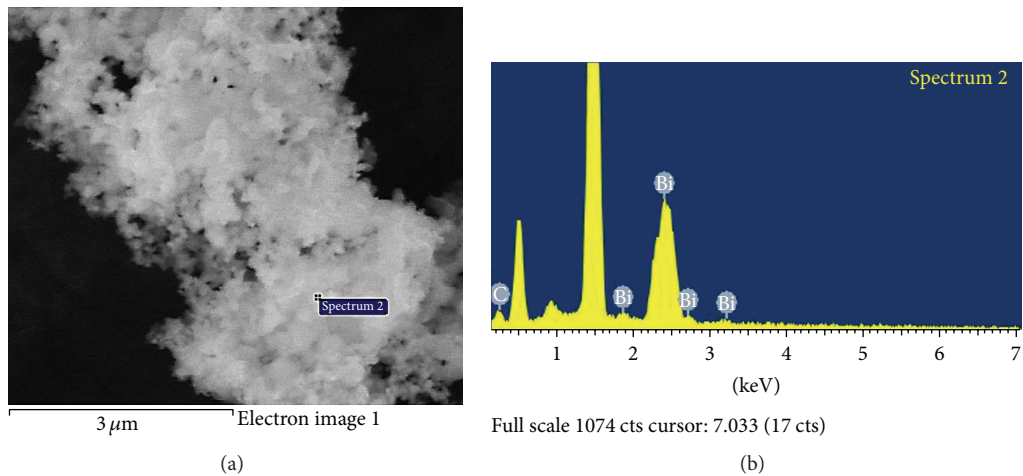


FIGURE 1: Lipophilic bismuth nanoparticles visualized by scanning electron microscopy. The dominant population of spherical shaped nanoparticles (<100 nm) showing the nanoparticle clusters interspersed among the lesser electron dense materials is shown in the TEM images (a). (b) Spectrum of elements in the sample observed by SEM.

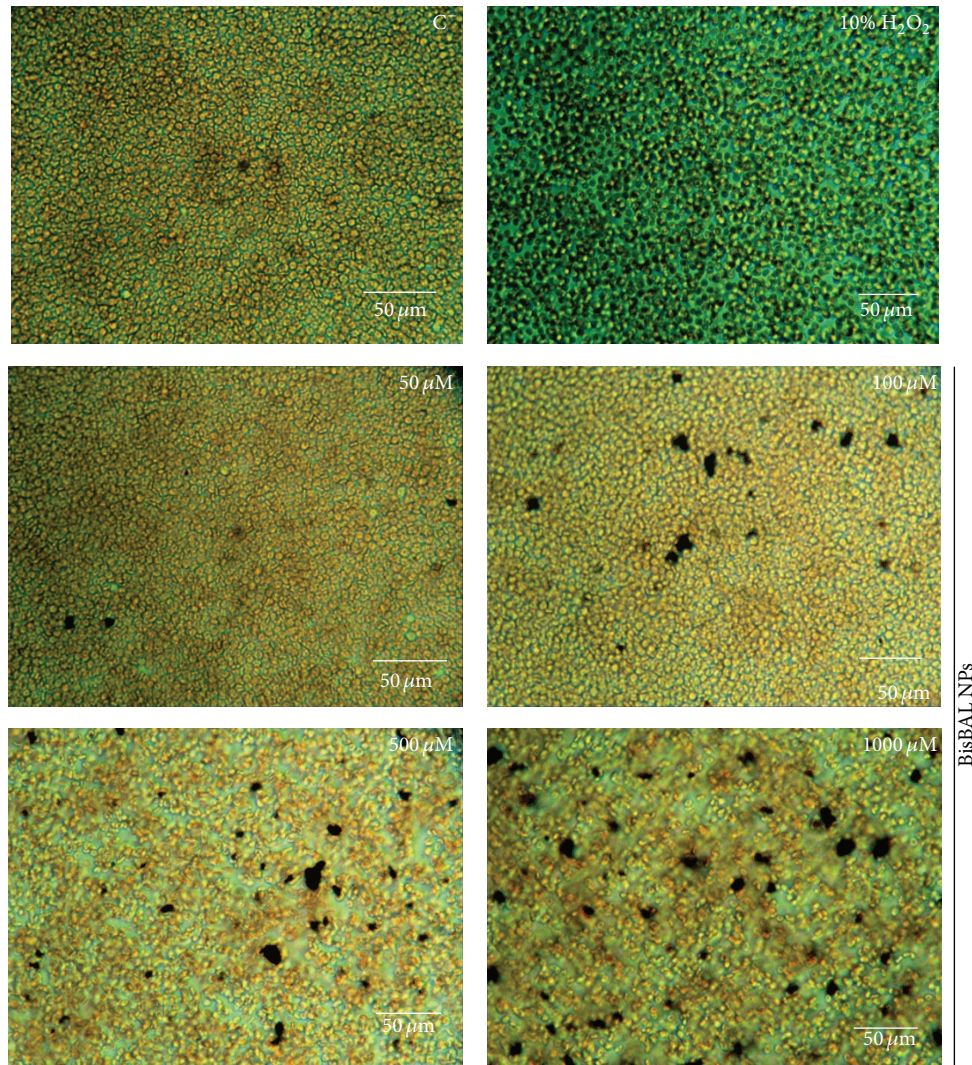


FIGURE 2: Effect of BisBAL nanoparticles on erythrocytes morphology. A monolayer of erythrocytes was obtained from a blood sample in 100 μL of minimum essential medium. 50, 100, 500, and 1000 μM of BisBAL NPs were added to cell culture, incubated for 1 hour at 37°C with 5% of CO₂ and their influence on erythrocyte culture was observed by optic microscopy using an inverter microscope (Motic, Hong Kong). The presence of cytopathic effect was identified by amorphous shape and light refractive cells. The bar indicates a size of 50 μm.

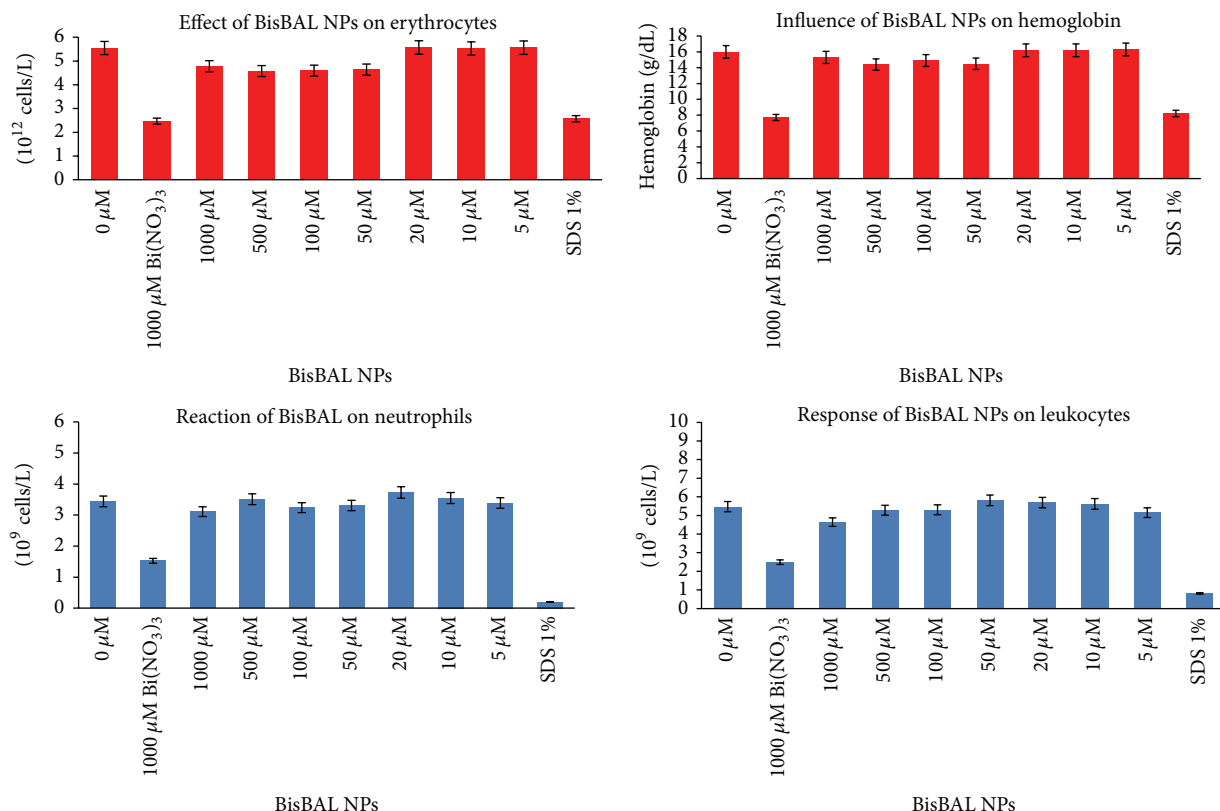


FIGURE 3: Impact of BisBAL nanoparticles on erythrocytes, leukocytes, and neutrophils count and hemoglobin level. Cell viability MTT assays were performed to determine the influence of 0, 5, 10, 20, 50, 100, 500, and 1000 μ M of BisBAL NPs, added to an erythrocytes, leukocytes, and neutrophils monolayer and incubated for 24 hrs. 1% of SDS was used as positive control and 1000 μ M of bismuth nitrate (bulk) was employed to compare with bismuth nanostructures. After that, the number of erythrocytes, leukocytes, and neutrophils and hemoglobin level were determined.

50% (Figure 3), showing a clear difference with same concentration of the bismuth nanocomposite. The viability did not change among cells growing with 0–20 μ L of BisBAL NPs with the same results in the level of hemoglobin. All these results suggest that bismuth nanoparticles did not cause significant damage on human blood cells in the experimental conditions analyzed.

3.4. Influence of Bismuth Nanoparticles on Cell Membrane of Erythrocytes by AM Calcein Assay and Fluorescence Microscopy. Previous results indicated a similar influence of BisBAL NPs on blood cells, which could mean the same target on this kind of cells. To analyze if plasmatic membrane of erythrocytes was affected by the presence of bismuth nanoparticles, a monolayer of erythrocytes was incubated with 50, 100, 500, and 1000 μ M of BisBAL NPs overnight.

After this, Calcein AM was added which is retained in the cytoplasm of living cells. When cells were observed by fluorescent microscopy, Calcein AM was retained only at 50 and 100 μ M of BisBAL NPs (Figure 4). In contrast, erythrocytes growing with 500 or 1000 μ M of BisBAL NPs did not retain the Calcein into their cytoplasm. The same result was found when red cells were growing with 10% of hydrogen

peroxide (Figure 4). Altogether these results strongly suggest that plasmatic membrane is affected by interaction with bismuth nanoparticles at high concentrations.

3.5. BisBAL Nanoparticles on Genomic DNA of Erythrocytes by Comet Assay and Fluorescence Microscopy. To determine a possible damage on genomic DNA of erythrocytes by bismuth nanoparticles, genotoxic assays were developed, employing the Comet Assay and fluorescence microscopy. As can be seen in Figure 5, after incubation with 1–1000 μ M of BisBAL NPs, the nuclei and indeed the entire cell appeared to be identical to nontreated cells, suggesting the absence of toxic effects on genomic DNA of erythrocytes by BisBAL NPs under our experimental conditions. In cells growing with 10% of H_2O_2 the classic stela of a comet was detected (Figure 5) indicating DNA damage. Based on these results, bismuth nanoparticles do not seem to affect DNA of host cells.

3.6. Apoptosis Performed by Erythrocytes Growing with Bismuth Nanoparticles. Based on last experiments, it was explored if bismuth nanoparticles could lead to apoptosis of host cells using the CF 488A/7-AAD Apoptosis Assay kit and

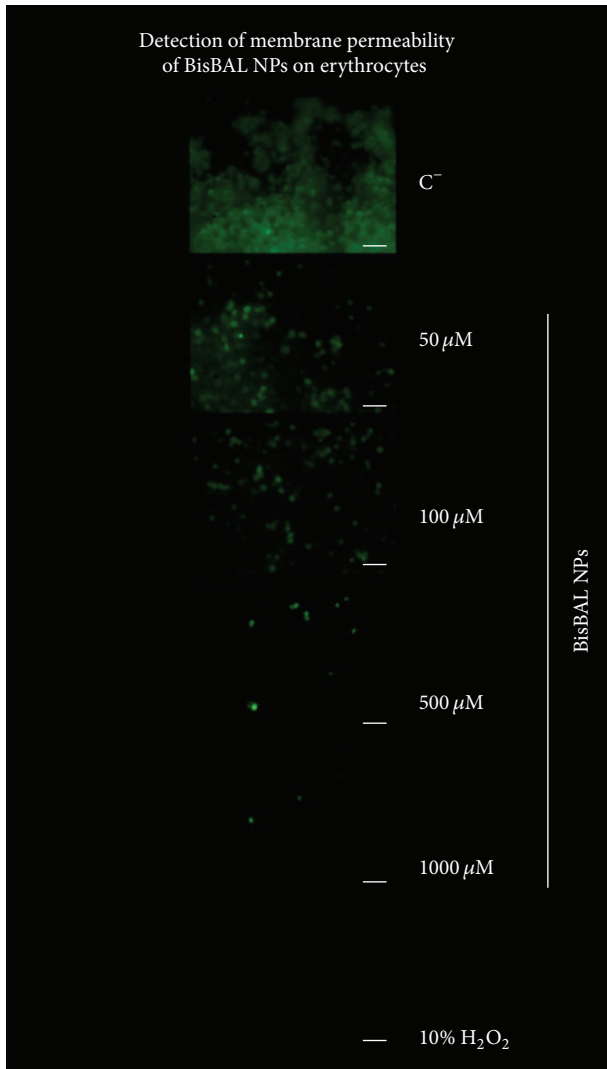


FIGURE 4: Influence of bismuth nanoparticles on membrane cell of erythrocytes by AM Calcein assay and fluorescence microscopy. Blood cells were treated with same techniques described above. After 24 h of incubation, the erythrocytes were stained with AM Calcein and observed under fluorescence microscopy at 485 and 358 nm (Thornwood, NY). The images were analyzed by using AxioVision software (Thornwood, NY). The bar indicates 5 μm .

fluorescence microscopy. The results indicate that BisBAL nanoparticles at concentrations 500 and 1000 μM promote apoptosis among erythrocytes (Figure 6). The fluorescent conjugate of Annexin V interacting with phosphatidylserine exposed by erythrocytes was clearly observed by fluorescence microscopy (Figure 6). 7-AAD (7-aminoactinomycin D) is a membrane-impermeant DNA-binding dye that is excluded by live cells; as can be seen in Figure 6, it was present in erythrocytes growing with 500 and 1000 μM of BisBAL NPs, suggesting their necrotic state. There was no difference between

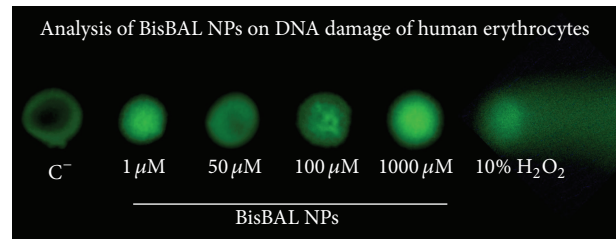


FIGURE 5: BisBAL nanoparticles on genomic DNA of erythrocytes by Comet Assay and fluorescence microscopy. To determine the possible damage in genomic DNA of erythrocytes after exposition to BisBAL NPs, Oxiselect Comet Assay was employed. Erythrocytes were incubated at 37°C and 5% of CO_2 overnight with 1–1000 μM of BisBAL NPs or 10% H_2O_2 . Erythrocytes growing only in culture media were used as negative control (C^-). After treatment, blood cells were analyzed by fluorescence microscopy at 485 nm (Thornwood, NY). The presence of a stela is indicative of DNA damage.

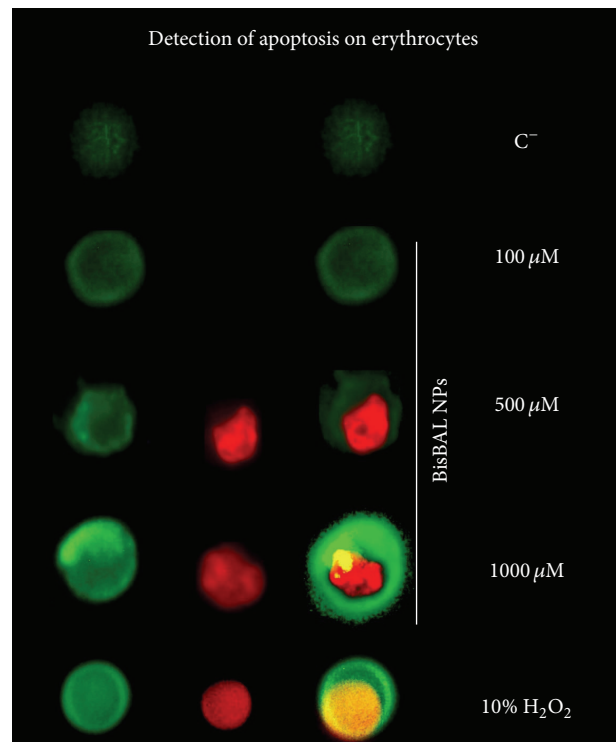


FIGURE 6: Apoptosis performed by erythrocytes growing with bismuth nanoparticles. The possible leading to apoptosis of blood cells by 100–1000 μM of BisBAL NPs was explored by Annexin V and 7-AAD assay using fluorescence microscopy at 485 nm (Thornwood, NY).

100 μM of BisBAL NPs and control (cells growing with only culture media). These results suggest that high concentrations of bismuth nanoparticles inhibit erythrocytes growth by altering basic functions and promoting programmed cell death.

4. Discussion

In this paper we described the synthesis and characterization of lipophilic bismuth nanoparticles and their effect on blood cells. These kinds of nanoparticles have strong antimicrobial and antibiofilm activities described by our group and others [5]. However, the lack of strong experimental evidence of their potential cytotoxicity limits their use in humans. The toxicological aspects of bismuth compounds are well established and the reported side effects include nephropathy, hepatitis, encephalopathy, gastroenteritis, and osteoarthropathy [38–41]. It has been published that bismuth salts cause extensive cytotoxicity on epithelial cells at final concentrations of 2.5 mg/mL [42]. More recently, it was described that bismuth nanoparticles are nontoxic at concentration of 0.5 nM. Nanoparticles at higher concentrations (50 nM) kill 45, 52, 41, and 34% of HeLa cells for bare nanoparticles, amine terminated bismuth nanoparticles, silica coated bismuth nanoparticles, and polyethylene glycol (PEG) modified bismuth nanoparticles, respectively [43]. However, our group has reported no cytotoxic effects on monkey kidney cells at 2 mM of bismuth oxide nanoparticles after 24 h. In this work, the presented data shows the influence of lipophilic bismuth nanoparticles on blood cells. Side effect was not detected when BisBAL nanoparticles were added to human culture cells. Tight decreasing was observed in cells count when 50–1000 μM of BisBAL NPs was added (Figure 3). Hemoglobin level correlated with blood cells alteration, supporting the hypothesis of no toxic effects of BisBAL nanoparticles. Previously, Braun et al. have described that 48 h exposure to $\geq 500 \mu\text{g/L}$ bismuth stimulated eryptosis promoting apoptosis, increasing cytosolic Ca^{2+} activity and phosphatidylserine expression on cell surface, decreasing erythrocyte size, and leading to erythrocyte death [44]. This datum correlates with our finding using 1000 μM of bulk (bismuth nitrate) inhibiting 50% of cell growth (Figure 3). In our results, employing 500 and 1000 μM of BisBAL NPs, the phosphatidylserine expression on cell surface and decreasing in erythrocyte size were observed (Figures 2 and 6). Swy et al. described histopathological changes in rats treated with 20 mg kg^{-1} of bismuth nanoparticles PGLA encapsulated, including transient kidney injury and periportal inflammatory process in the liver [45]. However, $\leq 100 \mu\text{M}$ of bismuth nanoparticles did not cause erythrocytes death, keeping their normal morphology and membrane integrity without leading to apoptosis (Figures 2, 4, and 6). This datum is very important taking into account that early reports indicate that BisBAL NPs kill pathogenic microorganisms at 0.5–10 μM as final concentration [5] and compete in efficiency with antibiotics like vancomycin as broad-spectrum antimicrobial agents [3–5, 46]. Altogether these results suggest that lipophilic bismuth nanoparticles could be used in humans without altering blood cells provided that they were used at final concentrations lower than 100 μM .

The action mechanism of how bismuth or its compounds damage cells is unknown. Early report of Swy et al. using doses lower than 20 mg kg^{-1} of bismuth nanoparticles PLGA encapsulated were internalized into cells and remain into the cytoplasm without side effects [45]. Based on our

experiments with Calcein AM and fluorescence microscopy, we can argue that in high doses (500–1000 μM) BisBAL nanoparticles enter the cell and stock into cytoplasm of host cells. The nanoparticles entry will alter the plasmatic membrane permeability of host cells, modifying their homeostasis and metabolism and finally leading to apoptosis.

5. Conclusions

In summary, lipophilic bismuth nanoparticles (BisBAL NPs) were not toxic to blood cells at final concentrations lower than 100 μM . Up to 500 μM , BisBAL NPs cause damage to plasmatic membrane of host cells, thereby leading to apoptosis or necrosis in the long term.

Conflict of Interests

The authors of this paper declare that there are not any potential competing interests regarding the publication of this work.

Acknowledgments

The authors wish to thank Nayeli Pineda-Aguilar from CIMAV for their technical assistance in scanning electron microscopy and MSP Gustavo I. Martinez-Gonzalez from FO-UANL for their technical assistance. Claudio Cabral-Romero wants to thank CONACyT for financing the Project no. 183825. Shankar Chellam was partially funded by the Texas Hazardous Waste Research Center. Financial support for the payment of the processing charges was made by Programa para el Desarrollo Profesional Docente para el Tipo Superior (PRODEP 2014).

References

- [1] P. Moayyedi, S. Soo, J. Deeks, B. Delaney, M. Innes, and D. Forman, "Pharmacological interventions for non-ulcer dyspepsia," *Cochrane Database of Systematic Reviews*, no. 4, Article ID CD001960, 2006.
- [2] Z. N. Adamian, H. V. Abovian, and V. M. Aroutiounian, "Smoke sensor on the base of Bi_2O_3 sesquioxide," *Sensors and Actuators B: Chemical*, vol. 35, no. 1–3, pp. 241–243, 1996.
- [3] R. Hernandez-Delgado, D. Velasco-Arias, D. Diaz et al., "Zerovalent bismuth nanoparticles inhibit *Streptococcus mutans* growth and formation of biofilm," *International Journal of Nanomedicine*, vol. 7, pp. 2109–2113, 2012.
- [4] R. Hernandez-Delgado, D. Velasco-Arias, J. J. Martinez-Sanmiguel et al., "Bismuth oxide aqueous colloidal nanoparticles inhibit *Candida albicans* growth and biofilm formation," *International Journal of Nanomedicine*, vol. 8, pp. 1645–1652, 2013.
- [5] A. R. Badireddy, R. Hernandez-Delgado, R. I. Sánchez-Nájera, S. Chellam, and C. Cabral-Romero, "Synthesis and characterization of lipophilic bismuth dimercaptopropanol nanoparticles and their effects on oral microorganisms growth and biofilm formation," *Journal of Nanoparticle Research*, vol. 16, no. 6, article 2456, 2014.
- [6] P. Domenico, R. J. Salo, S. G. Novick, P. E. Schoch, K. Van Horn, and B. A. Cunha, "Enhancement of bismuth antibacterial activity with lipophilic thiol chelators," *Antimicrobial Agents and Chemotherapy*, vol. 41, no. 8, pp. 1697–1703, 1997.

- [7] J. S. Kim, E. Kuk, K. N. Yu et al., "Antimicrobial effects of silver nanoparticles," *Nanomedicine*, vol. 3, no. 1, pp. 95–101, 2007.
- [8] W.-C. Huang, P.-J. Tsai, and Y.-C. Chen, "Functional gold nanoparticles as photothermal agents for selective-killing of pathogenic bacteria," *Nanomedicine*, vol. 2, no. 6, pp. 777–787, 2007.
- [9] J. C. Castillo-Martínez, G. A. Martínez-Castañón, F. Martínez-Gutiérrez et al., "Antibacterial and antibiofilm activities of the photothermal therapy using gold nanorods against seven different bacterial strains," *Journal of Nanomaterials*, vol. 2015, Article ID 783671, 7 pages, 2015.
- [10] Y. Hsueh, W. Ke, C. Hsieh et al., "ZnO nanoparticles affect *Bacillus subtilis* cell growth and biofilm formation," *PLoS ONE*, vol. 10, no. 6, Article ID e0128457, 2015.
- [11] N. Nataraj, G. S. Anjusree, A. A. Madhavan et al., "Synthesis and anti-staphylococcal activity of TiO₂ nanoparticles and nanowires in ex vivo porcine skin model," *Journal of Biomedical Nanotechnology*, vol. 10, no. 5, pp. 864–870, 2014.
- [12] S. Gaillet and J.-M. Rouanet, "Silver nanoparticles: their potential toxic effects after oral exposure and underlying mechanisms—a review," *Food and Chemical Toxicology*, vol. 77, pp. 58–63, 2015.
- [13] P. M. Favi, M. Gao, L. Johana Sepúlveda Arango et al., "Shape and surface effects on the cytotoxicity of nanoparticles: gold nanospheres versus gold nanostars," *Journal of Biomedical Materials Research Part A*, 2015.
- [14] M. Czajka, K. Sawicki, K. Sikorska, S. Popek, M. Kruszewski, and L. Kapka-Skrzypczak, "Toxicity of titanium dioxide nanoparticles in central nervous system," *Toxicology In Vitro*, vol. 29, no. 5, pp. 1042–1052, 2015.
- [15] T.-H. Chen, C.-C. Lin, and P.-J. Meng, "Zinc oxide nanoparticles alter hatching and larval locomotor activity in zebrafish (*Danio rerio*)," *Journal of Hazardous Materials*, vol. 277, pp. 134–140, 2014.
- [16] F. Danhier, E. Ansorena, J. M. Silva, R. Coco, A. Le Breton, and V. Pr at, "PLGA-based nanoparticles: an overview of biomedical applications," *Journal of Controlled Release*, vol. 161, no. 2, pp. 505–522, 2012.
- [17] J. A. Salvador, S. A. Figueiredo, R. M. Pinto, and S. M. Silvestre, "Bismuth compounds in medicinal chemistry," *Future Medicinal Chemistry*, vol. 4, no. 11, pp. 1495–1523, 2012.
- [18] T. Popescu, A. R. Lupu, M. Feder et al., "In vitro toxicity evaluation of Ti⁴⁺-stabilized γ -Bi₂O₃ sillenites," *Toxicology in Vitro*, vol. 28, no. 8, pp. 1523–1530, 2014.
- [19] Y. Fujiwara, C. Yamamoto, T. Inagaki, M. Satoh, and T. Kaji, "Bismuth protects against arsenite-induced inhibition of proteoglycan synthesis in cultured vascular endothelial cells," *Journal of Toxicological Sciences*, vol. 37, no. 4, pp. 837–843, 2012.
- [20] C. Seidl, C. Z ckler, R. Beck, L. Quintanilla-Martinez, F. Bruchertseifer, and R. Senekowitsch-Schmidtke, "177Lu-immunotherapy of experimental peritoneal carcinomatosis shows comparable effectiveness to 213Bi-immunotherapy, but causes toxicity not observed with 213Bi," *European Journal of Nuclear Medicine and Molecular Imaging*, vol. 38, no. 2, pp. 312–322, 2011.
- [21] S. Moeschlin, "Clinical-hematological demonstrations: a plastic anemia, acute leukemias, polyneuropathy in Waldenstrom's disease, acute porphyria," *Schweizerische Medizinische Wochenschrift*, vol. 105, no. 40, pp. 1289–1298, 1975.
- [22] M. F ller, S. M. Huber, and F. Lang, "Erythrocyte programmed cell death," *IUBMB Life*, vol. 60, no. 10, pp. 661–668, 2008.
- [23] K. Alzoubi, S. Calabr , J. Egler, C. Faggio, and F. Lang, "Triggering of programmed erythrocyte death by alantolactone," *Toxins*, vol. 6, no. 12, pp. 3596–3612, 2014.
- [24] A. Malik, R. Bissinger, G. Liu, G. Liu, and F. Lang, "Enhanced eryptosis following gramicidin exposure," *Toxins*, vol. 7, no. 5, pp. 1396–1410, 2015.
- [25] O. Aljanadi, K. Alzoubi, R. Bissinger, and F. Lang, "Stimulation of suicidal erythrocyte death by naphthazarin," *Basic & Clinical Pharmacology & Toxicology*, 2015.
- [26] R. Bissinger, S. Waibel, and F. Lang, "Induction of suicidal erythrocyte death by nelfinavir," *Toxins*, vol. 7, no. 5, pp. 1616–1628, 2015.
- [27] C. P. Berg, I. H. Engels, A. Rothbart et al., "Human mature red blood cells express caspase-3 and caspase-8, but are devoid of mitochondrial regulators of apoptosis," *Cell Death and Differentiation*, vol. 8, no. 12, pp. 1197–1206, 2001.
- [28] D. W. C. Dekkers, P. Comfurius, E. M. Bevers, and R. F. A. Zwaal, "Comparison between Ca²⁺-induced scrambling of various fluorescently labelled lipid analogues in red blood cells," *Biochemical Journal*, vol. 362, part 3, pp. 741–747, 2002.
- [29] A. R. Badireddy and S. Chellam, "Bismuth dimercaptopropanol (BiBAL) inhibits formation of multispecies wastewater flocs," *Journal of Applied Microbiology*, vol. 110, no. 6, pp. 1426–1437, 2011.
- [30] D. Buckner, R. Eisel, and S. Perry, "Blood cell separation in the dog by continuous flow centrifugation," *Blood*, vol. 31, no. 5, pp. 653–672, 1968.
- [31] Y. Liu, D. A. Peterson, H. Kimura, and D. Schubert, "Mechanism of cellular 3-(4,5-dimethylthiazol-2-yl)-2,5-diphenyltetrazolium bromide (MTT) reduction," *Journal of Neurochemistry*, vol. 69, no. 2, pp. 581–593, 1997.
- [32] J. Rosenblit, C. R. Abreu, L. N. Sztlerling et al., "Evaluation of three methods for hemoglobin measurement in a blood donor setting," *Sao Paulo Medical Journal*, vol. 117, no. 3, pp. 108–112, 1999.
- [33] D. Bozyczko-Coyne, B. W. McKenna, T. J. Connors, and N. T. Neff, "A rapid fluorometric assay to measure neuronal survival in vitro," *Journal of Neuroscience Methods*, vol. 50, no. 2, pp. 205–216, 1993.
- [34] A. L. Akesson and C. W. Woods, "A fluorometric assay for the quantitation of cell adherence to endothelial cells," *Journal of Immunological Methods*, vol. 163, no. 2, pp. 181–185, 1993.
- [35] M. De Boeck, N. Touil, G. De Visscher, P. A. Vande, and M. Kirsch-Volders, "Validation and implementation of an internal standard in comet assay analysis," *Mutation Research/Genetic Toxicology and Environmental Mutagenesis*, vol. 469, no. 2, pp. 181–197, 2000.
- [36] A. V. Zelenin, A. I. Poletaev, N. G. Stepanova et al., "7-Aminoactinomycin D as a specific fluorophore for DNA content analysis by laser flow cytometry," *Cytometry*, vol. 5, no. 4, pp. 348–354, 1984.
- [37] V. N. Richards, S. P. Shields, and W. E. Buhro, "Nucleation control in the aggregative growth of bismuth nanocrystals," *Chemistry of Materials*, vol. 23, no. 2, pp. 137–144, 2011.
- [38] J. A. James, "Acute renal failure due to a bismuth preparation," *California Medicine*, vol. 109, no. 4, pp. 317–319, 1968.

- [39] A. W. Czerwinski and H. E. Ginn, "Bismuth nephrotoxicity," *The American Journal of Medicine*, vol. 37, no. 6, pp. 969–975, 1964.
- [40] D. P. Boyette, "Bismuth nephrosis with anuria in an infant: report of a case," *The Journal of Pediatrics*, vol. 28, no. 4, pp. 493–497, 1946.
- [41] A. Slikkerveer and F. A. de Wolff, "Pharmacokinetics and toxicity of bismuth compounds," *Medical Toxicology and Adverse Drug Experience*, vol. 4, no. 5, pp. 303–323, 1989.
- [42] R. L. Ward, D. S. Sander, and D. R. Knowlton, "In vitro activities of bismuth salts against rotaviruses and other enteric viruses," *Antimicrobial Agents and Chemotherapy*, vol. 27, no. 3, pp. 306–308, 1985.
- [43] Y. Luo, C. Wang, Y. Qiao, M. Hossain, L. Ma, and M. Su, "In vitro cytotoxicity of surface modified bismuth nanoparticles," *Journal of Materials Science: Materials in Medicine*, vol. 23, no. 10, pp. 2563–2573, 2012.
- [44] M. Braun, M. Föllner, E. Gulbins, and F. Lang, "Eryptosis triggered by bismuth," *BioMetals*, vol. 22, no. 3, pp. 453–460, 2009.
- [45] E. R. Swy, A. S. Schwartz-Duval, D. D. Shuboni et al., "Dual-modality, fluorescent, PLGA encapsulated bismuth nanoparticles for molecular and cellular fluorescence imaging and computed tomography," *Nanoscale*, vol. 6, no. 21, pp. 13104–13112, 2014.
- [46] P. Nazari, R. Dowlatabadi-Bazaz, M. R. Mofid et al., "The antimicrobial effects and metabolomic footprinting of carboxyl-capped bismuth nanoparticles against *Helicobacter pylori*," *Applied Biochemistry and Biotechnology*, vol. 172, no. 2, pp. 570–579, 2014.

Research Article

Evaluation of Biological Toxicity of CdTe Quantum Dots with Different Coating Reagents according to Protein Expression of Engineering *Escherichia coli*

Wei Xu,¹ Ting Du,¹ Chaoyong Xu,¹ Heyou Han,¹ Jiangong Liang,¹ and Shaobo Xiao²

¹College of Science, State Key Laboratory of Agricultural Microbiology, Huazhong Agricultural University, Wuhan 430070, China

²College of Veterinary Medicine, State Key Laboratory of Agricultural Microbiology, Huazhong Agricultural University, Wuhan 430070, China

Correspondence should be addressed to Jiangong Liang; liangjg@mail.hzau.edu.cn and Shaobo Xiao; xiaoshaobo@mail.hzau.edu.cn

Received 29 April 2015; Accepted 13 August 2015

Academic Editor: Ecaterina Andronescu

Copyright © 2015 Wei Xu et al. This is an open access article distributed under the Creative Commons Attribution License, which permits unrestricted use, distribution, and reproduction in any medium, provided the original work is properly cited.

The results obtained from toxicity assessment of quantum dots (QDs) can be used to establish guidelines for the application of QDs in bioimaging. This paper focused on the design of a novel method to evaluate the toxicity of CdTe QDs using engineering *Escherichia coli* as a model. The toxicity of mercaptoacetic acid (MPA), glutathione (GSH), and L-cysteine (Cys) capped CdTe QDs was analyzed according to the heterologous protein expression in BL21/DE3, engineering *Escherichia coli* extensively used for protein expression. The results showed that the MPA-CdTe QDs had more serious toxicity than the other two kinds of CdTe QDs. The microscopic images and SEM micrographs further proved that both the proliferation and the protein expression of engineering *Escherichia coli* were inhibited after treatment with MPA-CdTe QDs. The proposed method is important to evaluate biological toxicity of both QDs and other nanoparticles.

1. Introduction

Semiconductor quantum dots (QDs) are a unique class of nanomaterials with good optical properties, such as broad excitation spectra, narrow emission spectra, high quantum yields, and good photostability [1, 2]. Since QDs were first reported for biological applications by Alivisatos, Nie and their coworkers [3, 4], the use of them in bioanalysis and bioimaging has dramatically increased [5, 6].

QD toxicity assessment is a hot topic and the findings will help to establish useful guidelines for the use of QDs for bioimaging [7–10]. In the past decade, various methods have been proposed for the evaluation of the toxicity of QDs [11–16]. Lovrić et al. reported that unmodified CdTe QDs could induce cells to death by triggering the generation of reactive oxygen species [17]. Su et al. found that the released cadmium ions played an important role in inducing damage to HEK293 cells and that some special properties of

nanoparticles contributed to the cytotoxicity of CdTe QDs at the same time [18]. Tan et al. investigated the relationship between cytotoxicity and the surface ligand of QDs and found that low cytotoxicity QDs could be designed and used as probes [19]. Ladhar et al. investigated the impact of dietary cadmium sulphide nanoparticles on zebrafish, and the results indicated that the toxicity of CdS nanoparticles was dependent on their size and concentration [16].

Up to now, several research groups have used *Escherichia coli* (*E. coli*) as a model to evaluate the toxicity of QDs and other nanoparticles [20–23]. Wang et al. studied the effects of CdTe QDs on *E. coli* cells, showing that CdTe QDs exhibited a dose-dependent inhibitory effect on cell growth [20]. Fang et al. investigated the effect of three different sizes of MPA-CdTe QDs on the growth of *E. coli* and found that CdTe QDs and their by-products had toxic effect on DNA, protein, enzyme, and so on in vivo [21]. Lai et al. investigated the inhibitory effects of different ligand-coated QDs on *E. coli* growth and

found that the QDs modified with MPA showed higher toxicity than the others [15]. Xiao et al. evaluated the toxic effects of CdSe QDs and CdSe/ZnS QDs on the growth of both *E. coli* and *Staphylococcus aureus* (*S. aureus*) by microcalorimetry [22] and proposed that the microcalorimetric technique is a useful and a more convenient tool for the quantitative analysis of the toxic effects of QDs on bacterial metabolism. The effect of QDs on *E. coli* cells has been widely investigated, but to our knowledge, no method has been developed based on the protein expression in engineering *E. coli*.

Engineering *E. coli* is not only a good tool for genome science but also an ideal model organism for biological research [24, 25]. It is one of the most widely used hosts for the production of heterologous proteins [26]. The recombinant proteins expressed in engineering *E. coli* might account for up to 50 percent of the total cellular proteins [27].

In the present work, the protein expression of engineering *E. coli* was used to study the toxicity mechanism of CdTe QDs coated with mercaptoacetic acid (MPA), glutathione (GSH), and L-cysteine (Cys). The results showed that MPA-CdTe QDs exhibited more influence than the other QDs on the heterologous protein expression of engineering *E. coli*. The reason was that both the proliferation and the protein expression of engineering *E. coli* were inhibited after treatment with MPA-CdTe QDs.

2. Experimental

The deionized distilled water used was prepared from a Milli-Q Academic water purification system (Millipore). CdCl₂·2.5H₂O, NaOH, NaBH₄, Na₂TeO₃, glutaraldehyde, MPA, GSH, and Cys were purchased from Sinopharm Chemical Reagent Co., Ltd. (Shanghai, China). Isopropyl β-D-1-thiogalactopyranoside (IPTG) was purchased from Sigma-Aldrich Co., LLC. All reagents were of analytical reagent grade and used as received.

The MPA, GSH, and Cys capped CdTe QDs were prepared according to references with some modifications [28–30]. Briefly, while synthesizing green MPA coated CdTe QDs (MPA-CdTe), cadmium chloride (68.5 mg) was dissolved in water (150 mL), followed by the addition of thioglycolic acid (30 μL) and 1M NaOH solution to a final pH value of 11. After that, the mixture was stirred under N₂ for 20 min, followed by the rapid addition of sodium citrate (161.4 mg), sodium tellurite (13.2 mg), and sodium borohydride (15.0 mg) to the solution under N₂ stirring. Subsequently, the reaction mixture was heated to reflux for 3 h under N₂. Finally, the resulting QD solution was mixed with ethanol at the rate of 1:1 and then centrifugalized (8000 rpm) for 5 min. After the precipitate was resuspended in deionized water, the purified QDs were obtained. GSH and Cys capped CdTe QDs were synthesized in similar way.

The UV-Vis spectra of CdTe QDs were obtained on a Thermo Nicolet Corporation Model Evolution 300 UV-Visible spectrometer. The FL spectra were acquired on a RF-5301PC (Shimadzu) fluorescence spectrometer. The TEM images of QDs were observed on a FEI Tecnai G20 transmission electron microscope.

The frozen engineering *E. coli* cells were revived in Luria-Bertani (LB) medium containing ampicillin for 12 h at 310 K. The engineering *E. coli* suspension obtained was transferred to a glass ampoule containing fresh LB medium and ampicillin, followed by 2 h incubation at 310 K. Subsequently, the IPTG and different amounts of QDs were added into each ampoule. After 5 h incubation, the *E. coli* cells were collected and prepared for sodium dodecyl sulfate-polyacrylamide gel electrophoresis (SDS-PAGE) [31]. The gel images were obtained using the GelDoc 2000Fluo (Bio-Rad) gel imaging system.

The engineering *E. coli* cells were first fixed with 25% glutaraldehyde for 2 h, then washed three times, and resuspended in water. After centrifugalizing (3000 rpm) for 5 min, the precipitate was collected and dehydrated with graded ethanol series (30%–100%). The samples were deposited onto gold platelets as a 1 μL droplet and then air-dried. A small amount of platinum was sputtered on the samples to avoid charging in the microscope.

To take the photomicrographs, bacteria of the midexponential growth phase were washed three times with sodium phosphate buffer (pH 7.2) and deposited/placed onto slides as a 5 μL droplet, which were immediately covered with coverslips. Photomicrographs were taken with an oil immersion microscope by IX70 (Olympus) fluorescence microscopy at magnification of 400x. The SEM images of engineering *E. coli* were observed on an S-570 Scanning Electron Microscope (Hitachi).

3. Results and Discussion

3.1. Characterization of CdTe QDs. The XRD patterns of CdTe QDs were obtained by a Bruker-D8 Advanced X-ray diffractometer. As shown in Figure S1 (see Supplementary Material available online at <http://dx.doi.org/10.1155/2015/583963>), the XRD patterns of Cys-CdTe QDs (Figure S1A), GSH-CdTe QDs (Figure S1B), and MPA-CdTe QDs (Figure S1C) were similar. The 2θ values of 26.3° and 39.2° correspond to the crystal planes (111) and (220) of cubic CdTe phase [32]. Figure 1 shows the TEM images of MPA-CdTe QDs (Figure 1(a)), GSH-CdTe QDs (Figure 1(b)), and Cys-CdTe QDs (Figure 1(c)). The sizes of MPA-CdTe QDs, GSH-CdTe QDs, and Cys-CdTe QDs were 2.7 ± 0.2, 2.5 ± 0.2, and 2.6 ± 0.2 nm, respectively. The concentrations of CdTe QDs were determined from the first absorption maximum of the UV-Vis absorption spectra (Figure 2) as reported previously by Yu et al. [33]. The peak emission wavelengths of MPA-CdTe QDs, GSH-CdTe QDs, and Cys-CdTe QDs were 560, 552, and 554 nm, respectively.

3.2. Toxicity Assay Based on Heterologous Protein Expression of Engineering *E. coli*. The toxicity of CdTe QDs was evaluated according to heterologous protein expression in BL21/DE3, engineering *E. coli* extensively used for protein expression. To this end, plasmid pGEX-KG encoding glutathione S-transferase (GST) was introduced into BL21/DE3 and induced by isopropyl β-D-1-thiogalactopyranoside (IPTG) as described previously, followed by a sodium dodecyl

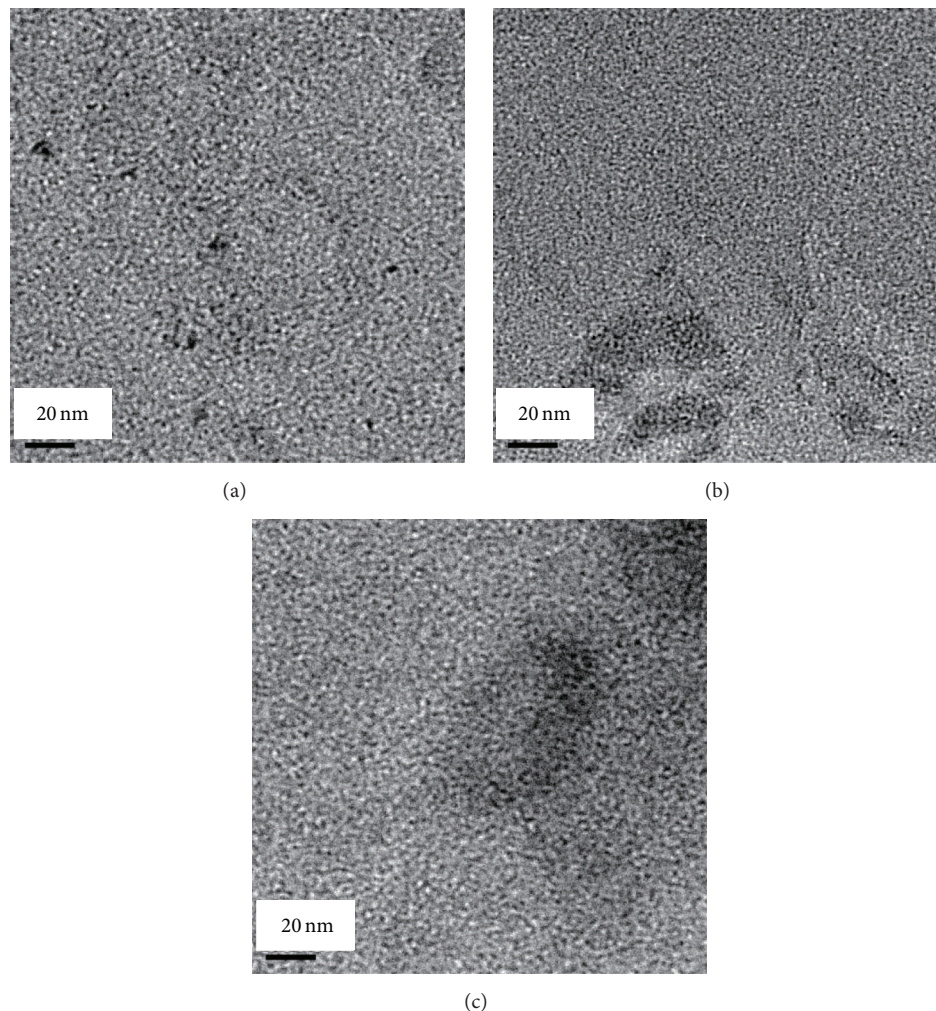


FIGURE 1: TEM images of MPA-CdTe QDs (a), GSH-CdTe QDs (b), and Cys-CdTe QDs (c).

sulfate-polyacrylamide gel electrophoresis (SDS-PAGE) analysis. The expression of the GST protein of *E. coli* cells after treatment with different concentrations of three kinds of CdTe QDs is presented in Figure 3. As shown in Figure 3(a), the expression of the GST protein significantly decreased in BL21/DE3 treated with MPA-CdTe QDs, indicating that 5 and 10 nM MPA-CdTe QDs did not confer detectable toxicity to *E. coli*. However, when the concentration of MPA-CdTe QDs increased to 50 nM, the protein expression was strongly inhibited, suggesting that high concentration of MPA-CdTe QDs had serious toxicity. Additionally, the other protein bands become lighter due to the reduction of concentration of engineering *E. coli*. Under the same concentration conditions, the GST expression did not show a significant change after treatment with GSH-CdTe QDs (Figure 3(b)) or Cys-CdTe QDs (Figure 3(c)), even at a higher concentration. These results indicate that the surface reagents play a key role in the biological toxicity of QDs. The inhibition of the GST protein expression might be attributed to two factors: (1) CdTe QDs

affect the proliferation of engineering *E. coli* and (2) CdTe QDs alter the physiological functions of engineering *E. coli*.

3.3. Toxicity Assay Based on Microscopic Images and SEM Micrographs. To further investigate the effect of CdTe QDs on engineering *E. coli*, we examined the microscopic images of engineering *E. coli* treated with and without CdTe QDs. As shown in Figure 4, the growing status of *E. coli* cells exhibited visual differences after treatment with three different CdTe QDs. The *E. coli* cells treated with MPA-CdTe QDs (Figure 4(b)) exhibited obviously a smaller number than those untreated with MPA-CdTe QDs, while the *E. coli* cells treated with GSH-CdTe QDs (Figure 4(c)) or Cys-CdTe QDs (Figure 4(d)) showed nearly the same number as the control (Figure 4(a)). The reason was due to the fact that MPA-CdTe QDs can strongly inhibit the growth of engineering *E. coli*, leading to the reduction of concentration of engineering *E. coli*. Lai et al. investigated the biotoxicity of CdTe QDs on Gram-negative *E. coli* by thermogenic curves of *E. coli* growth

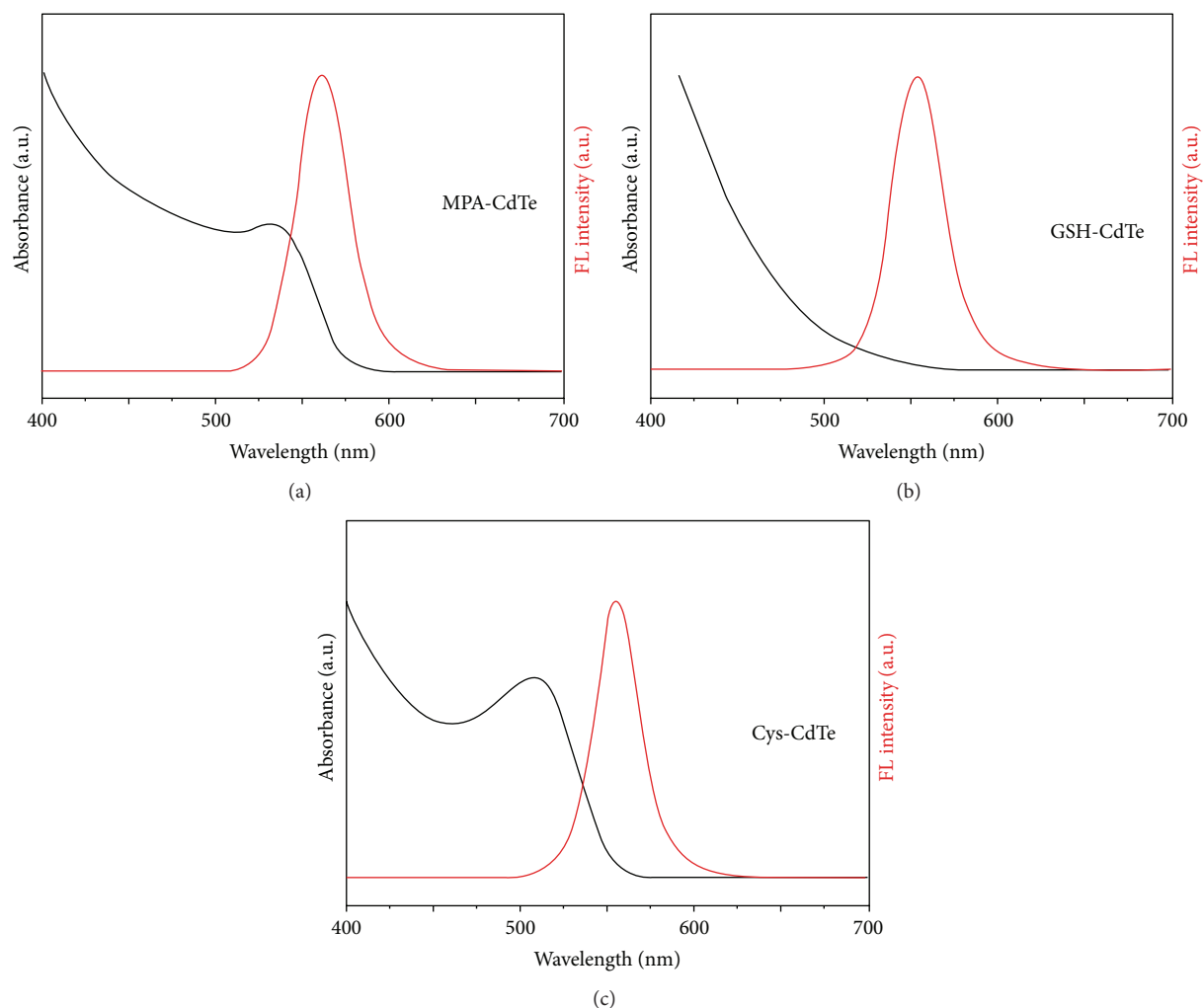


FIGURE 2: Absorption and emission spectra of three kinds of CdTe QDs. The peak emission wavelengths of MPA-CdTe QDs, GSH-CdTe QDs, and Cys-CdTe QDs were 560, 552, and 554 nm, respectively.

[15]. They also found MPA-CdTe QDs can inhibit the growth of *E. coli* more effectively. Compared to the method of Lai and his coworkers, it is more economic and rapid to use engineering *E. coli* as sensor to evaluate the biotoxicity of QDs.

The morphologies of the majority of the cells treated with MPA-CdTe QDs were found to have changed from rod shape to stick shape (Figure 4(b)). SEM micrograph analysis further confirmed that the rod-shaped cells turned to be longer and more irregular after treatment with MPA-CdTe QDs (Figure 5(b)), and a large number of broken cells were present. When compared to the untreated cells (Figure 5(a)), no number change was detected in the *E. coli* cells treated with GSH-CdTe QDs (Figure 5(c)) or Cys-CdTe QDs (Figure 5(d)). Wang et al. also used TEM to study the effect of MPA capped CdTe QDs on *E. coli* cells, and the results also showed that a higher concentration of QDs would lead to a dramatic change in the morphology of cells [20]. This means MPA-CdTe has a similar effect on both normal *E. coli* and engineering *E. coli*. Therefore, it could be

concluded from these results that both the proliferation and the protein expression of engineering *E. coli* were inhibited after treatment with MPA-CdTe QDs.

4. Conclusion

In summary, a novel method to evaluate the biological toxicity of CdTe QDs has been developed based on protein expression of engineering *E. coli*. The results indicated that the toxicity of MAA-CdTe QDs was more than that of GSH-CdTe QDs and Cys-CdTe QDs on the expression of the GST protein growth in engineering *E. coli*. The proposed method can be used not only to test the interaction between QDs and bacteria but also to test the biological toxicity of other nanoparticles.

Conflict of Interests

The authors declare that there is no conflict of interests regarding the publication of this paper.

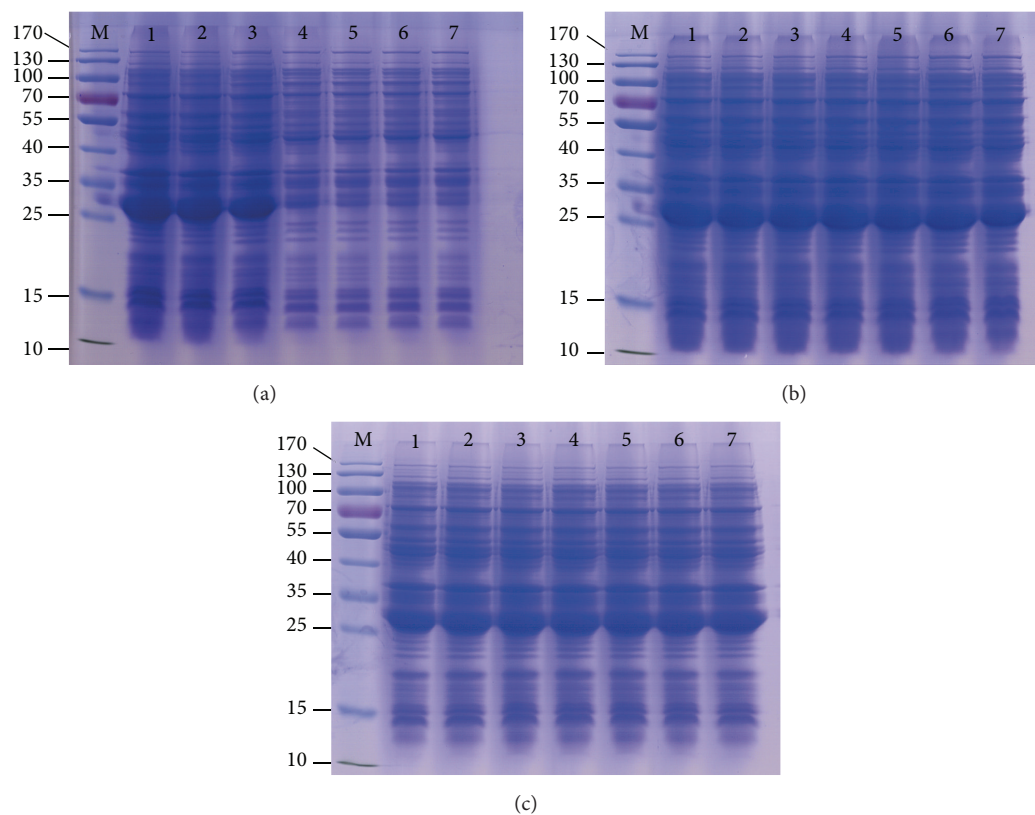


FIGURE 3: The expression of the GST protein of engineering *E. coli* cells after treatment with different concentrations of MPA-CdTe QDs (a), GSH-CdTe QDs (b), and Cys-CdTe QDs (c). Lane 1: the control (untreated engineering *E. coli* cells). Lanes 2–7: engineering *E. coli* cells treated with CdTe QDs at a concentration range (left to right) of 5, 10, 50, 100, 200, and 500 nM.

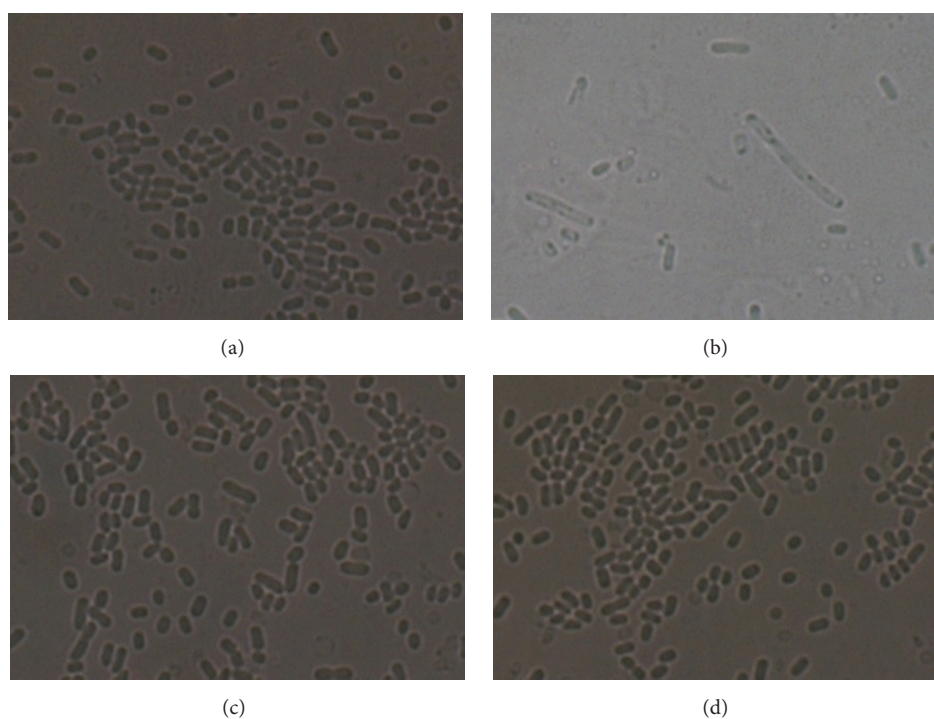


FIGURE 4: Microscopic images of engineering *E. coli* cells before (a) and after treatment with MPA-CdTe QDs (b), GSH-CdTe QDs (c), and Cys-CdTe QDs (d) at an identical concentration of 50 nM.

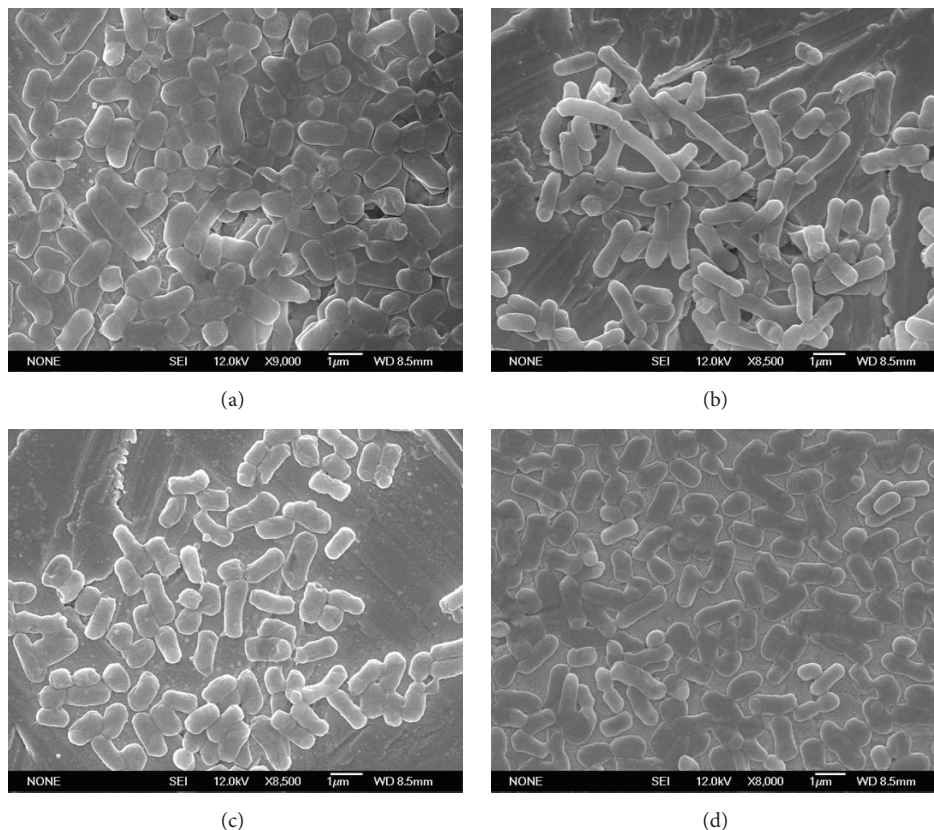


FIGURE 5: SEM micrograph of engineering *E. coli* cells before (a) and after treatment with MPA-CdTe QDs (b), GSH-CdTe QDs (c), and Cys-CdTe QDs (d) at an identical concentration of 50 nM. The scale bar is 1 μm .

Acknowledgments

The authors gratefully acknowledge the support for this research by National Nature Science Foundation of China (31372439, 31225027) and Natural Science Foundation of Hubei Province Innovation Team (2011CDA115).

References

- [1] P. Zrazhevskiy, M. Sena, and X. Gao, "Designing multifunctional quantum dots for bioimaging, detection, and drug delivery," *Chemical Society Reviews*, vol. 39, no. 11, pp. 4326–4354, 2010.
- [2] X. Michalet, F. F. Pinaud, L. A. Bentolila et al., "Quantum dots for live cells, *in vivo* imaging, and diagnostics," *Science*, vol. 307, no. 5709, pp. 538–544, 2005.
- [3] M. Bruchez Jr., M. Moronne, P. Gin, S. Weiss, and A. P. Alivisatos, "Semiconductor nanocrystals as fluorescent biological labels," *Science*, vol. 281, no. 5385, pp. 2013–2016, 1998.
- [4] W. C. W. Chan and S. Nie, "Quantum dot bioconjugates for ultrasensitive nonisotopic detection," *Science*, vol. 281, no. 5385, pp. 2016–2018, 1998.
- [5] Y. Wang, R. Hu, G. Lin, I. Roy, and K. T. Yong, "Functionalized quantum dots for biosensing and bioimaging and concerns on toxicity," *ACS Applied Materials and Interfaces*, vol. 5, no. 8, pp. 2786–2799, 2013.
- [6] A. Taylor, K. M. Wilson, P. Murray, D. G. Fernig, and R. Lévy, "Long-term tracking of cells using inorganic nanoparticles as contrast agents: are we there yet?" *Chemical Society Reviews*, vol. 41, no. 7, pp. 2707–2717, 2012.
- [7] K. T. Yong, W. C. Law, R. Hu et al., "Nanotoxicity assessment of quantum dots: from cellular to primate studies," *Chemical Society Reviews*, vol. 42, no. 3, pp. 1236–1250, 2013.
- [8] F. M. Winnik and D. Maysinger, "Quantum dot cytotoxicity and ways to reduce it," *Accounts of Chemical Research*, vol. 46, no. 3, pp. 672–680, 2013.
- [9] X. Bellanger, P. Billard, R. Schneider, L. Balan, and C. Merlin, "Stability and toxicity of ZnO quantum dots: interplay between nanoparticles and bacteria," *Journal of Hazardous Materials*, vol. 283, pp. 110–116, 2015.
- [10] R. Hardman, "A toxicologic review of quantum dots: toxicity depends on physicochemical and environmental factors," *Environmental Health Perspectives*, vol. 114, no. 2, pp. 165–172, 2006.
- [11] K. C. Nguyen, W. G. Willmore, and A. F. Tayabali, "Cadmium telluride quantum dots cause oxidative stress leading to extrinsic and intrinsic apoptosis in hepatocellular carcinoma HepG2 cells," *Toxicology*, vol. 306, pp. 114–123, 2013.
- [12] Y. C. Song, D. Feng, W. Shi, X. H. Li, and H. M. Ma, "Parallel comparative studies on the toxic effects of unmodified CdTe quantum dots, gold nanoparticles, and carbon nanodots on live cells as well as green gram sprouts," *Talanta*, vol. 116, pp. 237–244, 2013.
- [13] B. R. Singh, B. N. Singh, W. Khan, H. B. Singh, and A. H. Naqvi, "ROS-mediated apoptotic cell death in prostate cancer LNCaP cells induced by biosurfactant stabilized CdS quantum dots," *Biomaterials*, vol. 33, no. 23, pp. 5753–5767, 2012.

- [14] A. Sadaf, B. Zeshan, Z. Wang et al., "Toxicity evaluation of hydrophilic CdTe quantum dots and CdTe@SiO₂ nanoparticles in mice," *Journal of Nanoscience and Nanotechnology*, vol. 12, no. 11, pp. 8287–8292, 2012.
- [15] L. Lai, C. Lin, C. Q. Xiao et al., "Adhesion of quantum dots-induced membrane damage of *Escherichia coli*," *Journal of Colloid and Interface Science*, vol. 389, no. 1, pp. 61–70, 2013.
- [16] C. Ladhar, B. Geffroy, S. Cambier et al., "Impact of dietary cadmium sulphide nanoparticles on Danio rerio zebrafish at very low contamination pressure," *Nanotoxicology*, vol. 8, no. 6, pp. 676–685, 2014.
- [17] J. Lovrić, S. J. Cho, F. M. Winnik, and D. Maysinger, "Unmodified cadmium telluride quantum dots induce reactive oxygen species formation leading to multiple organelle damage and cell death," *Chemistry and Biology*, vol. 12, no. 11, pp. 1227–1234, 2005.
- [18] Y. Su, M. Hu, C. Fan et al., "The cytotoxicity of CdTe quantum dots and the relative contributions from released cadmium ions and nanoparticle properties," *Biomaterials*, vol. 31, no. 18, pp. 4829–4834, 2010.
- [19] S. J. Tan, N. R. Jana, S. Gao, P. K. Patra, and J. Y. Ying, "Surface-ligand-dependent cellular interaction, subcellular localization, and cytotoxicity of polymer-coated quantum dots," *Chemistry of Materials*, vol. 22, no. 7, pp. 2239–2247, 2010.
- [20] Q. Wang, T. Fang, P. Liu, X. Min, and X. Li, "Study of the bioeffects of CdTe quantum dots on *Escherichia coli* cells," *Journal of Colloid and Interface Science*, vol. 363, no. 2, pp. 476–480, 2011.
- [21] T. T. Fang, X. Li, Q. S. Wang, Z. J. Zhang, P. Liu, and C. C. Zhang, "Toxicity evaluation of CdTe quantum dots with different size on *Escherichia coli*," *Toxicology in Vitro*, vol. 26, no. 7, pp. 1233–1239, 2012.
- [22] Q. Xiao, S. Huang, W. Su, P. Li, and Y. Liu, "Evaluate the potential toxicity of quantum dots on bacterial metabolism by microcalorimetry," *Thermochimica Acta*, vol. 552, pp. 98–105, 2013.
- [23] J. S. Mcquillan and A. M. Shaw, "Whole-cell *Escherichia coli*-based bio-sensor assay for dual zinc oxide nanoparticle toxicity mechanisms," *Biosensors and Bioelectronics*, vol. 51, pp. 274–279, 2014.
- [24] P. Liu, W. Duan, Q. Wang, and X. Li, "The damage of outer membrane of *Escherichia coli* in the presence of TiO₂ combined with UV light," *Colloids and Surfaces B: Biointerfaces*, vol. 78, no. 2, pp. 171–176, 2010.
- [25] V. A. Nadtochenko, A. G. Rincon, S. E. Stanca, and J. Kiwi, "Dynamics of *E. coli* membrane cell peroxidation during TiO₂ photocatalysis studied by ATR-FTIR spectroscopy and AFM microscopy," *Journal of Photochemistry and Photobiology A: Chemistry*, vol. 169, no. 2, pp. 131–137, 2005.
- [26] F. Baneyx, "Recombinant protein expression in *Escherichia coli*," *Current Opinion in Biotechnology*, vol. 10, no. 5, pp. 411–421, 1999.
- [27] D. M. Francis and R. Page, "Strategies to optimize protein expression in *E. coli*," in *Current Protocols in Protein Science*, chapter 5, unit 5.24, pp. 21–29, John Wiley & Sons, 2010.
- [28] Z. Sheng, H. Han, and J. Liang, "The behaviors of metal ions in the CdTe quantum dots-H₂O₂ chemiluminescence reaction and its sensing application," *Luminescence*, vol. 24, no. 5, pp. 271–275, 2009.
- [29] Y. Zheng, S. Gao, and J. Y. Ying, "Synthesis and cell-imaging applications of glutathione-capped CdTe quantum dots," *Advanced Materials*, vol. 19, no. 3, pp. 376–380, 2007.
- [30] H. Bao, E. Wang, and S. Dong, "One-pot synthesis of CdTe nanocrystals and shape control of luminescent CdTe-cystine nanocomposites," *Small*, vol. 2, no. 4, pp. 476–480, 2006.
- [31] J. Brosius, M. Erfle, and J. Storella, "Spacing of the -10 and -35 regions in the tac promoter. Effect on its in vivo activity," *The Journal of Biological Chemistry*, vol. 260, no. 6, pp. 3539–3541, 1985.
- [32] Z. Xiao, D. Liu, Z. Tang, H. Li, and M. Yuan, "Synthesis and characterization of poly(lactic acid)-conjugated CdTe quantum dots," *Materials Letters*, vol. 148, pp. 126–129, 2015.
- [33] W. W. Yu, L. H. Qu, W. Z. Guo, and X. G. Peng, "Experimental determination of the extinction coefficient of CdTe, CdSe, and CdS nanocrystals," *Chemistry of Materials*, vol. 15, no. 14, pp. 2854–2860, 2003.

Research Article

Impact of Silver and Iron Nanoparticle Exposure on Cholesterol Uptake by Macrophages

Jonathan H. Shannahan,¹ Hari Sowrirajan,² Indushekhar Persaud,¹
Ramakrishna Podila,^{3,4} and Jared M. Brown¹

¹Department of Pharmaceutical Sciences, Skaggs School of Pharmacy and Pharmaceutical Sciences,
The University of Colorado Anschutz Medical Campus, Aurora, CO 80045, USA

²Cherry Creek High School, Greenwood Village, CO 80111, USA

³Department of Physics and Astronomy, Clemson University, Clemson, SC 29634, USA

⁴Clemson Nanomaterials Center and COMSET, Clemson University, Anderson, SC 29625, USA

Correspondence should be addressed to Jared M. Brown; jared.brown@ucdenver.edu

Received 16 June 2015; Revised 8 September 2015; Accepted 9 September 2015

Academic Editor: Abdelwahab Omri

Copyright © 2015 Jonathan H. Shannahan et al. This is an open access article distributed under the Creative Commons Attribution License, which permits unrestricted use, distribution, and reproduction in any medium, provided the original work is properly cited.

Macrophages are central to the development of atherosclerosis by absorbing lipids, promoting inflammation, and increasing plaque deposition. Nanoparticles (NPs) are becoming increasingly common in biomedical applications thereby increasing exposure to the immune and vascular systems. This project investigated the influence of NPs on macrophage function and specifically cholesterol uptake. Macrophages were exposed to 20 nm silver NPs (AgNPs), 110 nm AgNPs, or 20 nm Fe₃O₄NPs for 2 h and NP uptake, cytotoxicity, and subsequent uptake of fluorescently labeled cholesterol were assessed. Macrophage uptake of NPs did not induce cytotoxicity at concentrations utilized (25 µg/mL); however, macrophage exposure to 20 nm AgNPs reduced subsequent uptake of cholesterol. Further, we assessed the impact of a cholesterol-rich environment on macrophage function following NP exposure. In these sets of experiments, macrophages internalized NPs, exhibited no cytotoxicity, and altered cholesterol uptake. Alterations in the expression of scavenger receptor-B1 following NP exposure, which likely influences cholesterol uptake, were observed. Overall, NPs alter cholesterol uptake, which may have implications in the progression of vascular or immune mediated diseases. Therefore, for the safe development of NPs for biomedical applications, it is necessary to understand their impact on cellular function and biological interactions in underlying disease environments.

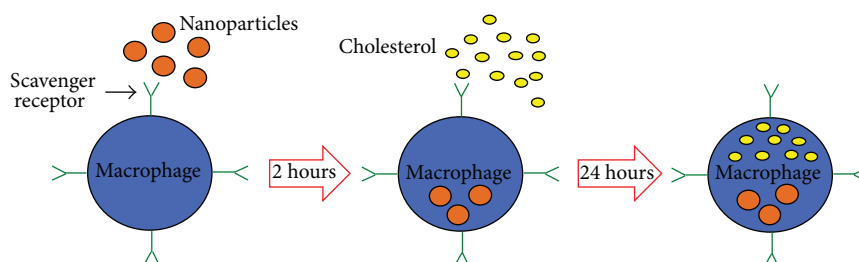
1. Introduction

Nanotechnology is a rapidly expanding field that is transforming numerous areas of technology including a variety of biomedical applications. Specifically, through the development of unique nanoparticles (NPs) there has been the expansion of various drug delivery platforms. Two particular NPs, which have gained interest for a variety of biomedical applications, include silver NPs (AgNPs) and iron oxide NPs (Fe₃O₄ NPs). AgNPs are increasingly being utilized due to their antimicrobial properties and have been incorporated in products such as textiles, household appliances, food storage containers, and medical devices such as i.v. catheters and lines [1–4]. Fe₃O₄ NPs have been proposed as drug delivery platforms and for their use as magnetic resonance imaging

contrast agents [5–7]. Although NPs are increasingly being incorporated into every aspect of our society, we currently lack sufficient knowledge regarding their toxicity. Specifically, AgNPs have been shown to induce a variety of toxic responses including oxidative stress, inflammatory responses, apoptosis, and cytotoxicity in a variety of different cell types [8–12]. Investigation regarding the toxicity of Fe₃O₄ NPs has demonstrated limited toxicity in terms of no observed genotoxicity and minor cytotoxicity at high concentrations (>100 µg/mL) [13, 14].

Additional research is also needed to understand how NP exposures can modify normal cell function at concentrations that do not elicit overt cytotoxicity. Furthermore, few studies have evaluated the influence of underlying disease states on NP-induced toxicity or the influence of NP exposure on

Scenario #1: impact of nanoparticle exposure on macrophage function



Scenario #2: influence of cellular environment on macrophage function

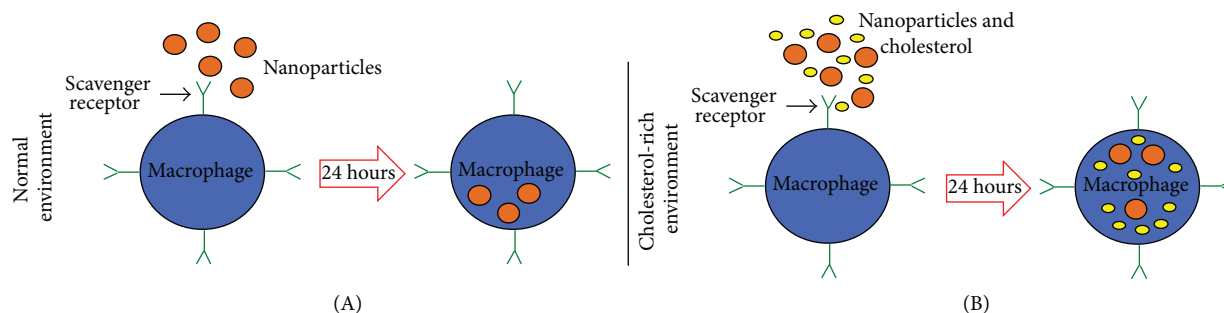


FIGURE 1: Overview of macrophage exposure scenarios. Scenario #1 investigates the impact of NP exposure on macrophage function. Macrophages were exposed for 2 h to 20 nm AgNPs, 110 nm AgNPs, or 20 nm Fe₃O₄ NPs. Media containing NPs were then removed and cells were treated with cholesterol (20 μg/mL) for 24 h. Alterations in toxicity and macrophage function (cholesterol uptake) were assessed. Scenario #2 examined the influence of the cellular environment on macrophage function during an exposure to NPs. This scenario included (A) an environment without cholesterol present and (B) an environment with cholesterol present. Macrophages were exposed for 24 h to 20 nm AgNPs, 110 nm AgNPs, or 20 nm Fe₃O₄ NPs for 24 h in (A) serum-free media or (B) serum-free media containing cholesterol (20 μg/mL). Alterations in macrophage toxicity and function were then assessed.

progression and development of disease states. Individuals with underlying cardiovascular disease and/or obesity comprise a significant and growing portion of the population. *In vivo* animal studies have demonstrated that these individuals may be increasingly sensitive to toxicological insults [15–17]. To more accurately screen NPs for toxicity, it is necessary to understand how common underlying disease states alter the cellular environments (such as high cholesterol), modify NP function, and alter biological responses.

A disease of primary concern for our population is atherosclerosis. The development of atherosclerosis is mediated by macrophage uptake of cholesterol within artery walls leading to inflammation and the formation of an atherosclerotic plaque. Due to their location and immune surveillance properties, macrophages are likely one of the first cell types to interact with NPs when introduced into the circulation mediating their clearance. Macrophages interact with both cholesterol and NPs through scavenger receptors expression on their surface [18–20]. Scavenger receptors are pattern recognition receptors that are classified into three types: Class A, Class B, and Class C. These receptors recognize a number of ligands including oxidized-lipoproteins, pathogens, and negatively charged foreign particles such as NPs [18, 21]. Association of ligands with scavenger receptors facilitates cellular uptake, ligand removal, and proinflammatory responses [12, 22]. Further scavenger receptors are known to be involved in lipid metabolism as well as atherosclerosis development

[23]. Specifically, AgNPs interact with scavenger receptors on the surface of macrophages thus facilitating uptake and apoptosis [24]. Previously, we have demonstrated that inhibition of scavenger receptor-B1 (SR-B1) can reduce the uptake of AgNPs by rat aortic endothelial cells as well as reduce AgNP-induced cytotoxicity and inflammatory response [12]. Mice deficient in SR-B1 have demonstrated increased levels of plasma cholesterol compared to wild-type [23]. This finding as well as the high affinity of SR-B1 for lipoproteins suggests a critical role for SR-B1 in lipoprotein metabolism.

Based on the need for studies examining how exposure to NPs influences macrophage function and understanding alterations in biological responses to NPs in different cellular environments, we utilized two *in vitro* exposure scenarios (Figure 1). Scenario #1 was designed to evaluate the impact of NP exposure on macrophage function. In these experiments, macrophages were exposed to NPs (20 nm AgNPs, 110 nm AgNPs, or 20 nm Fe₃O₄ NPs) and then treated with cholesterol to assess alterations in cholesterol uptake. Scenario #2 was designed to investigate how different cellular environments influence macrophage responses to NPs. In these experiments, macrophages were exposed to NPs in either serum-free media or serum-free media containing high levels of cholesterol. Lastly, these studies evaluated the role of SR-B1, a receptor known to be involved in macrophage responses to both NPs and cholesterol.

2. Materials and Methods

2.1. NP Characterization. 20 nm and 110 nm AgNPs suspended in citrate and 20 nm Fe₃O₄ NPs suspended in PVP were procured from NanoComposix (San Diego, CA) at a concentration of 1 mg/mL. The hydrodynamic size and zeta potentials (ZetaSizer Nano-ZS, Malvern) were characterized in DI water with NPs at a concentration of 25 µg/mL ($n = 3/\text{particle}$). Another set of NPs (25 µg/mL) were incubated for 24 h in cholesterol (20 µg/mL) and assessed for hydrodynamic size and zeta potential following a series of centrifugations and washes with deionized water. The concentrations of NPs evaluated were chosen due to the use of these concentrations in our previous studies and the work of others [12, 25, 26]. The cholesterol concentration utilized was based on the manufacturer's instructions for the measurements of cholesterol uptake (Cayman Chemical Company, Ann Arbor, MI). NPs were further characterized by hyperspectral darkfield microscopy (Cytoviva, Auburn, AL). Bare NPs or NPs incubated for 24 h in cholesterol (20 µg/mL) were loaded onto premium clean microscope slides and mean spectrums were created utilizing pixels with an intensity of 1000 or greater. Mean spectrums were then compared between bare NPs and NPs incubated in cholesterol for the assessment of alterations in NP spectra indicative of cholesterol coating or formation of a NP biocorona.

2.2. Cell Culture. Mouse macrophages (RAW264.7) (ATCC, Manassas, VA) were cultured in Dulbecco's modified eagle media (DMEM) containing 10% FBS and maintained in flasks under standard conditions of 37°C and 5% CO₂. All experiments were performed at 90% confluency and in serum-free media conditions in order to inhibit protein-NP interactions resulting in protein corona formation.

2.3. Cytotoxicity. Macrophages were grown to 90% confluency in 96-well plates (Costar) and exposed to 20 nm AgNPs, 110 nm AgNPs, or 20 nm Fe₃O₄ NPs at concentrations of 6.25, 12.5, 25, or 50 µg/mL for 2 h or 24 h. The concentration range evaluated for cytotoxicity was selected based on previous *in vitro* experimentation of NPs [12, 25]. Changes in cell viability were assessed using the MTS assay (Promega, Madison, WI) via manufacturer's instructions using a spectrophotometer (BioTek Synergy HT, BioTek, Winooski, VT). A NP concentration of 25 µg/mL was selected for subsequent experiments due to limited induction of cytotoxicity at this concentration.

Macrophages were grown to 90% confluency in 96-well plates (Costar) and exposed to 20 nm AgNPs, 110 nm AgNPs, or 20 nm Fe₃O₄ NPs at a concentration of 25 µg/mL in serum-free media for 2 h and then treated with cholesterol (20 µg/mL) for 24 h. In a separate set of experiments macrophages were exposed to 20 nm AgNPs, 110 nm AgNPs, or 20 nm Fe₃O₄ NPs at a concentration of 25 µg/mL in serum-free media containing cholesterol (20 µg/mL) or without cholesterol present for 24 h. Changes in cell viability were again assessed using the MTS assay (Promega, Madison, WI) via manufacturer's instructions using a spectrophotometer (BioTek Synergy HT, BioTek, Winooski, VT).

2.4. Macrophage Uptake of NPs. Macrophages were grown to 90% confluency in 24-well plates (Costar) or microscope chamber slides. Macrophages were exposed for 2 h to 20 nm AgNPs, 110 nm AgNPs, or 20 nm Fe₃O₄ NPs at a concentration of 25 µg/mL in serum-free media. In a separate set of experiments macrophages were exposed for 24 h to 20 nm AgNPs, 110 nm AgNPs, or 20 nm Fe₃O₄ NPs at a concentration of 25 µg/mL in serum-free media with cholesterol (20 µg/mL) or without. Following exposure cells in 24-well plates were washed with PBS and collected by detachment with 250 µL of trypsin and neutralization with an equal volume of media. NP uptake was evaluated by alterations in side scatter shift through flow cytometry (Accuri C6 Flow Cytometer, BD Biosciences, San Jose, CA). Side scatter shift values were normalized to controls and expressed as a fold change. Following exposure, cells in microscope chamber slides were fixed with 2% paraformaldehyde. Darkfield microscopy (Cytoviva, Auburn, AL) was utilized to confirm NP uptake within macrophages.

2.5. Alterations in Cholesterol Uptake due to NP Exposure. Cholesterol uptake was measured utilizing a cholesterol uptake cell-based assay kit via manufacturer's instructions (Cayman Chemical Company, Ann Arbor, MI). This kit uses fluorescently labeled cholesterol to assess cellular uptake of cholesterol. Macrophages were grown to 90% confluency in 96-well plates (Costar) and exposed to 20 nm AgNPs, 110 nm AgNPs, or 20 nm Fe₃O₄ NPs for 2 h in serum-free media. Following the 2 h exposure to NPs macrophages were treated with fluorescently labeled cholesterol at a concentration of 20 µg/mL for 24 h or serum-free media without cholesterol present. In a separate set of experiments macrophages were exposed for 24 h to 20 nm AgNPs, 110 nm AgNPs, or 20 nm Fe₃O₄ NPs at a concentration of 25 µg/mL in serum-free media with (20 µg/mL) or without cholesterol present. Media were then removed and replaced with a cell assay buffer and read using a fluorescent plate reader (BioTek Synergy HT, BioTek, Winooski, VT) to measure cholesterol uptake via manufacturer's instructions (Cayman Chemical, Ann Arbor, MI) and background fluorescence was subtracted. Cholesterol uptake was qualitatively confirmed by fluorescent microscopy (Nikon Eclipse TE 2000-E, Tokyo, Japan) in macrophages grown on microscope slides and exposed to 110 nm AgNPs with or without cholesterol present. Nuclei were stained with DAPI and visualized as blue whereas cholesterol was visualized as green.

2.6. NP-Induced Alterations in Scavenger Receptor-BI Expression. Macrophages were grown to 90% confluency in 24-well plates (Costar) and exposed to 20 nm AgNPs, 110 nm AgNPs, or 20 nm Fe₃O₄ NPs for 2 h in serum-free media. In a separate set of experiments macrophages were exposed for 24 h to 20 nm AgNPs, 110 nm AgNPs, or 20 nm Fe₃O₄ NPs at a concentration of 25 µg/mL in serum-free media with (20 µg/mL) or without cholesterol present. Macrophages were washed with PBS and collected by detachment with 250 µL of trypsin and neutralization with an equal volume of media. Macrophages were then treated with 2% paraformaldehyde

TABLE 1: Hydrodynamic size and zeta potential of NPs suspended in water or cholesterol.

Nanoparticle	Suspended in water		Suspended in cholesterol (20 $\mu\text{g/mL}$)	
	Hydrodynamic size (nm)	Zeta potential (mV)	Hydrodynamic size (nm)	Zeta potential (mV)
20 nm AgNP	29.3 \pm 0.2	-54.7 \pm 0.7	31.1 \pm 0.2	-50.0 \pm 0.4
110 nm AgNP	106.7 \pm 0.3	-61.2 \pm 1.1	110.6 \pm 0.6	-58.4 \pm 0.3
20 nm Fe ₃ O ₄	37.72 \pm 0.1	-43.8 \pm 1.2	40.23 \pm 0.3	-38.0 \pm 0.8

and stained with a fluorescently labeled scavenger receptor-B1 (SR-B1) antibody (1:100) (NB400-104, Novus Biologicals, Littleton, CO). Following a series of washes macrophage surface expression of SR-B1 was evaluated by flow cytometry (Accuri C6 Flow Cytometer, BD Biosciences, San Jose, CA). The mean fluorescent signal from no stain controls was subtracted from SR-B1 stained samples to remove any background autofluorescence.

2.7. Statistical Test. A one-way ANOVA test was performed using Dunnett's post hoc analysis where applicable to determine significant differences in the dataset ($p < 0.05$). All data is presented as mean \pm standard error of means ($n = 3-6/\text{group}$).

3. Results and Discussion

3.1. NP Characterization. Dynamic light scattering verified the sizes of procured NPs while all NPs demonstrated negative ζ -potentials (Table 1). Specifically, the citrate suspended AgNPs were determined to have a more negative ζ -potential as compared to the PVP suspended Fe₃O₄ NPs. Incubation with cholesterol (20 $\mu\text{g/mL}$) for 24 h resulted in slight increases in hydrodynamic size as well as a reduction in ζ -potential for all NPs (Table 1). Hyperspectral analysis was performed on NPs to determine differences in spectra following 24 h incubation in cholesterol (Figure 2). A comparison of all NPs demonstrates differences in spectra that were likely based on NP identity, suspension material, and size. 20 nm AgNPs were red shifted compared to 110 nm AgNPs likely due to differences in size upon addition of cholesterol (Figure 2). 20 nm AgNPs and Fe₃O₄ NPs demonstrated similar spectral peaks at 572 nm; however Fe₃O₄ NPs exhibited a broader curve. The identical spectral peaks are likely due to both NPs having similar sizes (thus similar scattering) whereas the 20 nm AgNPs have a narrower peak due to their metallic nature. Incubation with cholesterol resulted in a red shift for the AgNPs indicative of association of cholesterol with the surface of the AgNPs (Figure 2). However the incubation of Fe₃O₄ NPs with cholesterol did not demonstrate any shifts in the spectral peak but exhibited a slight broadening of the spectrum.

The alterations we observed in hydrodynamic size, ζ -potential, and shifts in spectra are similar to changes we have seen in our previous work investigating the implications of biocorona on AgNP toxicity [12, 27]. The biocorona forms on NPs following their introduction in physiological environments as biomolecules interact and coat the NP surface [27, 28]. Specifically, we have demonstrated slight increases in hydrodynamic size, decreases in ζ -potential, and red shifts

in spectra following addition of proteins such as albumin and high-density lipoprotein onto the surface of AgNPs [27]. This is likely occurring in our current study because cholesterol associates with the surface of the NPs. In these previous studies, we have also demonstrated that addition of these individual proteins can influence cell-NP interactions [12]. Further, in an assessment of proteins that bind to NPs following incubation in 10% fetal bovine serum, we have identified multiple apolipoproteins that ubiquitously associate with AgNPs [27]. Based on this binding of apolipoprotein binding to AgNPs as previously reported, it was expected that the cholesterol utilized in our current study would also associate with NPs. This biocorona formed following incubation in cholesterol is of interest for further study and has high human relevance. Specifically, individuals are known to have differing amounts of cholesterol within their circulation, which will influence the identity of the NP biocorona in terms of differential biocoronal cholesterol content. These alterations in cholesterol content of the biocorona will likely influence cell-NP interactions and toxicity on an individual basis due to the cholesterol content within the circulation.

3.2. Nanoparticle-Induced Cytotoxicity. A dose-response study was conducted on macrophages to determine a NP concentration for use in subsequent evaluation that did not induce overt cytotoxicity (Figure 3). No significant cytotoxicity was determined following a 2 h exposure to 20 nm AgNPs, 110 nm AgNPs, or 20 nm Fe₃O₄ NPs at concentrations of 6.25, 12.5, 25, or 50 $\mu\text{g/mL}$ (Figure 3(a)). Exposure to NPs at the same concentrations for 24 h was only found to induce significant cytotoxicity in macrophages exposed to 50 $\mu\text{g/mL}$ of 20 nm AgNPs (Figure 3(b)). Based on this cytotoxicity data, a NP concentration of 25 $\mu\text{g/mL}$ was utilized for all subsequent experiments, as it did not induce overt cytotoxicity.

In comparison to our previous work across the same range of concentrations in rat lung epithelial cells and rat aortic endothelial cells, the mouse macrophages used in this study are less susceptible to AgNP-induced cytotoxicity [12]. Specifically, previous studies revealed that rat aortic endothelial cells demonstrated significant cytotoxicity when exposed to 25 $\mu\text{g/mL}$ of 20 nm AgNP at 3 h. Further, both rat lung epithelial cells and rat aortic endothelial cells exhibited significant cytotoxicity at 6 h when exposed to 25 and 50 $\mu\text{g/mL}$ of 20 nm AgNPs, while rat aortic endothelial cells also demonstrated significant cytotoxicity at the concentration of 12.5 $\mu\text{g/mL}$ of 20 nm AgNPs. Based on these data from our current and previous work, there are cell specific differences in cytotoxicity in response to 20 nm AgNPs (macrophage < epithelial < endothelial). A critical

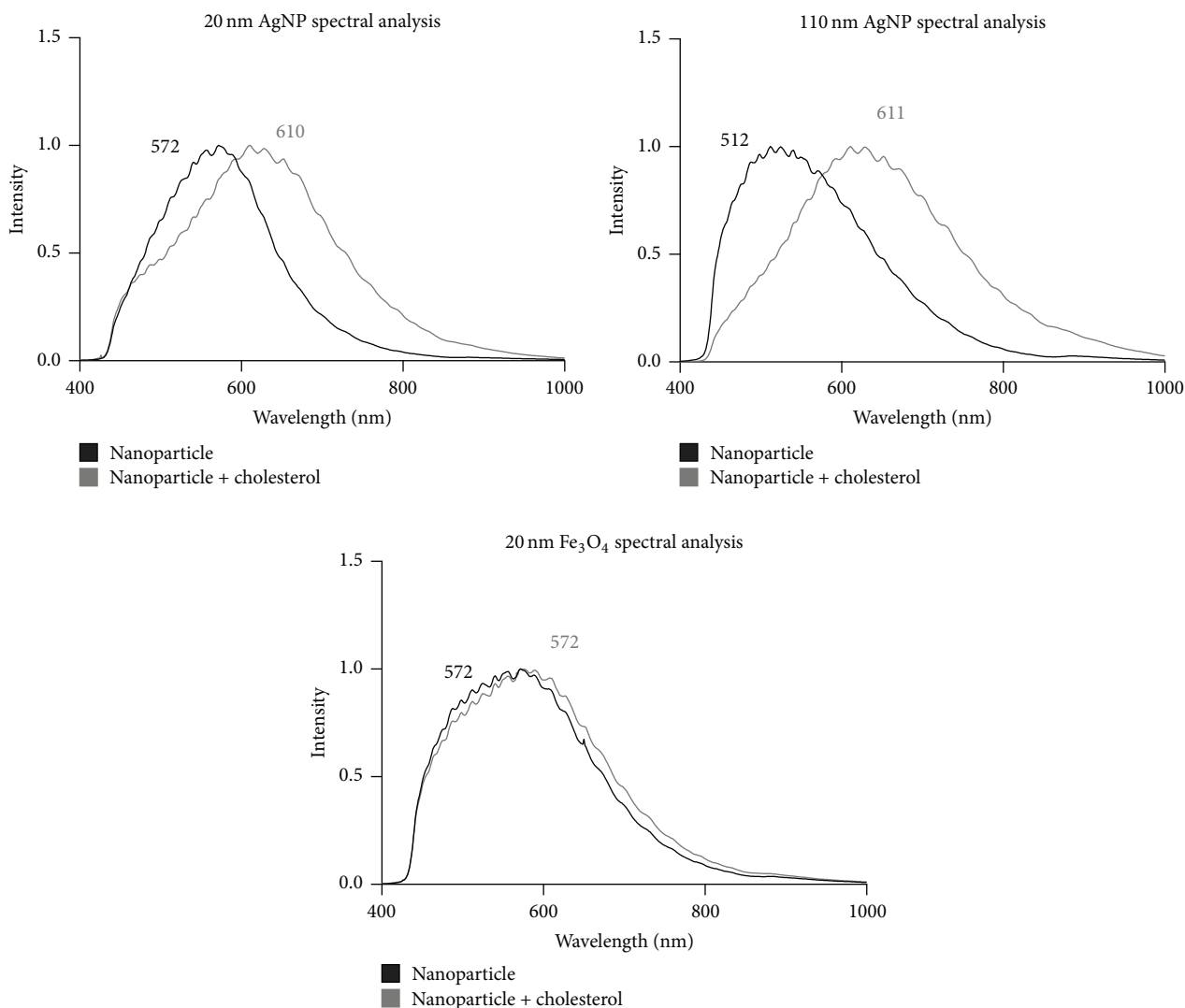


FIGURE 2: Hyperspectral profiles of 20 nm AgNPs, 110 nm AgNPs, and 20 nm Fe_3O_4 NPs in either water or cholesterol (20 $\mu\text{g}/\text{mL}$). Following a 24 h incubation in water or cholesterol (20 $\mu\text{g}/\text{mL}$) NPs were collected via centrifugation and underwent a series of washes. NPs were then loaded onto premium clean microscope slides and assessed by hyperspectral darkfield microscopy. NP spectra were created utilizing pixels with an intensity of greater than 1,000. Numbers represent the wavelength of the spectral peak; black denotes NPs in water whereas gray denotes NPs incubated with cholesterol.

implication of this finding is that conclusive assessments of NP toxicity cannot be gleaned from the investigation of cytotoxicity on one cell type, as they are variable in response. Cytotoxicity as an endpoint appears to be cell and NP specific therefore making broad generalizations regarding cytotoxicity inappropriate.

3.3. Impact of Cholesterol on Cytotoxicity. Macrophages were exposed to NPs at 25 $\mu\text{g}/\text{mL}$ for 2 h and, following exposure, NPs were removed and macrophages were treated for 24 h with either serum-free media containing cholesterol (20 $\mu\text{g}/\text{mL}$) or without cholesterol (Figure 3(c)). Following this 24 h cholesterol treatment, cell viability was assessed. As observed before, none of the NPs were found to induce significant cytotoxicity at the 25 $\mu\text{g}/\text{mL}$ concentration (Figure 3(c)). Treatment with cholesterol did not

induce cytotoxicity (Figure 3(c)). In a separate set of experiments macrophages were exposed to NPs (25 $\mu\text{g}/\text{mL}$) in conjunction with cholesterol (20 $\mu\text{g}/\text{mL}$) or in a cholesterol-free environment (serum-free media) for 24 h (Figure 3(d)). Following this coexposure, no differences were determined in the induction of cytotoxicity (Figure 3(d)). These results confirmed that there were no differences in cytotoxicity following cholesterol treatment and appropriate comparisons could be made in subsequent experiments investigating NP-induced alterations in macrophage function.

3.4. Macrophage Uptake of Nanoparticles. Uptake of NPs by macrophages was evaluated following a 2 h exposure to 20 nm AgNPs, 110 nm AgNPs, or 20 nm Fe_3O_4 NPs at a concentration of 25 $\mu\text{g}/\text{mL}$ (Figure 4(a)). To assess internalization of NPs, changes in mean side scatter of macrophages

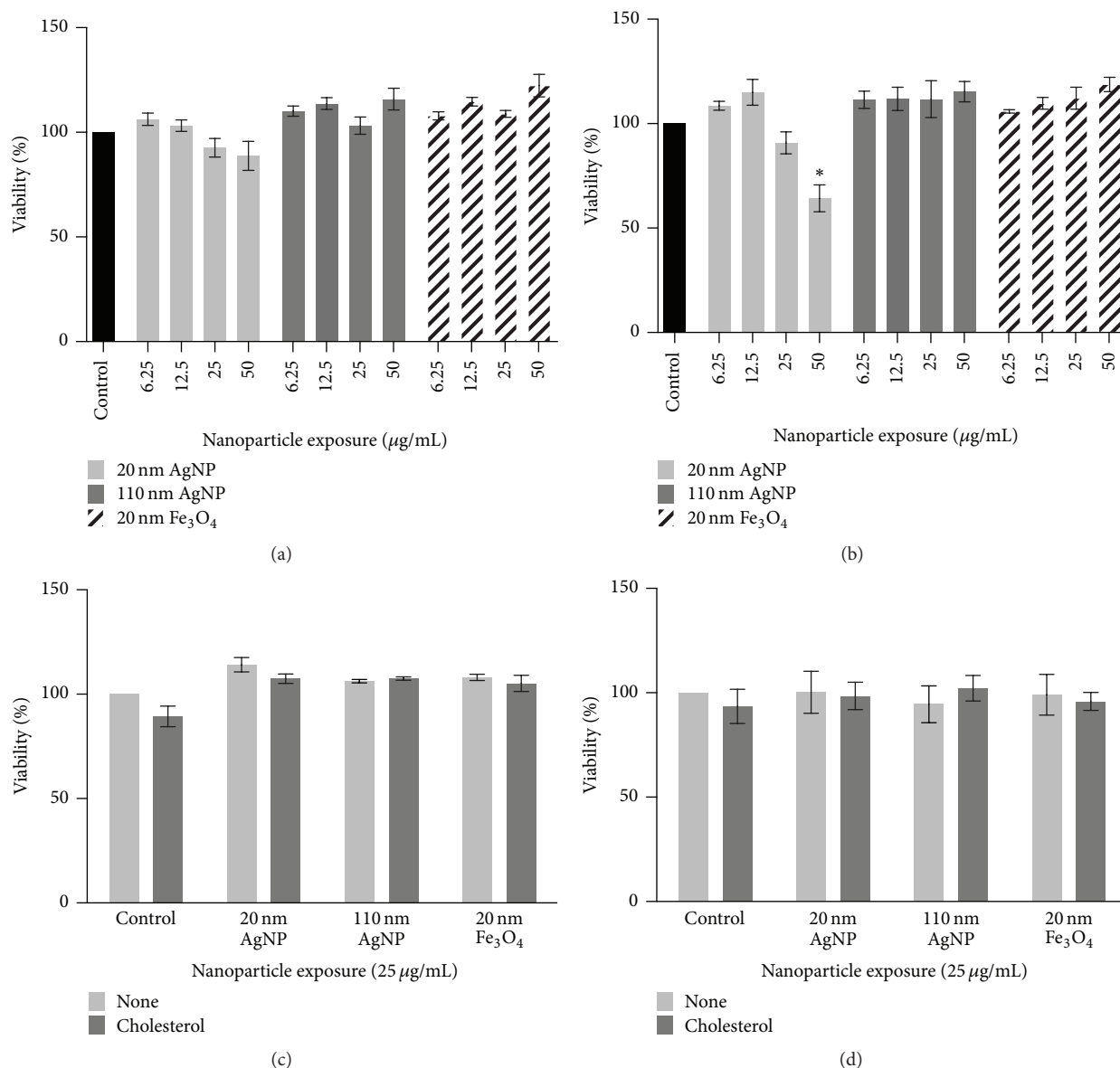


FIGURE 3: Cell viability changes in macrophages following exposure to 20 nm AgNPs, 110 nm AgNPs, or 20 nm Fe₃O₄ NPs at 6.25, 12.5, 25, or 50 μg/mL for (a) 2 h or (b) 24 h. (c) Alterations in cell viability following a 2 h exposure to 20 nm AgNPs, 110 nm AgNPs, or 20 nm Fe₃O₄ NPs (25 μg/mL) and a subsequent 24 h treatment to either serum-free media or serum-free media containing cholesterol (20 μg/mL). (d) Cell viability following a 24 h exposure to 20 nm AgNPs, 110 nm AgNPs, or 20 nm Fe₃O₄ NPs (25 μg/mL) in either serum-free media or serum-free media containing cholesterol (20 μg/mL). Values are expressed as mean ± SEM ($n = 3-6/\text{group}$). * indicates significant difference from controls (untreated) ($p < 0.05$).

were measured by flow cytometry. Briefly, increases in mean side scatter correspond to increases in granularity of the cell indicative of NP internalization [12, 29, 30]. Following a 2 h exposure to each NP, mean side scatter was increased demonstrating the uptake of NPs by macrophages (Figure 4(a)). In an experiment designed to evaluate modifications in macrophage uptake of NPs in an environment with cholesterol present, macrophages were exposed to NPs (25 μg/mL) in either serum-free media or serum-free media containing cholesterol (20 μg/mL) for 24 h (Figure 4(b)). Exposure to NPs resulted in increased side scatter demonstrating uptake of each individual NP during

the 24 h exposure (Figure 4(b)). When comparing the uptake following a 2 h exposure (Figure 4(a)) and a 24 h exposure (Figure 4(b)), similar changes in side scatter were observed. This demonstrates that the majority of uptake occurs within the first 2 h of an *in vitro* exposure. The cholesterol-rich environment resulted in increased uptake of 110 nm AgNP compared to the environment with cholesterol absent (Figure 4(b)). The cholesterol-rich environment however was not found to alter macrophage uptake of the 20 nm AgNPs or Fe₃O₄ NPs (Figure 4(b)). Uptake of NPs by macrophages was visually confirmed via enhanced darkfield microscopy (Figure 5).

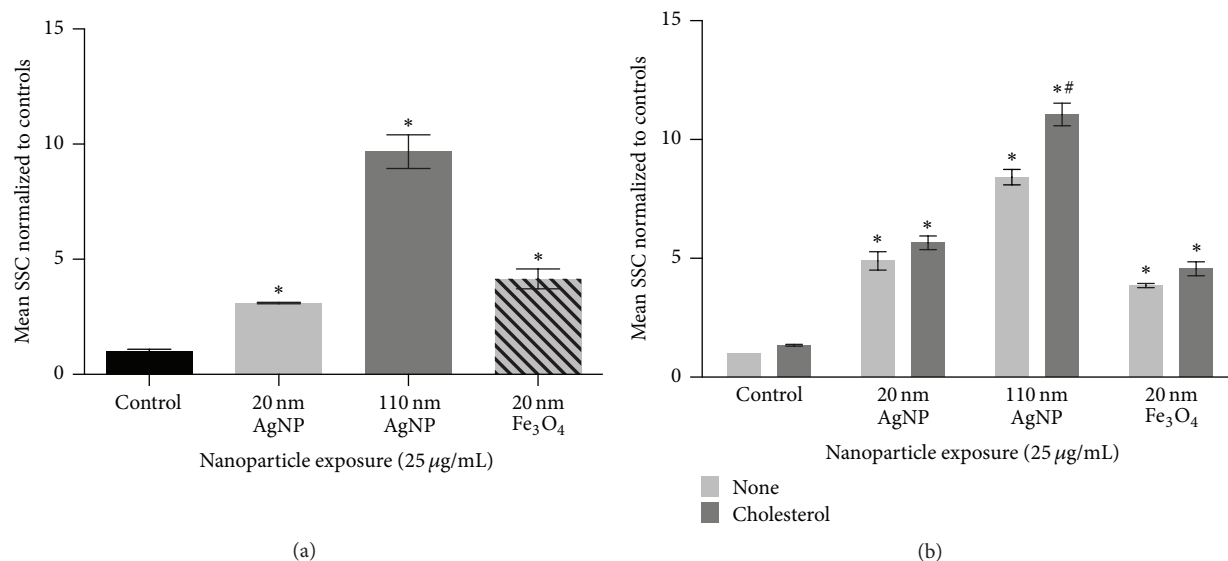


FIGURE 4: Measurement of NP uptake by assessment of changes in mean side scatter shift (SSC) via flow cytometry. (a) Macrophages were exposed to 20 nm AgNP, 110 nm AgNPs, or 20 nm Fe₃O₄ NPs at a concentration of 25 µg/mL for 2 h and assessed for changes in side scatter shift (SSC). (b) Macrophages were exposed to 20 nm AgNP, 110 nm AgNPs, or 20 nm Fe₃O₄ NPs at a concentration of 25 µg/mL for 24 h in either serum-free media or serum-free media containing cholesterol (20 µg/mL). SSC values of macrophages exposed to NPs were normalized to control macrophages to produce a fold change. Values are expressed as mean ± SEM ($n = 3/\text{group}$). * indicates significant difference from controls ($p < 0.05$). # indicates significant difference from NP exposure in serum-free media ($p < 0.05$).

All NPs in our current study were readily internalized by macrophages. This internalization was expected as *in vivo* studies have demonstrated localization of NPs within macrophages [31]. Macrophage uptake of NPs appears to occur quickly as there are only slight differences in uptake between 2 h and 24 h. Since this measurement of uptake utilizes changes in macrophage granularity it is difficult to make comparisons of uptake differences between NPs of variable size. However since two of our chosen NPs were of similar size (20 nm AgNP and Fe₃O₄) they can be more easily compared. The two 20 nm NPs (Ag and Fe) were taken up similarly at both time points even though they differed in composition (Ag and Fe) and suspension material (citrate and PVP), suggesting that size is a determining factor in internalization. When macrophages were exposed to NPs in a cholesterol-rich environment, uptake was increased, reaching significance only for 110 nm AgNPs. This finding suggests that certain NPs in individuals with high cholesterol may be differentially biodistributed compared to individuals with low cholesterol. This also suggests increased interactions with macrophages, which may enhance clearance and stimulate more robust inflammatory responses.

3.5. Modifications in Macrophage Function. In this study, we evaluated two exposure scenarios to determine how NP exposures may influence macrophage function and the influence of the cellular environment (Figure 1). Macrophage function was assessed by analyzing differences in cholesterol uptake. The concentration of 25 µg/mL NPs utilized for these experiments was not found to induce significant cytotoxicity (Figure 3); therefore any alterations in macrophage function are not due to decreases in macrophage viability or numbers.

3.6. Impact of NP Exposure on Macrophage Function. In our first exposure scenario (Figure 1), macrophages were exposed to NPs (25 µg/mL) for 2 h followed by measurement of cholesterol uptake (20 µg/mL). Following the 24 h cholesterol treatment, alterations in cholesterol uptake were assessed (Figure 6(a)). Exposure for 2 h to 20 nm AgNPs was found to reduce uptake of cholesterol compared to control (Figure 6(a)). No alterations in cholesterol uptake were demonstrated following a 2 h exposure to 110 nm AgNPs or 20 nm Fe₃O₄. These NP-induced modifications in cholesterol uptake by macrophages are likely driven by a variety of physicochemical properties including size, suspension material, and/or charge. NP size and surface area have been shown to be important for interactions with cells. Specifically, it has been shown in the study of NP immune cell interactions using mast cells that 20 nm AgNPs induce degranulation whereas 110 nm AgNPs do not [22]. In our current study, we utilized two AgNPs suspended in citrate while the Fe₃O₄ NPs were suspended in PVP. Interestingly, in our current study, cholesterol uptake was reduced following exposure to 20 nm AgNPs whereas no changes were exhibited following exposure to 20 nm Fe₃O₄ NPs. Although these NPs are of similar size they do differ based on suspension material and charge, which may alter NP-cell interactions.

3.7. Influence of Cellular Environment on Macrophage Function. In our second exposure scenario (Figure 1), macrophages were exposed to NPs (20 nm AgNPs, 110 nm AgNPs, or 20 nm Fe₃O₄ NPs) at 25 µg/mL in serum-free media or serum-free media with cholesterol (20 µg/mL) for 24 h (Figure 6(b)). Macrophages exposed to 20 nm AgNPs with cholesterol present for 24 h demonstrated a decrease in

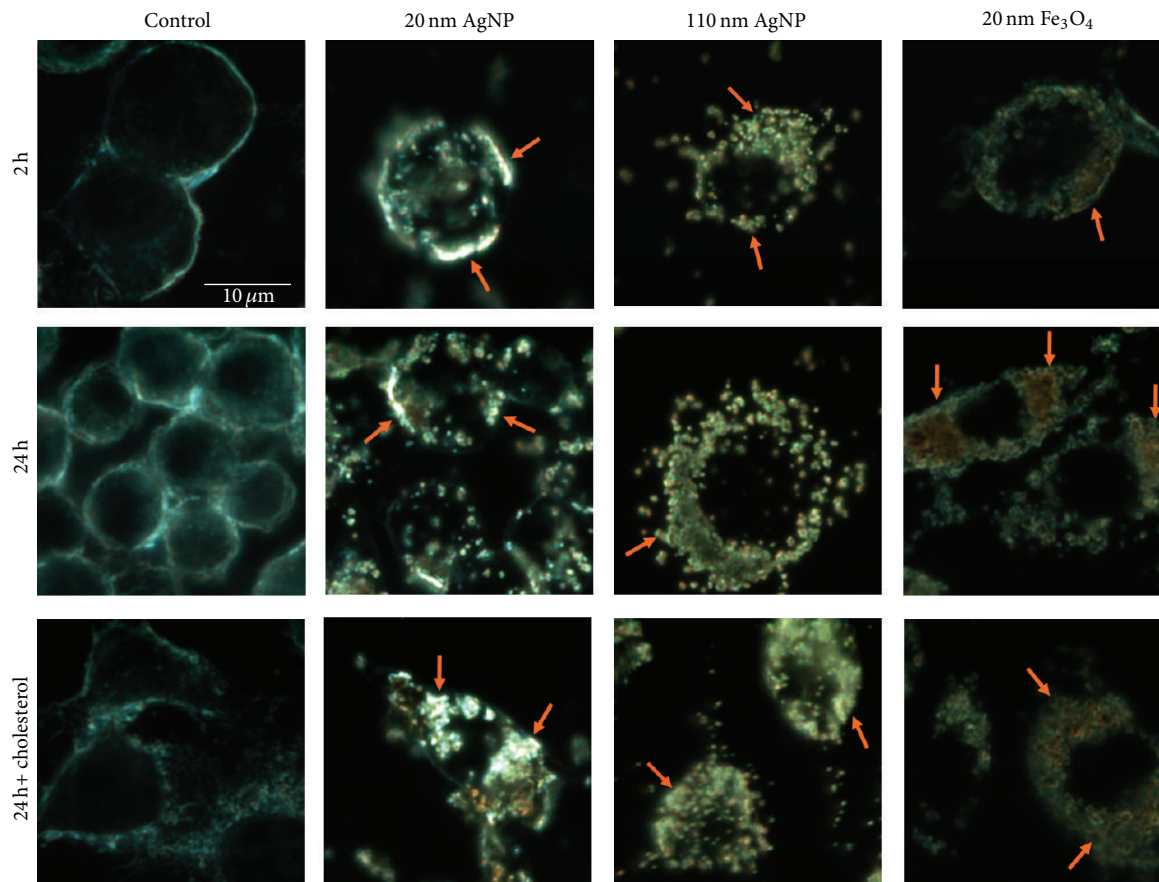


FIGURE 5: Representative enhanced darkfield images of macrophages exposed to 20 nm AgNPs, 110 nm AgNPs, or 20 nm Fe_3O_4 NPs visually demonstrating NP uptake. Images demonstrate macrophage uptake of NPs after 2 h and 24 h exposures in serum-free media or after a 24 h exposure in serum-free media containing cholesterol (20 $\mu\text{g}/\text{mL}$). All images were taken at 100x magnification. Arrows indicate macrophage internalized NPs.

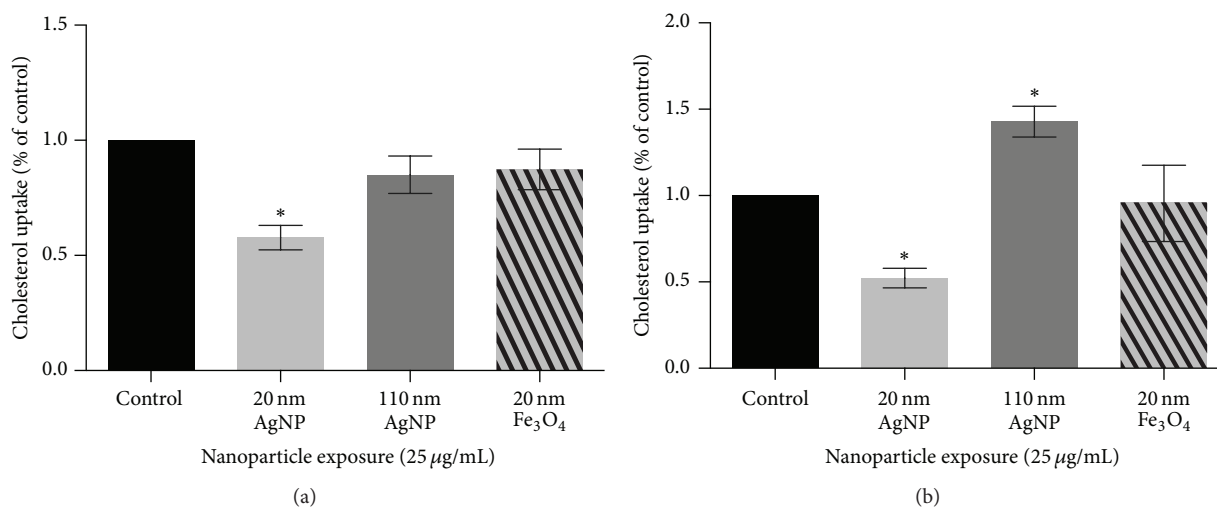


FIGURE 6: NP-induced alterations in macrophage uptake of cholesterol. (a) Macrophages were exposed to 20 nm AgNPs, 110 nm AgNPs, or 20 nm Fe_3O_4 NPs at a concentration of 25 $\mu\text{g}/\text{mL}$ for 2 h. NPs were removed prior to a 24 h treatment with fluorescently labeled cholesterol (20 $\mu\text{g}/\text{mL}$) in serum-free media. (b) Macrophages were exposed to 20 nm AgNP, 110 nm AgNPs, or 20 nm Fe_3O_4 NPs at a concentration of 25 $\mu\text{g}/\text{mL}$ for 24 h in either serum-free media or serum-free media containing cholesterol (20 $\mu\text{g}/\text{mL}$) and cholesterol uptake was measured at 24 h. Cholesterol uptake was measured via a spectrophotometer and normalized to control cholesterol uptake. Values are expressed as mean \pm SEM ($n = 3-8/\text{group}$). * indicates significant difference from controls ($p < 0.05$).

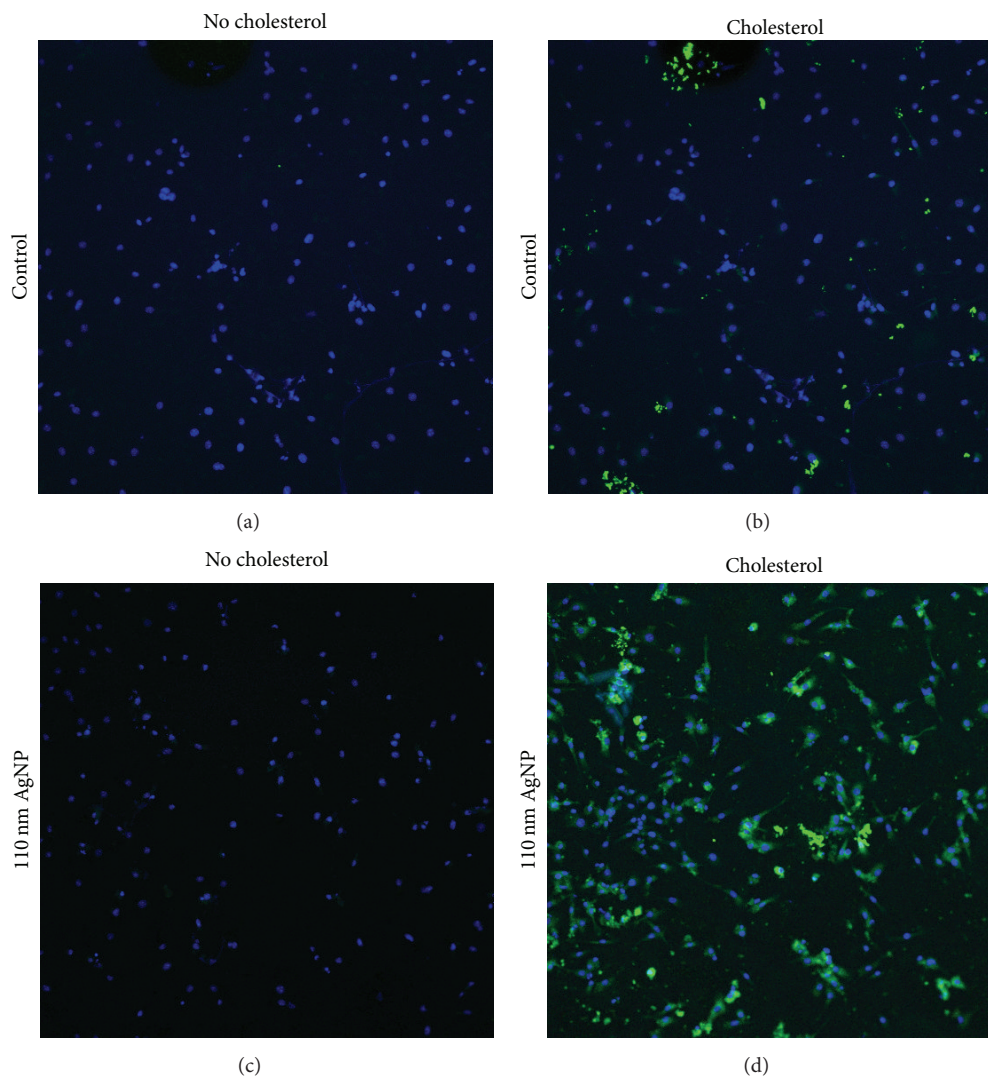


FIGURE 7: Confocal microscopy imaging of alterations in cholesterol uptake by macrophages exposed to NPs. (a) Control macrophages cultured in serum-free media for 24 h. (b) Macrophages cultured for 24 h in serum-free media containing cholesterol ($20 \mu\text{g}/\text{mL}$). (c) Macrophages exposed for 24 h to 110 nm AgNPs ($25 \mu\text{g}/\text{mL}$) in serum-free media. (d) Macrophages exposed for 24 h to 110 nm AgNPs ($25 \mu\text{g}/\text{mL}$) in serum-free media containing cholesterol ($20 \mu\text{g}/\text{mL}$). Blue represents DAPI stained nuclei whereas green areas represent fluorescently labeled cholesterol. All images were taken at 40x magnification with the confocal and detection parameters held constant between images.

cholesterol uptake whereas exposure to 110 nm AgNPs caused an increase in cholesterol uptake (Figure 6(b)). Since 20 nm and 110 nm AgNPs were found to have different effects, this suggests that size is important in modifying cholesterol uptake in cholesterol-rich environments. It is possible that 110 nm AgNPs increase cholesterol uptake by acting as a carrier for cholesterol into the cell. Based on our previous research we have demonstrated that NPs of different sizes can result in differential association of proteins [27]. It is likely that 110 nm AgNPs bind substantially more cholesterol onto their surfaces thereby increasing macrophage cholesterol content following internalization of 110 nm AgNPs. Cholesterol uptake as compared to controls was not modified following exposure to 20 nm Fe_3O_4 NPs in serum-free media with cholesterol (Figure 6(b)). This finding suggests

that Fe_3O_4 NPs may be useful for clinical applications, as it does not modify macrophage function in either the absence or presence of cholesterol. The increase in cholesterol uptake that occurred with 110 nm AgNP in serum-free media with cholesterol was visually confirmed via fluorescent microscopy (Figure 7). In an attempt to begin to understand the mechanism behind these responses we evaluated the receptor content on the surface of macrophages of the scavenger receptor-B1.

3.8. Nanoparticle-Induced Alterations in Macrophage Expression of Scavenger Receptor-B1. Following a 2 h exposure to NPs ($25 \mu\text{g}/\text{mL}$), macrophage cell surface expression of scavenger receptor-B1 (SR-B1) was analyzed via flow cytometry (Figure 8(a)). SR-B1 is involved in the uptake of both NPs

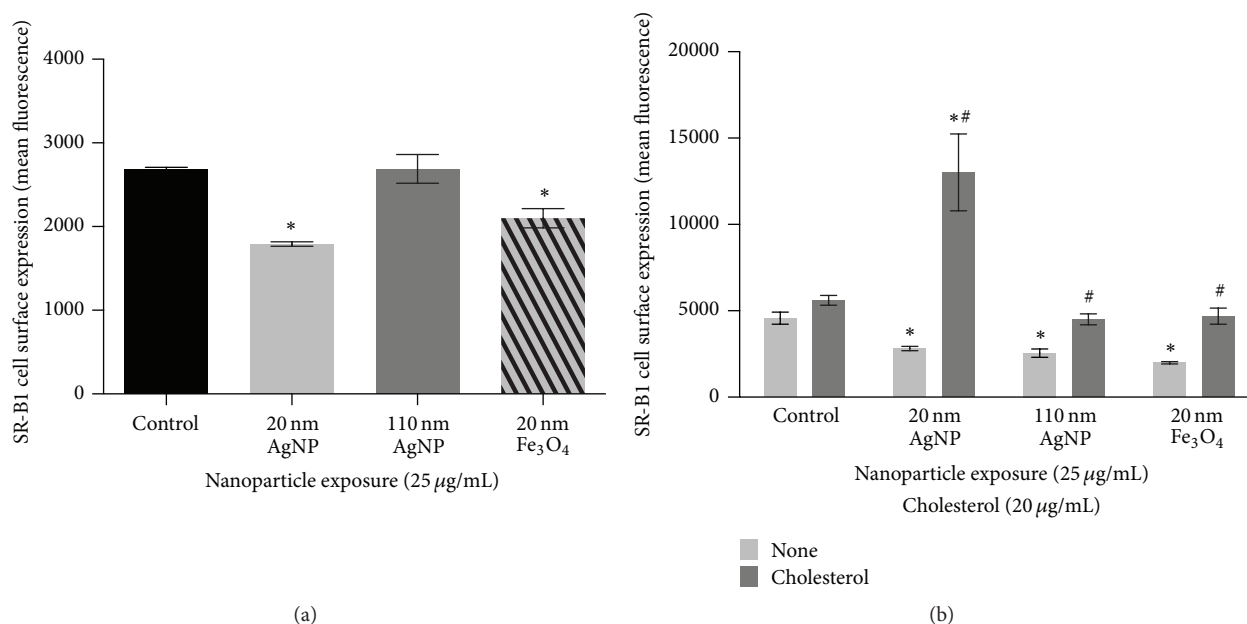


FIGURE 8: Alteration in macrophage surface receptor expression of scavenger receptor-B1 (SR-B1). (a) Macrophages were exposed to 20 nm AgNP, 110 nm AgNPs, or 20 nm Fe₃O₄ NPs at a concentration of 25 µg/mL for 2 h and assessed for changes in SR-B1 cell surface expression by flow cytometry. (b) Macrophages were exposed to 20 nm AgNP, 110 nm AgNPs, or 20 nm Fe₃O₄ NPs at a concentration of 25 µg/mL for 24 h in either serum-free media or serum-free media containing cholesterol (20 µg/mL) and assessed for changes in SR-B1 cell surface expression. The mean fluorescent signal from no stain controls was subtracted from SR-B1 stained samples to correct for any background autofluorescence. Values are expressed as mean ± SEM ($n = 3/\text{group}$). * indicates significant difference from controls ($p < 0.05$). # indicates significant difference from NP exposure in serum-free media ($p < 0.05$).

and cholesterol by macrophages [18, 32]. Therefore, it is likely that NP exposure may alter the expression of SR-B1 on the surface of macrophages thereby modifying macrophage responses to cholesterol. Exposure to 20 nm AgNPs and Fe₃O₄ NPs was found to decrease SR-B1 expression on the surface of macrophages whereas 110 nm AgNP exposure was not found to modify expression as compared to controls (Figure 8(a)). Specifically, a 2 h exposure to 20 nm AgNPs was found to reduce SR-B1 receptor expression more so than other NPs evaluated. This decrease in SR-B1 receptor expression (Figure 8(a)) likely contributes to the decrease in subsequent cholesterol uptake as observed in Figure 6(a). Fe₃O₄ NPs were also found to reduce SR-B1 expression but, however, were not found to alter cholesterol uptake compared to control. It is likely that 20 nm AgNPs more readily interact with SR-B1 and have a higher affinity for the receptor due to their more negative charge. This higher affinity may not only reduce receptor expression but may also antagonize subsequent cholesterol binding with the receptor. Previous research has demonstrated that amphiphilic as well as 20 nm ZnO and 20 nm TiO₂ NPs can reduce the expression of Class A scavenger receptors on cell surfaces [33, 34]. Further, amphiphilic NPs were also determined to competitively inhibit binding of oxidized low-density lipoprotein through NP-receptor interactions [33]. Our findings support these studies and demonstrate that NPs can also modulate surface expression of Class B scavenger receptors.

In addition to interactions with lipoproteins and negatively charged molecules/particles scavenger receptors are

also known to interact and facilitate the removal of pathogens. Specifically, SR-B1^{-/-} mice infected with *Mycobacterium tuberculosis* demonstrated significant reductions in TNF α , IFN γ , and IL-10 as compared to wild-type mice [35]. This NP-induced reduction in SR-B1 expression seen in our current study may inhibit the immune response to subsequent microbial exposures due to decreased macrophage cell surface expression of SR-B1. Cell surface expression of SR-B1 was also evaluated following a 24 h exposure to NPs in either serum-free media or serum-free media with cholesterol (20 µg/mL) (Figure 8(b)). All NPs were found to reduce cell surface receptor expression of SR-B1 as compared to controls following the 24 h exposure (Figure 8(b)). This demonstrates that prolonged exposure to NPs may reduce SR-B1 expression on the surface of macrophages and alter subsequent immune responses mediated via macrophages as well as normal macrophage function. This reduction may also limit the macrophage's ability to clear successive exposure to other foreign particles or pathogens that are normally cleared via SR-B1. Previous research has demonstrated that exposure to Fe₃O₄ NPs for 24 h, at a concentration that did not cause cytotoxicity or an inflammatory response, reduced the phagocytic activity of macrophages following treatment with *Streptococcus pneumoniae* [36]. Further macrophages exposed to Fe₃O₄ NPs were found to have suppressed induction of the IL-10 pathway, enhanced TNF- α production, and an inhibition of the transition from an M1- to M2-like activation state in response to *Streptococcus pneumoniae* treatment. This reduced response to *Streptococcus pneumoniae*

was hypothesized to be due to Fe₃O₄ NP-induced alterations in scavenger receptor expression. In the presence of cholesterol 20 nm AgNPs increased cell surface expression of SR-BI (Figure 8(b)). This increased expression of SR-BI suggests that individuals with high cholesterol may respond differently to NP exposures. Further this increased expression of SR-BI may also result in exacerbated inflammatory responses to secondary exposures. The presence of cholesterol however inhibited the reduction of SR-BI expression observed when macrophages were exposed to NPs alone (Figure 8(b)). Taken together the cholesterol-rich environment alters the macrophage response to NPs in terms of phenotypic expression of SR-BI.

4. Conclusions

Overall this study demonstrates that macrophage function, as assessed by alterations in cholesterol uptake, is modified following NP exposures. Further, our research demonstrates that these modifications in macrophage function are not uniform and likely are dictated by various NP characteristics. For example, exposure to 20 nm AgNPs resulted in decreased macrophage uptake of cholesterol compared to 20 nm Fe₃O₄ NPs, which did not alter macrophage function in a cholesterol-rich environment. This finding demonstrates that modulation of macrophage function is not solely driven by NP size. Although NP exposure may not result in overt cytotoxicity, NPs may cause modifications in the normal function of key cell types such as macrophages. These modifications in function may influence disease progression, biodistribution of nanomedicines, and cellular responses to subsequent exposures.

Disclaimer

Any opinions, findings, conclusions, or recommendations expressed herein are those of the authors and do not necessarily reflect the views of the National Institute of Environmental Health Sciences/NIH.

Conflict of Interests

The authors declare that there is no conflict of interests regarding the publication of this paper.

Acknowledgment

This paper was supported by NIEHS Grants R01 ES019311, U19 ES019525, and K99 ES024392.

References

- [1] J.-J. Lin, W.-C. Lin, R.-X. Dong, and S.-H. Hsu, "The cellular responses and antibacterial activities of silver nanoparticles stabilized by different polymers," *Nanotechnology*, vol. 23, no. 6, Article ID 065102, 2012.
- [2] F. Martínez-Gutiérrez, J. M. Guajardo-Pacheco, M. E. Noriega-Trevino et al., "Antimicrobial activity, cytotoxicity and inflammatory response of novel plastics embedded with silver nanoparticles," *Future Microbiology*, vol. 8, no. 3, pp. 403–411, 2013.
- [3] M. Ahamed, M. S. AlSalhi, and M. K. J. Siddiqui, "Silver nanoparticle applications and human health," *Clinica Chimica Acta*, vol. 411, no. 23–24, pp. 1841–1848, 2010.
- [4] T. M. Tolaymat, A. M. El Badawy, A. Genaidy, K. G. Scheckel, T. P. Luxton, and M. Suidan, "An evidence-based environmental perspective of manufactured silver nanoparticle in syntheses and applications: a systematic review and critical appraisal of peer-reviewed scientific papers," *Science of the Total Environment*, vol. 408, no. 5, pp. 999–1006, 2010.
- [5] H. Amiri, L. Bordonali, A. Lascialfari et al., "Protein corona affects the relaxivity and MRI contrast efficiency of magnetic nanoparticles," *Nanoscale*, vol. 5, no. 18, pp. 8656–8665, 2013.
- [6] H.-Y. Huang, S.-H. Hu, S.-Y. Hung et al., "SPIO nanoparticle-stabilized PAA-F127 thermosensitive nanobubbles with MR/US dual-modality imaging and HIFU-triggered drug release for magnetically guided in vivo tumor therapy," *Journal of Controlled Release*, vol. 172, no. 1, pp. 118–127, 2013.
- [7] A. K. Gupta and M. Gupta, "Synthesis and surface engineering of iron oxide nanoparticles for biomedical applications," *Biomaterials*, vol. 26, no. 18, pp. 3995–4021, 2005.
- [8] R. Foldbjerg, D. A. Dang, and H. Autrup, "Cytotoxicity and genotoxicity of silver nanoparticles in the human lung cancer cell line, A549," *Archives of Toxicology*, vol. 85, no. 7, pp. 743–750, 2011.
- [9] S. Grosse, L. Evje, and T. Syversen, "Silver nanoparticle-induced cytotoxicity in rat brain endothelial cell culture," *Toxicology in Vitro*, vol. 27, no. 1, pp. 305–313, 2013.
- [10] S. Lanone, F. Rogerieux, J. Geys et al., "Comparative toxicity of 24 manufactured nanoparticles in human alveolar epithelial and macrophage cell lines," *Particle and Fibre Toxicology*, vol. 6, article 14, 2009.
- [11] S. Park, Y. K. Lee, M. Jung et al., "Cellular toxicity of various inhalable metal nanoparticles on human alveolar epithelial cells," *Inhalation Toxicology*, vol. 19, supplement 1, pp. 59–65, 2007.
- [12] J. H. Shannahan, R. Podila, A. A. Aldossari et al., "Formation of a protein corona on silver nanoparticles mediates cellular toxicity via scavenger receptors," *Toxicological Sciences*, vol. 143, no. 1, pp. 136–146, 2014.
- [13] Z. Magdolenova, M. Drlickova, K. Henjum et al., "Coating-dependent induction of cytotoxicity and genotoxicity of iron oxide nanoparticles," *Nanotoxicology*, vol. 9, no. 1, pp. 44–56, 2015.
- [14] M. Watanabe, M. Yoneda, A. Morohashi et al., "Effects of Fe₃O₄ magnetic nanoparticles on A549 cells," *International Journal of Molecular Sciences*, vol. 14, no. 8, pp. 15546–15560, 2013.
- [15] M. S. Hazari, J. Griggs, D. W. Winsett et al., "A single exposure to acrolein desensitizes baroreflex responsiveness and increases cardiac arrhythmias in normotensive and hypertensive rats," *Cardiovascular Toxicology*, vol. 14, no. 1, pp. 52–63, 2014.
- [16] L. Sun, C. Liu, X. Xu et al., "Ambient fine particulate matter and ozone exposures induce inflammation in epicardial and perirenal adipose tissues in rats fed a high fructose diet," *Particle and Fibre Toxicology*, vol. 10, no. 1, article 43, 2013.
- [17] U. P. Kodavanti, M. C. Schladweiler, A. D. Ledbetter et al., "The spontaneously hypertensive rat as a model of human cardiovascular disease: evidence of exacerbated cardiopulmonary injury and oxidative stress from inhaled emission particulate matter," *Toxicology and Applied Pharmacology*, vol. 164, no. 3, pp. 250–263, 2000.

- [18] J. H. Shannahan, W. Bai, and J. M. Brown, "Implications of scavenger receptors in the safe development of nanotherapeutics," *Receptors & Clinical Investigation*, vol. 2, no. 3, article e811, 2015.
- [19] H. Wang, L. Wu, and B. M. Reinhard, "Scavenger receptor mediated endocytosis of silver nanoparticles into J774A.1 macrophages is heterogeneous," *ACS Nano*, vol. 6, no. 8, pp. 7122–7132, 2012.
- [20] A. Rigotti, H. E. Miettinen, and M. Krieger, "The role of the high-density lipoprotein receptor SR-BI in the lipid metabolism of endocrine and other tissues," *Endocrine Reviews*, vol. 24, no. 3, pp. 357–387, 2003.
- [21] J. Kzhyshkowska, C. Neyen, and S. Gordon, "Role of macrophage scavenger receptors in atherosclerosis," *Immunobiology*, vol. 217, no. 5, pp. 492–502, 2012.
- [22] A. A. Aldossari, J. H. Shannahan, R. Podila, and J. M. Brown, "Influence of physicochemical properties of silver nanoparticles on mast cell activation and degranulation," *Toxicology in Vitro*, vol. 29, no. 1, pp. 195–203, 2015.
- [23] A. Rigotti, B. L. Trigatti, M. Penman, H. Rayburn, J. Herz, and M. Krieger, "A targeted mutation in the murine gene encoding the high density lipoprotein (HDL) receptor scavenger receptor class B type I reveals its key role in HDL metabolism," *Proceedings of the National Academy of Sciences of the United States of America*, vol. 94, no. 23, pp. 12610–12615, 1997.
- [24] R. P. Singh and P. Ramarao, "Cellular uptake, intracellular trafficking and cytotoxicity of silver nanoparticles," *Toxicology Letters*, vol. 213, no. 2, pp. 249–259, 2012.
- [25] T. Xia, R. F. Hamilton Jr., J. C. Bonner et al., "Interlaboratory evaluation of in vitro cytotoxicity and inflammatory responses to engineered nanomaterials: the NIEHS Nano go consortium," *Environmental Health Perspectives*, vol. 121, no. 6, pp. 683–690, 2013.
- [26] N. A. Monteiro-Riviere, M. E. Samberg, S. J. Oldenburg, and J. E. Riviere, "Protein binding modulates the cellular uptake of silver nanoparticles into human cells: implications for in vitro to in vivo extrapolations?" *Toxicology Letters*, vol. 220, no. 3, pp. 286–293, 2013.
- [27] J. H. Shannahan, X. Lai, P. C. Ke, R. Podila, J. M. Brown, and F. A. Witzmann, "Silver nanoparticle protein corona composition in cell culture media," *PLoS ONE*, vol. 8, no. 9, Article ID e74001, 2013.
- [28] C. D. Walkey and W. C. W. Chan, "Understanding and controlling the interaction of nanomaterials with proteins in a physiological environment," *Chemical Society Reviews*, vol. 41, no. 7, pp. 2780–2799, 2012.
- [29] R. M. Zucker and K. M. Daniel, "Detection of TiO₂ nanoparticles in cells by flow cytometry," *Methods in Molecular Biology*, vol. 906, pp. 497–509, 2012.
- [30] Y. Toduka, T. Toyooka, and Y. Ibuki, "Flow cytometric evaluation of nanoparticles using side-scattered light and reactive oxygen species-mediated fluorescence-correlation with genotoxicity," *Environmental Science and Technology*, vol. 46, no. 14, pp. 7629–7636, 2012.
- [31] D. S. Anderson, E. S. Patchin, R. M. Silva et al., "Influence of particle size on persistence and clearance of aerosolized silver nanoparticles in the rat lung," *Toxicological Sciences*, vol. 144, no. 2, pp. 366–381, 2015.
- [32] G. Valacchi, C. Sticozzi, Y. Lim, and A. Pecorelli, "Scavenger receptor class B type I: a multifunctional receptor," *Annals of the New York Academy of Sciences*, vol. 1229, pp. E1–E7, 2011.
- [33] L. K. Petersen, A. W. York, D. R. Lewis et al., "Amphiphilic nanoparticles repress macrophage atherogenesis: novel core/shell designs for scavenger receptor targeting and down-regulation," *Molecular Pharmaceutics*, vol. 11, no. 8, pp. 2815–2824, 2014.
- [34] Y. Suzuki, S. Tada-Oikawa, G. Ichihara et al., "Zinc oxide nanoparticles induce migration and adhesion of monocytes to endothelial cells and accelerate foam cell formation," *Toxicology and Applied Pharmacology*, vol. 278, no. 1, pp. 16–25, 2014.
- [35] G. Schäfer, R. Guler, G. Murray, F. Brombacher, and G. D. Brown, "The role of scavenger receptor BI in infection with *Mycobacterium tuberculosis* in a murine model," *PLoS ONE*, vol. 4, no. 12, Article ID e8448, 2009.
- [36] V. Kodali, M. H. Littke, S. C. Tilton et al., "Dysregulation of macrophage activation profiles by engineered nanoparticles," *ACS Nano*, vol. 7, no. 8, pp. 6997–7010, 2013.

Research Article

Tetracycline Loaded Collagen/Hydroxyapatite Composite Materials for Biomedical Applications

Laura Cristina Rusu,¹ Ioan Avram Nedelcu,² Mădălina Georgiana Albu,³
Maria Sonmez,³ Georgeta Voicu,² Marius Radulescu,² Denisa Ficai,² Anton Ficai,²
Meda-Lavinia Negrutiu,¹ and Cosmin Sinescu¹

¹Department of Technology of Materials and Devices in Dental Medicine, "Victor Babeş" University of Medicine and Pharmacy Timișoara, Piața Eftimie Murgu, No. 2, 300041 Timișoara, Romania

²Faculty of Applied Chemistry and Material Science, Politehnica University of Bucharest, 1-7 Polizu Street, 011061 Bucharest, Romania

³Collagen Department, Leather and Footwear Research Institute, 93 Ion Minulescu, 031215 Bucharest, Romania

Correspondence should be addressed to Mădălina Georgiana Albu; albu_mada@yahoo.com

Received 19 May 2015; Accepted 28 July 2015

Academic Editor: Akiko Obata

Copyright © 2015 Laura Cristina Rusu et al. This is an open access article distributed under the Creative Commons Attribution License, which permits unrestricted use, distribution, and reproduction in any medium, provided the original work is properly cited.

The paper describes the preparation, characterisation, and testing of tetracycline loaded collagen-carboxymethylcellulose/hydroxyapatite ternary composite materials. The synthesis of this drug delivery system consists in two steps: the first step is the mineralization of collagen-carboxymethylcellulose gel while the second step corresponds to the loading of the ternary composite material with tetracycline. The obtained DDS is characterised by physicochemical, morphological, and release behaviour by using FTIR spectroscopy and microscopy, scanning electron microscopy, and UV-VIS spectroscopy. Based on the release study, it can be assumed that tetracycline is released in a prolonged way, assuring at least 6 days of antiseptic properties.

1. Introduction

Collagen (COLL) and hydroxyapatite (HA) are the main components of the bone [1]. This is why many materials designed for bone grafting and repair are based on collagen, hydroxyapatite, or composite materials containing the aforementioned components. The performances of these synthesized materials are strongly dependent on the composition and processing induced morphology [1–4].

Due to the compositional similitude with the bone, collagen/hydroxyapatite (COLL/HA) composite materials seem to be the most suitable material for bone engineering. Unfortunately, the lower properties of these materials comparing with natural bones made it necessary to improve the composition of these materials by adding third components [5] or to change the processing route in order to obtain certain morphology [2, 6, 7].

The collagen-carboxymethylcellulose/hydroxyapatite (COLL-CMC/HA) was previously obtained in our group and seems to be proper material for bone grafting and repair [5]. The three components seem to be highly compatible, the FTIR maps obtained at wavelength corresponding to CMC (carboxymethylcellulose) (715 cm^{-1}), COLL (1655 cm^{-1}), and HA (1033 cm^{-1}) revealing a very homogeneous material. COLL-CMC/HA composite material containing both fibres (CMC) and particles (HA) as reinforcing agent is a true hybrid material, expecting superior mechanical properties compared to COLL/HA composite materials.

One of the most important shortcomings of the surgical intervention is related to the possibility of infections. This is why, in many surgical interventions, systemic administration of antibiotic is prescribed in both pre- and postoperative steps [8–10]. Unfortunately, systemic administration of antibiotics

also involves systemic toxicity and high incidence of antibiotic resistance [11, 12]. To counter the increasing antibiotic resistance there are two solutions meaning to produce new and new antibiotics or, much better, to use antibiotics in a rational way in order to avoid the development of antibiotic resistance. The most important ways to avoid antibiotic resistance development are to avoid the irrational use of antibiotics, to avoid the excessive use of antibiotics, to use local instead of systemic therapies, the rational choice of the used antibiotic, and so forth [13–17]. Tetracycline, being a broad-spectrum antibiotic indicated against many bacterial infections, was chosen to be used in our study.

The aim of this work is to reduce the amount of antibiotics (tetracycline) by a more rational way of use. For this purpose, tetracycline is embedded in the COLL-CMC/HA composite material, the final tetracycline loaded composite materials being able to assure the osteoregeneration and to assure the anti-infective properties without the need of systemic administration of antibiotic. The locoregional delivery of tetracycline is very important because the overall systemic side effects are limited or even removed.

2. Materials and Methods

2.1. Materials and Reagents. Type I fibrillar collagen gel with a molecular weight of about 300.000 Da and acidic pH (2.6) was obtained in the Collagen Department of National Research & Development Institute for Textiles and Leather as we previously described [18] and purified by dialysis, against water free of endotoxins.

Carboxymethylcellulose sodium salt (low viscosity) and tetracycline hydrochloride (BioReagent, suitable for cell culture) were purchased from Sigma-Aldrich (Saint Louis, USA) and were used without any further purification.

Hydroxyapatite was obtained in situ, in the presence of the carboxymethylcellulose-collagen gel. The precursors used for HA synthesis were calcium hydroxide (puriss. p.a.) and sodium phosphate monobasic monohydrate (ACS reagent), both purchased from Sigma-Aldrich (Steinheim, Germany).

2.2. Synthesis of COLL/HA-Tetracycline Composite Material. COLL/HA-tetracycline was obtained as schematically presented in Figure 1.

The first step is devoted to the preparation of the support material, the second step to the loading with tetracycline, and the last step to the drying. The support preparation consists in homogenisation of the collagen gel and carboxymethylcellulose (COLL:CMC weight ratio is 2:1) followed by mineralization with $\text{Ca}(\text{OH})_2$ and $\text{NaH}_2\text{PO}_4 \cdot \text{H}_2\text{O}$ as previously presented [5, 7, 19], cross-linked with glutaraldehyde 1% (reported to the dry collagen), and finally washing with distilled water (three times, each washing step taking 30 min) to remove the soluble salts. The mineralization was performed in order to obtain COLL:CMC:HA composite support material with a mass ratio of 2:1:8. The loading with tetracycline was done by absorbing the corresponding amount of tetracycline hydrochloride (0.5 g tetracycline/10 g composite) as aqueous solution. The drying can be done by

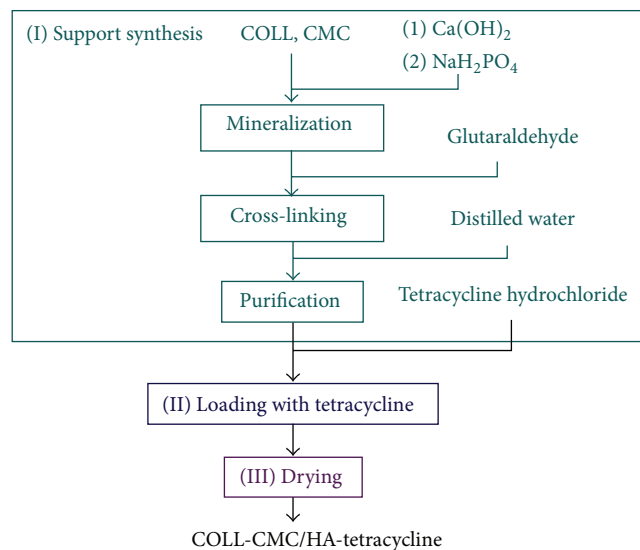


FIGURE 1: Schematic representation of preparation of COLL-CMC/HA-tetracycline.

controlled air drying or by freeze-drying, depending on the desired properties, as previously described by Andronescu et al. [1].

2.3. Characterisation and Testing. After synthesis and freeze-drying, the composite material was analyzed by using Fourier Transform–Infrared (FTIR) spectroscopy and microscopy and scanning electron microscopy (SEM). The release of tetracycline was monitored by using UV-VIS spectroscopy.

IR microscopy/spectroscopy was performed by using a Thermo FTIR Nicolet iN10 MX microscope; the spectra were recorded in ATR mode over the wave number range of $675\text{--}4000\text{ cm}^{-1}$, with a resolution of 4 cm^{-1} . For a better identification of the peaks, the obtained spectra were resolved using a Gaussian-Lorentzian peak resolve procedure, with no baseline (previously for all the spectra baseline correction was done). For IR microscopy, the data were recorded using an imaging detector (MCT array detector) in reflection mode over the $715\text{--}4000\text{ cm}^{-1}$ range, the collection time being 3 s.

SEM analyses were performed on a HITACHI S2600N electron microscope with EDAX, on samples covered with silver layer.

The drug released was evaluated by ultraviolet-visible spectrophotometry based on the peak from 270 nm using a Thermo Evolution 300 spectrophotometer, in quartz cuvettes of 10 mm with a scan speed of 240 nm/min and data interval of 1 nm while the bandwidth was set at 1 nm. For this purpose, 1 g of sample was immersed in 500 mL phosphate buffer, 0.1 M (7.4 pH), maintained at 37°C . At fixed time intervals, sample of 5 mL was extracted and replaced with the same volume of fresh, preheated acceptor phase. All samples were measured in triplicate.

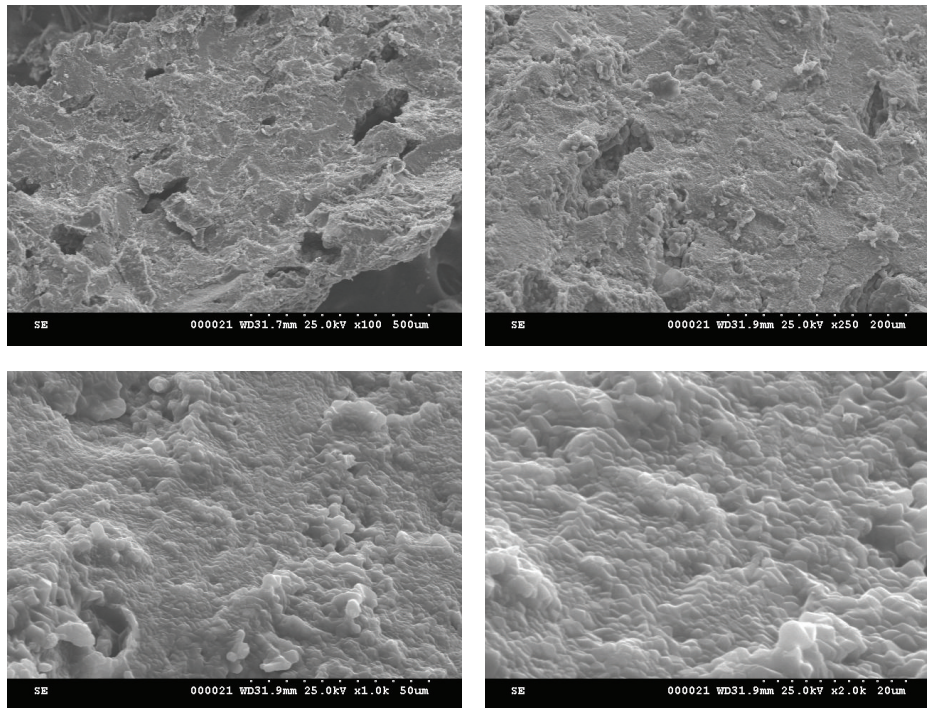


FIGURE 2: Representative SEM images of COLL-CMC/HA-tetracycline.

3. Results and Discussion

Scanning electron microscopy is a useful tool for characterizing materials, the morphology of the materials being essential both for bone grafts and for drug delivery systems. At low magnification (Figure 2 (right-down side)), spherical and ovaloidal pores can be identified, their size being optimal for bone cell colonization (20–150 μm) [20–23].

At higher magnification, micronic and submicronic structures can be identified which, based on our previous study, can be the ends of CMC microfibrils [24].

Figure 3 presents the experimental spectra of COLL/HA, COLL-CMC/HA, COLL-CMC/HA-tetracycline, tetracycline hydrochloride, and carboxymethyl cellulose.

FTIR spectrum of the COLL-CMC/HA-tetracycline sample exhibits the main absorption bands of collagen, carboxymethyl cellulose, and hydroxyapatite as well as the bands of tetracycline. The intensities of these bands are strongly influenced by composition and molar absorptivity of each characteristic vibration. The low content of tetracycline (5% tetracycline) as well as the moderate intensity of its characteristic peaks makes it difficult to clearly identify these peaks. For this reason the deconvolution of the spectrum over the 1200–1800 cm^{-1} spectral range is necessary. In this range, the deconvolution procedure permits the identification of over 30 absorption bands, some of them being assigned to the main bands of tetracycline (1235, 1283, 1384, 1406, 1468, 1515, 1551, 1585, 1616, 1645, and 1660 cm^{-1}). It is also worth mentioning that the relative intensity of these bands is similar to that from tetracycline and consequently proves the presence of the drug. Carboxymethyl cellulose can be also identified both in

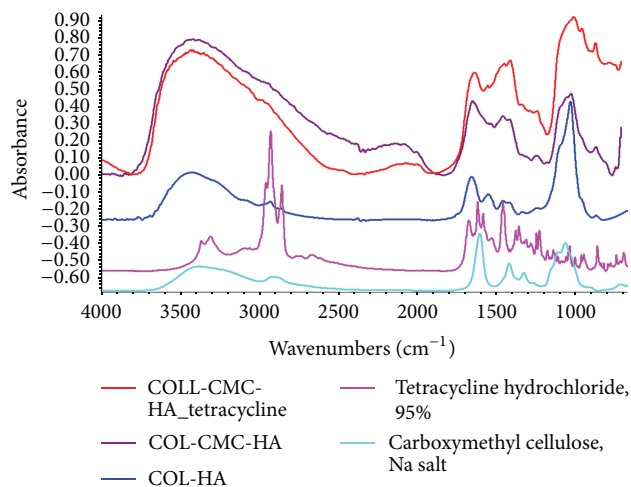


FIGURE 3: FTIR spectra of tetracycline, COLL/HA, and COLL/HA-tetracycline.

support material (COLL-CMC/HA) and in the antimicrobial DDS (COLL-CMC/HA-tetracycline). Based on the three experimental spectra, differences can be observed once the number of components increases. For instance, the spectrum of the ternary COLL-CMC/HA composite material differs comparing with the COLL/HA, especially in the region of the absorption bands of CMC (1200–1600 cm^{-1}).

The ternary composite material was also analyzed by FTIR microscopy. The maps were obtained based on the three main independent absorption bands of collagen (1650 cm^{-1}),

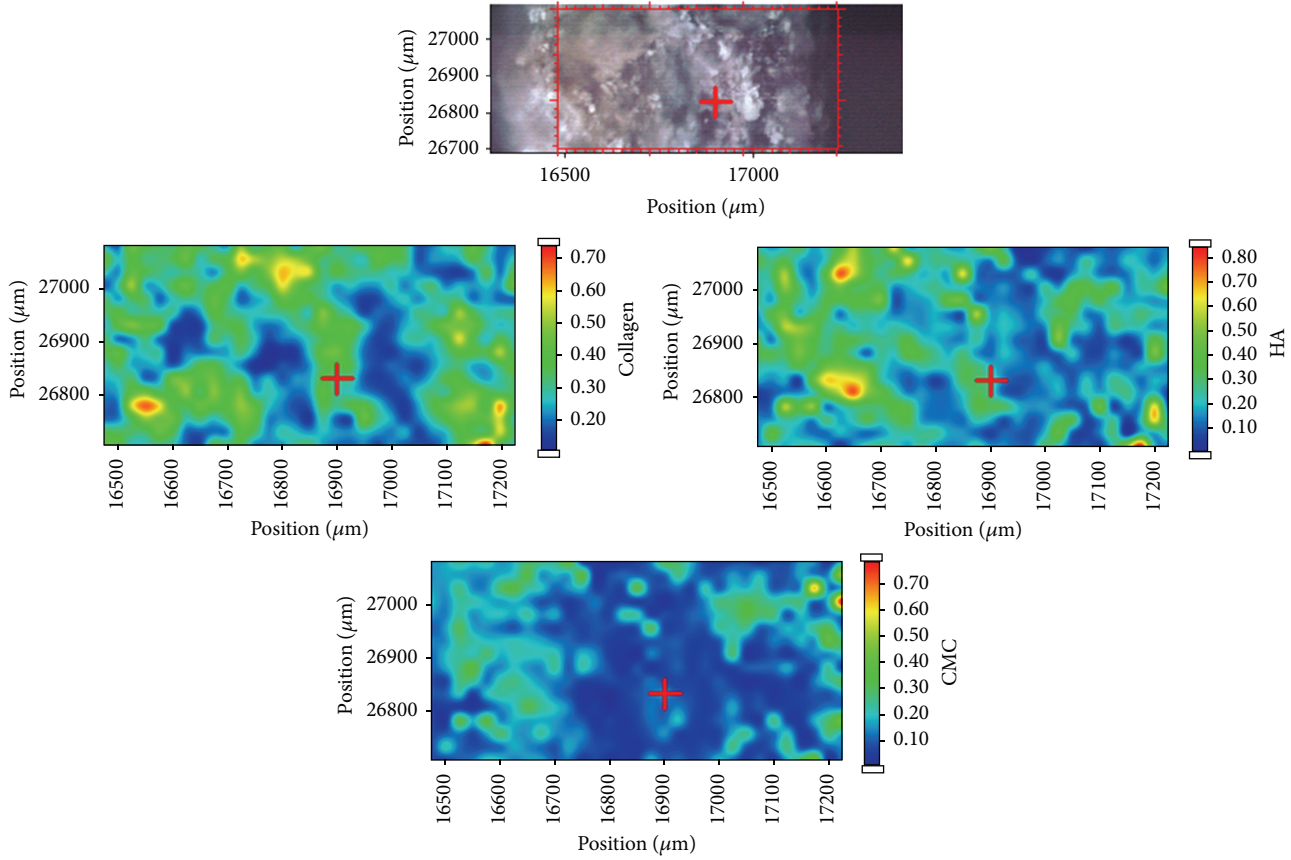


FIGURE 4: FTIR microscopy recorded on COLL-Cell/HA-tetracycline.

hydroxyapatite (1022 cm^{-1}), and cellulose (715 cm^{-1}). The three maps are presented in Figure 4.

The FTIR maps, colored from blue (low intensity) to red (high intensity), reveal the distribution and relative intensity of the monitored bands (components). Based on the correlation with the video image, as well as the relative intensities of the three monitored bands, it can be seen that collagen and hydroxyapatite are intimately associated but also carboxymethylcellulose microfibers are well dispersed into the COLL/HA hybrid composite material, the blue/red distribution being especially a result of the hill/valley topology of the analyzed section.

The release process was monitored by recording the UV-VIS spectra of the solutions at different times (Figure 5).

It can be seen that the COLL/HA samples are stable in time, the spectra recorded after three days being identical to that recorded after some minutes of immersion which means that only soluble salts are delivered into the solution. The delivery of tetracycline depends on time. The tetracycline spectra recorded after 1, 3, and 6 days clearly show that the absorbance of both peaks increases. Based on this we can affirm that these systems exhibit prolonged delivery and could be proper candidates as bone grafts for infected bone defects. For quantification, a calibration curve was plotted between $0.1\text{ }\mu\text{g/mL}$ and $10\text{ }\mu\text{L}$, the linearity being better than $R^2 = 99.98$. Based on the calibration curve, the correlation

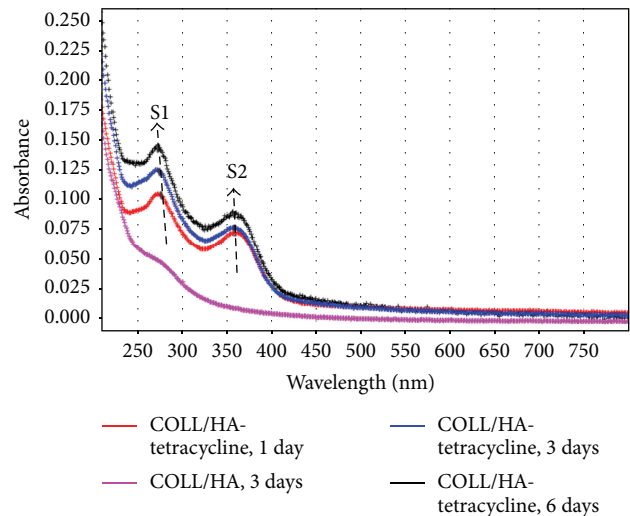


FIGURE 5: UV-VIS spectra of the solution recorded during the delivery process.

between absorbance and concentration is given by the equation $A = 0.0896 \cdot c + 0.0031$. Comparing with the theoretical concentration, after 6 days, the recovered tetracycline was 79.8% which is good enough to assure antimicrobial activity during the healing of the wound. In the case of infections,

over 6 days of delivery could be enough to treat the infections, and, if not, supplementary antibiotic can be administered in classical way.

4. Conclusions

New antimicrobial bone grafts with prolonged delivery of tetracycline were obtained by coprecipitation of hydroxyapatite in the presence of the carboxymethylcellulose-collagen gel followed by loading with tetracycline. This material was designed to be used only for infected bone defects. This locoregional delivery of tetracycline is essential to reduce the systemic side effects associated with the use of antibiotics. These materials can be considered with prolonged delivery because even after 6 days the recovery of tetracycline is lower than 80%. This result is consistent with the clinical protocols of treating infections but reduces the amount of tetracycline and reduces the systemic side effects.

Conflict of Interests

The authors declare no conflict of interests.

Acknowledgments

This work was supported by Romanian National Authority for Scientific Research, MPNS COST Action MPI301: New Generation Biomimetic and Customized Implants for Bone Engineering and Project no. PIII-C2-PCFI (2015-2016), DENTALOCT.

References

- [1] E. Andronescu, A. Fikai, M. G. Albu et al., "Collagen-hydroxyapatite/cisplatin drug delivery systems for locoregional treatment of bone cancer," *Technology in Cancer Research and Treatment*, vol. 12, no. 4, pp. 275–284, 2013.
- [2] A. Fikai, E. Andronescu, D. Fikai, M. Sonmez, M. G. Albu, and G. Voicu, "Mimicking the morphology of long bone," *Central European Journal of Chemistry*, vol. 10, no. 6, pp. 1949–1953, 2012.
- [3] S. V. Dorozhkin, "Calcium orthophosphate-based bioceramics," *Materials*, vol. 6, no. 9, pp. 3840–3942, 2013.
- [4] P. Fratzl and R. Weinkamer, "Nature's hierarchical materials," *Progress in Materials Science*, vol. 52, no. 8, pp. 1263–1334, 2007.
- [5] I.-A. Nedelcu, A. Fikai, D. Fikai, G. Voicu, M. G. Albu, and E. Andronescu, "Hybrid COLL-CMC/HA composite materials for bone tissue regeneration," *University Politehnica of Bucharest Scientific Bulletin Series B*, vol. 77, no. 1, pp. 3–14, 2014.
- [6] A. Fikai, M. G. Albu, M. Sonmez, D. Fikai, and E. Andronescu, "Synthesis of collagen/hydroxyapatite composite materials with oriented microstructure induced by the interaction of the flowing mineralised collagen gel with the support," *ChemXpress*, vol. 3, pp. 107–110, 2014.
- [7] A. Fikai, E. Andronescu, G. Voicu et al., "Self-assembled collagen/hydroxyapatite composite materials," *Chemical Engineering Journal*, vol. 160, no. 2, pp. 794–800, 2010.
- [8] M. Solignac, "New perspectives in antibiotic prophylaxis," *Presse Medicale*, vol. 27, no. 3, pp. 27–29, 1998.
- [9] D. Lebeaux, N. Fernández-Hidalgo, A. Chauhan et al., "Management of infections related to totally implantable venous-access ports: challenges and perspectives," *The Lancet Infectious Diseases*, vol. 14, no. 2, pp. 146–159, 2014.
- [10] A. Lipp and G. Lusardi, "Systemic antimicrobial prophylaxis for percutaneous endoscopic gastrostomy," *The Cochrane Database of Systematic Reviews*, no. 11, Article ID CD005571, 2013.
- [11] M. Zilberman and J. J. Elsner, "Antibiotic-eluting medical devices for various applications," *Journal of Controlled Release*, vol. 130, no. 3, pp. 202–215, 2008.
- [12] T. Y. Wu, Q. C. Zhang, W. P. Ren et al., "Controlled release of gentamicin from gelatin/genipin reinforced beta-tricalcium phosphate scaffold for the treatment of osteomyelitis," *Journal of Materials Chemistry B*, vol. 1, no. 26, pp. 3304–3313, 2013.
- [13] L. Zhang, Y. Huang, Y. Zhou, T. Buckley, and H. H. Wang, "Antibiotic administration routes significantly influence the levels of antibiotic resistance in gut microbiota," *Antimicrobial Agents and Chemotherapy*, vol. 57, no. 8, pp. 3659–3666, 2013.
- [14] C. García-Rey, J. E. Martín-Herrero, and F. Baquero, "Antibiotic consumption and generation of resistance in *Streptococcus pneumoniae*: the paradoxical impact of quinolones in a complex selective landscape," *Clinical Microbiology and Infection*, vol. 12, no. 3, pp. 55–66, 2006.
- [15] A. Rodríguez-Rojas, J. Rodríguez-Beltrán, A. Couce, and J. Blázquez, "Antibiotics and antibiotic resistance: a bitter fight against evolution," *International Journal of Medical Microbiology*, vol. 303, no. 6–7, pp. 293–297, 2013.
- [16] A. Dashti, D. Ready, V. Salih et al., "In vitro antibacterial efficacy of tetracycline hydrochloride adsorbed onto Bio-Oss bone graft," *Journal of Biomedical Materials Research Part B: Applied Biomaterials*, vol. 93, no. 2, pp. 394–400, 2010.
- [17] S. Praveen and M. Rohaizak, "Local antibiotics are equivalent to intravenous antibiotics in the prevention of superficial wound infection in inguinal hernioplasty," *Asian Journal of Surgery*, vol. 32, no. 1, pp. 59–63, 2009.
- [18] M. G. Albu, *Collagen Gels and Matrices for Biomedical Applications*, Lambert Academic Publishing, Saarbrücken, Germany, 2011.
- [19] E. Andronescu, M. Fikai, G. Voicu, D. Fikai, M. Maganu, and A. Fikai, "Synthesis and characterization of collagen/hydroxyapatite: magnetite composite material for bone cancer treatment," *Journal of Materials Science: Materials in Medicine*, vol. 21, no. 7, pp. 2237–2242, 2010.
- [20] A. Fikai, E. Andronescu, G. Voicu, and D. Fikai, "Advances in collagen/hydroxyapatite composite materials," in *Advances in Composite Materials for Medicine and Nanotechnology*, B. Attaf, Ed., chapter 1, InTech, Rijeka, Croatia, 2011.
- [21] B.-S. Chang, C.-K. Lee, K.-S. Hong et al., "Osteoconduction at porous hydroxyapatite with various pore configurations," *Biomaterials*, vol. 21, no. 12, pp. 1291–1298, 2000.
- [22] H. Develioglu, E. Koptagel, R. Gedik, and L. Dupoirieux, "The effect of a biphasic ceramic on calvarial bone regeneration in rats," *Journal of Oral Implantology*, vol. 31, no. 6, pp. 309–312, 2005.
- [23] O. Gauthier, J.-M. Bouler, E. Aguado, P. Pilet, and G. Daculsi, "Macroporous biphasic calcium phosphate ceramics: influence of macropore diameter and macroporosity percentage on bone ingrowth," *Biomaterials*, vol. 19, no. 1–3, pp. 133–139, 1998.
- [24] D. E. Fetterolf and R. J. Snyder, "Scientific and clinical support for the use of dehydrated amniotic membrane in wound management," *Wounds*, vol. 24, no. 10, pp. 299–307, 2012.

Review Article

A Review on the Synthesis Methods of CdSeS-Based Nanostructures

Hong Li,^{1,2} Chengbiao Wang,¹ Zhijian Peng,¹ and Xiuli Fu²

¹School of Engineering and Technology, China University of Geosciences, Beijing 100083, China

²State Key Laboratory of Information Photonics and Optical Communications and School of Science, Beijing University of Posts and Telecommunications, Beijing 100876, China

Correspondence should be addressed to Zhijian Peng; pengzhijian@cugb.edu.cn and Xiuli Fu; xiulifu@bupt.edu.cn

Received 10 June 2015; Accepted 7 September 2015

Academic Editor: Simeon Agathopoulos

Copyright © 2015 Hong Li et al. This is an open access article distributed under the Creative Commons Attribution License, which permits unrestricted use, distribution, and reproduction in any medium, provided the original work is properly cited.

As typical II–VI ternary alloyed chalcogenides, CdSeS nanostructures have attracted intensive worldwide attention due to their excellent tunable optical properties based on quantum confinement effect and optical nonlinear phenomenon. Because CdSeS-based nanostructures have presented a great potential for applications in biomedicine and optoelectronic devices, different synthesis methods have been proposed to prepare CdSeS-based nanostructures with divergent optical properties to meet the needs of those applications, such as fluorescent labeling, *in vivo* imaging, waveguides, and solar cell. In this review, the tricks, advantages, and disadvantages of all these synthesis methods were discussed, including hot-injection synthesis, one-pot noninjection synthesis, microwave irradiation, solvothermal synthesis, template-assisted electrodeposition, thermal evaporation, and pulsed laser deposition. Special emphasis was put on those methods that are safe, economic, environment-friendly, and suitable for large-scale production of alloyed CdSeS nanostructures with high photoluminescence, high stability, and low/no cytotoxicity.

1. Introduction

II–VI compound semiconductor nanostructures have attracted great attention due to their attractive optical and electrical properties [1, 2], presenting new developing direction for fundamental and application-oriented researches [3–6]. As a class of typical ternary II–VI semiconductive compounds, CdSeS alloyed nanostructures [7–13] have been intensively studied because of their fascinating and tunable optical and electrical properties [8, 14] based on quantum confinement effect, such as their tunable band-gaps which can be varied from visible (~2.42 eV for CdS) to near IR (~1.73 eV for CdSe) [14]. And their excellent optical properties such as large nonlinear susceptibilities, fast response times, and good photoconduction [15, 16] provide them with a wide range of potential applications in biomedicine [17–19] and optoelectronic devices [20–25]. In particular, those alloyed CdSeS nanostructures with high quantum efficiency, narrow spectral emission, wide band-gap energy, and easy color tunability are very good candidates for the next-generation optoelectronic and biomedical applications

[19, 26, 27], such as solar cell, fluorescent labeling, *in vivo* imaging, biosensors, and drug delivery. Consequently, the preparation of CdSeS nanostructures with excellent quality to satisfy the requirements of future applications is becoming more and more essential.

In the recent decades, many different synthesis methods for CdSeS nanostructures were proposed. They all have their own features and the resultant CdSeS nanostructures also have different morphologies and properties. To obtain CdSeS nanostructures with special properties suitable for specific application, the understanding of their synthesis methods is necessary, which is also conducive to develop some new ways to realize the controllable growth of CdSeS nanostructures. Thus in this paper, the existing synthesis methods of CdSeS nanostructures, including hot-injection synthesis, one-pot noninjection synthesis, microwave irradiation, solvothermal synthesis, template-assisted electrodeposition, thermal evaporation, and pulsed laser deposition, are reviewed. The advantages and disadvantages of these synthesis methods were discussed in detail. Special emphasis was put on those methods that are safe, economic, environment-friendly, and

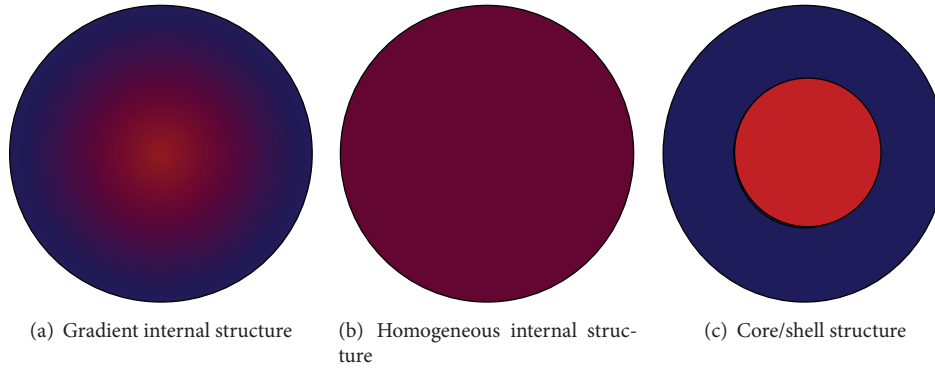


FIGURE 1: A schematic representation of three typical CdSeS quantum dots.

suitable for large-scale production of alloyed CdSeS nanostructures with high photoluminescence, high stability, and low/no cytotoxicity.

2. The Development History of CdSeS-Based Nanostructures

To date, there are many kinds of CdSeS-based nanostructures prepared by different synthesis methods, including nanostructures in zero-dimensional (0D, quantum dots, QDs, or nanocrystals), one-dimensional (1D, nanowires, whiskers, nanorods, nanoribbons, or nanobelts), and two-dimensional (2D, nanofilms or nanosheets) and CdSeS-based nanocomposite structures. These different forms of CdSeS nanostructures all have their own special properties and applications.

2.1. Zero-Dimensional CdSeS Nanostructures. Zero-dimensional CdSeS nanostructures have the advantages of not only high luminescent efficiency, color monochromaticity, and facile band-gap tunability in visible light region for making light-emitting diodes (LEDs) [28] to replace the conventional inorganic- or organic-based LEDs and applying to QDs-sensitized solar cells [16], but also high brightness, broad absorption and sharp emission spectra, tunable emission maxima, and longer fluorescence lifetime to be used for fluorescent labeling [29], *in vivo* imaging [30, 31], photovoltaics [32], and other applications [33, 34]. For CdSeS QDs or nanocrystals, band-gap engineering can be achieved via the control of their sizes, constituent stoichiometries, and internal structures (such as homogeneous versus gradient) [35]. The homogeneous CdSeS QDs have a uniform internal structure; thus the composition is the same everywhere on a single quantum dot, while in gradient CdSeS QDs, alloy compositions are varied radially; namely, the ratio of S and Se changes gradually from the core to surface of the QDs in a gradient internal structure. But unlike traditional core@shell structures, in such gradient internal structure there is no abrupt boundary between the Se-rich core and S-rich shell [36]. The as-described three structures of CdSeS QDs can be shown in Figure 1. The gradient alloy nanocrystals present optical properties that are significantly different from those of the homogeneous alloys [37]. To achieve homogeneous

alloys, the growth rates of the two constituent materials must be equal [12, 37], and the conditions necessary for the growth of one constituent cannot impede the growth of the other [38]. And CdSeS QDs with different internal structures can be prepared through the same synthesis methods by using different selenium and sulphur precursors [36]. Because the band-gap can be tuned by adjusting sizes, constituent stoichiometries, or internal structures, CdSeS QDs or nanocrystals with tunable optical properties would be obtained even in a constant size, which have promising applications in special field. For example, in *in vivo* imaging, very small CdSeS QDs with a certain size, which can achieve a range of fluorescence colors, are desired.

Various CdSeS QDs or nanocrystals were prepared successfully by different synthesis methods. As early as in 2001 [39], Elbaum et al. prepared CdSe_{1-X}S_X (0 < X < 1, the same below) crystals with a size distribution varied between 5 and 10 nm by a precipitation method. However, this method usually leads to crystals with surface properties that can vary considerably. But, for nanocrystalline semiconductors with very large surface-to-volume ratio, their properties are normally very sensitive to surface effects [40]. Then, in 2003 [12], Jang et al. prepared highly luminescent CdSeS QDs via a rapid hot-injection synthesis method, and the resultant CdSeS QDs have quantum efficiency up to 85% and the full width at half maximum (FWHM) of photoluminescence peaks was about 34 nm, which can present tunable luminescence properties from red to blue region. Meanwhile, the authors also claimed that it was hard to judge the structure of their QDs to be either core/shell or gradient. In 2005 [41], Qian et al. presented a seed-mediated approach for rapid synthesis of high quality alloyed QDs (CdSe-CdS) in aqueous phase by microwave irradiation. Although the QDs prepared in aqueous phase have excellent water solubility, stability, and biological compatibility, their quantum yield is usually very low due to the serious traps on their surface. In 2006 [38], Swafford et al. fabricated alloyed CdSe_{1-X}S_X QDs with homogeneous internal structure in all proportions by means of pyrolytic synthesis based on a swift hot-injection method, and they reported that the morphology of the resultant nanocrystals can be altered by changing the reaction conditions, generating structures ranging from homogeneous, spherical nanocrystals to one-dimensional

gradient nanorods. But these QDs also exhibited significant deep-trapping emission, causing decreased quantum yields, and this method is unsuitable for large-scale production and is not ecofriendly because it employed organic compound containing phosphine. In 2009 [35], a noninjection, one-pot approach with excellent synthetic reproducibility was reported to fabricate homogeneously alloyed CdSeS nanocrystals by Ouyang et al. And the resultant CdSeS QDs can be tuned easily to emit photons in the range of 470–550 nm of the electromagnetic spectrum. This method is a green approach with the avoidance of phosphines, but the quantum yield was below 5%, and it is worth noting that 2,2'-dithiobisbenzothiazole was used as nucleation initiator during synthesis and the nucleation initiator was the key to successfully prepare high quality quantum dots [42]. To make the method greener, in 2010 [43], Zou et al. prepared alloyed CdSe_{1-X}S_X QDs with high monodispersity and narrow size distribution by a noninjection method without nucleation initiators. However, the quantum yield was still quite low. In 2013 [44], Ünlü et al. proposed a two-phase thermal approach to prepare CdS_XSe_{1-X} ternary nanocrystals without injection, resulting in highly luminescent CdSe_{1-X}S_X nanocrystals with a high quantum yield of about 90% at low temperature, but, in this approach, the organic compound containing phosphine was also employed. In a word, it is a trend that the synthesis methods of 0D CdSeS nanostructures gradually shift from hot-injection to noninjection based ones. And new facile, green synthesis methods suitable for large-scale production of CdSeS QDs or nanocrystals are expected.

2.2. One-Dimensional CdSeS Nanostructures. One-dimensional CdSeS nanostructures have received considerable attention because of their special properties [45–51], such as dimensionality confined transport phenomena [51] and continuously tunable physical properties through the control of their compositions [48]. Consequently, they have shown great potential as the building blocks for new, nanoscaled electronic, and optoelectronic devices [52–54], for example, waveguides [20], lasers [55, 56], field-effect transistors [13], photosensor [57], photovoltaic cells [58], and photodetectors [59]. To apply the nanostructures in these applications, it is essential to synthesize 1D CdSeS nanostructures with controllable compositions and tunable physical properties. On the other hand, preparing CdSeS nanowires or nanobelts with tunable band-gap is important for investigating the mechanism of free carrier and electron-hole dynamics based photoconductivity and charge transport in 1D CdSeS nanostructures.

To date, 1D CdSeS nanostructures with different morphologies and properties have been fabricated by various synthesis methods. In 1999 [60], Yu et al. successfully prepared CdSe_{1-X}S_X nanowires by a low-temperature solvothermal route, and the morphology of the obtained CdSe_{1-X}S_X nanocrystallites could be well controlled by choosing an appropriate solvent. Through the same method, in 2006 [61], Liu et al. synthesized CdSe_{1-X}S_X nanorods with diameter of 10–20 nm and length up to 100–150 nm. The CdSe_{1-X}S_X nanorods could be obtained at a temperature as low as 120°C and the size distribution of the obtained nanorods would

not change with temperature and composition. Although the reaction temperature is relatively low in solvothermal synthesis, it needs long reaction time (usually more than 10 h) and the products need to be washed for many times by different solutions. In 2005 [62], alloyed ternary CdSe_{1-X}S_X nanowire arrays with continuous tuning of the band-gap through composition modulation were prepared by Liang et al. via an anodic aluminum oxide template-assisted electrodeposition method. But this method is energy-wasting due to the fact that the preparation was carried out under dc deposition conditions. In the same year [8], Pan et al. fabricated sword-like CdSe_{1-X}S_X nanobelts with color-tunable photoluminescence and site-controlled compositions via a simple physical evaporation process with Au catalyst. The nanobelts have a typical length of 20–60 μm and a thickness of 40–80 nm, and the width of the nanobelts is 100 nm to 1 μm at one end and tapers off to approximately 50–100 nm tip at the other end. And, later in 2006 [20], the same group of authors prepared single-crystal ultralong alloyed CdSe_{1-X}S_X whiskers through the similar Au-catalyzed thermal evaporation route. Moreover, in 2005 [63], Kwon et al. reported a pulsed laser deposition with Au catalyst to synthesize CdSe_{1-X}S_X nanowires, and the intensity of the optical luminescence of the obtained nanowires showed a quadratic relationship with their composition. However, in both thermal evaporation and pulsed laser deposition, due to the sensitivity of nanostructure composition to the local substrate temperature during the growth process, the products of different compositions with variable X are typically codeposited on a single substrate, and the composition X changes with the distance of the substrate from the evaporation sources. In other words, the uniformity and selectivity of stoichiometry of the nanostructures cannot be ensured. So, the synthesis methods to obtain ternary CdSe_{1-X}S_X with uniform and controllable compositions are desired. In 2009 [54], Li et al. prepared CdSe_{1-X}S_X nanoribbons via sulfurizing CdSe nanoribbons, and the obtained products presented tunable and sharp near-band-gap emissions and lasing action from 542 to 668 nm. It is the first time that 1D ternary CdSe_{1-X}S_X single-crystal nanoribbon with uniform and controllable compositions was prepared. But a H₂S-Ar atmosphere was used during this sulfurizing process. It is not environment-friendly. In 2011 [13], Lu et al. synthesized CdSe_{1-X}S_X nanobelts with accurately controllable compositions by a thermal evaporation method with a specially designed substrate holder. In recent years, more and more synthesis methods were proposed to prepare different 1D CdSeS nanostructures with excellent tunable optical and photoelectrical properties, and it is essential to develop simple and facile method to synthesize 1D ternary CdSeS nanostructures with uniform composition on large scale.

2.3. Two-Dimensional CdSeS Nanostructures. Compared with abundant literatures on 0D and 1D CdSeS nanostructures, there are only few reports on 2D CdSeS nanostructures. It is short of literatures reported on CdSeS 2D nanostructures (for instance, nanosheets and nanofilms) possibly because it is very difficult to maintain the 2D morphology of the nanostructures while precisely controlling the thickness at

atomic level during the synthesis. But such materials are of great importance for their many applications such as solid-state lighting, high efficient solar cells, discrete multicolor lasers, and multispectral detection [64, 65], owing to their wide tunable band-gaps, low surface activity, and good photoconductive and photoluminescent properties [66–68]. In 2009 [69], Kim et al. reported lateral heterostructure CdSeS nanosheets, which were synthesized by a physical vapor transport process, and strong red and green emissions could be observed by selective laser excitation focusing at the center and edge parts of these heterostructure nanosheets, respectively. However, nanosheets show a strong suppression effect of S incorporation during the growth dominated by the vapor-solid mechanism; namely, a strong preference for the incorporation of Se species may exist in the competition between S and Se species migrating toward the $\pm(0001)$ side surfaces. So, CdSSe nanosheets with very small level of S incorporation resulted even if a sufficient amount of S vapor is transported. So, it is of no benefit to the synthesis of CdSSe nanosheets with varied compositions for band-gap engineering. Then in 2014 [65], Maiti et al. reported a solution phase synthesis method to prepare homogeneous ultrathin alloyed $\text{CdSe}_{1-x}\text{S}_x$ nanosheets, and the optical properties of the resultant $\text{CdSe}_{1-x}\text{S}_x$ nanosheets showed a comparable or higher quantum yield with those of pure nanosheets. But stacking faults were detected in these CdSeS nanosheets, which may affect the optical properties of CdSeS nanosheets. Consequently, more novel delicate and low cost synthesis methods on 2D CdSeS nanostructures are needed to develop.

2.4. CdSeS-Based Nanocomposite Structures. CdSeS nanocomposite structures mainly exist in the form of radial core/shell heterostructures. The presence of such nanosized heterointerface between semiconductor shell and core provides significant advantages for both light absorption and charge separation. And they have exhibited diverse applications in field-effect transistor, solar cells, light-emitting diodes, high electron mobility devices, and memory devices [70–76]. In 2007 [77], Chong et al. prepared TiO_2 nanobelts/CdSeS QDs nanocomposite structures, and the corresponding visible light sensitizing effect shows a 3- to 4-fold increase in photocurrent in the coupled system. In 2008 [75], Pan et al. synthesized uniform Si@CdSeS core-shell nanowires with continuously tunable light emission in the visible region by thermal evaporation method. And these kinds of nanostructures may have potential applications in multicolor nanoscaled light-emitting devices. In 2010 [74], Myung et al. fabricated vertically aligned and composition-tuned ZnO@CdSSe core-shell nanowire arrays by chemical vapor deposition on pregrown ZnO nanowire arrays, which was a Zn containing alloy formed in the interface region between the ZnO core and shell, facilitating the growth of single-crystalline shell layers by reducing both the lattice mismatch and the number of defect sites, thus resulting in higher photoelectrochemical cell performance of the ZnO@CdSSe core-shell nanocables. In 2012 [76], Qin et al. reported stable CdSeS@ZnS core-shell colloidal QDs suitable for single dot imaging, and, compared with CdSe@ZnS core-shell QDs

with similar core size, the biexciton recombination rate and electron confinement energy are both smaller by about 40% in CdSeS@ZnS core-shell QDs. CdSeS nanocomposite structures combine the advantages of alloyed CdSeS nanostructure and its composited components. They have unique properties, which cannot be obtained from their individual component. So they can be used for some special applications like cancer diagnosis [78] through modification and conditioning. Therefore, the preparation of CdSeS nanocomposite structures is of great significance.

3. Synthesis Methods of CdSeS-Based Nanostructures

3.1. Hot-Injection Synthesis. Hot-injection synthesis is a very facile and useful method to prepare CdSeS nanostructures with high luminescence, which is also called organometallic high-temperature colloidal method [79]. Generally, there are three main steps in hot-injection synthesis. First, one should prepare a Cd precursor at elevated temperature under inert gas flow, in which the solvents are usually organic compounds. Second, a fresh Se and S mixed precursor solution with a fixed molar ratio should be prepared. Using different Se and S precursors and controlling their relative amounts can tune the internal structures of CdSeS nanostructures [36]. In the third step, the freshly prepared Se and S mixed precursor is rapidly injected into the hot Cd precursor under vigorous stirring, and then, by controlling the reaction time and temperature strictly, CdSeS nanostructures with different morphologies and properties can be obtained. Utilizing this hot-injection synthesis, CdSeS QDs with tunable luminescence properties were prepared for the first time in 2003 [12]. After that, many kinds of CdSeS nanostructures were prepared by this method or its variant with a little modification. Some typical CdSeS nanostructures prepared by such method are summarized in Table 1. From this table, it can be seen that, by employing hot-injection synthesis method, many forms of nanostructures, such as CdSeS QDs, nanocrystals, nanowires, nanorods, and nanocomposite structures could be fabricated, but in most of the cases this method is to prepare CdSeS QDs.

The as-described three steps are all crucial for hot-injection synthesis. The solvents, Se and S precursors, ratio of Se and S, reaction time, and temperature all have an important effect on the physical and optical properties of the prepared CdSeS nanostructures and even on the success in the preparation. For example, in 2007 [88], Al-Salim et al. systematically studied the effect of solvents on CdSeS nanocrystals prepared by hot-injection synthesis. They chose eight different solvents from coordinating to noncoordinating ones. The results indicated that the type of solvents played a significant role in developing the crystal phase, composition, size, shape, and optical properties of CdSeS nanocrystals. For details, please check Table 2.

Usually, in hot-injection synthesis, the solvents are organic compounds, and the capping agents are often chain organic compounds containing phosphine (such as trioctylphosphine and tributylphosphine). However, these organic compounds are often toxic, unstable at high temperature, and expensive.

TABLE 1: Different CdSeS nanostructures prepared by hot-injection synthesis.

The resulting nanostructure	Cd precursor	Se/S precursors	Reaction parameters	Crystalline structure	Quantum yield	Refs.
CdSeS QDs	CdO + oleic acid	Trioctylphosphine Se + trioctylphosphine S	300 °C, 10 s~4 min	No data	85%	[12]
CdSe _{1-x} S _x nanocrystals	CdO + oleic acid	Tri-n-butylphosphine Se + tri-n-butylphosphine S	315 °C, <15 min	Zinc blende	1-30%	[41]
CdSeS QDs	(CH ₃ COO) ₂ Cd + oleic acid	Trioctylphosphine Se + trioctylphosphine S	230~300 °C	Wurtzite or zinc blende	30-80%	[79]
CdSe _{1-x} S _x QDs	CdO + oleic acid	Trioctylphosphine Se + trioctylphosphine S	300 °C, ~4 min	Zinc blende	No data	[80]
CdSeS QDs	CdO + oleic acid	Tri-n-butylphosphine Se + tri-n-butylphosphine S	275~290 °C	No data	No data	[81]
CdSeS QDs	CdO + oleic acid	Trioctylphosphine Se + trioctylphosphine S	300 °C, 1 min	No data	40-60%	[27]
CdSeS/ZnS QDs	CdO + oleic acid	Trioctylphosphine Se + trioctylphosphine S	280 °C, 1 min	No data	No data	[82]
CdS _{1-x} Se _x nanorods	CdO + octadecylphosphonic acid	Trioctylphosphine oxide Se + trioctylphosphine oxide S	315 °C	Wurtzite	No data	[83]
CdSeS/ZnS QDs	CdO + oleic acid	Trioctylphosphine Se + trioctylphosphine S	280 °C, 4 min	Zinc blende	14-20%	[76]
CdSeS nanocrystals	CdO + oleic acid	Trioctylphosphine Se + trioctylphosphine S	300 °C	Zinc blende	No data	[84]
CdSeS QDs	CdO + oleic acid	Tri-n-butylphosphine Se + tri-n-butylphosphine S	220 °C, 2 h	Zinc blende	67%	[85]
CdSeS QDs	CdCl ₂ ·2.5H ₂ O + polyethylene glycol	Na ₂ SeO ₃ + Na ₂ S + 3-mercaptopropionic acid	80~260 °C	Zinc blende	49%	[86]
CdSeS nanowires	CdO + oleic acid	Trioctylphosphine Se + trioctylphosphine S	300 °C, 2 min	Wurtzite	No data	[87]

TABLE 2: CdSeS nanocrystals synthesized in different solvents by hot-injection synthesis [88].

	Solvents	Crystal size (nm)	Crystal phase	Influence
Coordinating	Trioctylphosphine oxide (TOPO)	2.5–4.5	Hexagonal	As potential ligands to chalcogen sites, they can activate the crystal surface along the c axis
	Trioctylphosphine (TOP)	3.5×6	Hexagonal	
	Oleylamine (OLA)	3.7×8	Hexagonal	
	Hexadecylamine (HDA)	No data	Hexagonal	
Weak or noncoordinating	Trioctylamine (TOA)	4–8	Cubic	Surface capped with oleic acid
	Diocetylamine (DOA)	5	Cubic	
	1-Octadecene (ODE)	5	Cubic	
Nonsurfactant	Triphenylphosphine (TPP)	9	Hybrid phase	Hexagonal/cubic phases

Thus, solvents which are less toxic, more stable at high temperature, and relatively cheaper are desired. In [86], glycerin was tried as a stabilizing agent replacing tri- n -octylphosphine oxide (TOPO) to fabricate CdSeS nanocrystals in cubic structure.

Hot-injection synthesis can prepare CdSeS nanostructures with tunable photoluminescence emission wavelength and narrow size distribution for many applications. However, the main drawback with it is the requirements of rapid injection and subsequently fast cooling. It is not easy to realize in industrial production. Consequently, hot-injection synthesis is not suitable for large-scale production. In addition, it performs poorly in synthesis reproducibility [35].

3.2. One-Pot, Noninjection Synthesis. One-pot, noninjection synthesis overcomes the disadvantages of hot-injection synthesis. It does not need to inject precursor solution rapidly and decrease the reaction temperature in a very short time. The main procedure of one-pot, noninjection synthesis is summarized below. First, one should prepare a Cd precursor in an organic system and prepare a Se and S precursor in organic or inorganic system (sometimes, just Se and S powders) under inert gas protection. Then, the two precursors are mixed in a designed proportion at a proper temperature and react at a selected temperature under inert gas flow. Finally, the resultant products are purified (usually washing and centrifuging for several times).

In 2009 [35], Ouyang et al. reported the method of one-pot, noninjection synthesis to prepare homogeneously alloyed CdSeS QDs with a cubic crystal structure, in which 2,2'-dithiobisbenzothiazole (MBTS) was used as nucleation initiator. The resultant CdSeS QDs could be easily tuned to emit photons in the range of 470–550 nm (see Figure 2 [35]) with a fixed Cd/Se/S feed molar ratio but different S/MBTS feed molar ratios. Such an emission window is hard to achieve within binary CdS and CdSe QDs alone [42]. In this method, Cd/Se/S and S/MBTS feed molar ratios affected the growth kinetics of the resultant QDs as well as their compositions, which determine the band-gap mainly. The higher the Cd/Se/S and the lower the S/MBTS feed molar ratios, the lower the band-gap of the resultant CdSeS QDs. But the nucleation initiators are often toxic and expensive. So, in 2010 [43], Zou et al. proposed an improved

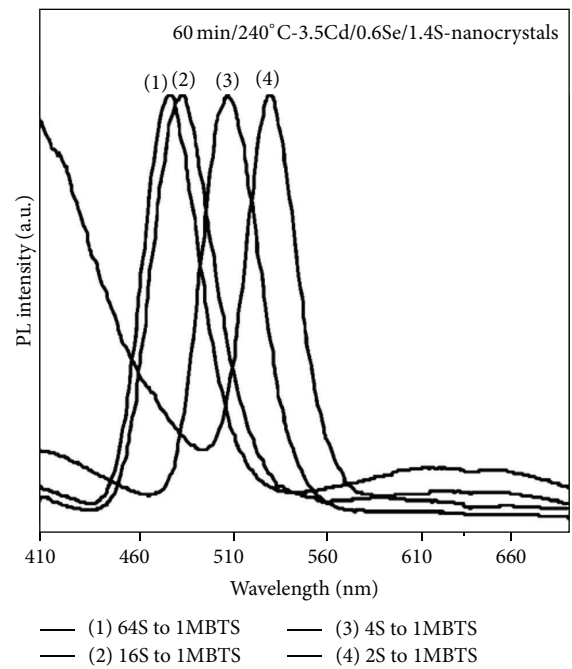


FIGURE 2: The normalized photoemission spectra of CdSeS QDs with a fixed 3.5Cd/0.6Se/1.4S feed molar ratio but different S/MBTS feed molar ratios prepared by one-pot, noninjection synthesis [35].

one-pot, noninjection synthesis method. They fabricated alloyed CdSe $_{1-x}$ S $_x$ QDs with tunable band-gap energy by adding oleic acid (OA) into the reaction mixture without any nucleation initiators, and the microstructure examination verified that highly monodispersed nanocrystals with narrow size distribution were obtained for the samples with all the molar ratios of S to Se, which can be seen in Figure 3 [43]. OA accelerated the nucleation just as the nucleation initiators do, and the difference is that OA increased the reactivity of Cd precursors while MBTS increased the reactivity of S. On the other hand, OA stabilizes the further growth of CdSeS nanocrystals. But the quantum yields of the CdSeS QDs obtained from the as-described two works are very low (below 5%). In 2013 [44], Ünlü et al. prepared highly luminescent CdSe $_{1-x}$ S $_x$ QDs with high quantum yields (up to 90%) via a one-pot, noninjection synthesis with further but

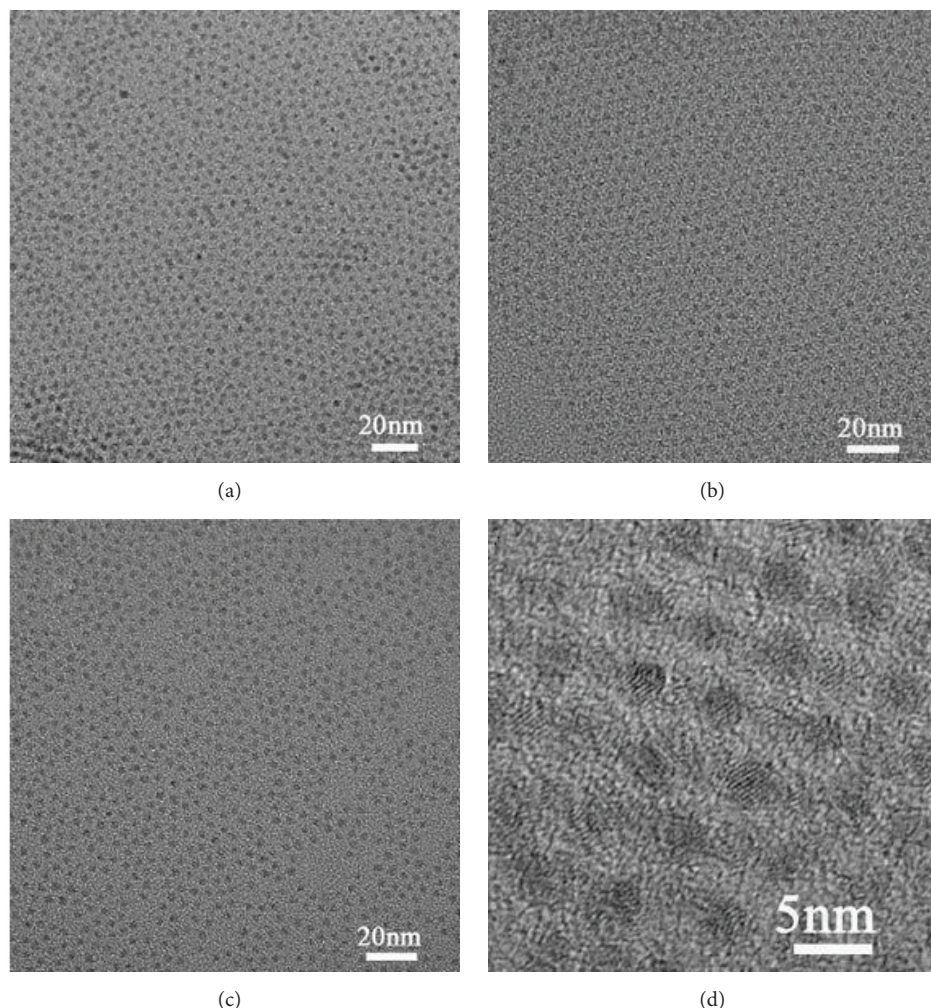


FIGURE 3: Transmission electron microscopy images of the CdSeS nanocrystals prepared at 240 °C with different Se/S feed molar ratios: (a) 1/3, (b) 1/1, and (c) 3/1. (d) High-resolution transmission electron microscopy image of the CdSeS nanocrystals shown in (b). They were prepared via the improved one-pot, noninjection synthesis without any nucleation initiators [43].

still slight modification. They also called their method two-phase thermal approach. In the synthesis process, organic Cd precursor and aqueous Se and S precursors were employed, and the hydrodynamic size of the obtained $\text{CdSe}_{1-x}\text{S}_x$ QDs could be varied from 1.4 to 10.0 nm with the reaction time. The CdSeS QDs formed at the interface of the two liquid phases, and the internal structure of the nanoalloys varies with the initial molar ratio and the reactivity of chalcogenides towards cadmium ions. But, before that, CdSeS QDs with composition gradient and homogeneous internal structures have also been successfully prepared in aqueous solution by using different Se and S precursors, because different Se and S sources could release selenium and sulphur ions at different rates or have different reaction rates of selenium or sulphur toward cadmium [36]. Then, in 2014 [89], employing one-pot, noninjection synthesis method with some modifications, Jia and Tian prepared $\text{CdSe}_{1-x}\text{S}_x$ QDs in liquid paraffin with a fluorescence emission covering the entire visible region from violet to red. Moreover, homogeneous, ultrathin alloyed $\text{CdSe}_{1-x}\text{S}_x$ nanosheets with a typical width of 20–40 nm and

length of several hundred nanometers were also prepared by this method [65].

One-pot, noninjection synthesis is an easy handling method, featuring in large-scale production with excellent synthesis reproducibility. But to obtain high quality CdSeS nanostructures with high quantum yield, more modifications are still needed in the synthesis process.

3.3. Microwave Irradiation. Microwave irradiation creates friction and collision of molecules at high temperature to decompose chemicals. It is a useful synthesis method in aqueous phase and works with the help of a microwave digestion/extraction system equipped with some exclusive Teflon inner vessels. In 2005 [41], utilizing microwave irradiation, Qian et al. synthesized alloyed gradient CdSeS QDs with good optical properties by using oxygen-free NaHSe solution and $\text{CdCl}_2/3$ -mercaptpropionic acid (MPA) mixed solution as Se and Cd precursor, respectively. During the synthesis, MPA also released sulfide ions in aqueous solution gradually. Later, another group of authors also prepared

CdSeS QDs composed of a CdSe-rich core and thick CdS shell with homogeneous size distributions in aqueous phase via microwave irradiation [90, 91]. The physical properties of some typical CdSeS QDs prepared by microwave irradiation are shown in Table 3.

Typical procedure of microwave irradiation synthesis is as follows. Firstly, a precursor solution containing tunable molar ratio of Cd:MPA:Se was first adjusted to an appropriate pH (usually, 9~9.5). Then, a certain amount of the precursor solution was sealed in an exclusive vessel and heated inside a microwave digestion furnace via microwave irradiation. After the reaction was completed, the solution was cooled down to ambient temperature naturally. The detailed reaction conditions for typical cases could be seen in Table 4. Typically, the CdSeS QDs fabricated by the microwave irradiation had a gradient internal structure with CdSe-rich core and CdS-rich shell, which resulted from their formation mechanism under microwave irradiation as schematically shown in Figure 4 [41]. At the initial stage, only CdSe monomers nucleated and grew because few S^{2-} anions were released by the decomposition of MPA at low temperature. As the temperature increased under microwave irradiation, a large number of MPA were decomposed into S^{2-} anion. At this stage, tiny CdSe monomers mentioned above served as seeds (the existing of CdSe seeds was very crucial for the synthesis of high quality QDs), and the released S^{2-} anion began to participate in the growth of CdSe nanocrystals. Finally, alloyed CdSeS QDs formed. The bias molar ratio of $Cd^{2+} : Se^{2-} : S^{2-}$ and the difference in the intrinsic reactivity of S and Se with cadmium would result in the formation of QDs with a gradient alloy structure. During the synthesis, the initial core was rich in Se due to the faster reaction of Se with cadmium. As the free CdSe monomers were depleted from the reaction mixture, the crystal growth mainly contributed to CdS deposition. Finally, alloyed QDs with a gradient Se concentration from the core to the surface were formed.

Comparing with conventional hydrothermal synthesis, the synthesis of nanocrystals by microwave irradiation is generally quite faster, simpler, and very much energy efficient [92, 93]. However, the mechanism of thermal effects and nonthermal effects of microwave irradiation has been poorly understood, limiting to some extent the use of microwave irradiation.

3.4. Solvothermal Synthesis. Solvothermal synthesis is a method in which poorly soluble or insoluble reactants were dissolved in a special sealed reactor (autoclave) under a relatively high temperature and high pressure reaction environment, and the solvent is organic or nonaqueous. Then a new material was formed by reacting and recrystallizing in this organic or nonaqueous reaction system.

Using solvothermal synthesis, 1D CdSeS nanostructures with different morphologies and physical properties have been fabricated. In 1999 [60], $CdSe_{1-x}S_x$ nanowires were successfully prepared via the solvothermal synthesis in ethylenediamine (en). CdC_2O_4 as Cd source, S powder as S source, and elemental Se as Se source in an appropriate ratio were put into a stainless steel autoclave filled with ethylenediamine up to its 80% capacity. And the autoclave

TABLE 3: The physical properties of CdSeS QDs prepared by microwave irradiation.

System	Internal structure	Size (nm)	Quantum yield	FWHM (nm)	Refs.
CdSeS QDs	Gradient	12	~25%	28	[41]
CdSeS QDs	Gradient	~3	~23.9%	44	[90]
CdSeS QDs	Gradient	2.1 ± 0.6	30%	44	[91]

was kept at 180~200°C for 12 h and then air cooled to room temperature. The resultant precipitates were subsequently filtered and washed with absolute ethanol, dilute HCl solution, distilled water, and absolute ethanol in turn. Then the products were collected after being dried in vacuum at 70°C for 4 h. Both temperature and solvent have significant effects on the synthesis and incorporating process for solid solution $CdSe_{1-x}S_x$ nanocrystallites. Higher temperature is needed for the formation of $CdSe_{1-x}S_x$ nanowires and effective incorporating process of the solid solution when compared with those in the cases of CdS or CdSe, because lower temperature cannot provide enough activation energy to form the solid solution $CdSe_{1-x}S_x$, and the activation energy to form a solid solution increases as the S and Se content becomes equal. Ethylenediamine is a protophilic base solvent and bidentate ligand containing two N-chelating atoms, which plays a key role in the formation of $CdSe_{1-x}S_x$ nanowires. When CdC_2O_4 was added into ethylenediamine, a complex ion $[Cd(en)_n]^{2+}$ formed in the solvothermal process. The formation mechanism of $CdSe_{1-x}S_x$ nanowires may be related to the N-chelating effect of the bidentate ligand with Cd^{2+} and the stronger hydrogen bonding action effect of the protophilic properties among ethylenediamine molecules. But the detailed formation mechanism of $CdSe_{1-x}S_x$ nanowires has not been clear yet. Later, in 2006 [61], $CdSe_{1-x}S_x$ nanorods were fabricated in ethylenediamine by a similar solvothermal process. In this case, $Cd(NO_3)_2 \cdot 4H_2O$, $CS(NH_2)_2$, elemental Se, and $N_2H_4 \cdot H_2O$ as reactants were used. The reaction was carried out at 120~140°C for 10 h, and then reaction mixture was cooled to room temperature naturally. The resultant precipitates were washed with absolute ethanol and distilled water subsequently and then dried in air at 60°C for 4 h. The authors indicated that the formation process of the $CdSe_{1-x}S_x$ nanorods could be divided into four steps: firstly, the reagents reacted to get amorphous $CdSe_{1-x}S_x$ particles; secondly, the particles stripped into soft thin fibers; thirdly, these fibers sclerosed to needle-like fragments; and finally the needles grew to be highly crystallized. They also proposed that, unlike the formation process of ME (M = Zn, Cd; E = S, Se) nanorods in ethylenediamine, there was not an ethylenediamine intercalated precursor in that of $CdSe_{1-x}S_x$ nanorods. Ethylenediamine as solvent was also crucial in the formation process of the rod-like morphology. And the reaction temperature decreased because a small amount of CdS nanorods formed in the process, which could

TABLE 4: The reaction conditions for CdSeS QDs synthesized by microwave irradiation.

System	Cd precursor	Se precursor	S precursor	Temperature (°C)	Time (min)	Refs.
CdSeS QDs	CdCl ₂ + MPA	NaHSe	MPA	140	5–60	[41]
CdSeS QDs	CdCl ₂ + MPA	Na ₂ SeSO ₃	MPA	130	30	[90]
CdSeS QDs	CdCl ₂ + MPA	Na ₂ SeSO ₃	MPA	No data	No data	[91]

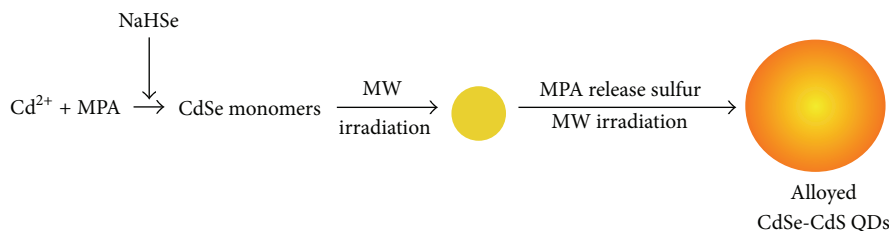


FIGURE 4: Schematic for the formation process of alloyed CdSeS QDs by microwave (MW) irradiation [41].

act as seeds for the crystallization of CdSe_{1-x}S_x crystals to reduce the formation energy of CdSe_{1-x}S_x products. In 2009 [94], employing the solvothermal synthesis route, CdSe_{1-x}S_x nanorods were also fabricated by using Cd(NO₃)₂·4H₂O, S, and Se, respectively, as Cd, S, and Se source, ethylenediamine as solvent, and polyethylene glycol 2000 as the polymer-controller matrix and reacting at 180°C for 24 h. Before the source and solvent were put into the stainless steel autoclave, a PEG gel dosed with Cd²⁺ needs to be made by adding Cd(NO₃)₂·4H₂O into polyethylene glycol 2000 gel and then stirring at room temperature for 5 h in order to achieve good dispersion of Cd²⁺ in the polymer matrix. The formation of the CdSe_{1-x}S_x nanorods may follow a chemical solution transport growth mechanism [95]. During the synthesis, ethylenediamine was a strong bidentate solvent, readily chelating divalent cadmium ions. Therefore, an effectively reversible pathway as $[CdSeS]_n \xrightleftharpoons{en} nCd^{2+} + nS^{2-} + nSe^{2-}$ might be established between the solution and solid phases, and this reversible pathway between the solution and solid phases played a key role in the crystal growth. Meanwhile, polyethylene glycol 2000 served as a molecular template in controlling the growth of CdS_xSe_{1-x} nanorods by connecting with the ethylenediamine to form chain structures with many pores. The possible growth model is shown in Figure 5. Due to the different processing parameters, the as-described 1D CdSeS nanowires or nanorods prepared by solvothermal synthesis method have different physical properties. For details, please check Table 5.

Solvothermal synthesis method is an efficient and facile method for preparing 1D CdSeS nanostructures. CdSeS nanowires or nanorods with high crystallinity and good orientation could be obtained by this method. However, there are some security issues within the process due to the volume expansion of the fluid in the sealed environment under heating treatment, which would create very high pressure. Hence, the compactedness of the autoclave should be cautious, which should not exceed 85% by volume (usually 80%). Moreover, the reaction process is unobservable because the reactions happened in a sealed reactor, and the reaction procedure is not monitored. So, it is difficult to

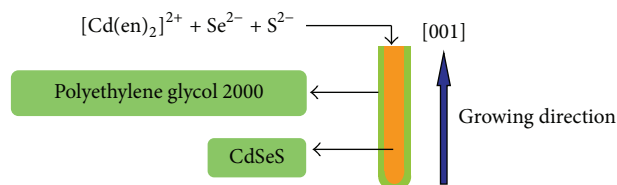


FIGURE 5: Possible growth model of CdSeS nanorods.

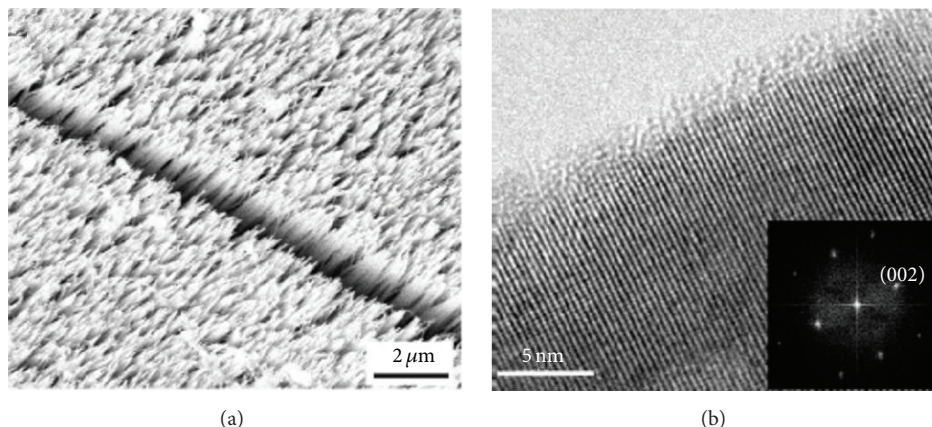
investigate the formation mechanism of CdSeS nanowires or nanorods.

3.5. Template-Assisted Electrodeposition. In 2005 [62], template-assisted electrodeposition was reported to prepare alloyed ternary CdSe_{1-x}S_x nanowires arrays, by which the ratio of S to Se in the nanowires could be controlled through adjusting the relative amounts of the starting materials. The detailed synthesis process is as follows: CdSe_{1-x}S_x nanowires were first galvanostatically electrodeposited into the pores of anodic aluminum oxide (AAO) membranes coated with a thin Au layer from a dimethyl sulfoxide solution containing CdCl₂, elemental S, and elemental Se at 160°C for 15 min, and the deposition current density was kept constant at 2.4 mA/cm². Then the nanowires embedded in the AAO template were annealed at 400°C under a N₂ atmosphere for 8 h. After that, the back Au layer of the nanowire/AAO/Au samples was removed by chemically dissolving them in 1.0 M NaCN aqueous solution. The resultant alloyed ternary CdSe_{1-x}S_x nanowires were highly crystalline (see Figure 6 [62]), and the band-gaps of these well-structured nanowires could be continuously tuned from 1.75 (CdSe) to 2.44 eV (CdS) through modulating the compositions of S and Se.

In the template-assisted electrodeposition process, the supplied electric field plays an important role in the synthesis of CdSe_{1-x}S_x nanowires. The higher potentials used in the ac deposition cycle (>5 V) could result in the codeposition of elemental Cd, and, for the ac process, the rate and direction of the diffusion would vary with the alternation of the electric field, thus resulting in a high density of defects and small

TABLE 5: Physical properties of 1D CdSeS nanostructures prepared by solvothermal synthesis.

CdSeS nanostructures	Diameter (nm)	Length (μm)	Crystal	Band-gaps (eV)	FWHM (nm)	Refs.
CdSeS nanowires	10–90	0.7–8	Hexagonal	No data	No data	[60]
CdSeS nanorods	10–20	100–150	Hexagonal	1.7–2.4	No data	[61]
CdSeS nanorods	15–20	100–200	Hexagonal	1.75–2.44	~25	[94]

FIGURE 6: (a) SEM image of the $\text{CdSe}_{1-x}\text{S}_x$ nanowire arrays and (b) HRTEM image of an individual 20 nm $\text{CdSe}_{1-x}\text{S}_x$ nanowire by template-assisted electrodeposition (insert in (b): the corresponding Fourier transformation of the entire HRTEM image) [62].

polycrystalline structure in the nanowires [96]. However, under dc deposition conditions, it is easy to control the potential as being no more than the codeposition potential of Cd, and the diffusing process is more likely to reach a steady state. Thus, the defects in the electrodeposited nanowires are largely decreased, and further alloyed ternary $\text{CdSe}_{1-x}\text{S}_x$ nanowires with a high crystallinity could be obtained [62].

The template-assisted electrodeposition synthesis is a feasible approach to prepare highly crystalline $\text{CdSe}_{1-x}\text{S}_x$ nanowires with continuous tunable band-gaps. It may open the possibilities of developing a variety of ternary or quaternary semiconductor nanowires based on II–IV and III–V materials. But, in such template-assisted electrodeposition synthesis, electric power supply is necessary, and it is an energy-wasting synthesis method.

3.6. Thermal Evaporation. Thermal evaporation is widely used to prepare CdSeS nanostructures via a vapor-liquid-solid (VLS) or vapor-solid (VS) process on a substrate coated with metal catalyst. It often comes true in a furnace at high temperature under inert gas flow. Typical process is shown in Figure 7.

In the thermal evaporation synthesis, the relative dominance between VLS and VS growth mechanisms determines the final shape of the nanostructures [97, 98]. At low substrate temperature under low vapor supply, the growth dominated by a VLS mechanism usually occurs and the resultant nanostructures usually have the form of nanowires. When both the vapor supply rate and substrate temperature increase, VS growth, which promotes side wall growth, starts to play a role, competing with the VLS mechanism. Those two combined growth mechanisms might result in tapered

nanobelts with catalysts on the tip [69]. In general, it requires more thermal energy to promote a VS growth than a VLS process [99]. Accordingly, more sample vapor and higher substrate temperature would enable a VS mechanism to play the governing role to grow nanobelts and nanosheets. In addition, the spontaneous polarization induced asymmetry (SPA) growth mechanism [100] could also happen in the growth of CdSeS nanostructures. In other words, self-catalyzed growth takes place predominantly on the chemically active, positively charged Cd side of the nanobelt, provided that sufficient thermal energy to surmount nucleation barrier is supplied, while the chemically inert, negatively charged Se/S side of the nanobelt is relatively flat [69]. Usually, the SPA growth mechanism results in toothed nanobelts or nanosaw structures. And this thermal evaporation synthesis often employs substrates coated with a thin gold film, and, during the growth, gold agglomeration takes place to form nanosized islands, which act as catalysts.

Another viewpoint has been proposed to explain the S suppression effect. It pointed out that the interplay between the VLS and VS mechanisms may play a role during the growth of CdSeS nanostructures [69]. In a traditional VLS model, supersaturated CdS/CdSe in molten gold droplets starts to precipitate at the interface between liquid and solid to form a nanowire. Solubility differences between S and Se species together with the relative vapor supply rates of both species will determine the molar fraction of CdSeS nanostructures. While a VS growth mechanism dominates, S and Se species initially arriving at the nanobelt top/bottom surfaces migrate toward the $\pm(0001)$ side surfaces for incorporation. The competition between S and Se species occurs and a strong preference for the incorporation of Se species may exist.

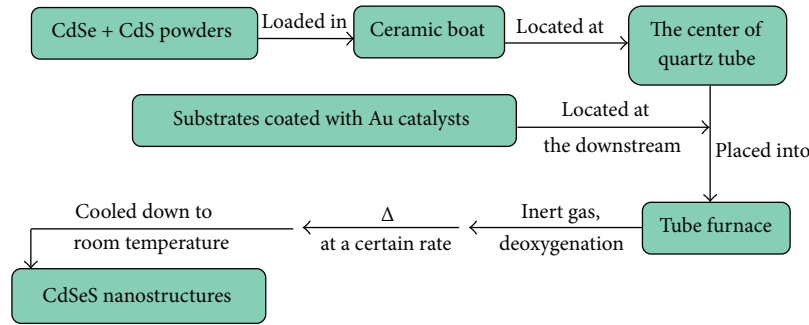


FIGURE 7: Typical process of thermal evaporation.

So, at high temperatures, CdSeS nanosheets with very small S incorporation would result even if a sufficient amount of S vapor is transported.

The thermal evaporation process of growing CdSeS nanostructures can be divided into one-step and two-step ones. In the one-step one, a CdSe and CdS mixture powder as the precursor was loaded into a ceramic boat and located at the center of quartz tube. Then by heating the precursor powder at an appropriate temperature, CdSeS nanostructures are formed onto the substrate under the gas flow downstream, while, in the two-step process, a CdSe powder was usually loaded into the ceramic boat alone in the quartz tube. And CdSe nanostructures were grown for a certain time firstly. Then after the temperature was decreased to a desired value while the flow of the forming gas was kept, the CdSe powder was replaced with CdS powder quickly to grow CdSeS nanostructures. The two-step process can overcome the difficulty in controlling S incorporation during the growth of large-area CdSeS nanosheets at high temperature [97].

In 2005 [8], Pan et al. reported the synthesis of single-crystal ternary CdSe_{1-x}S_x nanobelts with site-controlled compositions via one-step thermal evaporation process. The resultant CdSe_{1-x}S_x nanobelts have a strong single emission band near their band-edges, and these spectral peaks could be tuned from ~508 nm (for pure CdS) to ~705 nm (for pure CdSe). Using this one-step thermal evaporation synthesis, products covering the entire composition range (X varied from 1 to 0) could be typically obtained on a single substrate, but they were usually of less uniformity because the composition of the nanostructured CdSe_{1-x}S_x was highly dependent on the local substrate temperature [10]. To solve this problem, in 2011 [13], Lu et al. designed a special substrate holder and successfully synthesized CdSe_{1-x}S_x nanobelts with uniform chemical stoichiometry and accurately controlled compositions. The schematic of the alloyed nanobelts growth reactor using the special substrate holder is shown in Figure 8. With such holder, substrates could be slotted vertically so that the plane of the substrates would face the incoming flux of CdSe_{1-x}S_x vapor during the growth. The vertically positioned substrate could be maintained at a fixed temperature during the growth, so samples with highly uniform composition in a large area could be obtained.

Many CdSeS nanostructures with excellent properties could be prepared directly by one-step thermal evaporation

process under different reaction conditions. Typical results are shown in Table 6.

There are also some CdSeS nanostructures prepared by two-step thermal evaporation process. For example, CdS/CdSe lateral heterostructure nanobelts were synthesized by growing CdSe nanobelts at 900°C for 2 h firstly by thermal evaporation and then putting CdS source into furnace after the CdSe nanobelts samples were cooled down to room temperature, and the products were finally prepared at 700–850°C for 2 h via similar thermal evaporation process [104]. Ternary CdSe_{1-x}S_x single-crystal nanoribbons (NRs) with uniform and controllable compositions were prepared by two successive thermal evaporation steps involving (i) growing CdSe NRs at 850°C for 40 min and (ii) growing CdSe_{1-x}S_x NRs at 750°C by sulfurizing the as-synthesized CdSe NRs using a constant atmosphere of 10% H₂S and 90% Ar of 200 Torr [54]. And symmetrical composition-graded CdSe_{1-x}S_x nanowires were also fabricated by two-step thermal evaporation via growing CdS nanowires at 830°C for 30 min firstly and then putting CdSe source into furnace to react with the CdS nanowires for 15–30 min [56]. In addition, CdSeS lateral heterostructure nanosheets [64] were fabricated by such two-step thermal evaporation process, too. In the first step of the growth, only CdS powder was thermally evaporated at 880°C for 1 h. Then CdSe source was loaded into the furnace while the temperature was gradually lowered to 840°C and held for 40 min to grow the CdSeS lateral heterostructure nanosheets.

Thermal evaporation is a very good and facile method to prepare CdSeS nanostructures. However, it is hard to obtain high uniformity and selectivity of stoichiometry on a single substrate through this approach. Although special substrate holders, which can hold substrate vertically, can be designed and applied, it is not suitable for large-scale production. So an easy and feasible way to synthesize 1D ternary nanostructure with uniform composition on a reasonably large substrate is desired.

3.7. Pulsed Laser Deposition. Pulsed laser deposition (PLD) synthesizes materials via vapor-phase transport process of a source vapor ablated by pulsed laser of a certain wavelength onto a substrate. It works in a hot-wall high-temperature PLD system as shown in Figure 9 [9]. It can be used to synthesize 1D CdSeS nanowires. The main procedure of PLD synthesis

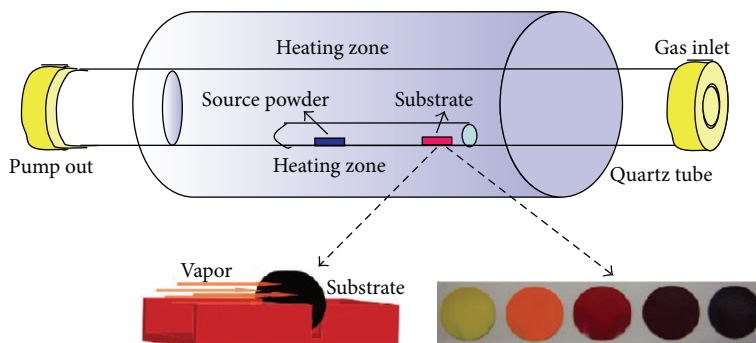


FIGURE 8: Schematic of alloyed nanobelts growth reactor using the special substrate holder [13].

TABLE 6: The reaction conditions for CdSeS nanostructures prepared by one-step thermal evaporation.

CdSeS nanostructures	Evaporation sources	Substrate	Catalyst layer	Protection gas	Temperature (°C)	Time (min)	Refs.
CdSe _{1-x} S _x nanobelts	CdS, CdSe	Silicon slices	Au, ~2 nm	He	900	60	[8]
CdSeS whiskers	CdS, CdSe	Silicon slices	Au, 10 nm	He	850	120	[20]
Si-CdSeS core-shell nanowires	CdS, CdSe, silicon wafer	Quartz substrate	Au, 6 nm	Ar	1080	60	[75]
CdSe _{1-x} S _x nanobelts	CdS, CdSe	Si substrate	Au	He	900	No data	[50]
CdSeS nanosheets	CdS, CdSe	Si substrate	Au, 5–10 nm	N ₂ + 10% H ₂	850–900	60	[69]
CdSeS nanowires	CdS, CdSe	Si wafers	Au, 2 nm	N ₂	(1) 830 (2) 800	(1) 40 (2) 60	[101]
CdSe _{1-x} S _x nanobelts	CdS, CdSe	Sapphire wafer	Au, ~1 nm	He	850	30	[13]
CdSeS nanowire arrays	CdS, CdSe	Mica substrate	Poly-l-lysine, 5 nm	Ar + 5% H ₂	750	30	[102]
CdSe _{1-x} S _x nanobelts	CdS, CdSe	C-plane sapphire	Au	He	850	30	[103]
CdSeS nanowires	CdS, CdSe	Silicon wafer	Au, 30 nm	He	900	60	[44]

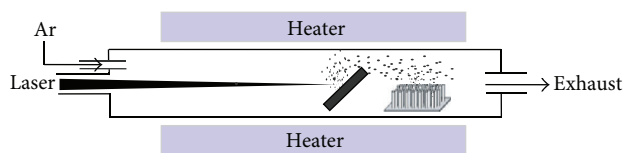


FIGURE 9: Schematic of a hot-wall high-temperature PLD system [9].

method to prepare CdSeS nanowires is shown as follows: (1) CdSeS compacts as targets were prepared by sintering pure CdS and CdSe powders at high temperature. (2) The as-prepared targets were ablated by an excimer laser, which were placed at the center of the reaction chamber, while the substrate coated with a thin Au layer (typically with a thickness of 5–30 Å) was located in the region where the temperature was sustained in a proper range and for a desired duration of time. The pressure in the processing tube was controlled within the range of 1–10 Torr.

In the synthesis, Au was used as catalyst, and the deposited Au layer contributed to the formation of Au-CdSe_{1-x}S_x eutectic alloying liquid when the reaction temperature is above the eutectic temperature. The liquid-phase

alloy enables the rapid growth of CdSe_{1-x}S_x nanostructure at a relatively low temperature. Laser ablation generates catalytic clusters with nanometer diameter that define the size and direct the growth of crystalline CdSeS nanowires by vapour-liquid-solid (VLS) mechanism in the synthesis process.

Several kinds of CdSeS nanowires were successfully prepared by different groups via PLD synthesis method. Their synthesis conditions of CdSeS nanowires were summarized in Table 7, and the physical properties of the corresponding prepared CdSeS nanowires are listed in Table 8.

PLD synthesis is an easy handling method to prepare CdSeS nanowires. But it is of high cost and has difficulty controlling the conditions to obtain CdSeS nanostructures with uniform size distribution and controllable structures.

4. Conclusions and Outlook

CdSeS alloy nanostructures have attracted more and more attention due to their diversity of electronic and optical properties, presenting great potential for the applications in tunable optoelectronic devices and biomedical sciences. Many CdSeS nanostructures with different morphologies and properties were prepared to meet the needs of applications

TABLE 7: The synthesis conditions of CdSeS nanowires in PLD synthesis.

System	Thickness of Au layer (Å)	Target sintering temperature (°C)	Laser wavelength (nm)	Laser energy density ($\text{J}\cdot\text{cm}^{-2}$)	Deposition temperature (°C)	Refs.
$\text{CdS}_x\text{Se}_{1-x}$ nanowires	5–30	700	248	1–5	400–1100	[54]
$\text{CdS}_x\text{Se}_{1-x}$ nanowires	5–30	1000	248	1–5	400–1100	[9]
$\text{CdS}_x\text{Se}_{1-x}$ nanowires	5–30	1000	248	1–5	550	[56]

TABLE 8: Typical properties of $\text{CdS}_x\text{Se}_{1-x}$ nanowires prepared by PLD.

System	Diameter (nm)	Length (μm)	Crystal structure	Band-gap (eV)	Refs.
$\text{CdS}_x\text{Se}_{1-x}$ nanowires	70–100	~10	Wurtzite	1.75–2.45	[54]
$\text{CdS}_x\text{Se}_{1-x}$ nanowires	50–100	10–50	Wurtzite	1.74–2.45	[9]
$\text{CdS}_x\text{Se}_{1-x}$ nanowires	100–200	Dozens	Wurtzite	1.73–2.43	[56]

by different synthesis methods. And, these synthesis methods have different advantages and disadvantages. Hot-injection synthesis is a good method to prepare CdSeS nanocrystals or quantum dots with high tunable luminescence properties and narrow size distribution, but it involves toxic organic solvents and performs poorly in synthesis reproducibility; so finding replaceable green solvents and improving the reproducibility of this method are needed. One-pot, noninjection synthesis is suitable for large-scale production of CdSeS nanostructures; however, how to enhance quantum yield of CdSeS nanostructures is still a problem. The thermal and nonthermal effects of microwave irradiation synthesis have been still poorly understood, which limits its application. Solvothermal synthesis can prepare 1D CdSeS nanostructures with high crystallinity and good orientation, but the reaction should be carried out in a sealed reactor, in which the procedure cannot be monitored in time; so the growth mechanism of CdSeS nanostructures by this method is difficult to study. Template-assisted electrodeposition synthesis is a high cost and energy-wasting method, due to the fact that it needs continuous electric power supply during the synthesis process. Thermal evaporation synthesis is an easy handling method to prepare CdSeS nanostructures; at present, the challenge for it is how to obtain CdSeS nanostructures with high uniformity for the large-scale production. And pulsed laser deposition synthesis has difficulty controlling the experimental conditions to prepare CdSeS nanostructures with controllable structures. Consequently, though so many synthesis methods were proposed to prepare CdSeS nanostructures and many attempts have been tried to improve these methods, methods which are safe, economic, environment-friendly, and suitable for large-scale production of alloyed CdSeS nanostructures with high photoluminescence, high stability, and low/no cytotoxicity are still much desired.

Conflict of Interests

The authors declare that there is no conflict of interests regarding the publication of this paper.

Acknowledgments

The authors would like to acknowledge the financial support for this work from the National Natural Science Foundation of China (Grant nos. 61274015, 11274052, and 51172030), Excellent Adviser Foundation in China University of Geosciences from the Fundamental Research Funds for the Central Universities, and Fund of State Key Laboratory of Information Photonics and Optical Communications (Beijing University of Posts and Telecommunications).

References

- [1] Z. R. Tian, J. A. Voigt, J. Liu et al., “Complex and oriented ZnO nanostructures,” *Nature Materials*, vol. 2, no. 12, pp. 821–826, 2003.
- [2] L. W. Yin and Y. Bando, “Semiconductor morphology: optimizing properties by tuning morphology,” *Nature Materials*, vol. 4, no. 12, pp. 883–884, 2005.
- [3] M. J. Bierman, Y. K. A. Lau, A. V. Kvit, A. L. Schmitt, and S. Jin, “Dislocation-driven nanowire growth and Eshelby twist,” *Science*, vol. 320, no. 5879, pp. 1060–1063, 2008.
- [4] X. D. Li, X. N. Wang, Q. H. Xiong, and P. C. Eklund, “Mechanical properties of ZnS nanobelts,” *Nano Letters*, vol. 5, no. 10, pp. 1982–1986, 2005.
- [5] B. Z. Tian, X. Zheng, T. J. Kempa et al., “Coaxial silicon nanowires as solar cells and nanoelectronic power sources,” *Nature*, vol. 449, no. 7164, pp. 885–889, 2007.
- [6] A. Pan, D. Liu, R. Liu, F. Wang, X. Zhu, and B. Zou, “Optical waveguide through CdS nanoribbons,” *Small*, vol. 1, no. 10, pp. 980–983, 2005.
- [7] P. K. Santra and P. V. Kamat, “Tandem-layered quantum dot solar cells: tuning the photovoltaic response with luminescent ternary cadmium chalcogenides,” *Journal of the American Chemical Society*, vol. 135, no. 2, pp. 877–885, 2013.
- [8] A. L. Pan, H. Yang, R. Liu, R. Yu, B. Zou, and Z. Wang, “Color-tunable photoluminescence of alloyed $\text{CdS}_x\text{Se}_{1-x}$ nanobelts,” *Journal of the American Chemical Society*, vol. 127, no. 45, pp. 15692–15693, 2005.

- [9] Y.-J. Choi, I.-S. Hwang, J.-H. Park, S. Nahm, and J.-G. Park, "Band gap modulation in $\text{CdS}_x\text{Se}_{1-x}$ nanowires synthesized by a pulsed laser ablation with the Au catalyst," *Nanotechnology*, vol. 17, no. 15, 2006.
- [10] Y. K. Liu, J. A. Zapien, Y. Y. Shan, H. Tang, C. S. Lee, and S. T. Lee, "Wavelength-tunable lasing in single-crystal $\text{CdS}_{1-x}\text{Se}_x$ nanoribbons," *Nanotechnology*, vol. 18, no. 36, Article ID 365606, 2007.
- [11] A. L. Pan, W. C. Zhou, E. S. P. Leong et al., "Continuous alloy-composition spatial grading and superbroad wavelength-tunable nanowire lasers on a single chip," *Nano Letters*, vol. 9, no. 2, pp. 784–788, 2009.
- [12] E. Jang, S. Jun, and L. Pu, "High quality CdSeS nanocrystals synthesized by facile single injection process and their electroluminescence," *Chemical Communications*, vol. 9, no. 24, pp. 2964–2965, 2003.
- [13] J. P. Lu, C. Sun, M. R. Zheng et al., "Facile one-step synthesis of $\text{CdS}_x\text{Se}_{1-x}$ nanobelts with uniform and controllable stoichiometry," *The Journal of Physical Chemistry C*, vol. 115, no. 40, pp. 19538–19545, 2011.
- [14] U. Rössler, Ed., *Semiconductors: II–VI and I–VII Compounds, Semimagnetic Compounds*, vol. 41B, Springer, Berlin, Germany, 1999.
- [15] G. Mei, "A photoluminescence study of $\text{CdS}_x\text{Se}_{1-x}$ semiconductor quantum dots," *Journal of Physics: Condensed Matter*, vol. 4, no. 36, pp. 7521–7528, 1992.
- [16] G. Perna, S. Pagliara, V. Capozzi, M. Ambrico, and T. Ligonzo, "Optical characterization of $\text{CdS}_x\text{Se}_{1-x}$ films grown on quartz substrate by pulsed laser ablation technique," *Thin Solid Films*, vol. 349, no. 1–2, pp. 220–224, 1999.
- [17] N. Hildebrandt, "Biofunctional quantum dots: controlled conjugation for multiplexed biosensors," *ACS Nano*, vol. 5, no. 7, pp. 5286–5290, 2011.
- [18] L. Tang, C. L. Zhang, G. M. Song, X. Jin, and Z. Xu, "In vivo skin penetration and metabolic path of quantum dots," *Science China Life Sciences*, vol. 56, no. 2, pp. 181–188, 2013.
- [19] X. Michalet, F. F. Pinaud, L. A. Bentolila et al., "Quantum dots for live cells, in vivo imaging, and diagnostics," *Science*, vol. 307, no. 5709, pp. 538–544, 2005.
- [20] A. L. Pan, R. B. Liu, F. F. Wang et al., "High-quality alloyed $\text{CdS}_x\text{Se}_{1-x}$ whiskers as waveguides with tunable stimulated emission," *The Journal of Physical Chemistry B*, vol. 110, no. 45, pp. 22313–22317, 2006.
- [21] X. H. Song, M. Q. Wang, J. P. Deng et al., "One-step preparation and assembly of aqueous colloidal $\text{CdS}_x\text{Se}_{1-x}$ nanocrystals within mesoporous TiO_2 films for quantum dot-sensitized solar cells," *ACS Applied Materials and Interfaces*, vol. 5, no. 11, pp. 5139–5148, 2013.
- [22] B. Z. Liu, R. F. Li, L. Hu, and H. Wu, "White light-emitting quantum dot diodes and tuning of luminescence processes," *Applied Physics A*, vol. 116, no. 3, pp. 941–945, 2014.
- [23] J. H. Kang, Y. Myung, J. W. Choi et al., " Nb_2O_5 nanowire photoanode sensitized by a composition-tuned $\text{CdS}_x\text{Se}_{1-x}$ shell," *Journal of Materials Chemistry*, vol. 22, no. 17, pp. 8413–8419, 2012.
- [24] T. K. Sung, J. H. Kang, D. M. Jang et al., "CdSSe layer-sensitized TiO_2 nanowire arrays as efficient photoelectrodes," *Journal of Materials Chemistry*, vol. 21, no. 12, pp. 4553–4561, 2011.
- [25] M. A. Hossain, J. R. Jennings, N. Mathews, and Q. Wang, "Band engineered ternary solid solution $\text{CdS}_x\text{Se}_{1-x}$ -sensitized mesoscopic TiO_2 solar cells," *Physical Chemistry Chemical Physics*, vol. 14, no. 19, pp. 7154–7161, 2012.
- [26] T. Nann and W. M. Skinner, "Quantum dots for electro-optic devices," *ACS Nano*, vol. 5, no. 7, pp. 5291–5295, 2011.
- [27] R. C. Han, M. Yu, Q. Zheng, L. J. Wang, Y. K. Hong, and Y. L. Sha, "A facile synthesis of small-sized, highly photoluminescent, and monodisperse CdSeS QD/ SiO_2 for live cell imaging," *Langmuir*, vol. 25, no. 20, pp. 12250–12255, 2009.
- [28] M. Ali, S. Chattopadhyay, A. Nag et al., "White-light emission from a blend of CdSeS nanocrystals of different Se:S ratio," *Nanotechnology*, vol. 18, no. 7, Article ID 075401, 2007.
- [29] P. Alivisatos, "The use of nanocrystals in biological detection," *Nature Biotechnology*, vol. 22, no. 1, pp. 47–52, 2004.
- [30] J. P. Zimmer, S.-W. Kim, S. Ohnishi, E. Tanaka, J. V. Frangioni, and M. G. Bawendi, "Size series of small indium arsenide-zinc selenide core-shell nanocrystals and their application to *in vivo* imaging," *Journal of the American Chemical Society*, vol. 128, no. 8, pp. 2526–2527, 2006.
- [31] E. Petryayeva and W. R. Algar, "Multiplexed homogeneous assays of proteolytic activity using a smartphone and quantum dots," *Analytical Chemistry*, vol. 86, no. 6, pp. 3195–3202, 2014.
- [32] I. Robel, V. Subramanian, M. Kuno, and P. V. Kamat, "Quantum dot solar cells. Harvesting light energy with CdSe nanocrystals molecularly linked to mesoscopic TiO_2 films," *Journal of the American Chemical Society*, vol. 128, no. 7, pp. 2385–2393, 2006.
- [33] M. Elisa, C. Vasiliu, J. Striber, D. Radu, J. H. Trodahl, and M. Dalley, "Optical and structural investigations on CdSSe-doped aluminophosphate glasses," *Journal of Optoelectronics and Advanced Materials*, vol. 8, no. 2, pp. 811–814, 2006.
- [34] P. O. Anikeeva, J. E. Halpert, M. G. Bawendi, and V. Bulović, "Quantum dot light-emitting devices with electroluminescence tunable over the entire visible spectrum," *Nano Letters*, vol. 9, no. 7, pp. 2532–2536, 2009.
- [35] J. Y. Ouyang, M. Vincent, D. Kingston et al., "Noninjection, one-pot synthesis of photoluminescent colloidal homogeneously alloyed CdSeS quantum dots," *The Journal of Physical Chemistry C*, vol. 113, no. 13, pp. 5193–5200, 2009.
- [36] X. Chen, J. L. Hutchison, P. J. Dobson, and G. Wakefield, "Tuning the internal structures of CdSeS nanoparticles by using different selenium and sulphur precursors," *Materials Science and Engineering B: Solid-State Materials for Advanced Technology*, vol. 166, no. 1, pp. 14–18, 2010.
- [37] R. E. Bailey and S. Nie, "Alloyed semiconductor quantum dots: tuning the optical properties without changing the particle size," *Journal of the American Chemical Society*, vol. 125, no. 23, pp. 7100–7106, 2003.
- [38] L. A. Swafford, L. A. Weigand, M. J. Bowers II et al., "Homogeneously alloyed $\text{CdS}_x\text{Se}_{1-x}$ nanocrystals: synthesis, characterization, and composition/size-dependent band gap," *Journal of the American Chemical Society*, vol. 128, no. 37, pp. 12299–12306, 2006.
- [39] R. Elbaum, S. Vega, and G. Hodes, "Preparation and surface structure of nanocrystalline cadmium sulfide (Sulfoselenide) precipitated from dimethyl sulfoxide solutions," *Chemistry of Materials*, vol. 13, no. 7, pp. 2272–2280, 2001.
- [40] A. P. Alivisatos, "Perspectives on the physical chemistry of semiconductor nanocrystals," *The Journal of Physical Chemistry*, vol. 100, no. 31, pp. 13226–13239, 1996.
- [41] H. F. Qian, L. Li, and J. C. Ren, "One-step and rapid synthesis of high quality alloyed quantum dots (CdSe-CdS) in aqueous phase by microwave irradiation with controllable temperature," *Materials Research Bulletin*, vol. 40, no. 10, pp. 1726–1736, 2005.

- [42] Y. C. Cao and J. H. Wang, "One-pot synthesis of high-quality zinc-blende CdS nanocrystals," *Journal of the American Chemical Society*, vol. 126, no. 44, pp. 14336–14337, 2004.
- [43] Y. Zou, D. S. Li, and D. Yang, "Noninjection synthesis of CdS and alloyed $\text{CdS}_x\text{Se}_{1-x}$ nanocrystals without nucleation initiators," *Nanoscale Research Letters*, vol. 5, no. 6, pp. 966–971, 2010.
- [44] C. Ünlü, G. Ü. Tosun, S. Sevim, and S. Özçelik, "Developing a facile method for highly luminescent colloidal $\text{CdS}_x\text{Se}_{1-x}$ ternary nanoalloys," *The Journal of Materials Chemistry C*, vol. 1, no. 17, pp. 3026–3034, 2013.
- [45] S. K. Lim, M. J. Tambe, M. M. Brewster, and S. Gradečak, "Controlled growth of ternary alloy nanowires using metalorganic chemical vapor deposition," *Nano Letters*, vol. 8, no. 5, pp. 1386–1392, 2008.
- [46] J. C. Blake, P. S. Eldridge, and L. Gundlach, "Spatial variation in carrier dynamics along a single CdSSe nanowire," *Chemical Physics*, vol. 442, pp. 128–131, 2015.
- [47] A. I. Hochbaum and P. Yang, "Semiconductor nanowires for energy conversion," *Chemical Reviews*, vol. 110, no. 1, pp. 527–546, 2010.
- [48] X. Duan, Y. Huang, R. Agarwal, and C. M. Lieber, "Single-nanowire electrically driven lasers," *Nature*, vol. 421, no. 6920, pp. 241–245, 2003.
- [49] A. L. Pan, X. Wang, P. B. He et al., "Color-changeable optical transport through Se-doped CdS 1D nanostructures," *Nano Letters*, vol. 7, no. 10, pp. 2970–2975, 2007.
- [50] L. Gundlach and P. Piotrowiak, "Ultrafast spatially resolved carrier dynamics in single CdSSe nanobelts," *The Journal of Physical Chemistry C*, vol. 113, no. 28, pp. 12162–12166, 2009.
- [51] M. H. Huang, S. Mao, H. Feick et al., "Room-temperature ultraviolet nanowire nanolasers," *Science*, vol. 292, no. 5523, pp. 1897–1899, 2001.
- [52] M. Law, J. Goldberger, and P. D. Yang, "Semiconductor nanowires and nanotubes," *Annual Review of Materials Research*, vol. 34, pp. 83–122, 2004.
- [53] H. J. Fan, P. Werner, and M. Zacharias, "Semiconductor nanowires: from self-organization to patterned growth," *Small*, vol. 2, no. 6, pp. 700–717, 2006.
- [54] G. H. Li, Y. Jiang, Y. Wang et al., "Synthesis of $\text{CdS}_x\text{Se}_{1-x}$ nanoribbons with uniform and controllable compositions via sulfurization: optical and electronic properties studies," *Journal of Physical Chemistry C*, vol. 113, no. 39, pp. 17183–17188, 2009.
- [55] Y. Lu, F. X. Gu, C. Meng et al., "Multicolour laser from a single bandgap-graded CdSSe alloy nanoribbon," *Optics Express*, vol. 21, no. 19, pp. 22314–22319, 2013.
- [56] P. F. Guo, X. J. Zhuang, J. Y. Xu et al., "Low-threshold nanowire laser based on composition-symmetric semiconductor nanowires," *Nano Letters*, vol. 13, no. 3, pp. 1251–1256, 2013.
- [57] Y.-J. Choi, K.-S. Park, and J.-G. Park, "Network-bridge structure of $\text{CdS}_x\text{Se}_{1-x}$ nanowire-based optical sensors," *Nanotechnology*, vol. 21, no. 50, Article ID 505605, 2010.
- [58] K. Premaratne, S. N. Akurathilaka, I. M. Dharmadasa, and A. P. Samantilleka, "Electrodeposition using non-aqueous solutions at 170 °C and characterisation of CdS, $\text{CdS}_x\text{Se}_{(1-x)}$ and CdSe compounds for use in graded band gap solar cells," *Renewable Energy*, vol. 29, no. 4, pp. 549–557, 2004.
- [59] T. Takahashi, P. Nichols, K. Takei et al., "Contact printing of compositionally graded $\text{CdS}_x\text{Se}_{1-x}$ nanowire parallel arrays for tunable photodetectors," *Nanotechnology*, vol. 23, no. 4, pp. 1–4, 2012.
- [60] S.-H. Yu, J. Yang, Z.-H. Han, R.-Y. Yang, Y.-T. Qian, and Y.-H. Zhang, "Novel solvothermal fabrication of $\text{CdS}_x\text{Se}_{1-x}$ nanowires," *Journal of Solid State Chemistry*, vol. 147, no. 2, pp. 637–640, 1999.
- [61] Y. Liu, Y. Xu, J.-P. Li, B. Zhang, D. Wu, and Y.-H. Sun, "Synthesis of $\text{CdS}_x\text{Se}_{1-x}$ nanorods via a solvothermal route," *Materials Research Bulletin*, vol. 41, no. 1, pp. 99–109, 2006.
- [62] Y. Q. Liang, L. Zhai, X. S. Zhao, and D. Xu, "Band-gap engineering of semiconductor nanowires through composition modulation," *The Journal of Physical Chemistry B*, vol. 109, no. 15, pp. 7120–7123, 2005.
- [63] S. J. Kwon, Y.-J. Choi, J.-H. Park, I.-S. Hwang, and J.-G. Park, "Structural and optical properties of $\text{CdS}_x\text{Se}_{1-x}$ nanowires," *Physical Review B*, vol. 72, no. 20, Article ID 205312, 2005.
- [64] F. Fan, Z. Liu, L. Yin et al., "Simultaneous two-color lasing in a single CdSSe heterostructure nanosheet," *Semiconductor Science and Technology*, vol. 28, no. 6, Article ID 065005, 2013.
- [65] P. S. Maiti, N. Meir, L. Houben, and M. Bar-Sadan, "Solution phase synthesis of homogeneously alloyed ultrathin $\text{CdS}_x\text{Se}_{1-x}$ nanosheets," *RSC Advances*, vol. 4, no. 91, pp. 49842–49845, 2014.
- [66] G. Gordillo, "Photoluminescence and photoconductivity studies on $\text{Zn}_x\text{Cd}_{1-x}\text{S}$ thin films," *Solar Energy Materials and Solar Cells*, vol. 25, no. 1-2, pp. 41–49, 1992.
- [67] N. Tschirner, H. Lange, A. Schliwa et al., "Interfacial alloying in CdSe/CdS heteronanocrystals: a raman spectroscopy analysis," *Chemistry of Materials*, vol. 24, no. 2, pp. 311–318, 2012.
- [68] J. I. Contreras-Rascón, J. Díaz-Reyes, R. S. Castillo-Ojeda, J. A. Balderas-López, J. S. Arias-Ceron, and J. E. Flores-Mena, "Growth and characterization of $\text{CdSe}_{1-y}\text{S}_y$ nanofilms obtained by chemical bath deposition," *Brazilian Journal of Physics*, vol. 44, no. 6, pp. 726–732, 2014.
- [69] Y. L. Kim, J. H. Jung, K. H. Kim et al., "The growth and optical properties of CdSSe nanosheets," *Nanotechnology*, vol. 20, no. 9, Article ID 095605, 2009.
- [70] J. Xiang, W. Lu, Y. Hu, Y. Wu, H. Yan, and C. M. Lieber, "Ge/Si nanowire heterostructures as high-performance field-effect transistors," *Nature*, vol. 441, no. 7092, pp. 489–493, 2006.
- [71] Y. Jung, S.-H. Lee, A. T. Jennings, and R. Agarwal, "Core-shell heterostructured phase change nanowire multistate memory," *Nano Letters*, vol. 8, no. 7, pp. 2056–2062, 2008.
- [72] F. Qian, S. Gradečak, Y. Li, C.-Y. Wen, and C. M. Lieber, "Core/multishell nanowire heterostructures as multicolor, high-efficiency light-emitting diodes," *Nano Letters*, vol. 5, no. 11, pp. 2287–2291, 2005.
- [73] L. Zhang, R. Tu, and H. Dai, "Parallel core-shell metal-dielectric-semiconductor germanium nanowires for high-current surround-gate field-effect transistors," *Nano Letters*, vol. 6, no. 12, pp. 2785–2789, 2006.
- [74] Y. Myung, D. M. Jang, T. K. Sung et al., "Composition-tuned ZnO-CdSSe core-shell nanowire arrays," *ACS Nano*, vol. 4, no. 7, pp. 3789–3800, 2010.
- [75] A. L. Pan, Y. Lide, Y. Qin et al., "Si-CdSSe core/shell nanowires with continuously tunable light emission," *Nano Letters*, vol. 8, no. 10, pp. 3413–3417, 2008.
- [76] W. Qin, R. A. Shah, and P. Guyot-Sionnest, "CdSeS/ZnS alloyed nanocrystal lifetime and blinking studies under electrochemical control," *ACS Nano*, vol. 6, no. 1, pp. 912–918, 2012.
- [77] S. V. Chong, N. Suresh, J. Xia, N. Al-Salim, and H. Idriss, "TiO₂ nanobelts/CdSSe quantum dots nanocomposite," *The Journal of Physical Chemistry C*, vol. 111, no. 28, pp. 10389–10393, 2007.

- [78] P. Kumar, S. C. Sharma, and A. Deep, "Bioconjugation of anti estrogen alpha antibody with CdSSe/ZnS quantum dots for molecular sensing of a breast cancer antigen," *Sensors and Actuators, B: Chemical*, vol. 202, pp. 404–409, 2014.
- [79] W. Z. Wu, H.-A. Ye, Y. C. Gao, Q. Chang, Z. Zheng, and Y. Yang, "Evolution of fluorescence resonance energy transfer between close-packed CdSeS quantum dots under two-photon excitation," *Journal of Colloid and Interface Science*, vol. 357, no. 2, pp. 331–335, 2011.
- [80] S. S. Brown, A. J. Rondinone, M. D. Pawel, and S. Dai, "Ternary cadmium sulphide selenide quantum dots as new scintillation materials," *Materials Technology*, vol. 23, no. 2, pp. 94–99, 2008.
- [81] M. D. Garrett, A. D. Dukes III, J. R. McBride, N. J. Smith, S. J. Pennycook, and S. J. Rosenthal, "Band edge recombination in CdSe, CdS and CdS_xSe_{1-x} alloy nanocrystals observed by ultrafast fluorescence upconversion: the effect of surface trap states," *The Journal of Physical Chemistry C*, vol. 112, no. 33, pp. 12736–12746, 2008.
- [82] M. Yu, Y. Yang, R. C. Han et al., "Polyvalent lactose-quantum dot conjugate for fluorescent labeling of live leukocytes," *Langmuir*, vol. 26, no. 11, pp. 8534–8539, 2010.
- [83] T. P. A. Ruberu and J. Vela, "Expanding the one-dimensional CdS-CdSe composition landscape: axially anisotropic CdS_{1-x}Se_x nanorods," *ACS Nano*, vol. 5, no. 7, pp. 5775–5784, 2011.
- [84] W. Z. Wu, D. Q. Yu, H.-A. Ye, Y. Gao, and Q. Chang, "Temperature and composition dependent excitonic luminescence and exciton-phonon coupling in CdSeS nanocrystals," *Nanoscale Research Letters*, vol. 7, no. 1, p. 301, 2012.
- [85] M. A. Harrison, A. Ng, A. B. Hmelo, and S. J. Rosenthal, "CdSSe nanocrystals with induced chemical composition gradients," *Israel Journal of Chemistry*, vol. 52, no. 11-12, pp. 1063–1072, 2012.
- [86] F. R. Jiang and G. L. Tan, "Fabrication and optical properties of water soluble CdSeS nanocrystals using glycerin as stabilizing agent," *PLoS ONE*, vol. 8, no. 10, Article ID 0077253, 2013.
- [87] J.-P. Kim, J. A. Christians, H. Choi, S. Krishnamurthy, and P. V. Kamat, "CdSeS nanowires: compositionally controlled band gap and exciton dynamics," *The Journal of Physical Chemistry Letters*, vol. 5, no. 7, pp. 1103–1109, 2014.
- [88] N. Al-Salim, A. G. Young, R. D. Tilley, A. J. McQuillan, and J. Xia, "Synthesis of CdSeS nanocrystals in coordinating and noncoordinating solvents: solvent's role in evolution of the optical and structural properties," *Chemistry of Materials*, vol. 19, no. 21, pp. 5185–5193, 2007.
- [89] J. Q. Jia and J. T. Tian, "One-pot synthesis in liquid paraffin of ternary alloy CdSe_xS_{1-x} nanocrystals with fluorescence emission covering entire visible region," *Journal of Nanoparticle Research*, vol. 16, no. 2, article 2283, 2014.
- [90] H.-J. Zhan, P.-J. Zhou, L. Ding, Z.-Y. He, and R. Ma, "Multi-spectroscopic techniques to evaluate the toxicity of alloyed CdSeS quantum dots," *Journal of Luminescence*, vol. 132, no. 10, pp. 2769–2774, 2012.
- [91] H.-J. Zhan, P.-J. Zhou, R. Ma, X.-J. Liu, Y.-N. He, and C.-Y. Zhou, "Enhanced oxidation stability of quasi core-shell alloyed CdSeS quantum dots prepared through aqueous microwave synthesis technique," *Journal of Fluorescence*, vol. 24, no. 1, pp. 57–65, 2014.
- [92] H. Grisar, O. Palchik, A. Gedanken, V. Palchik, M. A. Slifkin, and A. M. Weiss, "Microwave-assisted polyol synthesis of CuInTe₂ and CuInSe₂ nanoparticles," *Inorganic Chemistry*, vol. 42, no. 22, pp. 7148–7155, 2003.
- [93] J. J. Zhu, O. Palchik, S. G. Chen et al., "Microwave assisted preparation of CdSe, PbSe, and Cu_{2-x}Se nanoparticles," *The Journal of Physical Chemistry B*, vol. 104, no. 31, pp. 7344–7347, 2000.
- [94] C. Yang, X. C. Zhou, L. Y. Wang, X. Tian, Y. Wang, and Z. Pi, "Preparation and tunable photoluminescence of alloyed CdS_xSe_{1-x} nanorods," *Journal of Materials Science*, vol. 44, no. 12, pp. 3015–3019, 2009.
- [95] J. H. Zhan, X. G. Yang, S. D. Li, D. W. Wang, Y. Xie, and Y. T. Qian, "A chemical solution transport mechanism for one-dimensional growth of CdS nanowires," *Journal of Crystal Growth*, vol. 220, no. 3, pp. 231–234, 2000.
- [96] D. Routkevitch, A. A. Tager, J. Haruyama, D. Almalawi, M. Moskovits, and J. M. Xu, "Nonlithographic nano-wire arrays: fabrication, physics, and device applications," *IEEE Transactions on Electron Devices*, vol. 43, no. 10, pp. 1646–1658, 1996.
- [97] L. F. Dong, J. Jiao, M. Coulter, and L. Love, "Catalytic growth of CdS nanobelts and nanowires on tungsten substrates," *Chemical Physics Letters*, vol. 376, no. 5-6, pp. 653–658, 2003.
- [98] S. Kar and S. Chaudhuri, "Shape selective growth of CdS one-dimensional nanostructures by a thermal evaporation process," *The Journal of Physical Chemistry B*, vol. 110, no. 10, pp. 4542–4547, 2006.
- [99] Z. W. Pan, Z. R. Dai, and Z. L. Wang, "Nanobelts of semiconducting oxides," *Science*, vol. 291, no. 5510, pp. 1947–1949, 2001.
- [100] C. Ma, Y. Ding, D. Moore, X. Wang, and Z. L. Wang, "Single-crystal CdSe nanosaws," *Journal of the American Chemical Society*, vol. 126, no. 3, pp. 708–709, 2004.
- [101] F. X. Gu, Z. Y. Yang, H. K. Yu et al., "Spatial bandgap engineering along single alloy nanowires," *Journal of the American Chemical Society*, vol. 133, no. 7, pp. 2037–2039, 2011.
- [102] J. Pan, M. I. B. Utama, Q. Zhang et al., "Composition-tunable vertically aligned CdS_xSe_{1-x} nanowire arrays via van der Waals epitaxy: investigation of optical properties and photocatalytic behavior," *Advanced Materials*, vol. 24, no. 30, pp. 4151–4156, 2012.
- [103] H. W. Liu, J. P. Lu, H. F. Teoh et al., "Defect engineering in CdSe_xS_{1-x} nanobelts: an insight into carrier relaxation dynamics via optical pump-terahertz probe spectroscopy," *The Journal of Physical Chemistry C*, vol. 116, no. 49, pp. 26036–26042, 2012.
- [104] Y. L. Kim, J. H. Jung, H. S. Yoon et al., "CdS/CdSe lateral heterostructure nanobelts by a two-step physical vapor transport method," *Nanotechnology*, vol. 21, no. 14, Article ID 145602, 2010.